

POLITECNICO DI TORINO

DIPARTIMENTO DI INGEGNERIA MECCANICA E AEROSPAZIALE

MSc. in Mechanical engineering

Master Degree Thesis

**Design and FEM Simulation of dual
mass resonant MEMS Gyroscope**



Supervisors

Prof. Aurelio Somà

Candidates

Francesca PISTORIO

ACADEMIC YEAR 2019-2020

This work is subject to the Creative Commons Licence

*"Si faccia una vita interiore, di studio, di affetti,
che non siano soltanto di arrivare ma di essere
e vedrà che la vita avrà un significato."*

Abstract

This thesis presents a new design of a dual mass resonant mode-matched electrostatic z-axis MEMS gyroscope considering the foundry constraints of relatively low cost and commercially available Silicon-on-Insulator (SOI) based SOIMUMPs process. The novelty of the proposed MEMS gyroscope design lies in the use of two separate masses for the drive and sense axis while minimizing the cross-axis sensitivity by decoupling the drive and sense move displacements using a unique configuration of mechanical springs. For the compensation of the frequency mismatch between the drive and sense mode frequency due to microfabrication process tolerances and device operating temperature variations, comb-drive based electrostatic tuning is implemented in the design. A preliminary automatic mode-matching closed-loop system control is then implemented in SIMULINK environment to tune automatically the sense mode frequency. Finally, the performance improvement is checked against operating temperature variations.

Keywords: MEMS, Mechanical Design, FEM Analysis, Resonant Gyroscope, Mechanical Design, Electrostatic Tuning, Microfabrication.

Introduction

Microelectromechanical systems (MEMS) are interesting devices that nowadays are becoming of great importance, both for the new frontiers that they open in scientific field and the possible application in industrial products.

With the rapid development of MEMS technology, silicon micromachined gyroscopes, or MEMS gyroscopes, have attracted much attention. They are devices that measure angular velocity and, as an alternative to classical rate gyroscopes, they play an important role in inertial navigation and control systems of flight vehicles, and may have applications in automobile design, defence, consumer electronics and biomedical engineering. The benefits of micromechanical gyroscopes over classical gyroscope are robustness, low power consumption, potential for miniaturization and low cost. Vibrating structure gyroscopes, or Coriolis vibratory gyroscopes, constitute a wide group of MEMS gyroscopes. The underlying physical principle is that a vibrating object tends to continue to vibrate in the same plane as its support rotates. In gyroscopes, generally, an inertial mass is oscillating at the natural resonance frequency and the effect of the Coriolis force that originates on one or more detection elements in the presence of an external angular velocity is measured.

A variety of structures can be used to implement MEMS Coriolis vibratory gyroscopes. Broadly, based on the working principle, the MEMS Coriolis vibratory gyroscopes are divided into two main categories including resonant and non-resonant gyroscopes. In resonant MEMS gyroscopes, the device is operated at resonance and both the drive and sense mode resonant frequency values are matched which leads to high mechanical sensitivity. A major challenge faced by the MEMS designer is the fluctuation in the performance parameters of resonant MEMS gyroscopes as they are easily affected by any variation in ambient conditions and fabrication imperfections. These imperfections can cause a shift in resonance frequency which in turn causes a mismatch between the drive and sense mode frequencies and leads the device performance to reduce dramatically. Indeed, even a slight mismatch can reduce the amplitude response of a mode matched gyroscope significantly. To minimize these effects, complex structures have to be introduced in the design or additional feedback circuitry is required to reduce the mismatch between drive and sense mode frequencies.

Several methods to compensate the frequency mismatch between modes exist in literature. Due to low cost, little damage to the gyroscope structure, and easy adaptability in different gyroscopes, a more effective method at present is the electrostatic adjustment technology. It utilizes a structure-specific electrostatic negative stiffness effect to change the stiffness of the structure by adjusting the DC voltage, thereby altering the resonant frequency to achieve the purpose of mode-matching. This allows the designer to reduce the mismatch and to get the optimal performance of the gyroscope. The electrostatic tuning method can be realized by controlling the tuning voltage manually or automatically. The automatic control can be realized based on the frequency response characteristic of the mass-spring oscillator related to the drive and sense mode. When the gyroscope structure is excited in the drive direction at the natural frequency and the drive and sense mode frequencies are perfectly matched, the vibration amplitude in the sense direction achieves its maximum value and the phase delay caused by the sense dynamic is 90° degree. Thus, designing the automatic

control loop using the phase characteristic of the gyroscope output, the mode-matching condition can be automatically achieved.

Another import aspect to take into account during design of resonant MEMS gyroscopes is that the number of proof masses can affect the common mode errors and hence the performance of the device. The designs utilizing multiple proof masses operate in the anti-phase mode, this motion assures minimization of the net reaction forces and moments on the anchors, which mitigates the energy loss through the substrate. This design approach results in a larger overall size but better performance. Another approach is to use a single proof mass which results in a smaller footprint of the device, but the performance is worst. Consequently, trade-offs have to be made between optimal performance and keeping the size of the device to a minimum.

In this master's thesis project, a new design of resonant mode-matched z-axis MEMS gyroscope consisting of two separate masses for the drive and sense mode is presented, which allows to minimize the cross-axis sensitivity and common mode error. In particular, the new design considers the foundry constraints of relatively low cost and commercially available Silicon-on-Insulator (SOI) based SOIMUMPs process. The novelty of the proposed MEMS gyroscope design lies in the use of two separate masses for the drive and sense axis while minimizing the cross-axis sensitivity by decoupling the drive and sense mode displacements using a unique configuration of mechanical springs. For the compensation of the frequency mismatch between the drive and sense mode frequency due to micro-fabrication process tolerances and device operating temperature variations, comb-drive based electrostatic tuning is implemented in the design.

An analytical simplified lumped parameter model of the MEMS gyroscope structure is first developed based on the literature, and static and dynamical behaviour is deeply analyzed. A FEM analysis of the presented MEMS gyroscope is then carried out in ANSYS APDL. A particular attention is taken on the dynamical behaviour of the structure, which is strongly influenced by the electro-mechanical coupling. In addition, FEM simulation results are compared to the simplified analytical model solutions. A preliminary closed-loop mode-matching controller that provides a DC tuning potential is designed regarding the phase relationship between the drive and sense signals. In addition, the effects of the closed-loop control systems on the dynamical behaviour of the presented MEMS gyroscope structure are simulated in Matlab/SIMULINK environment. A final FEM-based analysis is carried out in Ansys to check the actual improvement in the MEMS gyroscope performance against operating temperature variations.

The thesis is structured around six chapters which firstly give an introduction to MEMS gyroscopes and then describe the implemented design with the related analysis.

More in details:

1. The first chapter provides an overview about the gyroscope history with a special focus on the MEMS technology.
2. The second chapter presents the dynamics of a generic MEMS gyroscope with an emphasis on the fundamental mechanical elements, the presentation and the analysis of common mechanical structures and various flexure systems. In addition, a discussion about the electrical design issues in a generic micro-electromechanical vibratory system to realize the complete gyroscopic system is provided, covering the fundamentals of electrostatic and capacitive sensing methods. A complete characterization of the major common dissipation mechanisms is finally provided.
3. The third chapter describes the simulation methodology used to analyze the proposed MEMS gyroscope devices. The general procedure of FEM simulation in Ansys is presented, including specialized simulation approaches using static, modal and harmonic FEM analysis. A special focus on the elements used to build the mesh of the FEM models implemented in Ansys is given and a more specialized discussion on some of the most important aspects for the

simulation of the proposed MEMS gyroscope structures, such as the Coriolis effect, damping and thermal effects modelling, is finally provided.

4. The fourth chapter presents a preliminary design of a single mass z-axis resonant MEMS gyroscope. This simple model has been designed with the precise objective of getting familiar with the basic MEMS design techniques both from an analytical perspective and from a FEM model implementation.
5. The fifth chapter presents in detail the proposed new design of resonant MEMS gyroscope consisting of two separate masses for the drive and sense mode. First, the MEMS gyroscope structure is described in detail, with a focus on the design process steps followed to determine the geometrical parameters. Then the analytical model is developed and static and dynamical behaviour analyses are presented. A FEM-based model is successively implemented in Ansys and a comparison between analytical and FEM-based model results is finally provided.
6. The sixth chapter presents the electrostatic tuning, which is one of the novelties implemented in the MEMS gyroscope structure developed for the compensation of the frequency mismatch between the drive and sense mode frequency due to microfabrication process tolerances and device operating temperature variations. First the electrostatic tuning is modelled analytically, based on the models available in literature, then a FEM-based analysis is carried out to check the actual device behaviour subjected to a tuning electrostatic voltage. A preliminary automatic mode-matching closed-loop system control is then implemented in SIMULINK environment to tune automatically the sense mode frequency. Finally, the performance improvement is checked against operating temperature variations.
7. The seventh chapter provides the conclusions about the thesis project and the related future works.

Acknowledgements

It is really curious how this section is put in the front but written at the last. Probably thinking about how to make an acknowledgement and to whom it should be addressed is the most difficult thing, harder than writing the whole document. Simply because using a paper and choosing the words to express gratitude is extremely difficult.

First of all I would thank Professor Aurelio Somà for his sincere help, empathy, expertise and patience. He has represented a fundamental figure in this difficult months and his continuous insights and suggestions have represented a fundamental contribution for this work.

Secondly I feel to strongly thank Professor Mubasher Saleem for the support and precious advices I have received during these months. His guidance has been fundamental during the design and analysis phase. I really appreciate his strong availability and the passion he puts into his work which has been transmitted to me during the collaboration. Thank you.

Contents

Abstract	I
Introduction	III
Acknowledgements	VII
List of Figures	XII
List of Tables	XIX
1 Gyroscopes overview	1
1.1 Background of Gyroscopes	1
1.1.1 Brief history of Gyroscopes development	1
1.1.2 Classification of Gyroscopes	4
1.2 MEMS Technology	7
1.2.1 MEMS origin	9
1.2.2 Applications	10
1.2.3 Technological process	10
1.3 MEMS Gyroscopes	11
1.3.1 Brief history of MEMS Gyroscopes development	12
1.3.2 Applications	15
1.3.3 MEMS Gyroscope performance requirements	17
1.3.4 MEMS Gyroscopes classification	18
2 MEMS Gyroscope Design Fundamentals	21
2.1 Working principle	21
2.2 Analytical Model	23
2.2.1 Drive-mode dynamics	25
2.2.2 Sense-mode dynamics	26
2.2.3 Mode-matching	28
2.3 Mechanical structure	28
2.3.1 Flexure elements	29
2.3.2 Frame Structures	31
2.4 Electrical design	32
2.4.1 Electrostatic actuation	34
2.4.2 Capacitive sensing	37
2.4.3 Pull-in and electrostatic spring softening effect	41
2.5 Damping	45
2.5.1 Viscous air-damping	45

2.5.2	Thermoelastic damping	49
2.5.3	Anchor losses	49
3	Simulation methodology	51
3.1	FEM simulation	51
3.1.1	Static analysis	53
3.1.2	Modal analysis	54
3.1.3	Harmonic analysis	55
3.2	Element types	58
3.2.1	Mechanical domain	58
3.2.2	Electromechanical coupling	60
3.2.3	Damping modelling	63
3.3	MEMS gyroscope simulation methodology	63
3.3.1	Coriolis effect	63
3.3.2	Modelling Damping	65
3.3.3	Modelling electromechanical coupling	67
4	Preliminary design and analysis	71
4.1	Mechanical design and working principle	71
4.2	Analytical model	74
4.2.1	Calculation of mechanical stiffness	75
4.2.2	Electrical design	75
4.2.3	Air damping analysis	77
4.3	Analytical model results	80
4.3.1	Static analysis	80
4.3.2	Modal analysis	81
4.3.3	Harmonic analysis	81
4.4	FEM Model	82
4.4.1	Structural mesh	82
4.4.2	Damping modelling	83
4.4.3	Electromechanical coupling modelling	84
4.5	FEM model results	85
4.5.1	Static Analysis	85
4.5.2	Modal Analysis	85
4.5.3	Harmonic analysis	88
5	Dual mass resonant MEMS gyroscope model	95
5.1	Mechanical design and working principle	95
5.2	Analytical model	100
5.2.1	Calculation of mechanical stiffness	101
5.2.2	Electrical Design	103
5.2.3	Air Damping Analysis	105
5.3	Analytical model results	109
5.3.1	Static analysis	109
5.3.2	Modal analysis	110
5.3.3	Harmonic analysis	111
5.4	FEM Model	113
5.4.1	Structural mesh	114
5.4.2	Damping modelling	115
5.4.3	Electromechanical coupling modelling	116
5.5	FEM model results	118

5.5.1	Static analysis	119
5.5.2	Modal analysis	119
5.5.3	Harmonic analysis	121
6	Electrostatic tuning	125
6.1	Analytical model	125
6.2	Analytical model results	128
6.3	FEM model	129
6.4	FEM model results	132
6.5	Automatic mode-matching control system	138
6.5.1	Control-loop system design	138
6.5.2	Control-loop system analysis	141
6.5.3	Simulation analysis for automatic mode-matching	144
6.6	Temperature variations	148
6.6.1	Thermal effects	149
6.6.2	Compensation of temperature variation effects	158
7	Conclusion	163
7.1	Project findings	163
7.2	Future works	164
A	Single-degree-of-freedom oscillator	165
B	SOIMUMPs Fabrication process	169
C	Applying Prestress Effects in a Modal Analysis	175
D	Automatic mode-matching system control implemented in SIMULINK	177
	Bibliography	181

List of Figures

1.1	The <i>Machine</i> invented by Bohnenberger.	2
1.2	The Foucault pendulum in the Panthéon.	3
1.3	A Tuning Fork Gyroscope scheme.	5
1.4	Hemispherical Resonator Gyroscope (Smithsonian Institution).	5
1.5	Ring laser gyroscope produced by Ukrainian "Arsenal" factory on display at MAKSS-2011 airshow.	7
1.6	A MEMS device compared to a matchstick [29].	8
1.7	A clearly idea of the potentialialities of miniaturization behind the microsystems technology [16].	8
1.8	MEMS devices on a silicon wafer [29].	11
1.9	The Double gimbal bulk-silicon MEMS gyroscope developed by Draper Laboratory [36].	12
1.10	First working prototype tuning fork gyroscope from the Draper Laboratory [36].	13
1.11	Die photograph of the z-axis gyroscope developed by UC Berkeley in 1996 [36].	14
1.12	Dual axis MEMS gyroscope developed by UC Berkeley in 1997 [36].	14
1.13	SEM of the M2-TFG developed by Georgia Institute of Technology and illustration of the mode shapes [36].	15
1.14	SEM picture of the multiple-beam tuning-fork gyroscope (MB-TFG) design developed by Old Dominion University and University of Utah [36].	16
1.15	Combined inertial sensor for vehicle dynamic control (Bosch GmbH).	16
1.16	Micro-Rate integrating gyroscope (mRIG) architectures classification [32].	20
2.1	An object moving in a rotating reference frame is subjected to the Coriolis force, acting perpendicular to the object movement and the axis of rotation.	22
2.2	A generic MEMS design for a linear vibratory rate gyroscope designed to measure the angular velocity around the z-axis. A proof-mass is suspended above the substrate using a beams suspension system. One set of electrodes is needed to excite the drive-mode oscillator, and another set of electrodes detects the sense-mode response.	22
2.3	Position vector of the material point P in a fixed inertial frame of reference XYZ and in a non-inertial frame of reference xyz	23
2.4	Two degrees-of-freedom spring-mass damper system is shown as lumped description of a single mass Coriolis vibratory gyroscope. The arrow in x-direction indicates the drive direction, whereas the arrow orthogonal to the first shows the sense direction of motion.	25
2.5	The sense-mode response amplitude of the two degrees-of-freedom MEMS gyroscope system with varying the drive and sense frequency mismatch. The highest response corresponds to the case where the drive and sense modes are matched, while the response amplitude diminishes as the mismatch increases.	29
2.6	Typical beam element of vibratory MEMS gyroscope structures.	30

2.7	Standard suspensions design alternatives for supporting orthogonal linear motions.	32
2.8	Drive frame implementation with U-beam suspensions, minimizing the component of the actual drive motion along the sense detection axis.	33
2.9	Sense frame implementation with U-beam suspensions, minimizing the undesired capacitance change in the sense electrodes due to the drive motion.	33
2.10	Parallel-plate actuator: one electrode is fixed and the other can move in the y -direction. The initial gap between plates is y_0 (a), which becomes $y_0 - y$ when a bias tension V is applied (b).	34
2.11	Comb-drive actuator.	35
2.12	The balanced driving actuation scheme, based on applying $V_1 = V_{DC} + V_{AC}$ to one set of combs, and $V_2 = V_{DC} - V_{AC}$ to the opposing set.	36
2.13	Sensing parallel-plate capacitor: the y deflection due to the Coriolis force F_c causes a change in the capacitance between the fixed and moving electrode.	37
2.14	Interdigitated-comb capacitor for sense-mode detection.	38
2.15	The principle of differential capacitance sensing: a movable central plate is placed between two independent fixed electrodes. In the initial position, the two capacitor-pairs have the same capacitance value. As the structure deflected, capacitance changes are in opposite directions.	39
2.16	The principle of the gap-antigap based differential capacitance sensing.	40
2.17	Mono-dimensional model with lumped parameters: parallel plates capacitor connected to a mechanical spring.	41
2.18	One-dimensional electromechanical model static equilibrium, for a bias voltage V below the pull-in voltage V_{PI} : equilibrium points in green and red represent the stable and unstable equilibrium position, respectively.	42
2.19	One-dimensional electromechanical model static equilibrium for a variable bias voltage V : the purple dot represents the pull-in condition.	43
2.20	The two major sources of viscous air damping: (a) slide film damping; (b) squeeze film damping.	46
3.1	Structure of an APDL script for FE simulations in Ansys.	52
3.2	Beam188 element geometry: I and J are the element nodes, while the cross-section is represented in grey [6].	59
3.3	Shell181 element geometry: I, J, K, and L are the element nodes [6].	59
3.4	Trans126 element connects a node of the mechanical mesh k to a fixed node j , representing the behaviour of a fixed electrode.	61
3.5	Generic capacitance-stroke law: C_0, C_1, C_2, C_3, C_4 are the polynomial coefficients, which can be directly assigned or fit from data sets. GAP represents the initial gap between conductors surfaces, while GAPMIN is the minimum gap.	62
3.6	Combin14 elements geometry: I and J are the elements nodes [6].	63
4.1	Single mass resonant MEMS gyroscope design: it consists of a single proof mass free to oscillate in two orthogonal directions. It is set into oscillations in the x-axis by using comb-drive based electrostatic actuator, while parallel sensing plates arranged in the gap-antigap configuration are used to detect the displacement due to the Coriolis force.	72
4.2	Details of drive mass, sense frame and external anchors for the single mass MEMS gyroscope design.	73
4.3	Two degrees-of-freedom mass–spring–damper model for the proposed single mass MEMS gyroscope. The arrow in x-direction indicates the drive direction, whereas the arrow orthogonal to the first shows the sense direction of motion.	74

4.4	Detail of crab-leg mechanical spring for the proposed single mass MEMS gyroscope design.	76
4.5	Comb-drive based electrostatic actuator implemented in the MEMS gyroscope design.	76
4.6	Sensing parallel-plates arranged in differential gap–antigap configuration implemented in the MEMS gyroscope design.	78
4.7	Analytical static displacement in the drive direction for the proposed single mass MEMS gyroscope design.	80
4.8	The analytical frequency response in the drive direction for the proposed single mass MEMS gyroscope design (<i>logarithmic scale</i>), normalized with respect to the driving force amplitude F_0	82
4.9	The analytical frequency response in the sense direction for the proposed single mass MEMS gyroscope design (<i>logarithmic scale</i>), normalized with respect to the driving force amplitude F_0 , with $\Omega_z = 300^\circ/\text{s}$	83
4.10	Meshed FEM model of the MEMS gyroscope mechanical structure.	84
4.11	: Combin14 elements in FEM model for the MEMS gyroscope mechanical structure.	84
4.12	Setup of Trans 126 elements for FEM based electrostatic analysis.	86
4.13	Comparison between analytical and Ansys static displacement in the drive direction for the proposed single mass MEMS gyroscope design.	87
4.14	Drive and sense resonant frequencies variation with increase of mesh number of elements.	87
4.15	CPU time variation to perform FEM-based modal analysis with increase of mesh number of elements.	88
4.16	Modal analysis results and the corresponding mode shapes for the proposed MEMS gyroscope (a) 1st mode (10273 Hz) (b) 2nd mode (10278 Hz) and (c) 3rd mode (14542 Hz) and (d) 4th mode (26018 Hz).	89
4.17	The FEM-based frequency response in the drive direction for the proposed MEMS gyroscope design (<i>logarithmic scale</i>), with $V_{DC} = 50\text{ V}$ and $V_{AC} = 5\text{ V}$	90
4.18	Comparison of the analytical and FEM-based harmonic analysis results in the drive direction (<i>logarithmic scale</i>), with $V_{DC} = 50\text{ V}$ and $V_{AC} = 5\text{ V}$ (a) Magnitude and (b) Phase.	91
4.19	The FEM-based frequency response in the sense direction for the proposed MEMS gyroscope design (<i>logarithmic scale</i>), with $\Omega_z = 300^\circ/\text{s}$	92
4.20	Comparison of the analytical and FEM-based harmonic analysis results in the sense direction (<i>logarithmic scale</i>), with $\Omega_z = 300^\circ/\text{s}$ (a) Magnitude and (b) Phase.	93
5.1	Dual mass resonant MEMS gyroscope design: it consists of two separate masses for the drive and sense axis which are fully decoupled. The drive mass is set into oscillations in the x-axis by using comb-drive based electrostatic actuator, while parallel sensing plates arranged in the gap-antigap configuration are used to detect the displacement due to the Coriolis force.	96
5.2	Details of drive mass, sense frame and external anchors for the dual mass MEMS gyroscope design.	98
5.3	Iteration scheme for design process of the proposed dual mass MEMS gyroscope.	99
5.4	Two degrees-of-freedom mass–spring–damper model for the proposed dual mass MEMS gyroscope. The arrow in x-direction indicates the drive direction, whereas the arrow orthogonal to the first shows the sense direction of motion.	100
5.5	Mechanical suspension systems for the proposed dual mass MEMS gyroscope design.	101
5.6	Details of drive and sense mechanical springs for the proposed dual mass MEMS gyroscope design.	102

5.7	Comb-drive based electrostatic actuator implemented in the dual mass MEMS gyroscope design.	103
5.8	Sensing parallel-plates arranged in differential gap–antigap configuration implemented in the dual mass MEMS gyroscope design.	104
5.9	Electrostatic tuning combs implemented in the dual mass MEMS gyroscope design.	105
5.10	Effect of oscillation frequency on squeeze film air damping.	109
5.11	Analytical static displacement in the drive direction for the proposed dual mass MEMS gyroscope design.	110
5.12	The analytical frequency response in the drive direction for the proposed dual mass MEMS gyroscope design (<i>logarithmic scale</i>), normalized with respect to the driving force amplitude F_0	112
5.13	The analytical frequency response in the sense direction for the proposed MEMS gyroscope design (<i>logarithmic scale</i>), normalized with respect to the driving force amplitude F_0 , with $\Omega_z = 300^\circ/s$	113
5.14	Meshed FEM model of the MEMS gyroscope mechanical structure.	114
5.15	Boundary conditions and constraint equations applied to the mechanical structure of the dual mass MEMS gyroscope.	115
5.16	Details of constraint equations to couple Beam188 and Shell181 elements of the FEM model for the MEMS gyroscope mechanical structure.	116
5.17	Combin14 elements in FEM model for the MEMS gyroscope mechanical structure.	117
5.18	Details of boundary conditions applied to Combin14 elements.	117
5.19	Setup of Trans 126 elements for FEM based electrostatic analysis.	118
5.20	Comparison between analytical and Ansys static displacement in the drive direction for the proposed dual mass MEMS gyroscope design.	119
5.21	Modal analysis results and the corresponding mode shapes for the proposed dual mass MEMS gyroscope (a) 1st mode (11014 Hz) (b) 2nd mode (11511 Hz) and (c) 3rd mode (34037 Hz) and (d) 4th mode (42861 Hz).	120
5.22	The FEM-based frequency response in the drive direction for the proposed dual mass MEMS gyroscope design (<i>logarithmic scale</i>), with $V_{DC} = 50\text{ V}$ and $V_{AC} = 5\text{ V}$	122
5.23	The FEM-based frequency response in the sense direction for the proposed dual mass MEMS gyroscope design (<i>logarithmic scale</i>), with $\Omega_z = 300^\circ/s$	122
5.24	Comparison of the analytical and FEM-based harmonic analysis results in the drive direction (<i>logarithmic scale</i>), with $V_{DC} = 50\text{ V}$ and $V_{AC} = 5\text{ V}$ (a) Magnitude and (b) Phase.	123
5.25	Comparison of the analytical and FEM-based harmonic analysis results in the sense direction (<i>logarithmic scale</i>), with $\Omega_z = 300^\circ/s$ (a) Magnitude and (b) Phase.	124
6.1	Scheme of the main idea behind the automatic mode-matching system control development.	126
6.2	Configuration scheme of comb-drive based electrostatic tuning.	127
6.3	Analytical frequency tuning characteristics of drive and sense resonant modes as a function of the applied tuning tension V_t . The mode-matching condition (represented in grey) is achieved with $V_t = 21.73\text{ V}$	129
6.4	The analytical frequency response in the drive direction for the proposed dual mass MEMS gyroscope design with tuning application (<i>logarithmic scale</i>), normalized with respect to the driving force amplitude F_0	130
6.5	The analytical frequency response in the sense direction for the proposed dual mass MEMS gyroscope design (<i>logarithmic scale</i>), normalized with respect to the driving force amplitude F_0 , with $\Omega_z = 300^\circ/s$. In black and red are represented the responses with and without the tuning application, respectively.	131

6.6	Setup of Trans 126 elements for FEM based electrostatic analysis.	132
6.7	FEM-based frequency tuning characteristics of drive and sense resonant modes as a function of the applied tuning tension V_t . The mode-matching condition (represented in grey) is achieved with $V_t = 14.903\text{ V}$	133
6.8	Modal analysis results and the corresponding mode shapes for the proposed dual mass MEMS gyroscope (a) 1st mode (11014 Hz) (b) 2nd mode (11014 Hz) and (c) 3rd mode (34022 Hz) and (d) 4th mode (42567 Hz).	134
6.9	Comparison FEM-based and analytical frequency tuning characteristics of drive and sense resonant modes as a function of the applied tuning tension V_t (a) without fitting (b) with fitting.	135
6.10	The FEM-based frequency response in the sense direction for the proposed dual mass MEMS gyroscope (<i>logarithmic scale</i>), with $\Omega_z = 300^\circ$ and tuning tension $V_t = 14.903\text{ V}$	136
6.11	Comparison between the FEM-based frequency response amplitudes in the sense direction (<i>logarithmic scale</i>) obtained applying a tuning tension $V_t = 0$ and $V_t = 14.903\text{ V}$, with $\Omega_z = 300^\circ/\text{s}$	137
6.12	Comparison between drive and sense FEM-based frequency response amplitudes (<i>logarithmic scale</i>), obtained applying an actuation voltage of 50 V DC and 5 V AC, a DC tuning tension $V_t = 14.903\text{ V}$ and an angular velocity $\Omega_z = 300^\circ/\text{s}$ in the z-direction.	137
6.13	The phase relationship between the drive mode and sense mode signals.	140
6.14	Schematic control-loop for the automatic frequency tuning system.	141
6.15	Relationship between resonant mode frequency mismatch and ϕ_y and V_{error}	143
6.16	Simulation outputs obtained during the automatic mode-matching operation for the proposed MEMS gyroscope device: (a) Tuning voltage V_t (b) Phase detector output V_{error} and (c) Resonant frequency of sense mode ω_s	146
6.17	Simulated response amplitude of drive and sense mode outputs of the gyroscope in the presence of a Coriolis force during the mode-matching operation (a) Not mode-matching ($\omega_d \neq \omega_s$) and (b) Mode-matching ($\omega_d = \omega_s$).	147
6.18	Influence of different input angular velocity on tuning voltage and sense-mode resonant frequency: (a) influence of different input angular velocities on tuning voltage V_t and (b) influence of different input angular velocities on sense mode resonant frequency ω_s	148
6.19	Young's modulus of silicon in the temperature range of 40° C to 100° C.	150
6.20	Thermally induced Von Mises stress in MEMS gyroscope (a) at -40° C, (b) at 100° C, with reference temperature T_F of 25° C.	151
6.21	Maximum Von Mises stress with temperature change in the range of -40° C to 100° C.	152
6.22	Maximum thermal deformation with temperature change in the range of -40° C to 100° C.	152
6.23	Structural thermal deformation in MEMS gyroscope at -40° C, with reference temperature T_F of 25° C (scale 20).	153
6.24	Structural thermal deformation in MEMS gyroscope at 100° C, with reference temperature T_F of 25° C (scale 20).	154
6.25	Drive and sense mode resonant frequency variation in the temperature range of -40° C to 100° C, with reference temperature of $T_F = 25^\circ\text{ C}$	155
6.26	Frequency mismatch between drive and sense mode resonant frequency in the temperature range of -40° C to 100° C, with reference temperature of $T_F = 25^\circ\text{ C}$	155
6.27	Thermal deformation paths along with the drive mass and sense frame.	156

6.28	Thermal deformation analysis path <i>a</i> along with the drive mass (a) thermal deformation at -40°C (b) thermal deformation at 100°C	157
6.29	Thermal deformation analysis path <i>b</i> along with the sense frame (a) thermal deformation at -40°C (b) thermal deformation at 100°C	157
6.30	Thermal deformation analysis path <i>c</i> along with the sense frame (a) thermal deformation at -40°C (c) thermal deformation at 100°C	158
6.31	Energy loss factor for the proposed MEMS gyroscope with varying operating temperature in the range of -40°C to 100°C (a) Drive direction $\frac{1}{Q_d}$ (b) Sense direction $\frac{1}{Q_s}$	158
6.32	Tuning voltage V_t compensating the mismatch between drive and sense mode for a temperature variation in the range of -40°C to 100°C , with a reference temperature of $T_F = 25^{\circ}\text{C}$ (a) Analytical (b) FEM-based analysis.	160
6.33	Mechanical sensitivity of the proposed dual mass MEMS gyroscope design in the temperature range of -40°C to 100°C , with reference temperature of $T_F = 25^{\circ}\text{C}$ (a) without tuning and (b) with tuning.	161
A.1	Single-degree-of-freedom oscillator.	166
A.2	Harmonic response of the damped linear oscillator $U(\omega) = U(\omega) e^{j\phi(\omega)}$. Amplitude $ U $ normalized by using the factor F/k and phase ϕ diagrams.	167
B.1	The SOI wafer consists of a 10 μm Silicon layer, a 1 μm Oxide layer, and a 400 μm Substrate layer. A Bottom Side Oxide layer is also initially present on the wafer.	170
B.2	The top surface of the silicon layer is doped by depositing a phosphosilicate glass (PSG) layer and then annealing is done at 1050°C in Argon. The PSG layer is subsequently removed using wet chemical etching.	171
B.3	The wafer is coated with a negative photoresist and lithographically patterned by exposing the photoresist with light through the first level mask, also namely Padmetal mask, and then developing it. A metal stack of 20 nm of chrome and 500 nm of gold is deposited using e-beam evaporation.	171
B.4	The photoresist is lifted-off and the metal layer on top is also removed this way. The remaining metal parts define the first metallization layer.	171
B.5	Silicon is lithographically patterned with second mask level SOI. DRIE (Deep Reactive Ion Etching) is used for etching the silicon down to the Oxide layer. Photoresist is removed afterwards.	172
B.6	A frontside protection material is applied to the top surface of the Silicon layer. The wafers are then reversed, and the Substrate layer is lithographically patterned from the bottom side using the third mask level, TRENCH. This pattern is then etched into the Bottom Side Oxide layer using Reactive Ion Etching (RIE). A DRIE silicon etch is subsequently used to etch these features completely through the Substrate layer.	172
B.7	A wet oxide etch process is then used to remove the Oxide layer in the regions defined by the TRENCH mask. The protective layer is then removed by dry etch process. After that, the remaining oxide layer is removed from the top surface using a vapor HF process and making the structures suspended.	172
B.8	The shadow mask is then aligned and temporarily bonded to the SOI wafer, and the Metal is evaporated using an E-Beam tool. The Blanket Metal layer, consisting of 50 nm Cr and 600 nm Au, is deposited on the top surface of the Silicon layer only in the through hole regions of the shadow mask.	173

B.9	The shadow mask is removed, leaving a patterned Metal layer on the SOI wafer. The wafers are diced using a laser, then the chips sorted and packaged for shipment.	173
C.1	Main steps to carry out a prestressed modal analysis in Ansys via PSTRES command.	175
C.2	Main steps to carry out a prestressed modal analysis in Ansys using Linear perturbation analysis procedure.	176
D.1	Entire model of the automatic mode-matching system control implemented in SIMULINK.	177
D.2	Drive mode oscillator block.	178
D.3	$F_{Coriolis}$ computation block.	178
D.4	Sense mode oscillator block.	178
D.5	Sense displacement to ΔC transform block.	179
D.6	ΔC to V_s transform block.	179
D.7	Phase detector block.	179
D.8	PI controller block.	180
D.9	V_t to ω_s transform block.	180

List of Tables

1.1	Advantages and disadvantages of MEMS technology.	9
1.2	Gyroscope performance classification [24, 35].	20
2.1	Stiffness values of the most used beam elements in MEMS vibratory gyroscopes. .	30
2.2	Knudsen number range and corresponding flow regimes [31].	47
3.1	Elecromechanical coupling methods in Ansys [11].	61
3.2	Main steps to carry out a prestressed modal analysis in Ansys [8].	69
3.3	Main steps to carry out a prestressed full harmonic analysis in Ansys [8].	70
4.1	Silicon structural material data.	72
4.2	Design parameters of the single mass resonant MEMS gyroscope.	73
4.3	Mechanical crab-leg springs design parameters.	75
4.4	Comb-drive based electrostatic actuator design parameters.	77
4.5	Sensing parallel-plates design parameters.	78
4.6	Data related to slide-film damping in the drive direction for the proposed MEMS gyroscope design.	79
4.7	Data related to squeeze-film damping in the sense direction.	80
4.8	Analytical resonant frequency values of the proposed single mass MEMS gyroscope design.	81
4.9	Comparison of the analytical and FEM-based modal analysis results related to the drive and sense mode.	88
4.10	Comparison of the analytical and FEM-based harmonic analysis results related to the drive and sense resonant frequency.	90
5.1	Silicon structural material data.	97
5.2	Design parameters of the dual mass resonant MEMS gyroscope.	99
5.3	Mechanical springs design parameters.	102
5.4	Comb-drive based electrostatic actuator design parameters.	104
5.5	Sensing parallel-plates design parameters.	105
5.6	Electrostatic tuning combs design parameters.	106
5.7	Data related to slide-film damping in the drive direction for the proposed dual mass MEMS gyroscope design.	106
5.8	Data related to squeeze-film damping in the sense direction.	108
5.9	Analytical resonant frequency values of the proposed dual mass MEMS gyroscope design.	111
5.10	Comparison of the analytical and FEM-based modal analysis results related to the drive and sense mode.	120

5.11	Comparison of the analytical and FEM-based harmonic analysis results related to the drive resonant frequency.	121
5.12	Comparison of the analytical and FEM-based harmonic analysis results related to the sense resonant frequency.	123
6.1	Mechanical sensitivity comparison in the case of different frequency mismatch values.	138
6.2	Simulation dynamical parameters of the proposed dual mass MEMS gyroscope dynamics.	145
6.3	Simulation electrical parameters of the proposed dual mass MEMS gyroscope.	145
6.4	Simulation parameters of the displacement-to-voltage conversion block.	147

List of Symbols

α	Thermal coefficient expansion
Δf	Frequency mismatch
ϵ	Permittivity
κ	Thermal Conductivity coefficient
λ	Mean free path
μ	Viscosity
ν	Poisson's ratio
Ω	Angular velocity
ω_d	Drive-mode resonant frequency
ω_n	Resonant frequency
ω_s	Sense-mode resonant frequency
ρ	Density
σ	Squeeze number
ζ	Damping ratio
C	Capacitance
c	Damping coefficient
C_V	Heat capacity at constant volume coefficient
E	Young's Modulus
F_d	Driving force
F_c	Coriolis force
i	Current
k	Stiffness coefficient
K_B	Boltzmann's constant
K_n	Knudsen number

L	Beam length
m	Proof-mass
P	Pressure
Q	Quality factor
R_e	Reynolds's number
T	Temperature
t	Layer thickness
V	Voltage
w	Beam width

List of Acronyms

AIG	Atomic Interferometer Gyroscope
APDL	Ansys Parametric Design Language
ASG	Atomic Spin Gyroscope
CTE	Thermal coefficient expansion
CVG	Coriolis Vibratory Gyroscope
DOF	Degree-of-Freedom
MEMS	Micro-Electro-Mechanical-System
FE	Finite Element
FEM	Finite Element Method
FOG	Fiber Optic Gyroscope
GUI	Graphical user interface
HRG	Hemispherical Resonator Gyroscope
IC	Integrated Circuit
IMU	Inertial Measurement Unit
RIG	Rate-integrating gyroscope
RLG	Ring Laser Gyroscope
SOI	Silicon On Insilutor
TFG	Tuning Fork Gyroscope

Chapter 1

Gyroscopes overview

The aim of this Chapter is to provide a brief overview of gyroscopes development history and MEMS technology. Starting from the definition of gyroscope, the history of this device is presented, from Foucault experiments to the modern concept. The Chapter then analyzes the state of the art about MEMS gyroscopes and their main applications. Particular emphasis is given to the innovative MEMS technology and the relative manufacturing process, which is crucial in the final overall device performance. Concerning micromachined gyroscopes, the working principles and the Coriolis effect are described in detail. The last section of the Chapter deals with the detailed presentation of the classification of the different MEMS gyroscopes.

However, the reader should be aware that this chapter is meant for introducing the world of MEMS gyroscopes in order to be preparatory for the presentation of the main topic of this thesis project and the related developed design.

1.1 Background of Gyroscopes

In the simplest terms, a gyroscope can be defined as a sensor which is adopted in order to measure the orientation or the angular velocity of a system relative to an inertial reference frame.

The sensor's name was coined during the experiments to measure the Earth rotation conducted by the physicist Léon Foucault and it was the result of the combination of two Greek words: *skopeein* and *gyros* which respectively means *to see* and *rotation* [35].

During the years many different gyroscopes were developed. In particular, they can be classified depending on the operating physical principle and the involved technology. Those sensors can be used alone or included as a part of complex systems, such as Gyrocompass, Inertial Measurement Unit, Inertial Navigation System and Attitude Heading Reference System [35].

1.1.1 Brief history of Gyroscopes development

Essentially, in the early stages of its development, the gyroscope was constituted by a rotating momentum wheel attached to a gimbal structure.

The first known apparatus commonly recognized as the ancestor of the modern gyroscope is the *Whirling Speculum*, also commonly known as *Serson's Speculum*, that was invented by Jhon Serson in 1743 with the objective of locating the horizon in foggy or misty conditions during sailing. The device was composed of a spinning top with a mirror that attempted to maintain the horizontal position during the navigation. Consequently it was more closed to a level, but due to its structure it is commonly recognized as the first ever gyroscope.

Only in the 1817 Johann Gottlieb Friedrich Von Bohnenberger, a German astronomer and professor

at the University of Tübingen, introduced an instrument called *Machine* which is commonly recognized as the first instrument used more like a modern gyroscope (Figure 1.1). The so-called *Machine* was mainly constituted by a rotating massive sphere and used as a device to illustrate the inertia of free rotating bodies and to study the precession motion of the earth [14]. In the 1830's a similar device was developed independently also by an American physicist, Walter R. Johnson. His device was really closed to the one developed by Von Bohnenberger with the only difference of a rotating disc used at the place of the spherical mass used by the latter. This explains why this device was called by the inventor as *rotorscope*.

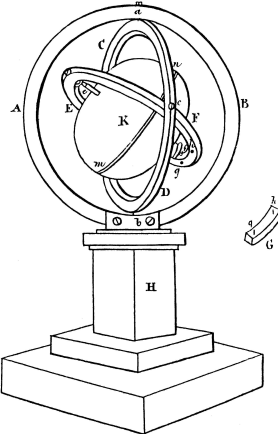


Figure 1.1: The *Machine* invented by Bohnenberger.

It was only in the 1852 that the commonly recognized father of the gyroscope got in contact with the device ancestors. During that year at the Ecole Polytechnique in Paris, Léon Foucault, a French physicist, was conducting experiments in order to study the rotation of the Earth. Because of those activities, the *Machine* was recommended as a technical aid by the French mathematician Pierre-Simon Laplace. After analyzing the concept, Foucault started adopting it in his experiments that were based on the concept of the tendency of a pendulum to preserve a constant plane of oscillation independently from the earth's rotation. Consequently he suspended a 28 kg lead mass with a 67 m long wire from the dome of the Pantheon in Paris (Figure 1.2). He used this instrument with the objective of measuring the rotation velocity of the Earth that was correlated to the rate of the oscillation plane of this pendulum. The phenomenon was observable in the first 8 to 10 minutes before friction effects start slowing down the spinning rotor. This instrument was recognized as the first modern gyroscope and Foucault was commonly recognized both as the father of such a device and as the inventor of its name.

The limitations caused by the friction and experienced also by Foucault during his experiments were finally overcame in the 1860s when the advent of the electric motors made it possible for a gyroscope to spin indefinitely even in presence of the friction which affects the mechanical design. This improvement lead to a performance increasing for the device that culminated in the first prototype heading indicators and in the gyrocompass, a rather more complex device which is a type of non-magnetic compass based on a fast-spinning disc and the rotation of the Earth (or another planetary body if used elsewhere in the universe) to find geographical direction automatically. The first patented application of the gyrocompass dates back to the 1904 and was made by the German inventor Hermann Anschütz-Kaempfe.

During those years other nations apart from Germany realized the military importance of the invention mainly because during that period the naval prowess was the major source of military power. This lead to a growing interest in the technology that culminated in a huge growth of



Figure 1.2: The Foucault pendulum in the Panthéon.

gyroscope industries: an example is represented by the Sperry Gyroscope Company which quickly expanded in order to provide both naval and aircraft stabilizers.

The importance of the gyroscope grew enormously during the Word War II. Indeed the sensor was the prime component for aircraft and anti-aircraft gun sights as well as for the autopilot systems, torpedos and ballistic missiles.

A milestone in the gyroscope development is then represented by the so-called *midget gyroscopes*. They were the result of the race to the miniaturization of the device which followed the World War II and was driven by the necessities imposed by the need to adopt the sensor for guided missiles and weapons navigation systems. The *midget gyroscopes* were the answer to this need and were characterized by a weight of less than 85 g, a diameter of approximately 2.5 cm and some of them could even reach a speed of 24000 revolutions per minutes in less than 10 seconds with an incredible precision of the measurements.

During the last decades of the last century the device went finally through a transformation from the mechanical gimbal structure to a modern compact device that could detect the angular rate with extreme precision. Moreover in recent years three-axis MEMS-based gyroscopes started to be adopted in portable electronic devices like tablets, smartphones and smartwatches. This adds to the 3-axis acceleration sensing ability available on previous generations of devices. Together these sensors provide 6 component motion sensing: accelerometers for X, Y, and Z movement, and gyroscopes for measuring the extent and rate of rotation in space (roll, pitch and yaw). The remarkable aspect of the latest developments is that newer MEMS-based inertial measurement units incorporate up to all nine axes of sensing in a single integrated circuit package, providing inexpensive and widely available motion sensing. Consequently the introduction of such a category of gyroscopes open a large portion of applications that lead these devices to be employed not only in the military and research fields but also in the consumer market in a growing range of products.

1.1.2 Classification of Gyroscopes

The wide range of available gyroscopes can be classified by cost, physics, materials utilized and underlying technology and operating principle. The following provides a first classification of existing types of such a device based on the operation principle.

Three main categories of gyroscopes can be identified:

1. Mechanical gyroscopes
2. Optical gyroscopes
3. Atomic gyroscopes.

Mechanical gyroscopes are traditionally constituted by a gimbal spinning wheel which is called rotor. The rotor itself is mounted on a fixed frame and, since the link is realized using a set of gimbals, it is able to rotate freely around three axis. When the sensor is connected to the system of interest, the fixed frame remains solid respect to the system while the rotor remains in its fixed position thanks to the conservation of the angular momentum. At this point, measuring the relative angles between the fixed frame and the rotor at the bearings of the gimbals, it is possible to determine the angle of rotations of the system of interest on which the device is anchored [35]. The mechanical gyroscopes are characterized by the advantage of a direct measurement: since the sensor is directly mounted or included in the system of interest and the measurement based on relative angles between mechanical parts, there is no arise of cumulative errors and high precision measurements can be easily achieved. On the contrary, since the gyroscope operational principle is based on the relative movement between mechanical parts, there is the presence of friction that affects the device performances. Basically the friction of the gimbals will cause precession which is observable as an orientation drift. In order to prevent this issue there is the need to adopt high precision mechanical moving parts that makes those devices bulky and expensive for modern applications.

A sub-category of mechanical gyroscopes is *Coriolis Vibratory Gyroscopes* (CVG). Those devices are characterized by the fact that the sense element is no longer constituted by gimballed moving parts, but by vibrating structures. Consequently, the conservation of the angular momentum is substituted by the vibrating element's response to a rotation-induced inertial force called *Coriolis force*. Details of the operation principle will be discussed in the next chapter. CVG not only allows a smaller form factor but also eliminates problems of friction and wear in traditional mechanical gyroscopes. Those gyroscopes allow smaller design and eliminate the limitations related to friction and wear respect to the traditional mechanical gyroscopes [35].

Successful examples of CVG are:

1. *Tuning Fork Gyroscope* (TFG) which is characterized by a particular structure made of two vibrating masses, as shown in Figure 1.3. Here, tines are driven to oscillate in the opposite directions, but along the same axis. When external rotation around vertical axis is applied, a motion of tines, orthogonal both to the driving and rotation axis, occurs in opposite directions as well. In addition to this, Coriolis forces at each tine, being combined, produce harmonic torque around vertical axis, which is proportional to the rotation detected by the sensor.
2. *Hemispherical Resonator Gyroscope* (HRG), also called wine-glass gyroscope, is a compact and robust device without moving parts (Figure 1.4). It is based on the flexural resonant modes of a bowl-shaped structure fixed on a stem. The device is excited with vibratory displacements normal to the edges of the bowl. When it is rotated around the stem axis, the nodes of vibrations modes rotate around the stem at a rate proportional to the input angular velocity. HRGs can deliver extremely high reliability with very low power dissipation, but

they require expensive high-precision manufacture which limits them to mostly aerospace applications [35].

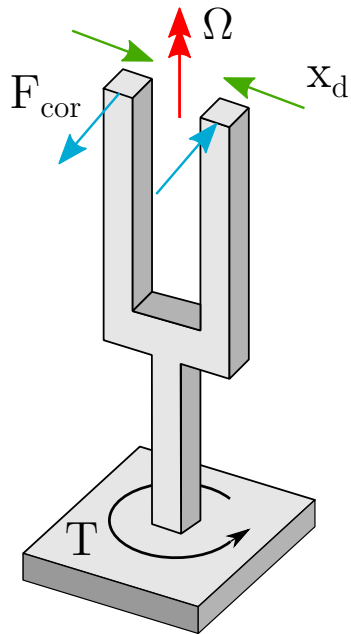


Figure 1.3: A Tuning Fork Gyroscope scheme.



Figure 1.4: Hemispherical Resonator Gyroscope (Smithsonian Institution).

Optical gyroscopes are based on the Sagnac effect. Sagnac effect, also called Sagnac interference, describes the phenomenon that two light beams with the same frequency traveling around a closed path in opposite directions have different phase shift under rotation due to the invariance of

light speed in all inertial frames. The interference pattern of such two light beams can therefore be used as a measurement of the rotation. Optical gyroscopes have no moving parts and can provide high-accuracy rotation measurement. They are widely used in aerospace and marine applications for navigational guidance [35].

Among the various optical gyroscopes, of great importance are:

1. *Ring laser gyroscope (RLG)*, which relies on the Sagnac effect to measure a rotation about its sensitive axis (Figure 1.5). This implies that the orientation in inertial space will be known at all times. The elements that measure actual accelerations can therefore be resolved into the appropriate directions. An input laser beam is split into two beams that travel the same path but in opposite directions: one clockwise and the other counter-clockwise. The beams are recombined and sent to the output detector. In the absence of rotation, the path lengths will be the same and the output will be the total constructive interference of the two beams. If the apparatus rotates, there will be a difference (to be shown later) in the path lengths travelled by the two beams, resulting in a net phase difference and destructive interference. The net signal will vary in amplitude depending on the phase shift, therefore the resulting amplitude is a measurement of the phase shift, and consequently, the rotation rate.
2. *Fiber optic gyroscope (FOG)* also uses the Sagnac effect, but with optical fibres as the propagation medium. Two beams from a laser are injected in the same fibre but in opposite directions. Due to the Sagnac effect, the beam travelling against the rotation experiences a slightly shorter path delay than the other beam. The resulting differential phase shift is measured through interferometry, thus translating one component of the angular velocity into a shift of the interference pattern which is measured photometrically.

Despite the great advantage of not having moving mechanical parts, both RLG and FOG have the disadvantage of not being suitable for applications in portable or hand-held devices. Basically, in order to reach extremely high accuracy and high reliability those devices rely on a large effective area of the closed path and consequently their miniaturization is quite prohibitive. This limitation is no longer valid if we consider that those sensor, in particular large RLGs, are employed for earth rotation measurements and gravitational wave detection due to their performances under the precision and reliability point of view [35].

Atomic gyroscopes They are a new group of gyroscopes developed in recent years due to progresses in the modern physics and based on the atomise phenomenon. There are two types of such devices:

1. *Atomic Interferometer Gyroscope (AIG)*, which is an ultra-high precision gyroscope based on a principle like the Sagnac effect using atoms instead of photons, as it utilizes the atomic interferometer to sense rotation.
2. *Atomic Spin Gyroscope (ASG)*, which is a compact high precision gyroscope which is based on the nuclear magnetic resonance and utilizes the atomic spin to sense rotation. It also have the great advantage of having also the possibility to be reduced at a chip-scale dimension.

Potentially they are ones of the most promising devices in the field, however, at the current state the manipulation of atoms and the control of temperature and the magnetic field involve expensive and bulky equipment as well as long start-up time. [20, 35]

In recent years, thanks to the low-cost batch fabrication silicon micro-machining technologies, a growing interest followed by several achievements has been put on the design of MEMS gyroscope. The considerable interest in such a technology is related to its flexibility: MEMS gyroscope has demonstrated incomparable capability to satisfy the requirements of several applications, inertial navigation and control systems of flight vehicles, and may have applications in automobile



Figure 1.5: Ring laser gyroscope produced by Ukrainian "Arsenal" factory on display at MAKS-2011 airshow.

design, defence, consumer electronics and biomedical engineering. The benefits of micromechanical gyroscopes over classical gyroscope are robustness, low power consumption, potential for miniaturization and low cost. Being MEMS gyroscope a recent technology currently under strong development, as the maturity level can suggest, they are far from reaching the same performance of more mature designs such as the mechanical and the optical ones.

However, considering the advantages in terms of low cost, small size and high integrability of the design, MEMS gyroscopes seems to be the most promising way to enable emerging portable inertial navigation system applications.

1.2 MEMS Technology

Micro-Electro-Mechanical Systems, or MEMS, is a technology that in its most general form can be defined as miniaturized mechanical and electro-mechanical elements, i.e. devices and structures, that are made using the techniques of microfabrication. Devices like the one shown in Figure 1.6 are fabricated using photolithography based techniques, that allow the realization of micrometer scale features and the integration of both electrical and mechanical functions.

As the name implies, the critical physical dimensions of MEMS devices can vary from well below one micron on the lower end of the dimensional spectrum, all the way to several millimeters. At this scale, the relative importance of the physical phenomena are different: when the dimensions shrink, the masses are tiny and thus the frequencies very high; the surface-to-volume ratio increases linearly, resulting in small inertial forces but significant electrostatic forces [29]. In addition, Figure 1.7 gives an immediate feeling of the microsystems' dimensions. It shows schematically a commercial product. The fully packaged device has dimensions $3.5\text{ mm} \times 3\text{ times} \times 1\text{ mm}$ and, thus, a volume of 10.5 mm^3 . Inside the device there are three sensors: a three-axis accelerometer, a three-axis gyroscope and a three-axis magnetometer: this is why the device is called a nine-axis module. By superposing the device of Figure 1.7a on a 1 euro cent coin, it is possible to realize that more than 16 nine-axis MEMS can be arranged on its surface, as shown in Figure 1.7b. MEMS devices, as the name may suggest, integrates mechanical and electro-mechanical elements. Electric and electronic component are needed to create connections between the MEMS and the

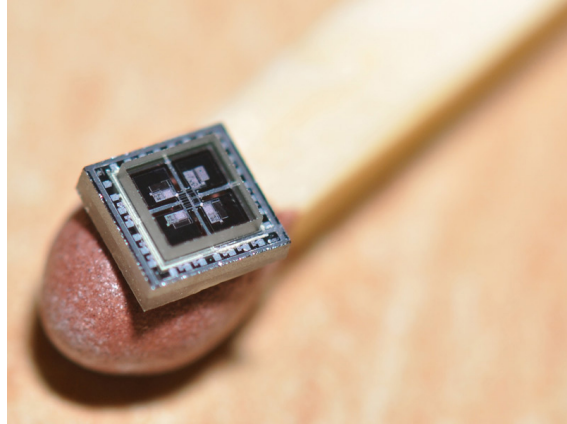
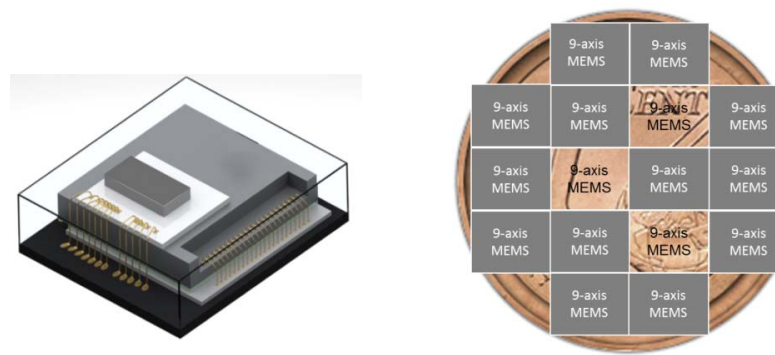


Figure 1.6: A MEMS device compared to a matchstick [29].

external world, to transform physical information (inertia forces, pressure, . . .) in electric signals and also to activate movements inside the device. In addition to the electronic components needed to make the MEMS core work, it is always necessary to add read-out electronic circuits. In Figure 1.7a, electric and electronic components are represented by the small wires that connect various components and by the thin lower plate that represents the application-specific integrated circuit for read-out control [16]. Finally, the main criterion which allows to define MEMS devices as mechanical systems is that there are at least some elements having some sort of mechanical functionality whether or not these elements can move. For instance, inside the MEMS there can be very small beams or plates that are loaded by inertia forces caused by the overall acceleration of the device and that can be considered as structural components. From this point of view, the types of MEMS devices can vary from relatively simple structures having no moving elements, to extremely complex electromechanical systems with multiple moving elements under the control of integrated microelectronics.



(a) Typical commercial microsystem: a nine-axis accelerometer, gyroscope, magnetometer

(b) 16 nine-axis MEMS superposed on a 1 euro cent coin

Figure 1.7: A clearly idea of the potentialities of miniaturization behind the microsystems technology [16].

Table 1.1 summarizes advantages and disadvantages of MEMS technology.

Advantages	Disadvantages
<ul style="list-style-type: none">• Extremely scalable in manufacturing, resulting in very low unit costs when mass produced• MEMS sensors possess extremely high sensitivity• MEMS switches and actuators can attain very high frequencies• MEMS devices require very low power consumption• MEMS can be readily integrated with microelectronics to achieve embedded mechatronic systems• Scaling effects at microscopic levels can be leveraged to achieve designs and dynamic mechanisms otherwise not possible at macro-scales	<ul style="list-style-type: none">• Very expensive during the research and development stage for any new MEMS design or devices• Very expensive upfront setup cost for fabrication clean-rooms and foundry facilities• Fabrication and assembly unit costs can be very high for low quantities. Therefore, MEMS are not suitable for niche applications, unless cost is not an issue• Testing equipment to characterise the quality and performance can also be expensive

Table 1.1: Advantages and disadvantages of MEMS technology.

1.2.1 MEMS origin

The idea of producing something in an extremely small scale was inspired by the famous talk held by Nobel prize physicist Richard Feynman at Caltech University in 1959. The lecture is remembered nowadays for the famous key-sentence *There's a plenty of room at the bottom*. The physicist would bring to attention the possibility of exploring the new field of microscopic and nanoscale world, beginning from the already known technologies. During the '50s, many physicists started to explore the possibilities to produce something that small. In addition, a good precision and a cheap process were necessary requirements to take full advantage.

The history of micromachining is tied to the development of integrated circuit (IC) technology. Starting in the 1960s, researchers experimented with using IC fabrication technologies (for example lithography, silicon etching, and thin film growth) to make mechanical structures. Some of the early devices such as the resonant gate transistor were not commercially successful but the work lead to a commercial adoption of pressure sensors and accelerometers in the 1970s. During the next decade, many companies focused their attention and researches on the silicon microfabrication: using the IC fabrication process, they were able to create three-dimensional structures at micro scale. The ink-jet printers were one of the first industrial applications. They were developed during the 80s, and their nozzle was produced with MEMS components. From then on, MEMS technology was deeply studied as a new possibility to produce highly precise devices, combining small dimensions and low cost.

The significant research and development effort in the 1980s and 1990s have lead to new fabrication

technologies, devices, and markets for MEMS. Notably, surface micromachining has enabled integration of mechanical components with the integrated circuits leading to low cost accelerometers, ink jet printer heads and micro-mirror arrays. Building on the technological advancements, MEMS market is currently growing by all measures. The number of MEMS devices sold is increasing and new products are coming out every year. While the future for the MEMS is bright, it remains to be seen whether the technology will saturate or if new manufacturing processes and applications will be invented to further drive the development. [22, 29]

1.2.2 Applications

MEMS promises to revolutionize nearly every product category by bringing together silicon-based microelectronics with micromachining technology, making possible the realization of complete systems-on-a-chip. The complexity of MEMS can be seen by the extensive range of different markets and applications. For instance, MEMS can be found in systems ranging across automotive, medical, electronic, consumer products, wireless and optical communications, fluidics, semi-conductor, defense, aerospace, and more. Some applications of current interest are:

- Sensors such as MEMS accelerometers, MEMS gyroscopes, MEMS pressure sensors, MEMS tilt sensors and other types of MEMS resonant sensors
- Actuators such as MEMS switches, micro-pumps, micro-levers and micro-grippers
- Generators and energy sources such as MEMS vibration energy harvesters, MEMS fuel cells and MEMS radioisotope power generators
- Biochemical and biomedical systems such as MEMS biosensors, lab-on-chips, and MEMS air microfluidic and particulate sensors
- MEMS oscillators for accurate time keeping and frequency control applications.

Some examples of current MEMS devices include accelerometers for airbag sensors, inkjet printer heads, computer disk drive heads, projection display chips, blood pressure sensors, optical switches, microvalves, biosensors and many other products that are all manufactured in high commercial volumes. As an emerging technology, new applications for MEMS products are being discovered continuously.

1.2.3 Technological process

As previously introduced, MEMS are complex systems combining various components: the electric and electronic parts, the mechanical parts, and possibly other parts, such as optical components. Moreover, they may be produced by means of complex fabrication processes and complex integration of different portions. The fabrication of microsystems is a complex process that was mainly adapted from those used in the fabrication of integrated circuits. In this section only few concepts are given with reference to one of the possible fabrication processes. However, the reader can refer to specialized textbook for further details, e.g. Madou [26], Maluf [27] and Senturia [33].

The starting point for current microsystems is a wafer of mono-crystalline silicon, which is used as a support on top of which various materials can be subsequently deposited by means of various techniques. Therefore, as depicted in Figure 1.8, one of the success of microelectronics is based on the batch fabrication of a great number of identical components on this single silicon wafer. Beside the stratification, or *deposition*, of various materials, microsystems fabrication has another recurrent and fundamental step, which is the selective elimination of portions of one or more deposited layers. This is the so-called *photolithography* process, which consists in transferring a desired pattern to the material layers, by projecting a mask onto a photoresist deposited on the

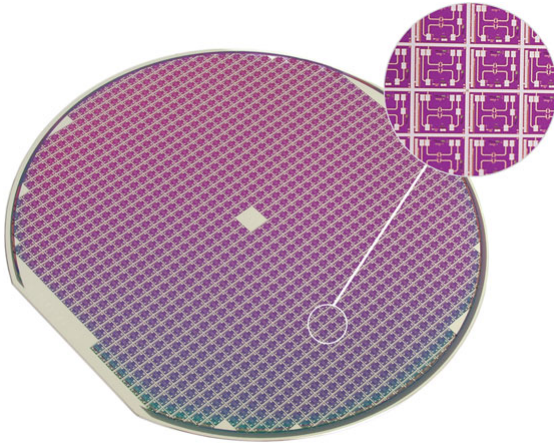


Figure 1.8: MEMS devices on a silicon wafer [29].

wafer. During a photolithographic phase, a thin film, called resist, is first exposed to light only on some portions of the surface, depending on the pattern or drawings to be reproduced on the wafer. The exposure of thin films to light modifies them in such a way that when chemical substances are subsequently deposited on the resist, portions of it are eliminated and therefore can be used as a mask that covers the wafer surface, following the desired drawing. At this point, the mask can be used on top of the wafer and additional chemical substances can selectively eliminate portions of the predeposited layers on the wafer surface, again depending on the desired pattern. The subtracting technique of removing material according to transfer the pattern creates on the resist by the photolithography to the structural layers is known as *etching*.

Because microsystems are very small, it is possible to pattern many small devices on the same wafer (e.g. with a 20.32 cm diameter). Accordingly, the real advantage of silicon-related technology is to produce hundred of identical devices on the same wafer, meaning unit cost and also high yield in mass production, since the differences among various devices are really reduced.

The fabrication process does not end with the patterned wafer, but a second wafer must be prepared, usually with much simpler patterning than the first one, to be used as a cap for the whole set of devices patterned on the first wafer. A procedure called *wafer-to-wafer* bonding is there necessary. Basically, some kind of glue is deposited on strips of the wafers that separate each device, then the two wafers are pressed towards each other by a machine that also controls the processing temperature. At the end of the thermocompressive bonding process, the two wafers are glued along the corresponding separation strips. To obtain single devices, the two glued wafers must be cut, e.g. with hydro-jets, corresponding to the separation strips. A so-called *die* is thus obtained. Finally, to obtain the final product, the die must be connected to the electronic circuit and possibly to other dies, as shown in Figure 1.7a, and everything must be protected by the final package. [16, 29]

1.3 MEMS Gyroscopes

With the rapid development of MEMS technology, silicon microelectromechanical gyroscopes, or MEMS gyroscopes, have attracted much attention. They are devices that measure angular velocity and, as an alternative to classical rate gyroscopes, they play an important role in inertial navigation

and control systems of flight vehicles, and may have applications in automobile design, defence, consumer electronics and biomedical engineering. The benefits of micromechanical gyroscopes over classical gyroscope are robustness, low power consumption, potential for miniaturization and low cost.

Vibrating structure gyroscopes, or Coriolis vibratory gyroscopes, constitute a wide group of MEMS gyroscopes. Within the past decade they have demonstrated significant progress, satisfying the requirements of several applications, such as guidance, robotics, tactical-grade navigation, and automotive applications. The underlying physical principle is that a vibrating object tends to continue to vibrate in the same plane as its support rotates. In gyroscopes, generally, an inertial mass is oscillating at the natural resonance frequency and the effect of the Coriolis force that originates on one or more detection elements in the presence of an external angular velocity is measured.

The following sections summarize the development of the silicon MEMS gyroscope and its key technologies. An overview of the main applications for this sensor are also proposed. Finally, the last section deals with the possible classification about the variety of structures that exist in literature.

1.3.1 Brief history of MEMS Gyroscopes development

The history of microelectromechanical gyroscopes dates back to the early 1990s, when Draper Laboratory reported the first micromachined gyroscope, utilizing a double-gimbal single crystal silicon structure suspended by torsional flexures (Figure 1.9). This gyroscope, fabricated on silicon wafers using electroformed nichel for the active vibrating elements, had a size of $300\text{ }\mu\text{m} \times 600\text{ }\mu\text{m}$. Through the drive electrodes, the outer gimbal is driven by electrostatic force, and this oscillation is transferred to the inner gimbal along the stiff axis of the inner flexures. When it is applied a rotation normal to the plane of the sensor, the induced Coriolis force causes the inner gimbal to oscillate with a frequency equal to the drive frequency. In a practical application, is operated by closed loop to increase its measuring precision.

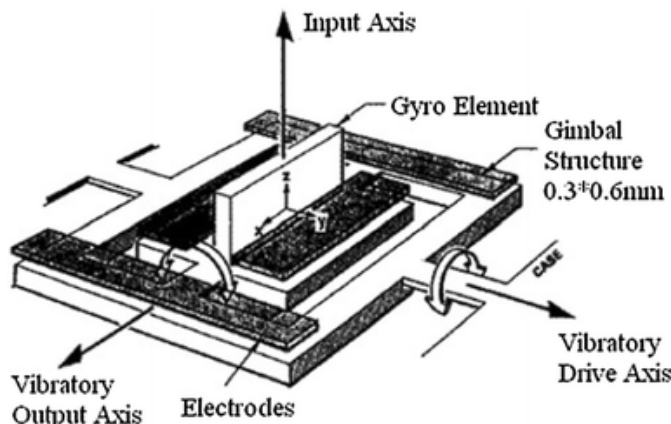


Figure 1.9: The Double gimbal bulk-silicon MEMS gyroscope developed by Draper Laboratory [36].

In 1993, the same Draper Laboratory, developed their second generation of silicon MEMS gyroscopes, which consists in a silicon-on-glass tuning fork gyroscope. It has a size smaller than 1 mm and it is fabricated by silicon on glass technology which has the advantage of low stray capacitance. Moreover, the tuning fork gyroscope is actuated electrostatically by comb-drives

and detected by capacitive measurement method and, in order to minimize damping, it employs perforated proof masses.

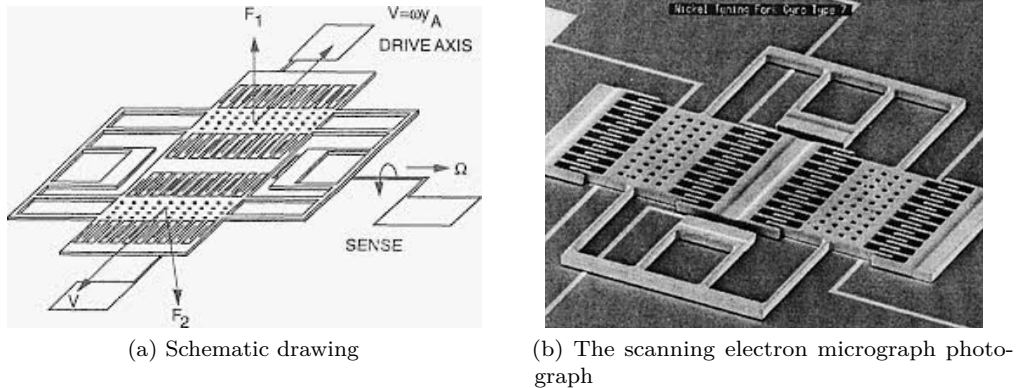


Figure 1.10: First working prototype tuning fork gyroscope from the Draper Laboratory [36].

In 1995, Draper Laboratory improved the double gimbal silicon MEMS gyroscope which was fabricated in 1991, exchanging functions between inner and external gimbal. The sense electrodes are placed in correspondence of the outer gimbal, while the drive function is respectively transferred to the inner gimbal plate. This gives the chance to improve the signal to noise ratio of gyroscopes and, under conditions of torque restoration or re-balance to the sense plate, there is no superimposed signal from the drive motion. Furthermore, in 1996 the Draper Laboratory developed the vibrating wheel gyroscope, which had a diameter of about 1 mm and it was fabricated using the same dissolved wafer process employed in the tuning fork gyroscope of 1993. Comparing to the gyroscope using the tuning fork as its sensitive element, this kind of sensor possess the simpler structure in which the outer ring of the wheel-shaped structure acts as the proof mass. It is driven in rotary motion using a comb-drive mechanism. The style of drive can easily realize the consistency of resonant frequency between dive mode and sense mode, which greatly improved the precision of the gyroscope.

Besides Draper Laboratory, UC Berkeley has also made tremendous progress in the development of MEMS gyroscopes. In 1996, this University developed an integrated z-axis gyroscope, which employed a single proof-mass driven into resonance in-plane and sensitive to Coriolis motion in the in-plane orthogonal direction (Figure 1.11). Drive and sense modes were electrostatically tuned to match, and the quadrature error due to structural imperfections were compensated electrostatically. The gyroscope is fabricated in an integrated MEMS technology with a minimum gate length of 2 μm for CMOS electronics and a 2.25 μm -thick poly-silicon layer for the mechanical elements.

In 1997 this institute reported an x-y dual axis gyroscope using surface micromachining technology (Figure 1.12). The dual axis simultaneous operation is allowed by the use of circular inertial rotor with the symmetrical quad, a torsional drive-mode excitation and two orthogonal sense modes.

In 1999, Murata investigated the mechanical coupling between the drive and detection modes of micro-machined vibrating rate gyroscopes, and developed a DRIE-based 50 μm -thick bulk micromachined single crystal silicon gyroscope with independent beams for drive and detection modes, which aimed to minimize undesired coupling.

In the 2000s, thanks to the results achieved in the theory and the processing development of MEMS gyroscopes and due to the growing market demand, huge efforts were put into the improvement and the commercialization of new devices. Since a great deal of research has been carried out and the technology went through a huge development phase, only some of the main achievements are summarized below. If the reader is interested in more details about those, he can refer to Acar

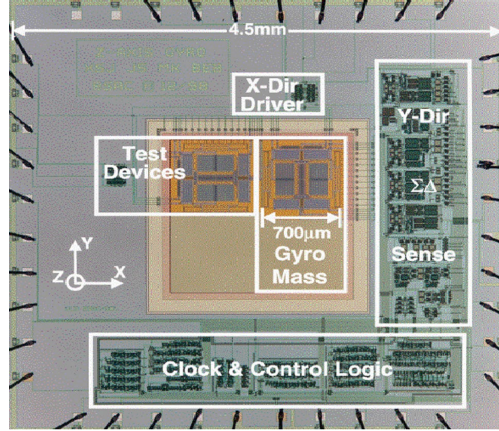


Figure 1.11: Die photograph of the z-axis gyroscope developed by UC Berkeley in 1996 [36].

and Shkel [3].

The first commercial MEMS z-axis gyroscope came from ADI in 2002. It consists in a dual-resonator, with a 4 μm-thick poly-silicon structural layer. The device utilized two identical proof masses driven into resonance in opposite directions to reject external linear acceleration and the differential output of the two Coriolis signals was detected. On-chip control and detection electronics provided self oscillation, phase control, demodulation and temperature compensation. In the same year, UC Berkeley reported an integrated micromachined gyroscope with resonant sensing. Based on bulk silicon technology, it was fabricated at Sandia National Laboratories and it adopted resonant tuning fork plane vibratory to measure angle rate.

Georgia Institute of Technology is also one of the representative organizations which made great progress in the research field of MEMS gyroscopes. In 2006, this institute reported the first demonstration of in-plane tuning fork gyroscope with automatic mode-matching and operating with non-degenerate resonant modes, called M2-TFG (Figure 1.13). It was fabricated on 50 μm-thick SOI substrate using a simple two-mask process. The proof-masses vibrate along the x-axis through the comb-drive electrodes, and when a rotation is applied along the z-axis, the Coriolis force induced along the y-axis is detected by capacitance. This design can effectively improve the

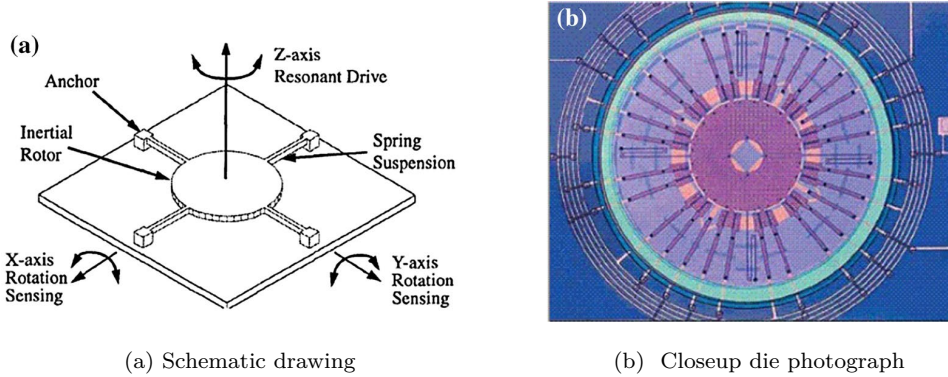


Figure 1.12: Dual axis MEMS gyroscope developed by UC Berkeley in 1997 [36].

performance of the device, such as sensitivity, bias stability and noise floor. In 2007 the same institute improved the previous design architecture of the mode-matched tuning fork gyroscope using a closed-loop servo circuit which could automatically keep the matched-mode and in 2008 this institution again improved the design of the tuning-fork through using two high-quality-factor resonant flexural modes.

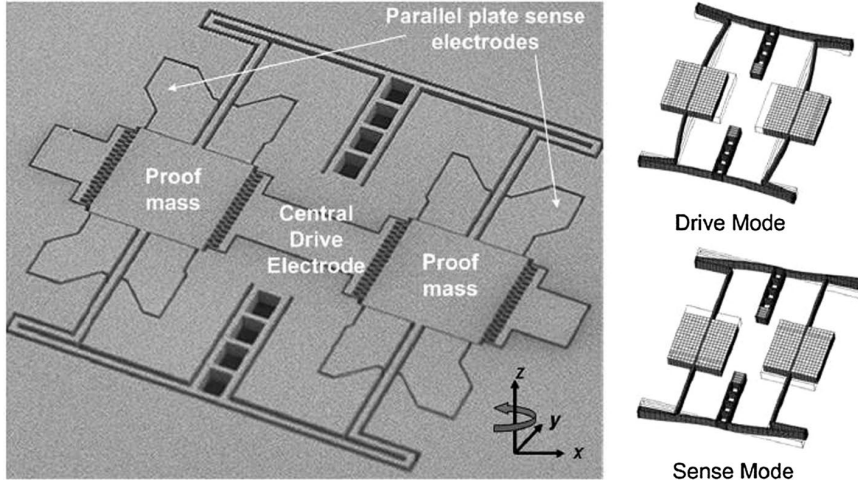


Figure 1.13: SEM of the M2-TFG developed by Georgia Institute of Technology and illustration of the mode shapes [36].

In 2009 the University of California reported a vibratory MEMS z-axis tuning fork rate gyroscope architecture, whose quality factor was greatly improved. In 2011 the same institute developed new dual mass vibratory MEMS z-axis MEMS gyroscope that provided the improved ordering of the mechanical vibratory modes. At the same time, it also offered the more complete schemes of calculation and realization. The new design provides a path toward ultra-high scale factor without compromising the sensitivity to external accelerations. At the same year, on the basis of the mode-matched tuning fork gyroscope developed by Georgia Institute of Technology, Old Dominion University and University of Utah together reported a multiple beam tuning fork gyroscope, called MB-TFG, with high quality factors (Figure 1.14). [36] [3]

In the last decade, the growing interest in personal electronics brought again a huge costumer market for MEMS gyroscopes and boosted their development in the direction of low-cost compact integrated multi-axis gyroscope units. Since several researches have been carried out and more and more types of MEMS gyroscopes have been developed with the purpose of improving performances and increase reliability, only few of those have been cited here to not overload the discussion. The reader can refer to the following chapters if interested in having more details about the MEMS design methodology and FEM simulations.

1.3.2 Applications

In the early stages of MEMS gyroscopes technology development, the accuracy of these devices was much lower than the one of their competitors, such as optical and mechanical gyroscopes. Consequently, their applications were restricted to low-end ones. However, in the last 10-15 years, as their performance keeps constantly improving in time, micromachined gyroscopes are becoming a viable alternative to expensive and bulky conventional inertial sensors. Indeed, high performance angular rate sensors, such as precision fiber-optic gyroscopes, ring laser gyroscopes, and conventional

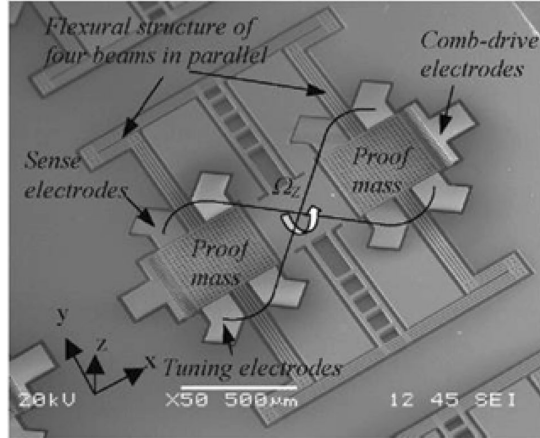


Figure 1.14: SEM picture of the multiple-beam tuning-fork gyroscope (MB-TFG) design developed by Old Dominion University and University of Utah [36].

rotating wheel gyroscopes are usually too expensive and too large for being used in the majority of emerging applications, such as smartphones or wearable devices. Micromachining process, which derived from IC technology, allows batch production of very small devices. Consequently the achieved unit costs are not reachable with any other technology. Moreover, these fabrication techniques allow electronics to be integrated on the same silicon chip together with the mechanical sensor elements, providing an unmatched integration capability. Therefore, MEMS gyroscopes are already becoming an attractive solution to current inertial sensing market needs, and even opening new market opportunities.

Thanks to the benefits in terms of the small size and weight, low costs and due to improved precision and performance, MEMS gyroscopes are applied in different sectors, such as aerospace, military industry, automotive and consumer electronics markets. The automotive industry applications are various: examples are the advanced automotive safety systems such as electronic stability control (ESC), high performance navigation and guidance systems, ride stabilization, roll-over detection and prevention, and next generation of airbag and brake systems (ABS). Figure provides an example of sensor able to detect accelerations and angular rotation on a vehicle.

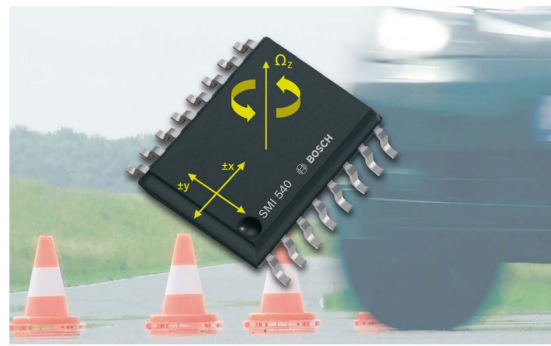


Figure 1.15: Combined inertial sensor for vehicle dynamic control (Bosch GmbH).

Another relevant application is related to emerging technologies such as autonomous vehicles, self-driving cars and Unmanned Aerial Vehicles (UAVs). A wide range of consumer electronics

applications with very high volumes include Optical Image Stabilization (OIS) in digital cameras and camcorders, smartphones, gamer consoles, head tracking in Augmented Reality (AR) and Virtual Reality (VR), inertial pointing devices and computer gaming industry. Miniaturization of gyroscopes also enable high-end applications including micro-satellites, micro-robotics, and even implantable devices to cure vestibular disorders. It should be noted that in many applications more sensors are combined together to form the so called Inertial Measurement Unit (IMU). [3]

1.3.3 MEMS Gyroscope performance requirements

As introduced in the previous section, MEMS gyroscopes applications are widespread in all markets. Consequently, they offer very different performance levels depending on the target application, which strongly influences the specifications of the sensor. The *IEEE Standard Specification Format Guide and Test Procedure for Coriolis Vibratory Gyros* [1] describes the standard specifications and test procedures for rate gyroscopes, intended to be either a macroscopic devices or a micro-electro-mechanical systems (MEMS). The standard requirements for these devices are specified in terms of their *performances*, their *mechanical* and *electrical interface characteristics*, the *environmental requirements*, the *sensor life time* and *reliability* (usually measured as Mean Time Between Failure or MTBF).

The following is a summary of the most important key parameters to define MEMS gyroscopes performances, whose terminology and definitions are taken from the *Standard for Inertial Sensor Terminology* [2, 3].

Scale factor: the ratio of a change in output to a change in the input intended to be measured, typically specified in [$mV/\text{°}/\text{sec}$]. It is evaluated as the slope of the least squares straight line fit to input-output data. Deviation from ideal input-output characteristic can be grouped in different error classes:

- *Linearity error*: the deviation of the output from a least-squares linear fit of the input-output data. It is generally expressed as a percentage of the full scale, or percentage of the output. In some applications, *Non-linearity* may be specified. Non-linearity involves only systematic deviations from a straight line.
- *Asymmetry error*: the difference between the scale factor measured with positive input and that measured with negative input, specified as a fraction of the scale factor measured over the input range.
- *Scale factor stability*: the variation in scale factor over a specified time of continuous operation. Ambient temperature, power supply and additional factors pertinent to the particular application should be specified.
- *Scale factor sensitivities*: the change in scale factor resulting from a change in steady state operating temperature (*scale factor temperature sensitivity*) or the constant acceleration along any axis (*scale factor acceleration sensitivity*). Additional sensitivities may be specified such as those due to variations in supply voltage (including frequency, voltage, ripple, starting and operating current), orientation, vibration, magnetic field, radiation, and other environments pertinent to the particular application.

Drift rate: the component of gyro output that is functionally independent of input rotation. The systematic component of the drift rate (*systematic drift rate*) includes:

1. *Bias* (or *zero rate output - ZRO*): the averaged output of the sensor measured over a specified time and at specified operating conditions in absence of input rotations. It is typically expressed in [$\text{°}/\text{sec}$] or [$\text{°}/\text{hr}$].

2. *Environmentally sensitive drift rate*: the components of systematic drift rate that are sensitive to temperature (steady state, gradient, ramp), acceleration, vibration and other quantities.

The random component of the drift rate (*random drift rate*) includes:

1. *Angle Random Walk* (ARW): the angular error buildup with time that is due to white noise in angular rate, typically expressed in [$^{\circ}/\sqrt{hr}$] or [$^{\circ}/sec/\sqrt{hr}$].
2. *Rate Random Walk* (RRW): the drift rate error buildup with time that is due to white noise in angular acceleration, typically expressed in [$^{\circ}/hr/\sqrt{hr}$].
3. *Bias Instability*: the random variation in bias as computed over specified finite sample time and averaging time intervals, characterized by a $1/f$ power spectral density. It represents the minimum detectable rate input within the gyroscope and is reported using unit [$^{\circ}/hr$].

Resolution: the smallest input change, for inputs greater than the noise level, that can be reliably detected. It is usually evaluated as the minimum input change that produces a change in output equal to some specified percentage (at least 50%) of the change in output expected using the nominal scale factor.

Operating Range (Full-scale range) : the range of positive and negative angular rates that can be detected without saturation.

Bandwidth: the range of frequency of the angular rate input that the gyroscope can detect. Typically specified as the cutoff frequency coinciding to the $-3dB$ point. Alternatively, the frequency response or transfer function could be specified.

Activation time: it includes the *turn-on time*, which is the time from the initial application of power until a sensor produces a specified useful output, though not necessarily at the accuracy of full specification performance, and the *warm-up time*, which is the time from the initial application of power to reach specified performance under specified operating conditions.

Linear and angular vibration sensitivity: the ratio of the change in output due to linear and angular vibration about a sensor axis to the amplitude of the angular vibration causing it.

Shock resistance: maximum shock that an operating or non-operating device can endure without failure, and conform to all performance requirements after exposure. Pulse duration and shape have to be specified. Full recovery time after exposure can also be specified.

Reliability requirements such as operating life, operating temperature range, thermal shock, thermal cycling, humidity, electrostatic discharge (ESD) immunity, and electromagnetic emissions and susceptibilities are also typically specified in many applications.

1.3.4 MEMS Gyroscopes classification

The majority of MEMS gyroscopes types measure the rotational rate which represents the amount of the angle spanned in a rotation during unit time. While this signal can be readily used in some applications, such as stability control for vehicle dynamics, other applications require the rate signal to be integrated in order to extract the angle, such as inertial navigation systems. Consequently, a first classification of MEMS gyroscopes is based on the physical quantity they measure and this allows to divide them into two broad types:

- Rate-integrating gyroscopes (RIG): also known as *whole-angle gyroscope (WAMG)*, they measure the absolute angle of rotation directly from the proof-mass motion, without numerical integration of the angular rate signal. They aim at high-performance applications, such as inertial navigation systems. These devices require the highest level of symmetry to exploit the precession of vibration as a result of energy transfer between two normal vibration modes. Realization of rate-integrating MEMS gyroscopes follows two main paths: realization of asymmetrical 2D oscillator using a discrete vibrating mass-spring-damper system or trying to replicate 3D shapes common in the macro-scale high-performance sensors. [4]
More precisely, rate-integrating gyroscopes can be divided into three main categories based on the geometry of the proof-mass or more generally of the resonator element: (a) *lumped mass systems*, (b) *ring/disk systems* (c) *micro-wineglasses*. Moreover, ring/disk systems are further divided into three categories: (a) *rings*, (b) *concentring rings systems*, (c) *disks*. Whereas, micro-wineglasses are divided into two categories according to fabrication technology: *surface micro-machined* and *bulk micro-machined wineglass gyroscope architectures*. The scheme shown in Figure 1.16 summarizes these divisions. [32]
- Rate gyroscopes: they measure the angular rotation rate and represent the vast majority of MEMS gyroscope applications, achieving commercial success in an amount of different fields. These devices can be divided into two main categories based on their operation, resonant MEMS gyroscopes and non-resonant MEMS gyroscopes. Resonant MEMS gyroscopes are operated at resonance and both the drive and sense mode resonant frequency values are matched, which leads to high mechanical sensitivity. Non-resonant gyroscopes typically have multiple masses and operate between resonant frequencies and the resonant frequency values do not need to be matched.

Among the various categories presented in this paragraph, the one of rate gyroscopes will be analyzed in this thesis project. In particular, the main aim is to develop and simulate a new resonant MEMS gyroscope design, in order to compensate the most common errors and achieve optimal performance parameters.

The further classification of MEMS gyroscopes divides them into three different classes based on their performance:

- rate grade devices, whose principal applications are in automotive, consumer, medical areas.
- tactical grade devices, whose principal applications are in robotic and military areas.
- inertial grade devices, whose principal applications are in inertial navigation and aerospace areas.

Table 1.2 summarizes the performance requirements for each of these categories. Over the past decade, much of the effort in developing micromachined MEMS gyroscopes has been concentrated on rate-grade devices, primarily because of their use in automotive applications. Despite this, lately progresses are being made in order to reduce size of commercial gyroscope devices while gradually improving their resolutions from rate grade to tactical grade. Efforts are still needed for MEMS to be a viable substitute for RLG or FOG in the highest grade markets.

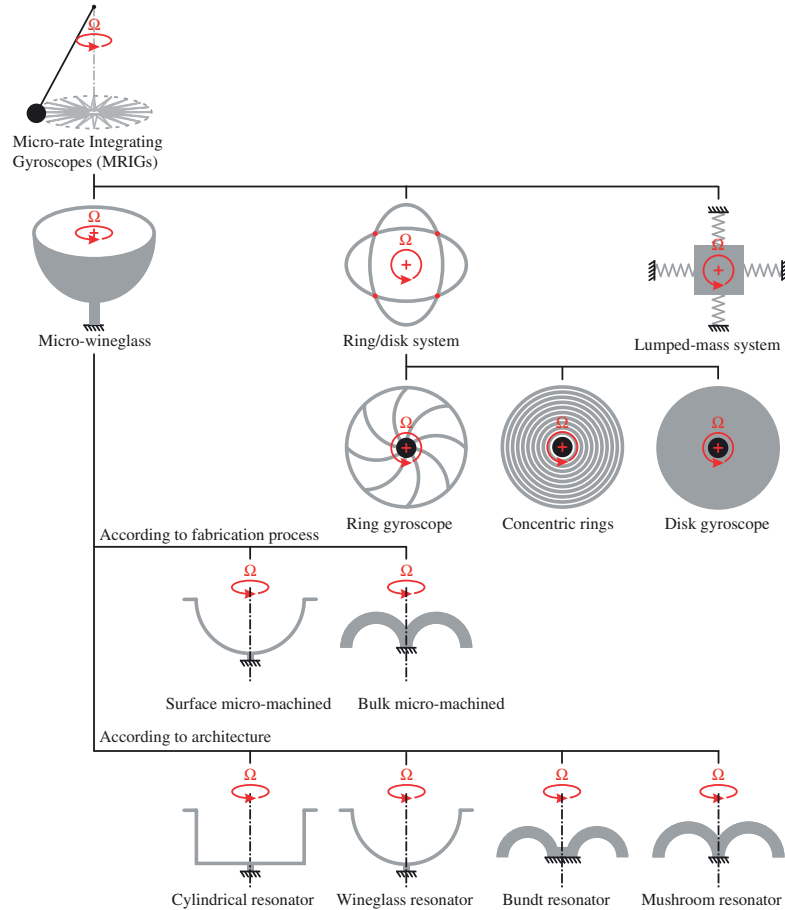


Figure 1.16: Micro-Rate integrating gyroscope (mRIG) architectures classification [32].

Parameter	Rate grade	Tactical grade	Inertial grade
Full-scale range ($^{\circ}/s$)	50–1000	> 500	> 400
Bandwidth (Hz)	> 70	~ 100	~ 100
Angle Random Walk ($^{\circ}/\sqrt{hr}$)	> 0.5	0.5–0.05	< 0.001
Bias Instability ($^{\circ}/hr$)	10–1000	0.1–10	< 0.01
Resolution ($^{\circ}/s$)	0.1–1	0.01–0.1	< 0.001

Table 1.2: Gyroscope performance classification [24, 35].

Chapter 2

MEMS Gyroscope Design Fundamentals

In this Chapter the dynamics of a generic vibratory rate gyroscope is developed, and the operation principle of a MEMS implementation is discussed in details. Explaining the basics of the drive and sense-mode oscillators, it is first illustrated that the performance of the gyroscope is very sensitive to variations in system parameters that shift the drive or sense resonant frequencies. This concept will be explained in more detail in the following chapters, as the achievement of a stable response with constant performance constitutes the main idea behind the development of the new structure design proposed in thesis project.

A focus on the fundamental mechanical elements in the implementation of MEMS gyroscopes is given, presenting and analyzing common mechanical structures and various flexure systems. Then, a discussion about the electrical design issues in a generic micro-electromechanical vibratory system to realize the complete gyroscopic system is provided, covering the fundamentals of electrostatic and capacitive sensing methods. Finally, a complete characterisation of the major energy dissipation mechanism is carried out, with a particular focus on the viscous damping effect, as it is the dominant dissipation mechanism for the vibratory MEMS gyroscopes operated at atmospheric pressure.

2.1 Working principle

Microelectromechanical gyroscopes, also known as MEMS gyroscopes, are devices that measure the angular velocity. As an alternative to classical rate gyroscopes, they play an important role in inertial navigation and control systems of flight vehicles and may have applications in automotive design, defence, consumer electronics and biomedical engineering. The benefits of micromechanical gyroscopes over classical gyroscopes are robustness, low power consumption, potential for miniaturization and low cost.

Vibrating structure gyroscopes, or Coriolis Vibratory Gyroscopes (CVG), constitute a wide group of MEMS gyroscopes. They rely on the Coriolis force, a fictitious force which appears to act on objects that are in motion within a reference frame that rotates with respect to an inertial one. Referring to Figure 2.1, the Coriolis force acts perpendicularly to the object movement and its amplitude can be expressed as:

$$F_c = -2m \{\Omega\} \times \{v_r\} \quad (2.1)$$

where m is the mass of the moving object, $\{v_r\}$ is the relative velocity with respect to the reference frame rotating at an angular rate $\{\Omega\}$.

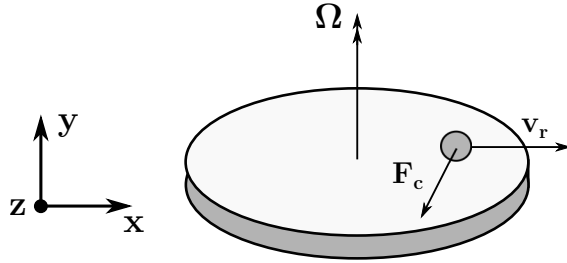


Figure 2.1: An object moving in a rotating reference frame is subjected to the Coriolis force, acting perpendicular to the object movement and the axis of rotation.

The most basic design for a micromachined vibratory rate gyroscope consists in a single proof mass suspended above the substrate using flexible beams, which makes the mass free to oscillate in two orthogonal directions, namely the drive and the sense directions. As shown in the generic architecture design of Figure 2.2, an oscillatory motion along the drive direction is imposed to the proof mass by means of usage of comb-drive structures. When the gyroscope is subjected to an external angular velocity, a Coriolis force and a consequent vibration is induced in the sense direction, which is orthogonal to both the drive direction and the angular rotation axis. The resulting oscillation amplitude in the sense direction is proportional to the Coriolis force and thus to the angular velocity to be measured: sense electrodes are used to pick up the resulting displacement and the angular velocity is then computed.

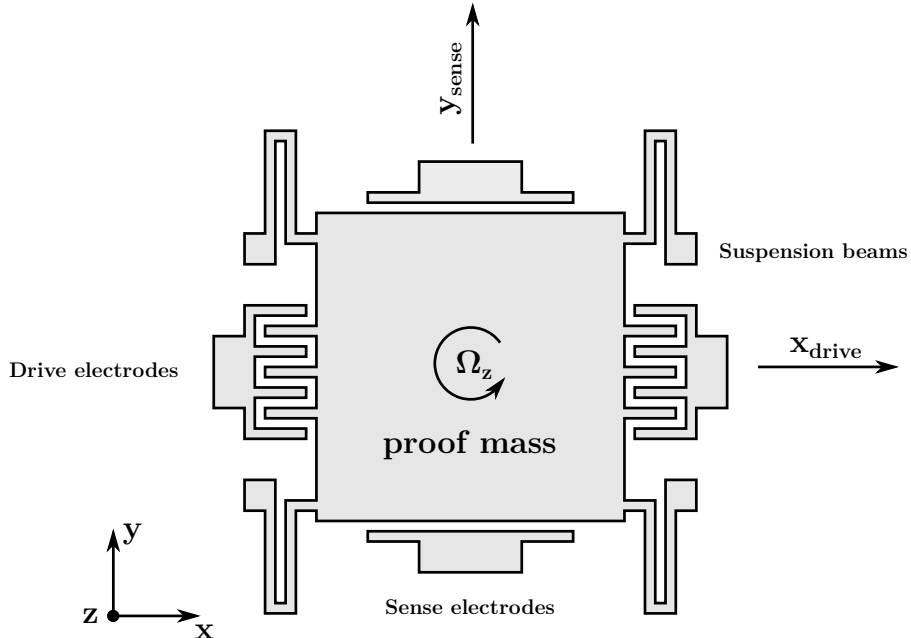


Figure 2.2: A generic MEMS design for a linear vibratory rate gyroscope designed to measure the angular velocity around the z-axis. A proof-mass is suspended above the substrate using a beams suspension system. One set of electrodes is needed to excite the drive-mode oscillator, and another set of electrodes detects the sense-mode response.

2.2 Analytical Model

Consider a fixed inertial frame of reference XYZ with origin in O and a non-inertial frame of reference xyz whose origin is located in O' and that rotates at the angular velocity $\{\Omega\}$ with respect to the fixed one. As shown in Figure 2.3, a material point P , which represents the proof mass of a vibrating element gyroscope, is constrained to in-plane motion in the rotating reference frame, within the inertial reference frame.

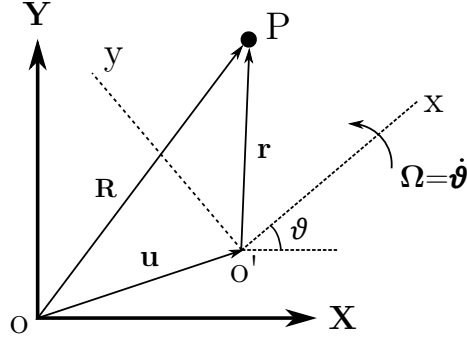


Figure 2.3: Position vector of the material point P in a fixed inertial frame of reference XYZ and in a non-inertial frame of reference xyz .

The position of the point P in the inertial reference frame and in the non-inertial one is described by the vectors $\{R(t)\}$ and $\{r(t)\}$, respectively. Denoting by $\{u(t)\}$ the position vector of origin O' in the inertial reference frame, the relation between the position vectors in the two reference frames is described by

$$\{R\} = \{u\} + \{r\} \quad (2.2)$$

The first time derivative $\{\dot{R}(t)\}$ of the position vector represents the velocity of the material point P as measured in the inertial frame XYZ

$$\{\dot{R}\} = \{\dot{u}\} + \{\Omega\} \times \{r\} + \{\dot{r}\} \quad (2.3)$$

In Equation 2.3, the term $(\{\dot{u}\} + \{\Omega\} \times \{r\})$ represents the drag velocity, i.e. the velocity of point P as dragged by the non-inertial frame, while the term $\{\dot{r}\}$ is the relative velocity vector, i.e. the velocity of point P as seen in the non-inertial frame xyz . Differentiating 2.3 with respect to time gives the acceleration of the point P as measured in the inertial reference frame XYZ

$$\{\ddot{R}\} = \{\ddot{u}\} + \{\dot{\Omega}\} \times \{r\} + \{\Omega\} \times (\{\Omega\} \times \{r\}) + \{\ddot{r}\} + 2\{\Omega\}\{\dot{r}\} \quad (2.4)$$

The acceleration in Equation 2.4 has three terms: the drag $(\{\ddot{u}\} + \{\dot{\Omega}\} \times \{r\} + \{\Omega\} \times (\{\Omega\} \times \{r\}))$ and the relative $\{\ddot{r}\}$ acceleration vectors, with analogous meanings to the relative and drag velocities, and the term $2\{\Omega\}\{\dot{r}\}$, which is the Coriolis acceleration that causes the fictitious force observed in the rotating frame.

The 2-DOF spring-mass-damper arrangement that is typically used to model the mechanical structure of a single-mass Coriolis vibrating gyroscope (as the one in Figure 2.2) is depicted in Figure 2.4. Following the previously adopted notation, XYZ is the inertial reference frame and xyz is the non-inertial reference frame connected to the gyroscope structure. If the coupling effects arising from nonidealities (anisoelasticity and anisodamping terms coupling drive and sense) are neglected, the lumped parameters of the model are:

- m , the proof mass free to oscillate in the x- and y-directions

- k_x and k_y , the stiffness of the flexible elements which suspend the proof mass above the substrate
- c_x and c_y , the equivalent viscous damping coefficients.

Applying Equation 2.4 to the proof mass m position vector, the governing dynamic equation reads

$$\{F_{ext}\} = m \left[\{\ddot{u}\} + \{\dot{\Omega}\} \times \{r\} + \{\Omega\} \times (\{\Omega\} \times \{r\}) + \{\ddot{r}\} + 2\{\Omega\}\{\dot{r}\} \right] \quad (2.5)$$

In Equation 2.5, $\{F_{ext}\}$ is the total external force applied on the proof mass, $\{\ddot{u}\}$ is the linear acceleration and $\{\dot{\Omega}\}$ is the angular velocity of the rotating gyroscope frame, $\{r\}$, $\{\dot{r}\}$ and $\{\ddot{r}\}$ are the position, velocity and acceleration vectors of the proof mass with respect to the gyroscope reference frame.

Given that

$$\{r\} = \begin{Bmatrix} x \\ y \\ 0 \end{Bmatrix} \quad \{\dot{r}\} = \begin{Bmatrix} \dot{x} \\ \dot{y} \\ 0 \end{Bmatrix} \quad \{\ddot{r}\} = \begin{Bmatrix} \ddot{x} \\ \ddot{y} \\ 0 \end{Bmatrix} \quad (2.6)$$

$$\{\Omega\} = \begin{Bmatrix} \Omega_x \\ \Omega_y \\ \Omega_z \end{Bmatrix} \quad \{\dot{\Omega}\} = \begin{Bmatrix} \dot{\Omega}_x \\ \dot{\Omega}_y \\ \dot{\Omega}_z \end{Bmatrix} \quad (2.7)$$

Projecting Equation 2.5 in the x- and y-directions, and assuming that the linear accelerations are negligible, one can obtain the following system of two differential equations, describing the motion of the single mass Coriolis vibratory gyroscope sensitive element [3]

$$\begin{aligned} m\ddot{x} + c_x\dot{x} + (k_x - m(\Omega_y^2 + \Omega_z^2))x + m(\Omega_x\Omega_y - \dot{\Omega}_z)y &= F_x + 2m\Omega_z\dot{y} \\ m\ddot{y} + c_y\dot{y} + (k_y - m(\Omega_x^2 + \Omega_z^2))y + m(\Omega_x\Omega_y + \dot{\Omega}_z)x &= F_y - 2m\Omega_z\dot{x} \end{aligned} \quad (2.8)$$

where F_x and F_y are the external forces in the x- and y-directions, Ω_x , Ω_y , Ω_z are the components of the angular velocity vector $\{\Omega\}$.

Moreover, the assumption that only the z-axis component of the angular velocity exists (as in Figure 2.4) leads to the simpler form of motion equations as

$$\begin{aligned} m\ddot{x} + c_x\dot{x} + (k_x - m\Omega_z^2)x - m\dot{\Omega}_z y &= F_x + 2m\Omega_z\dot{y} \\ m\ddot{y} + c_y\dot{y} + (k_y - m\Omega_z^2)y + m\dot{\Omega}_z x &= F_y - 2m\Omega_z\dot{x} \end{aligned} \quad (2.9)$$

As shown in Equation 2.9, in this ideal case the drive and sense modes are coupled only by means of the angular velocity Ω_z . It means that given the absence of any external forces acting on the proof mass along the y-direction, any forced displacement in this direction will be caused only by the angular rate.

Finally, if the angular velocity is constant and small comparing to the excitation frequency (i.e. $\dot{\Omega}_z = 0$ and $\Omega_z^2 \approx 0$), since the sense-mode response is usually orders of magnitude smaller in amplitude than its respective counterpart in the drive direction (i.e. $2m\Omega_z\dot{y} \approx 0$), the most simplified form of the generalized equations of motion for a Coriolis vibratory gyroscope can be obtained as follows

$$\begin{aligned} m\ddot{x} + c_x\dot{x} + k_x x &= F_x \\ m\ddot{y} + c_y\dot{y} + k_y y &= F_y - 2m\Omega_z\dot{x} \end{aligned} \quad (2.10)$$

Vast majority of micromachined vibratory gyroscopes employ a combination of proof-masses and flexible elements to form single degree-of-freedom oscillators in both the drive and sense directions. The dynamics and response of the drive and sense oscillators will be directly analyzed in the following paragraphs. However, in order to avoid weighting down the discussion, the reader can refer to the *Appendix A* for more details about the dynamics and response characteristics of a generic single-degree-of-freedom oscillator.

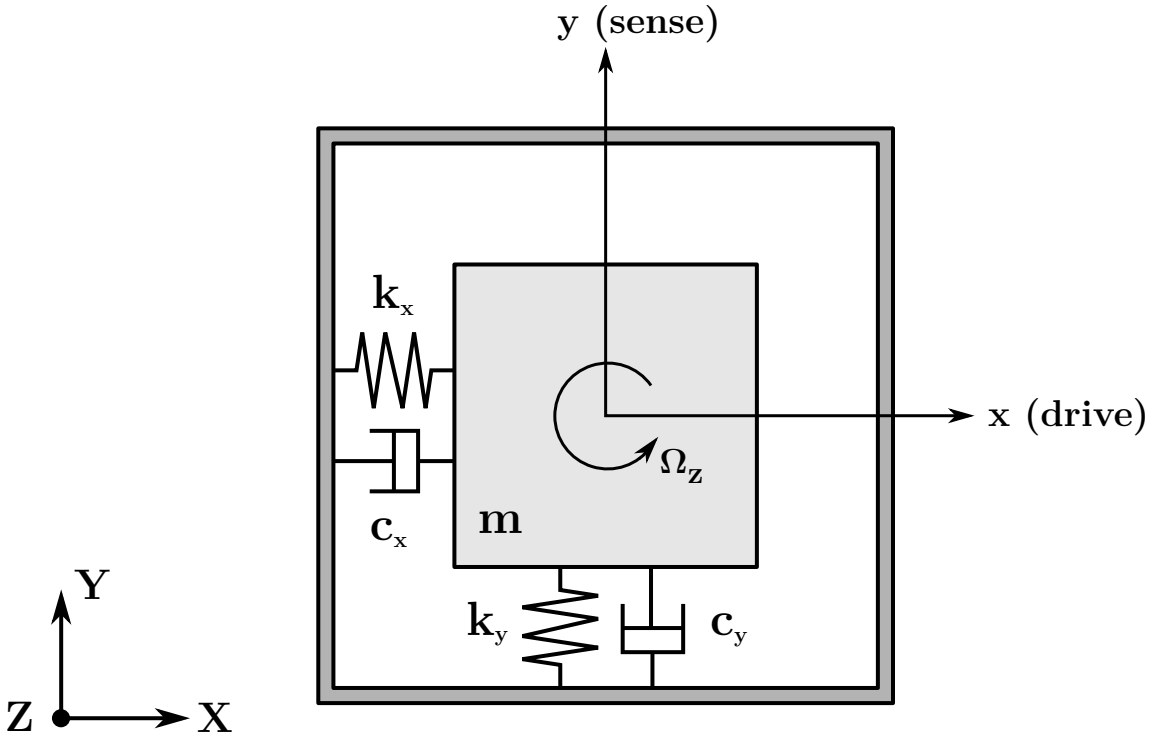


Figure 2.4: Two degrees-of-freedom spring-mass damper system is shown as lumped description of a single mass Coriolis vibratory gyroscope. The arrow in x -direction indicates the drive direction, whereas the arrow orthogonal to the first shows the sense direction of motion.

2.2.1 Drive-mode dynamics

Consider the simplified form of the equations of motion for a generic Coriolis vibratory gyroscope described in 2.10. As mentioned above, the proof mass dynamics in the x -direction is that of a single-degree-of-freedom oscillator and it is therefore governed by the following equation

$$m_d \ddot{x} + c_x \dot{x} + k_x x = F_x \quad (2.11)$$

where:

- m_d , the proof mass which moves in the drive direction
- c_x , the equivalent viscous and thermoelastic damping in the drive direction
- k_x , the equivalent stiffness in the drive direction
- F_x , the driving force, i.e. the excitation force that generates the driving motion

Moreover, the definition of the drive-mode resonant frequency ω_d and the drive-mode quality factor Q_d is

$$\omega_d = \sqrt{\frac{k_x}{m_d}} \quad (2.12)$$

$$Q_d = \frac{m_d \omega_d}{c_x} \quad (2.13)$$

Assuming a sinusoidal driving force $F_x = F_0 \sin(\omega t)$, the drive-mode steady-state response becomes

$$x = X_d \sin(\omega t + \phi_d) \quad (2.14)$$

where X_d and ϕ_d are the amplitude and the phase of the drive-mode response, respectively expressed by the two following expressions

$$X_d = \frac{F_0/k_x}{\sqrt{\left[1 - \left(\frac{\omega}{\omega_d}\right)^2\right]^2 + \left[\frac{1}{Q_d} \frac{\omega}{\omega_d}\right]^2}} \quad (2.15)$$

$$\phi_d = -\arctan \left[\frac{\frac{1}{Q_d} \frac{\omega}{\omega_d}}{1 - \left(\frac{\omega}{\omega_d}\right)^2} \right] \quad (2.16)$$

For a given driving force amplitude, the drive-mode response x has the largest amplitude at resonance, i.e. when $\omega = \omega_d$. Substituting $\omega = \omega_d$ into 2.15 and 2.16 gives

$$X_d = Q_d \frac{F_0}{k_x} \quad (2.17)$$

$$\phi_d = -90^\circ \quad (2.18)$$

Equation 2.17 shows that Q_d times higher drive amplitude can be achieved when the gyroscope is actuated at its drive-mode natural frequency compared to a quasi-static drive-mode response with an off-resonance actuation force. Therefore, in practice it is always favorable to operate the gyroscope with $\omega = \omega_d$ to achieve optimum actuation efficiency and minimize the power consumption. In particular under this point of view, low damping in the drive direction helps to save driving force and thus area and mass that are needed for implementing driving capacitances and/or voltages. In addition, the scale factor of the gyroscope is directly proportional to the drive-mode oscillation amplitude. The phase and the frequency of the drive oscillation directly determines the phase and the frequency of the Coriolis force, and subsequently the sense-mode response. Thus, it is extremely critical to maintain a drive-mode oscillation with stable amplitude, phase and frequency [3]. Accordingly, operating at resonance is a common and convenient method to achieve a stable drive-mode amplitude and phase.

2.2.2 Sense-mode dynamics

As previously introduced, when the sensor is subjected to an angular velocity in the z-direction, the drive and sense-modes are coupled by the Coriolis force. According to Equation 2.10, also the proof mass dynamics in the y-direction is governed by the equation of motion of a single-degree-of-freedom oscillator as follows

$$m_s \ddot{y} + c_y \dot{y} + k_y y = -2m_c \Omega_z \dot{x} \quad (2.19)$$

The parameters of terms on the left side are:

- m_s , the proof mass which moves in the sense direction
- c_y , the equivalent viscous and thermoelastic damping in the sense direction
- k_y , the equivalent stiffness in the sense direction.

The term on the right side represents the Coriolis force, where:

- m_c , the portion of the driven proof mass that contributes to the Coriolis force
- Ω_z , the angular velocity in the z-axis
- \dot{x} , the drive velocity.

Moreover, the definition of the sense-mode resonant frequency ω_s and the sense-mode Q -factor Q_s is

$$\omega_s = \sqrt{\frac{k_y}{m_s}} \quad (2.20)$$

$$Q_s = \frac{m_s \omega_s}{c_y} \quad (2.21)$$

With the assumption that the drive-mode is operated at drive resonant frequency ω_d , and the drive motion amplitude is regulated to be of the form $x = X_d \sin(\omega_d t + \phi_d)$ with a constant amplitude x_0 , Equation 2.19 becomes

$$m_s \ddot{y} + c_y \dot{y} + k_y y = -2m_c X_d \omega_d \Omega_z \cos(\omega_d t + \phi_d) \quad (2.22)$$

which can be also rewritten maintaining the sinusoidal form as

$$m_s \ddot{y} + c_y \dot{y} + k_y y = 2m_c X_d \omega_d \Omega_z \sin(\omega_d t + \phi_d - 90^\circ) \quad (2.23)$$

Consequently, the sense-mode steady-state response becomes

$$y = Y_d \sin(\omega_d t + \phi_s) \quad (2.24)$$

where Y_d and ϕ_s are the amplitude and phase of the sense-mode response, respectively expressed by the two following expressions

$$Y_d = \Omega_z \frac{m_c \omega_d}{m_s \omega_s^2} \frac{2X_d}{\sqrt{\left[1 - \left(\frac{\omega_d}{\omega_s}\right)^2\right]^2 + \left[\frac{1}{Q_s} \frac{\omega_d}{\omega_s}\right]^2}} \quad (2.25)$$

$$\phi_s = -\arctan \left[\frac{\frac{1}{Q_s} \frac{\omega_d}{\omega_s}}{1 - \left(\frac{\omega_d}{\omega_s}\right)^2} \right] + \phi_d - 90^\circ \quad (2.26)$$

To achieve the maximum possible gain, the conventional gyroscopes are generally designed to operate at or near the peak of the sense-mode response curve. This is typically achieved by matching drive and sense resonant frequency values [3]. When operating at the sense-mode resonance, i.e. $\omega_d = \omega_s$, the amplitude and the phase reduce to

$$Y_d = \Omega_z \frac{2Q_s X_d m_c}{m_s \omega_s} \quad (2.27)$$

$$\phi_s = -180^\circ + \phi_d \quad (2.28)$$

Investigating the resonant amplitude of the sense-mode Coriolis response given in 2.27, the sensitivity of the gyroscope to the angular rate input Ω_z can be improved by:

- Increasing the drive-mode oscillation amplitude X_d

- Increasing Q_s by decreasing damping, usually by vacuum packaging
- Maximizing the mass m_C that generates the Coriolis force, while minimizing the total mass m_s excited by the Coriolis force.

It is important to point out that, in a simple single-mass design as the one shown in Figure 2.4, m_C , m_d and m_s are equal and, thus, the only way to improve the gyroscope sensitivity is to operate with high Q_s and X_d values.

2.2.3 Mode-matching

Since the vibratory MEMS gyroscope output directly depends on the sense-mode displacement, high sensitivity and significant performance improvement can be achieved maximizing the sense-mode response, that means operating at or near the peak of the sense-mode response curve, with the drive and sense-mode frequencies perfectly matched. Devices operating at resonance with both the drive and sense-mode resonant frequency values matched are commonly referred as MEMS resonant gyroscopes.

A major challenge faced by the MEMS designer is the fluctuation in the performance parameters of resonant MEMS gyroscopes as they are easily affected by any variation in ambient conditions and fabrication imperfections, as these imperfections can cause a shift in resonance frequency which in turn causes a mismatch between the drive and sense mode frequencies. Figure 2.5 provides an example of the sense-mode response variation for a two degrees-of-freedom MEMS gyroscope system varying the relative position of the sense-mode resonant frequency with respect to the drive-mode operating frequency. If $\omega_d = \omega_s$, the system is in resonance in the drive direction and the maximum possible Coriolis force acting on the proof mass is expected. The system is also in resonance in the sense direction and the sense response has one combined resonant peak, which will provide a much larger response amplitude due to coinciding drive and sense resonant peaks. On the contrary, when $\omega_d \neq \omega_s$, the sense-mode response amplitude has two distinct peaks and this can cause the performance of the gyroscope to reduce dramatically as the even a slight mismatch can reduce the amplitude response of a mode matched gyroscope significantly.

For the compensation of the frequency mismatch between the drive and sense mode frequency due to microfabrication process tolerances and device operating temperature variations, complex structures, have to be introduced in the design or additional feedback circuitry is required to reduce the mismatch between drive and sense mode frequencies. Another possibilities to reduce sensitivity of response gain and phase to frequency fluctuations is operating away from the resonant frequency of the sense-mode, where the frequency variations have reduced effect on the output gain and phase. This is achieved by setting the sense-mode frequency ω_s spaced by a certain percentage away from the drive-mode frequency ω_d . This frequency separation is commonly referred as [3]

$$\Delta\omega = \omega_s - \omega_d \quad (2.29)$$

Typical mismatch is around 2%-10% of the resonance frequency.

2.3 Mechanical structure

Various vibratory MEMS gyroscopes have been reported in the literature based on a wide range of mechanical structures. The common goal of all vibratory gyroscope structures is to realize two orthogonal drive and sense mode dynamical systems coupled by the Coriolis force. The following sections outline the basics of the mechanical gyroscope design. Common mechanical gyroscope structure elements are presented and analyzed, with a special focus on the mayor design issues to achieve robustness against structural and environmental parameter variations.

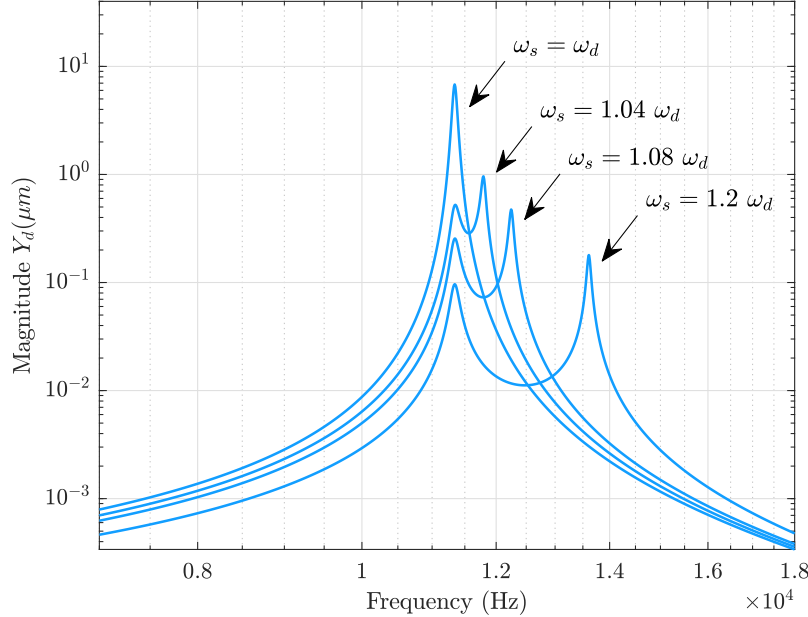


Figure 2.5: The sense-mode response amplitude of the two degrees-of-freedom MEMS gyroscope system with varying the drive and sense frequency mismatch. The highest response corresponds to the case where the drive and sense modes are matched, while the response amplitude diminishes as the mismatch increases.

2.3.1 Flexure elements

As previously introduced, vibratory MEMS gyroscopes are based on sustaining a drive oscillatory motion, and detecting a linear sense-mode response to the induced Coriolis force due to the presence of an external angular velocity. Since the induced Coriolis force is orthogonal to the drive-mode vibration, the proof-mass is required to be free to oscillate in two orthogonal directions, and desired to be constrained in other vibrational modes. The suspension system design which suspends the proof-mass above the substrate becomes critical in achieving these objectives.

In vibratory MEMS gyroscopes, the suspension systems usually consists of thin flexible beams, formed in the same structural layer as the proof-mass and designed to be compliant along the desired motion direction and stiff in the other directions. Typically, the narrow dimensions w is aligned normal to the motion axis and the precise value of the thickness t is adopted based on the fabrication process (Figure 2.6). The most commonly used beam elements in MEMS vibratory gyroscopes suspension systems are:

- fixed-guided beams
- folded beams
- double-folded beams
- serpentine beams
- crab-leg beams.

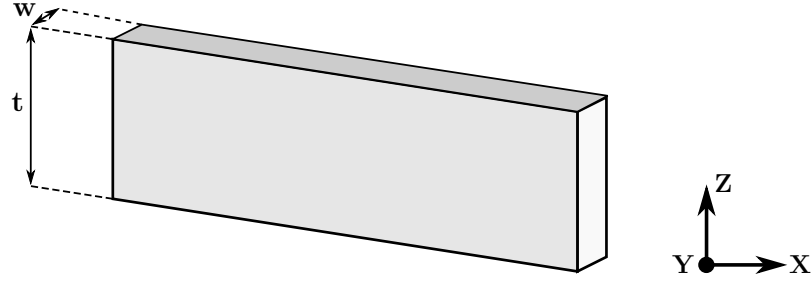


Figure 2.6: Typical beam element of vibratory MEMS gyroscope structures.

In practice, as shown in Figure 2.7, common suspension systems utilized to support orthogonal linear motions of vibrating MEMS gyroscopes are a combination of these beam elements. The stiffness values of beams elements are summarized in Table 2.1. The reader can also refer to [21] for the exact calculation. It is important to point out that, even though theoretical expressions of the beam elements could be a practical guide during the design process, finite element analysis simulations are absolutely necessary for accurate estimation of the flexure characteristics and, thus, of resonant frequencies. In addition, in complete suspension systems, a number of flexure elements are connected to the proof-mass and the total stiffness in a certain direction could be approximated by the sum of all flexure stiffness values in that direction. However, this approximation assumes that the compliance of the proof-mass, frame structures, and flexure in other directions are negligible. In reality, these factors dramatically reduce the overall stiffness value.

Beam elements	Schematic	k_x	k_y	k_z
fixed-guided end		$\frac{Ewt}{L}$	$\frac{Et w^3}{L^3}$	$\frac{Et w^3}{L^3}$
folded		$\frac{Ewt}{2L}$	$\frac{Et w^3}{2L^3}$	$\frac{Et w^3}{2L^3}$
double-folded		$\frac{Ewt}{L}$	$\frac{Et w^3}{L^3}$	$\frac{Et w^3}{L^3}$
serpentine		$\frac{n^1 Ewt}{L}$	$\frac{n^1 Et w^3}{L^3}$	$\frac{n^1 Et w^3}{L^3}$

¹ n represents the number of folds in the serpentine beam. For example, for the scheme in the table $n = 4$.

Table 2.1: Stiffness values of the most used beam elements in MEMS vibratory gyroscopes.

The main characteristics of the most common suspension types are summarized as follows:

- Fixed-guided suspensions are susceptible to residual stress or external axial loads that may lead to buckling. Since the lateral endpoints have a fixed distance, it features also an increased non-linearity. With growing deflections there emerges a non-linearly increasing axial load that requires increasing additional deflection forces. Thus, this kind of suspension is not suited for large deflections as are necessary, for instance, for the drive-direction suspensions.
- Folded-beam suspensions consist of two fixed-guided beams in series, and eliminate the non-linearity and axial-loading limitations of single fixed-guided beams. One limitation of the folded beams is the reduced axial stiffness. The distance between the two beams results in a moment arm under an axial load, and causes bending. This could become a disadvantage in designs that require substantial suppression of axial motion. Using doubly folded beams, which contain two symmetrically connected folded beams and provide excellent axial stiffness and linearity, can avoid this effect.
- Serpentine beams exist in two versions: the intrinsically serpentine suspension and the hairpin suspension. In a hairpin suspension the serpentine length L_s is considerably smaller than the outer length of the spring chain members and often located at one of their ends.
- The crab-leg and H-type suspensions are known to provide better symmetry among the drive and sense-modes, allowing to easily locate the drive and sense modes closer.

Finally, in the crab-leg, serpentine and hairpin suspensions, drive motion results in deflections also in the sense-mode beams, which often causes undesired energy transfer into the sense-mode. Thus, H-type suspensions and especially folded-beam suspensions with decoupling frames provide better mode-decoupling, which will be discussed in the next section [3].

2.3.2 Frame Structures

Suspension systems similar to crab-leg, serpentine or hairpin suspensions are compliant in two orthogonal directions. The same beams experience deflections in both modes, resulting in undesired coupling between the drive and sense modes. Since the drive-mode amplitude is orders of magnitude larger than sense-mode one, it is often required to isolate the drive motion from the sense motion. It is also desired to limit the deflection direction of the drive and sense electrodes, so that drive electrodes deflect only in drive direction, and sense electrodes deflect only in sense direction. This enhances the precision and stability of the drive actuation and sense detection electrodes [3].

To decouple the drive motion and sense motion, it is common to implement a frame structure that nest the proof mass. The two basic approaches in frame implementation are the drive frame and the sense frame, provided in Figure 2.8 and 2.9 respectively. In the drive frame implementation, the proof mass is nested inside a frame that is constrained to move only in the drive direction. Accordingly, when an excitation force is applied to the structure using comb-drive based actuators attached to the external frame, the proof mass can move only in the drive direction inside the frame. When the structure is subjected to an angular velocity in the z-direction, a Coriolis force appears in the sense direction and this force induces the proof mass to move in the sense direction. This approach assures that the drive motion is very well aligned with the designed drive axis, and minimizes the component of the actual drive motion along the sense detection axis. It also provides improved side stability and minimal parasitic sense-direction forces in the drive actuators. On the contrary, the sense frame implementation is based on nesting the proof mass inside a frame that is constrained to move only in the sense direction. The proof mass is set into oscillations in the drive direction by using comb-drive based actuators. For an input angular velocity in the z-direction, a Coriolis force is induced in the sense axis direction. The mechanical suspensions

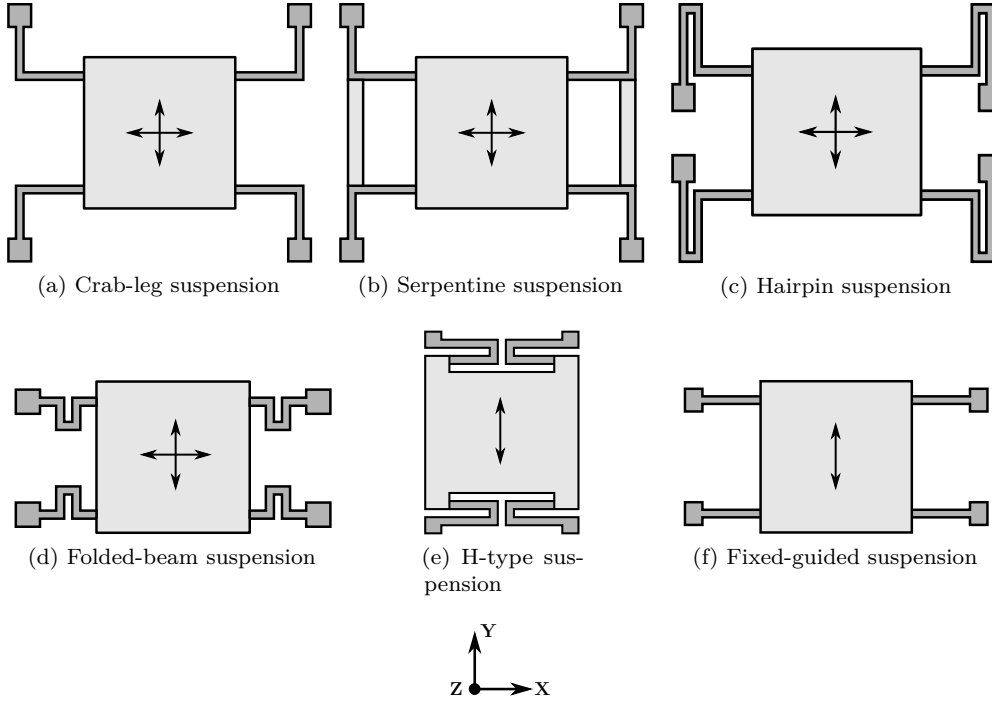


Figure 2.7: Standard suspensions design alternatives for supporting orthogonal linear motions.

attached to the proof mass does not allow its oscillation in the sense direction. However, since the drive mass is nested inside the sense mass, both the drive and sense mass move in the sense direction corresponding to rotation induced Coriolis force. The sense electrodes are attached to the external frame, and relative motion in the sense electrodes along the drive direction is prevented. This approach minimizes the undesired capacitance change in the sense electrodes due to the drive motion. It is anticipated that, the MEMS gyroscope design proposed in this thesis project, which will be analyzed in detail in the next Chapters, will use this frame implementation. It will consist in two separate masses for the drive and sense axis while minimizing the cross-axis sensitivity by decoupling the drive and sense move displacements using a unique configuration mechanical springs.

2.4 Electrical design

Micromachined gyroscopes are active devices which require both actuation and detection mechanisms. Various vibratory MEMS gyroscopes have been reported in the literature employing a wide range of actuation and detection methods. For exciting the gyroscope drive mode oscillator, the most common actuation methods are electrostatic, piezoelectric, magnetic and thermal actuation. Most common Coriolis response detection techniques include capacitive, piezoelectric, piezoresistive, optical, and magnetic detection. In many MEMS applications, capacitive detection and electrostatic actuation are known to offer several benefits compared to other sensing and actuation means, especially due their ease of implementation. Capacitive methods do not require integration of a special material, which makes them compatible with almost any fabrication process. They also provide good DC response and noise performance, high sensitivity, low drift, and low temperature sensitivity [3].

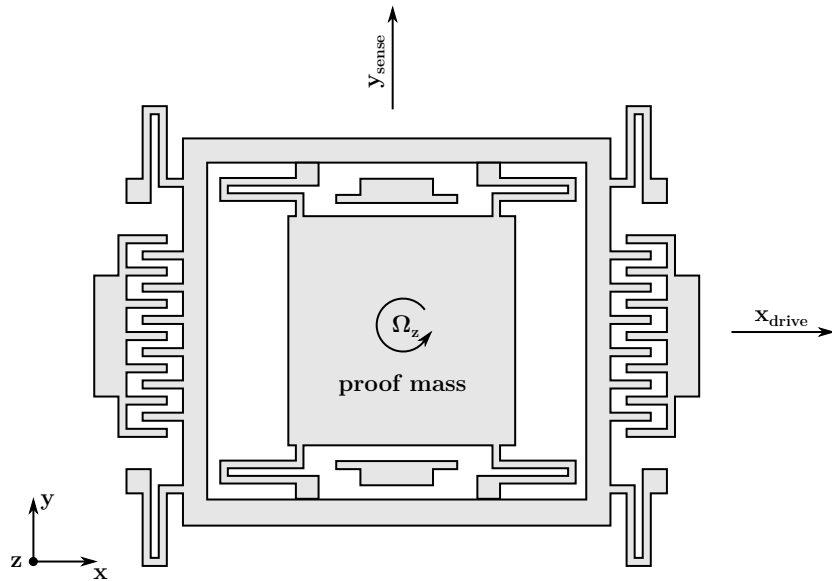


Figure 2.8: Drive frame implementation with U-beam suspensions, minimizing the component of the actual drive motion along the sense detection axis.

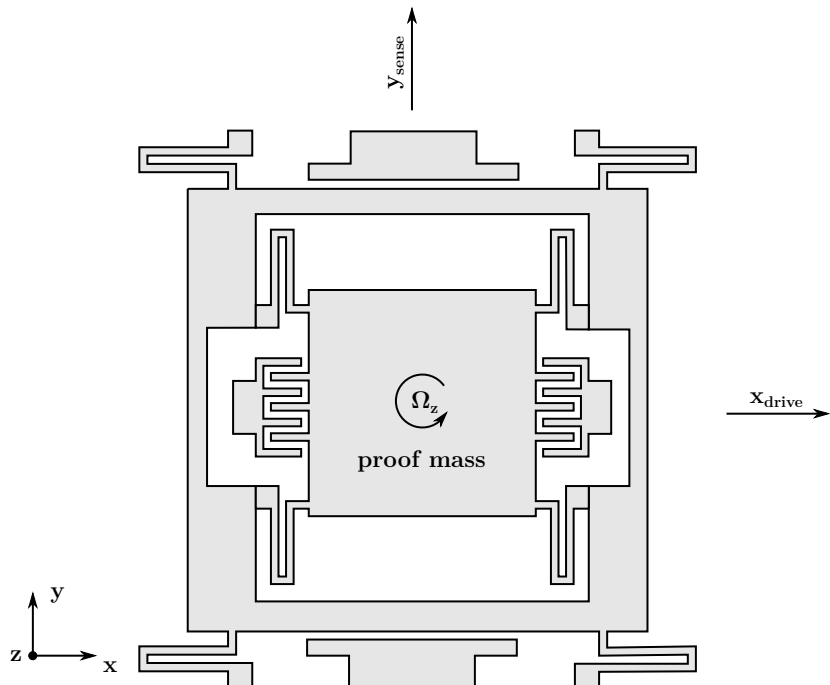


Figure 2.9: Sense frame implementation with U-beam suspensions, minimizing the undesired capacitance change in the sense electrodes due to the drive motion.

2.4.1 Electrostatic actuation

In most vibratory MEMS gyroscopes, electrostatic actuation is produced by the electric field of moving capacitors. The two basic configurations of capacitors for electrostatic actuation in a vibratory MEMS gyroscope are the parallel-plate and the interdigitated-comb capacitor configurations and they can either be arranged as single-sided or a differential pair.

Parallel-plate

The parallel-plate actuator consists of two isolated conductors, one fixed and the other movable in the y -direction, as represented in Figure 2.10.

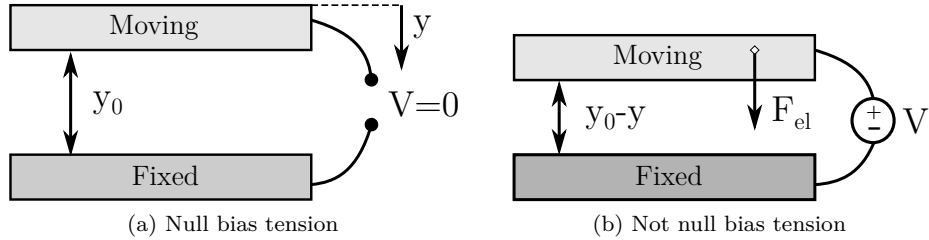


Figure 2.10: Parallel-plate actuator: one electrode is fixed and the other can move in the y -direction. The initial gap between plates is y_0 (a), which becomes $y_0 - y$ when a bias tension V is applied (b).

The capacitance between the parallel plates is

$$C = \frac{\epsilon_0 A}{y_0 - y} \quad (2.30)$$

where ϵ_0 is the free space permittivity, y_0 is the nominal gap, y is the moving plate displacement from the initial position and A the plate area. When a bias tension V is applied between the parallel plates, the electrostatic force can be determined as follows

$$F_{el} = \frac{1}{2} \frac{\partial C}{\partial y} V^2 = \frac{1}{2} \frac{\epsilon_0 A}{(y_0 - y)^2} V^2 \quad (2.31)$$

Even though the parallel-plate actuation provides much larger force per area compared to comb-drive actuators, the main disadvantage is that the electrostatic force is a nonlinear function of the displacement y . A decrease of the gap between the plates results in an increase of the electrostatic force F_{el} . This particular condition is commonly recognized to result in the *pull-in* instability, this is when the plates collapse due to the electrostatic force. In addition, the nonlinear electrostatic force always reduces the structure resonant frequency with increasing the bias tension across the electrodes. Therefore, this so-called electrostatic spring softening effect can be used to tune the resonant frequency of the driving or detection modes to achieve smaller frequency splitting. Since the MEMS gyroscope design proposed in this thesis project will be based on the electrostatic spring softening effect, for the sake of clarity a detailed description of this phenomenon and pull-in condition will be provided in Section 2.4.3.

Interdigitated-comb

In order to apply a constant electrostatic force with respect to the displacement and to avoid electrostatic instability phenomena, the actuation force for the drive mode is usually ensured by interdigitated comb-drive actuators (Figure 2.11). They consist in two interdigitated finger

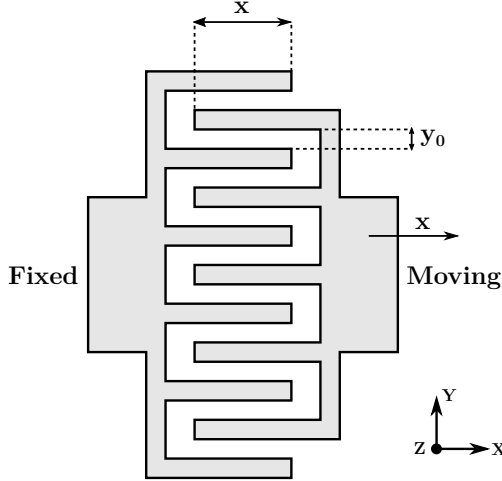


Figure 2.11: Comb-drive actuator.

structures, one fixed and the other movable, which can slide parallel to each-other when a voltage V is applied.

In a comb-drive structure made of N fingers, each finger forms two parallel-plate pairs, and when there is no electrostatic force, the total capacitance is

$$C = 2N \frac{\epsilon_0 x_0 t}{y_0} \quad (2.32)$$

where N is the number of fingers, x_0 is the overlap length of the capacitor plates, y_0 the gap between them and t the thickness of the silicon layer. Because the distance between the comb fingers is constant, capacitance changes linearly based on the overlapping plates area during such a movement. Considering the structure of Figure 2.11 and keeping the direction of motion along the x-axis, total capacitance becomes

$$C = 2N \frac{\epsilon_0 (x_0 - x)t}{y_0} \quad (2.33)$$

Consequently, the electrostatic force is

$$F_{el} = \frac{1}{2} \frac{\partial C}{\partial x} V^2 = -N \frac{\epsilon_0 xt}{y_0} V^2 \quad (2.34)$$

From Equation 2.34, it can be noticed that one of the key advantages of the comb-drive actuator is that the electrostatic force generated by the microstructure is independent from the displacement x of the movable plates and the overlap length x_0 . Consequently, a good practice in comb-drive design is to keep the overlap length minimum, while greater than the expected actuation peak amplitude so as to consider negligible the fringing field effects. When this happens, since the partial derivative of the electrostatic force with respect to the displacement x is zero, the comb-drive actuator does not result in a negative electrostatic spring constant.

Balanced actuation scheme

Since the drive mode of a vibratory MEMS gyroscope requires a linear oscillation to establish the Coriolis coupling between the drive and sense modes, the electrostatic force applied by the

comb-drive actuators must be harmonic. A very common configuration is the balanced-actuation scheme, which allows to linearize the electrostatic force with respect to a constant bias voltage V_{DC} and a time-varying voltage V_{AC} applied on two stationary electrodes arranged symmetrically on both sides of the movable fingers. Figure 2.12 shows a pictorial representation.

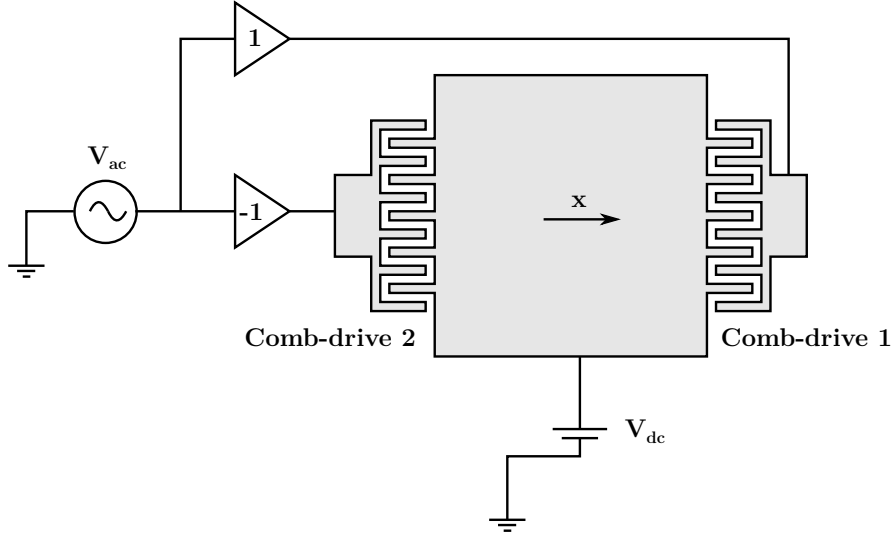


Figure 2.12: The balanced driving actuation scheme, based on applying $V_1 = V_{DC} + V_{AC}$ to one set of combs, and $V_2 = V_{DC} - V_{AC}$ to the opposing set.

Considering two equal opposite comb-drives with N interdigitated fingers, the total capacitance values C_1 and C_2 can be expressed as a function of the displacement in x-direction

$$\begin{aligned} C_1(x) &= C_0 + C(x) = 2N \left(\frac{\epsilon_0 x_0 t}{y_0} + \frac{\epsilon_0 x t}{y_0} \right) \\ C_2(x) &= C_0 - C(x) = 2N \left(\frac{\epsilon_0 x_0 t}{y_0} - \frac{\epsilon_0 x t}{y_0} \right) \end{aligned} \quad (2.35)$$

If the voltage applied to the two opposing electrode sets is

$$\begin{aligned} V_1 &= V_{DC} + V_{AC} \sin(\omega_d t) \\ V_2 &= V_{DC} - V_{AC} \sin(\omega_d t) \end{aligned} \quad (2.36)$$

The total generated drive force F_x is

$$F_x = \frac{1}{2} \frac{\partial C_1}{\partial x} V_1^2 + \frac{1}{2} \frac{\partial C_2}{\partial x} V_2^2 = \frac{1}{2} \frac{\partial C}{\partial x} V_1^2 - \frac{1}{2} \frac{\partial C}{\partial x} V_2^2 \quad (2.37)$$

By substituting the Equation 2.36 in the Equation 2.37, the following expression can be obtained

$$F_x = \frac{1}{2} \frac{\partial C}{\partial x} \left[\left(V_{DC} + V_{AC} \sin(\omega_d t) \right)^2 - \left(V_{DC} - V_{AC} \sin(\omega_d t) \right)^2 \right] \quad (2.38)$$

From the previous equations, it is possible to express the drive force F_x using a harmonic form:

$$F_x = 2 \frac{\partial C}{\partial x} V_{DC} V_{AC} \cdot \sin(\omega_d t) \quad (2.39)$$

Finally, considering Equation 2.35, the total drive force F_x in a balanced actuation scheme becomes

$$F_x = 4N \frac{\epsilon_0 t}{y_0} V_{DC} V_{AC} \cdot \sin(\omega_d t) \quad (2.40)$$

2.4.2 Capacitive sensing

In a MEMS vibratory gyroscope, electrostatic capacitance sensing is a frequently used method to detect the y displacement in the sense direction, due to the Coriolis force. Both the parallel-plate and interdigitated comb-finger capacitor configurations can be used.

Parallel-plate

Parallel-plate capacitors are the most commonly adopted solution for the detection of small displacements. When the parallel plates are oriented normal to the motion direction, the deflections cause a change in the initial gap y_0 and a consequent variation of the capacitance between plates, as shown in Figure 2.13.

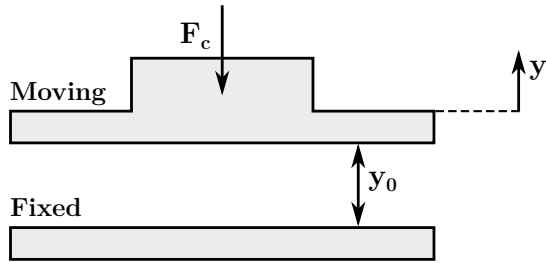


Figure 2.13: Sensing parallel-plate capacitor: the y deflection due to the Coriolis force F_c causes a change in the capacitance between the fixed and moving electrode.

The capacitance between the parallel plates is

$$C = \frac{\epsilon_0 A}{(y_0 - y)} \quad (2.41)$$

where ϵ_0 is the free space permittivity, y_0 is the nominal gap, y is the moving plate displacement from the initial position and A the plate area. Similarly to what was highlighted for the parallel-plate actuator, Equation 2.41 shows that the capacitance is a non-linear function of the displacement y in the sense direction. However, for very small deflections relative to the initial gap, i.e. $y \ll y_0$, the capacitance change can be linearized as follows

$$\Delta C = \frac{\epsilon_0 A}{(y_0 - y)} - \frac{\epsilon_0 A}{y} \approx \frac{\epsilon_0 A}{y_0^2} \quad (2.42)$$

Interdigitated-comb

Interdigitated-comb capacitors (Figure 2.14) are an ideal design alternative when the detected motion magnitudes are larger, especially either when the parallel-plate capacitors become significantly nonlinear. Denoting y as the displacement in the motion direction parallel to the plates, the total capacitance can be written as

$$C = 2N \frac{\epsilon_0 (y_0 + y)t}{x_0} \quad (2.43)$$

where N is the number of fingers, y_0 is the overlap length of the capacitor plates, x_0 the gap between them and t the thickness of the silicon layer. Finally, the total capacitance change can be expressed as

$$\Delta C = 2N \frac{\epsilon_0 (y_0 + y)t}{x_0} - 2N \frac{\epsilon_0 y_0 t}{x_0} = 2N \frac{\epsilon_0 y t}{x_0} \quad (2.44)$$

which is a linear function with respect to the y displacement in the sense direction.

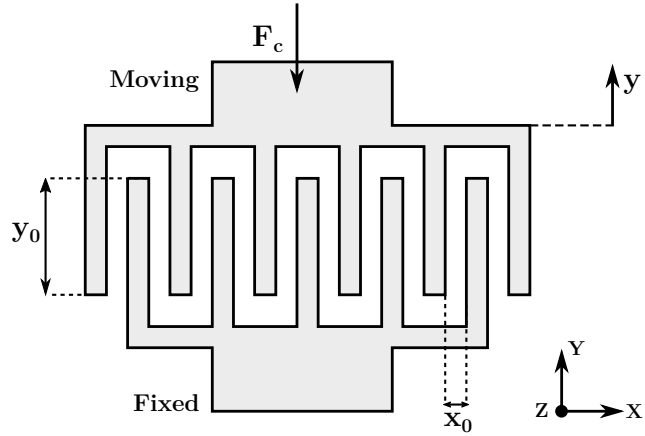


Figure 2.14: Interdigitated-comb capacitor for sense-mode detection.

Differential capacitance sensing

As introduced in the previous section, the sense displacement of the moving electrode due to the Coriolis force results in a change of capacitance ΔC . In order to linearize the capacitance change with respect to the deflection when the parallel-plate capacitor solution is adopted, the differential capacitance sensing is generally employed. As shown in the pictorial scheme of Figure 2.15, a basic differential detection is achieved by symmetrically placing independent fixed electrodes on two opposite sides of the moving one, such that the capacitance change in the electrodes are in opposite directions. In the initial position, the central plate stays in the middle of the two electrode and consequently the two capacitor-pairs have the same capacitance value. When the moving plate is subjected to a displacement in the positive y-direction, the central plate moves upwards increasing the capacitance C_{s+} and decreasing the capacitance C_{s-} , according to the following expressions

$$C_{s1} = \frac{\epsilon_0 A}{(y_0 - y)} \quad (2.45)$$

$$C_{s2} = \frac{\epsilon_0 A}{(y_0 + y)}$$

where ϵ_0 is the free space permittivity, y_0 is the nominal gap, y is the moving plate displacement from the initial position and A is the plate area. Under small deflection approximation, i.e. $y \ll y_0$, the previous capacitance expressions modify as follow

$$C_{s1} = \frac{\epsilon_0 A}{(y_0 - y)} = \frac{\epsilon_0 A}{y_0 \left(1 - \frac{y}{y_0}\right)} \approx \frac{\epsilon_0 A}{y_0} \left(1 + \frac{y}{y_0}\right) \quad (2.46)$$

$$C_{s2} = \frac{\epsilon_0 A}{(y_0 + y)} = \frac{\epsilon_0 A}{y_0 \left(1 + \frac{y}{y_0}\right)} \approx \frac{\epsilon_0 A}{y_0} \left(1 - \frac{y}{y_0}\right)$$

Therefore, the differential capacitance change ΔC can be expressed as a linear function of the moving plate y displacement

$$\Delta C = C_{s+} - C_{s-} = \frac{\epsilon_0 A}{y_0} \cdot \frac{2y}{y_0} = 2 \frac{\epsilon_0 A}{y_0^2} y \quad (2.47)$$

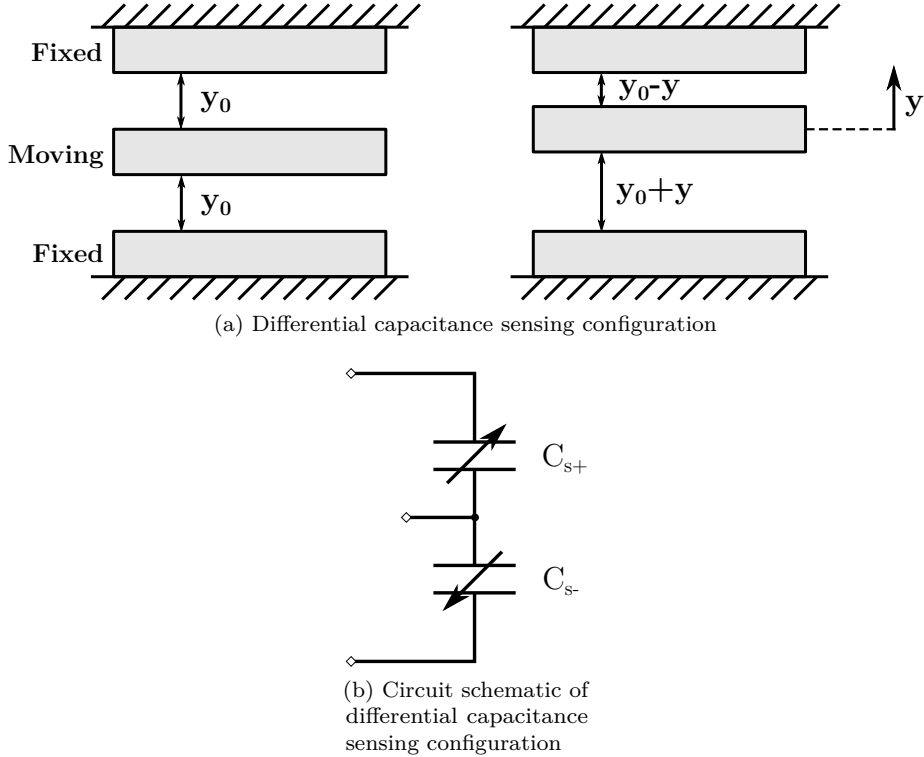


Figure 2.15: The principle of differential capacitance sensing: a movable central plate is placed between two independent fixed electrodes. In the initial position, the two capacitor-pairs have the same capacitance value. As the structure deflects, capacitance changes are in opposite directions.

Depending on the fabrication process, differential capacitive electrodes could be designed in several ways. The most common design method for the differential sensing of vibratory MEMS gyroscopes is the gap–antigap-based differential configuration shown in Figure 2.16. The movement of the proof mass in the positive y -direction leads to a capacitance change between parallel-plates. It can be found that the capacitance of C_{1a} and C_{2b} increases, while the capacitance of C_{1b} and C_{2a} decreases. In the initial position, the capacitance formed by the finger gap C_{0a} and anti-finger gap C_{0b} is given by

$$C_{0a} = \frac{\epsilon_0 A}{d_1} \quad (2.48)$$

$$C_{0b} = \frac{\epsilon_0 A}{d_2}$$

where ϵ_0 is the air permittivity, A is the total area between fingers, d_1 is the gap spacing, d_2 is anti-gap spacing. As the proof mass deflects, the capacitance values under y displacement is given by the following expressions

$$C_{1a} = \frac{\epsilon_0 A}{(d_1 - y)} \quad C_{1b} = \frac{\epsilon_0 A}{(d_2 + y)} \quad (2.49)$$

$$C_{2a} = \frac{\epsilon_0 A}{(d_1 + y)} \quad C_{2b} = \frac{\epsilon_0 A}{(d_2 - y)}$$

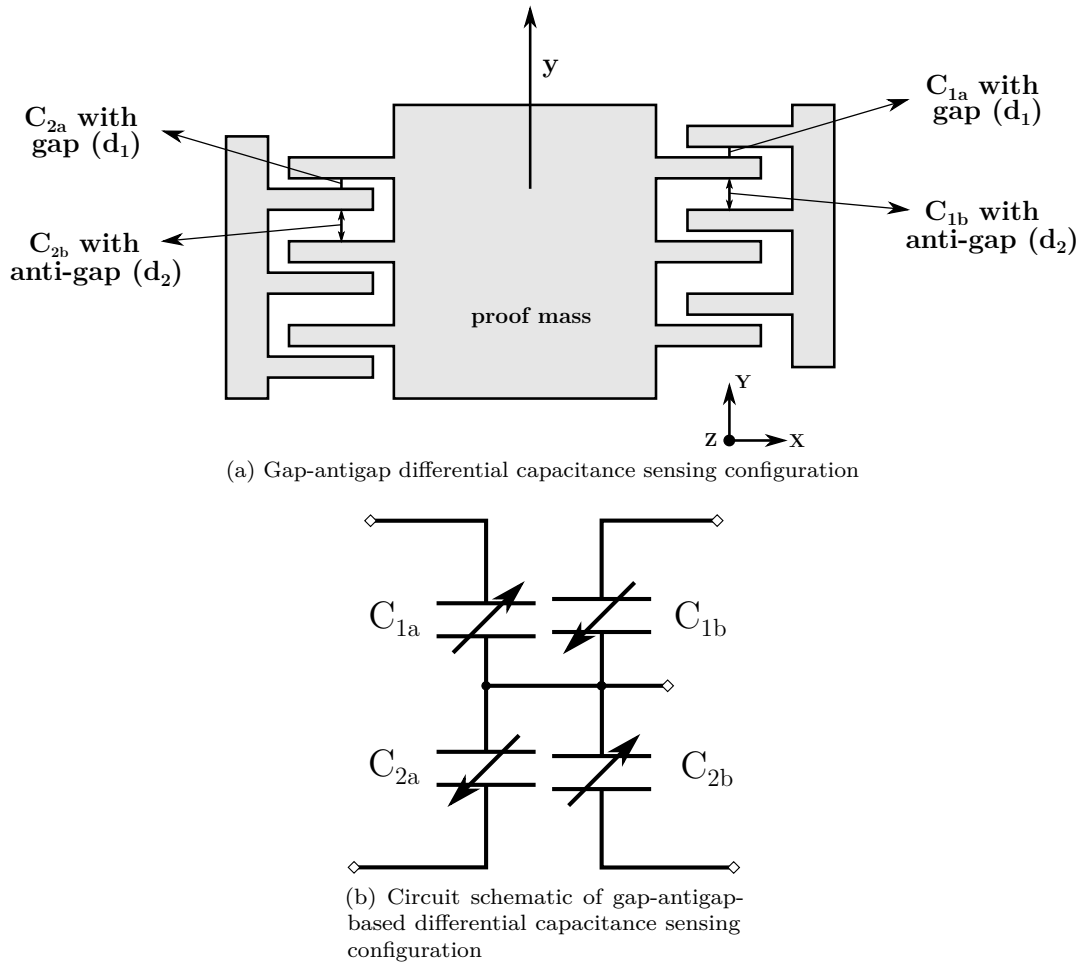


Figure 2.16: The principle of the gap-antigap based differential capacitance sensing.

Therefore, the differential capacitance change ΔC can be expressed as

$$\Delta C = (C_{1a} + C_{1b}) - (C_{2a} + C_{2b}) = \frac{2\epsilon_0 A y (d_2^2 - d_1^2)}{(d_1^2 - y^2) \cdot (d_2^2 - y^2)} \quad (2.50)$$

Under small deflection approximation, i.e $y \ll d_1$ and $y \ll d_2$, following the same approximation of Equation 2.46, the capacitance values become

$$\begin{aligned} C_{1a} &\approx \frac{\epsilon_0 A}{d_1} \left(1 + \frac{y}{d_1} \right) & C_{1b} &\approx \frac{\epsilon_0 A}{d_2} \left(1 - \frac{y}{d_2} \right) \\ C_{2a} &\approx \frac{\epsilon_0 A}{d_1} \left(1 - \frac{y}{d_1} \right) & C_{2b} &\approx \frac{\epsilon_0 A}{d_2} \left(1 + \frac{y}{d_2} \right) \end{aligned} \quad (2.51)$$

Accordingly, the differential capacitance change ΔC becomes

$$\Delta C = 2\epsilon_0 A y \left(\frac{1}{d_1^2} - \frac{1}{d_2^2} \right) \quad (2.52)$$

From the previous equation, it can be noticed that, if the anti-gap spacing d_2 is close to the gap spacing d_1 , ΔC will be very small, however if d_2 is much larger than d_1 , its effects becomes negligible and ΔC can be further reduced to

$$\Delta C = \frac{2\epsilon_0 A y}{d_1^2} \quad (2.53)$$

Equation 2.53 shows that the differential capacitance change is independent of the anti-gap spacing d_2 , nevertheless, large d_2 means fewer finger pairs and consequently a decreases in the total overlap area A between fingers. In addition, since ΔC is inversely proportional to the square of the initial gap d_1 , its values should be minimized. As conclusion, taking into account the fabrication process limitation, by adjusting d_1 and d_2 higher sensitivity could be achieved.

It is important to point out that the differential capacitor structure enables differential sensing, which can cancel many adverse or common mode effects to first order.

2.4.3 Pull-in and electrostatic spring softening effect

In the previous section it was shown that electrostatic fields from sensing or actuating parallel-plates schemes can introduce nonlinear forces on the structure. If on one side the nonlinearities introduced by sensing parallel-plates can be neglected assuming small displacements in the sense direction, on the other side electrostatic forces produced by parallel-plates actuators are non-linear functions of the displacement in the drive direction. As previously introduced, this nonlinear relation may influence the dynamic of the MEMS gyroscope mechanical structure due to the so-called phenomenon of electrostatic spring softening. In addition the electrostatic force increases as the gap between the plates decreases, which is widely known to result in the pull-in instability, that is when the plates collapse due to the electrostatic force.

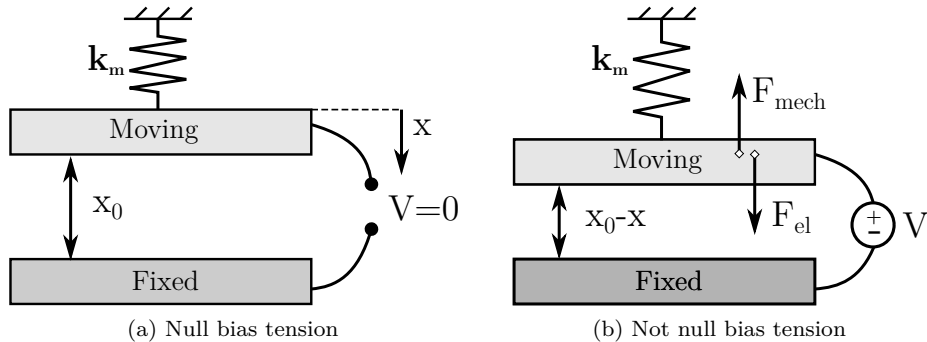


Figure 2.17: Mono-dimensional model with lumped parameters: parallel plates capacitor connected to a mechanical spring.

At this point, the mono-dimensional model shown in Figure 2.17 is useful to describe the interaction between mechanical and electrostatic domains of parallel-plates based actuators used in vibratory MEMS gyroscopes. This model is essentially a parallel-plate capacitor of area A , with a fixed ground plate, and a moving plate restrained by a linear spring of known stiffness k_m . In the rest position, the bias tension applied between the plates, the displacement and electrostatic force values are equal to zero, while when a bias tension is applied between plates, an electrostatic force F_{el} occurs. This force can be expressed by Equation 2.31. The linear spring guarantees a mechanical force F_{mech} which stands against the gap reduction between plates due to the electrostatic force. The force balance equation for this model can be written by summing

together the actuating nonlinear electrostatic force, F_{el} , and the linear restoring force due to the spring, F_{mech} , as in the following Equation

$$F_{mech} + F_{el} = k_m x - \frac{1}{2} \frac{\epsilon_0 A}{(x_0 - x)^2} V^2 = 0 \quad (2.54)$$

where ϵ_0 is the free space permittivity, x_0 is the nominal gap, x is the moving plate displacement from the initial position, A is the plate area and k_m the stiffness of the mechanical spring. Real solutions of Equation 2.54 can be qualitatively analyzed evaluated as shown in Figure 2.18.

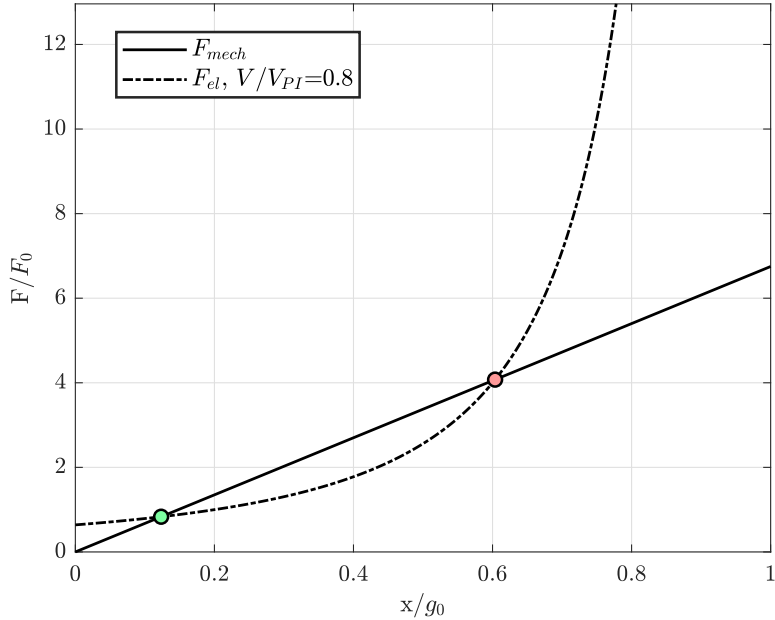


Figure 2.18: One-dimensional electromechanical model static equilibrium, for a bias voltage V below the pull-in voltage V_{PI} : equilibrium points in green and red represent the stable and unstable equilibrium position, respectively.

The two curves, representing the amplitude of the mechanical and electrostatic force, are drawn as a function of the dimensionless displacement $\frac{x}{x_0}$ of the movable electrode. In addition, the amplitude

has been made dimensionless with respect to the factor $F_0 = \frac{\epsilon_0 A V_{PI}^2}{2x_0^2}$. For a fixed bias tension V value, the mechanical spring force F_{mech} is a linear function of the displacement x , while according to Equation 2.31, the electrostatic force is represented by a hyperbole. Balance of forces is attained at the intersection points of mechanical and electrical force curves. Due to the nonlinearity of Equation 2.31, two equilibrium positions are obtained for each bias tension V applied. It is possible to demonstrate that the solution corresponding to the position x furthest from the fixed plate (represented in green in the plot) is a stable equilibrium position. In this position, if a small displacement is applied to the system, the forces restore the starting configuration. Indeed, if the gap diminishes, as the displacement x grows, the mechanical force becomes preponderant, if the gap increases the electrostatic force does. The second solution, corresponding to the position x closest to the fixed plate (represented in red in the plot), is an unstable equilibrium position: if the gap is lowered, the electrostatic force becomes greater and greater as the gap becomes smaller,

thus leading the two electrodes to touch, if the gap is increased, the mechanical force overcomes until the stable equilibrium position is reached.

The graphical method may be used to determine equilibrium positions when varying the bias voltage V applied. Figure 2.19 shows the equilibrium positions of the system for three representative bias voltages. When the voltage is increased, the hyperbola representing the electric force moves upward and, thereby, shifts the point of stable equilibrium further to the right, which corresponds to a larger displacement. At the particular bias tension V_{PI} , called pull-in voltage, the two curves representing the mechanical and electrostatic forces intersect tangentially at one single point. Accordingly, the equilibrium of forces becomes unstable. The pull-in voltage V_{PI} is the maximum voltage bearable by the system: if the applied voltage lies above the pull-In voltage, no equilibrium position can be obtained and the two faces of the capacitor slam one against each other closing the circuit. The voltage and displacement values required to induce the pull-in condition are important

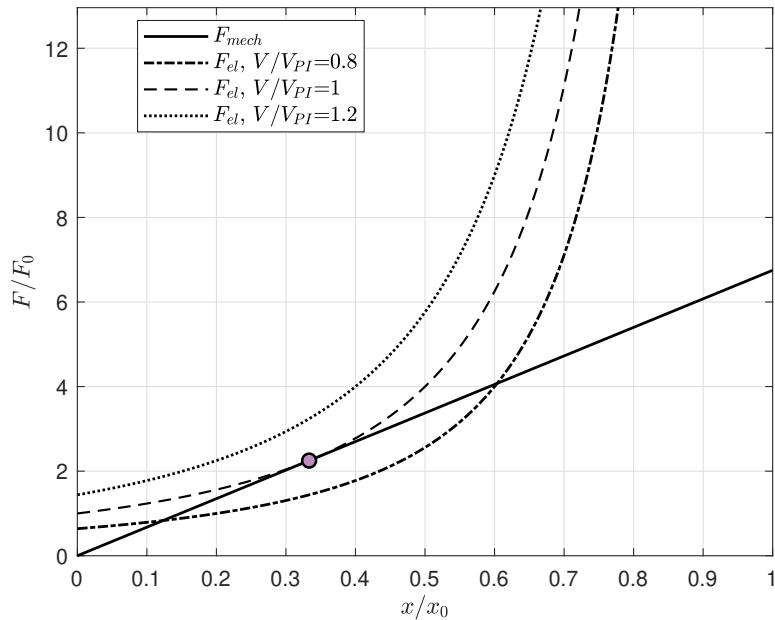


Figure 2.19: One-dimensional electromechanical model static equilibrium for a variable bias voltage V : the purple dot represents the pull-in condition.

parameters for the modelling of micro-devices, such as vibratory MEMS gyroscopes. Although the effect of the pull-in can be explained quite easily through graphical methods, analytic relationships are indispensable to provide exact values of voltage and displacement. Under pull-in conditions, as it has been shown graphically, the curves of the electrostatic and mechanical force intersect tangentially in one single point. By equalizing the modules of two curves, the following expression is obtained

$$k_m x = \frac{1}{2} \frac{\epsilon_0 A}{(x_0 - x)^2} V^2 \quad (2.55)$$

The tangency condition also implies that the gradients of the two curves are equal in correspondence of the point of intersection. By deriving Equation 2.55 with respect to the x displacement, the stiffness of the mechanical spring is

$$k_m = \frac{\epsilon_0 A}{(x_0 - x)^3} V^2 \quad (2.56)$$

Substituting Equation 2.71 in 2.55, the displacement of the moving plate when the pull-in condition is reached can be expressed as

$$x_{PI} = \frac{x_0}{3} \quad (2.57)$$

The pull-in voltage is therefore

$$V_{PI} = \sqrt{\frac{8}{27} \frac{k_m x_0^3}{\epsilon_0 A}} \quad (2.58)$$

The pull-in voltage V_{PI} depends on the stiffness of the mechanical spring k_m and initial gap x_0 , while the displacement of the moving plate at the pull-in condition depends only on the initial gap. Definitely, this conclusion is only valid for a one-dimensional electromechanical model. However, even for multi-degrees-of-freedom MEMS gyroscope structures, the pull-in displacement may be similar to the value expressed by Equation 2.57.

The parallel plate capacitor model represented in Figure 2.17 is also suitable to explain the resonance frequency shift caused by the electromechanical coupling between the movable structure and the fixed electrode in presence of a static load. Assuming that the suspended part is charged by static voltage V , the electrostatic force F_{el} acting on the movable electrode is proportional to the distance between the electrodes and is expressed by Equation 2.31. If a vibration is imposed on the charged capacitor, then the generated electric force is nonlinearly dependent on the distance of the variable armatures. A simple procedure to investigate the effect of the electromechanical coupling on the system dynamics is to consider the generic $x(t) = x_i$ deformed configuration of the structure and to expand the nonlinear electrostatic force in a Taylor series around this position, as in the following expression [18]

$$F_{el} = F_{el0} + \frac{\partial F_{el}}{\partial x} \Big|_{x=x_i} (x - x_i) + \frac{\partial^2 F_{el}}{\partial x^2} \Big|_{x=x_i} (x - x_i)^2 + \frac{\partial^3 F_{el}}{\partial x^3} \Big|_{x=x_i} (x - x_i)^3 + \dots \quad (2.59)$$

by introducing the force expressed by Equation 2.31 the series expansion becomes [18]

$$F_{el} = \frac{1}{2} \frac{\epsilon_0 A}{(x_0 - x_i)^2} V^2 \left\{ 1 + 2 \frac{(x - x_i)}{(x_0 - x_i)} + 3 \frac{(x - x_i)^2}{(x_0 - x_i)^2} + 4 \frac{(x - x_i)^3}{(x_0 - x_i)^3} + \dots \right\} \quad (2.60)$$

The relation between the electrostatic force and the displacement can be approximated as linear if the Taylor series is stopped at the first order

$$F_{el} = \frac{1}{2} \frac{\epsilon_0 A}{(x_0 - x_i)^2} V^2 \left(1 + 2 \frac{x - x_i}{x_0 - x_i} \right) \quad (2.61)$$

Indicating with m the mass of the movable electrode and neglecting dissipation effects, the governing equation describing the system dynamics is

$$m\ddot{x} + k_m x - F_{el} = m\ddot{x} + k_m x - \frac{1}{2} \frac{\epsilon_0 A}{(x_0 - x)^2} V^2 = 0 \quad (2.62)$$

It is possible to rewrite Equation 2.62 by using the linearized electrostatic force expressed in Equation 2.61, obtaining

$$m\ddot{x} + k_m x - \frac{1}{2} \frac{\epsilon_0 A}{(x_0 - x_i)^2} V^2 \left(1 + 2 \frac{x - x_i}{x_0 - x_i} \right) = 0 \quad (2.63)$$

It is evident that the electrostatic force generates an equivalent electrostatic stiffness k_{el} that contributes to a reduction of the global stiffness of the system. The equivalent electrostatic stiffness constant is

$$k_{el} = \frac{\epsilon_0 A}{(x_0 - x_i)^3} V^2 \quad (2.64)$$

Accordingly, in presence of an electrostatic force, when the structure is vibrating around its deformed configuration x_i , the resonant frequency depends on the tension V applied between parallel plates

$$\omega = \sqrt{\frac{k_m - k_{el}}{m}} = \sqrt{\frac{k_m}{m} - \epsilon_0 \frac{AV^2}{m(x_0 - x_i)^3}} \quad (2.65)$$

If the Taylor expansion of the electrostatic force F_{el} is performed around the initial position, so that $x_i = 0$, Equation 2.65 becomes

$$\omega = \sqrt{\frac{k_m}{m} - \frac{1}{2} \frac{\epsilon_0 A}{mx_0^3} V^2} \quad (2.66)$$

2.5 Damping

As introduced in Section 2.2, the drive and sense resonant mode response in a vibratory MEMS gyroscope strongly depends on their respective damping factors. Since the total damping factor is a combination of multiple effects, its correct estimation is essential in the MEMS gyroscope design. Being the quality factor the measure of damping in a system, it is a measurable parameter that can be used to evaluate the damping factor of the gyroscope resonant modes. In this section, various dissipation mechanisms contributing to the overall Quality-factor are reviewed.

In general, the Quality-factor of a MEMS gyroscope depends on many different dissipation effects. Some of the known and frequently considered mechanisms that contribute to the total quality factor are:

- Viscous air-damping
- Thermoelastic damping
- Anchor losses.

The total quality factor of a vibratory structure can be calculated from the contribution of individual dissipation mechanisms and it can be expressed as a combination of each dissipation effects [3]

$$\frac{1}{Q_{total}} = \frac{1}{Q_{viscous}} + \frac{1}{Q_{TED}} + \frac{1}{Q_{anchor}} + \frac{1}{Q_{electronics}} + \frac{1}{Q_{other}} \quad (2.67)$$

where $Q_{viscous}$ is due to air-damping dissipation, Q_{TED} is due to thermoelastic damping, $Q_{electronics}$ is due to electronics damping, Q_{anchor} corresponds to the anchor losses and Q_{other} captures remaining damping effects.

As shown in Equation 2.67, the total Q-factor is dominated by the dissipation mechanism with lowest Q-factor. For this reason, each mechanism can be considered as an individual Q-factor limiting value, with the lowest individual quality factor value dominating the overall quality factor of the MEMS gyroscope.

2.5.1 Viscous air-damping

Viscous air damping is typically the dominant dissipation mechanism for the vibratory MEMS gyroscopes operated at atmospheric pressure. The interaction between the surface of the movable structure and the surrounding gas molecules dissipates significant amounts of energy. In the gyroscope dynamical system, viscous damping is dominated by the internal friction of the gas between the proof-mass and the substrate, and between the comb-drive and sense capacitor fingers.

A precise estimation of the damping factors due to the interaction between the structure surface and the air molecules requires accurate fluid dynamics modeling which extends beyond the scope of this thesis. However, in the following section, two general models capable of approximating with good accuracy the damping factors of sensors that operate at atmospheric pressure, i.e. the slide film damping and squeeze film damping, are presented.

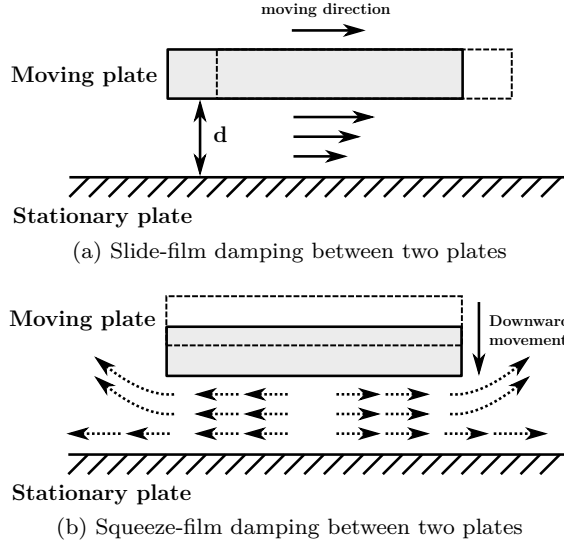


Figure 2.20: The two major sources of viscous air damping: (a) slide film damping; (b) squeeze film damping.

Squeeze film damping

Squeeze film damping occurs when two parallel plates move toward each other and squeeze the fluid film in between (Figure 2.20b). When the air spacing between the plates is reduced due to downward deflection of the moving one, a certain amount of air flow is squeezed out, resulting in an increase in the air pressure between the plates and, consequently, in a damping pressure which causes a resistive force and energy dissipation. The damping pressure consists of two main components: the component which causes the viscous flow of air when the air is squeezed out of the plate region and the one which causes the compression of the air film. The force component related to the viscous flow is referred to as the viscous damping force, and the force component related to the air compression is referred to as the elastic damping force. If the plates oscillate with a low frequency, or, the plates move with a slow speed, the gas film is not compressed appreciably. In this case, the viscous damping force dominates. On the other hand, if the plate oscillates with a very high frequency, or moves with a high speed, the gas film is compressed but fails to escape. In this case, the gas film works like a bellows. Thus, the elastic force is predominant [12].

The squeeze film damping model requires the solution of Navier–Stokes equations. In a continuum regime, the continuity equation of fluid flow is dictated by Navier–Stokes momentum equations for compressible and viscous flows. For the application of fluid lubrication, Reynolds first formulated the theory for the film between two surfaces in relative motion. Considering two parallel plates moving perpendicular to each other and in case of small displacement, the Reynolds equation can be simplified in a linear form, given by [12, 23]

$$\left[\frac{\partial^2 p}{\partial x^2} + \frac{\partial^2 p}{\partial y^2} \right] = \frac{12\mu_{eff}}{P_a h_a^3} \left[h_a \frac{\partial p}{\partial t} + P_a \frac{\partial h}{\partial t} \right] \quad (2.68)$$

where P_a is the ambient pressure, p is a small pressure change in P_a due to the variation of the plate spacing h , h_a is the initial gap between plates and the term μ_{eff} is the effective viscosity of the air at a given temperature and pressure, relates to the air viscosity at ambient condition. Indeed, one of the most significant effects present in squeeze film flow in MEMS structures is that of rarefaction. This effect arises because of the extremely small gaps in which the air or gas is forced to flow. The effective viscosity μ_{eff} is given as [3]

$$\mu_{eff} = \frac{\mu}{1 + 9.638K_n^{1.1}} \quad (2.69)$$

In the above equation, μ is the air viscosity at ambient temperature T and K_n is the Knudsen number. The Knudsen number is defined as the ratio of the mean free path λ of air to the thickness of the air gap, as follows

$$K_n = \frac{\lambda}{h_a} \quad (2.70)$$

where h_a is the air gap thickness and λ the mean free path of air at a given operating temperature and pressure. Since several types of flow regimes can exist for the thin air film, the Knudsen number can be used to define the operating flow regime and change the effective viscosity by using Equation 2.69. Table 2.2 shows a classification of flow regimes based on the K_n values.

K_n value	$K_n < 0.01$	$0.01 < K_n < 0.1$	$0.1 < K_n < 10$	$K_n > 10$
Flow regime	Continuum Flow	Slip Flow	Transitional Flow	Molecular Flow

Table 2.2: Knudsen number range and corresponding flow regimes [31].

Finally, the mean free path of air λ can be computed as

$$\lambda = \frac{P_0 \lambda_0}{P_a} \quad (2.71)$$

where λ_0 is the mean free path at pressure P_0 . An alternative calculation is based on physical model which is given by the following equation [30]

$$\lambda = \frac{\mu}{p} \sqrt{\frac{\pi K_B T}{2m_{air}}} \quad (2.72)$$

where μ is the air viscosity at atmospheric pressure, m_{air} is the mass of air, p is the air pressure, T is the air temperature and $K_B = 1.38 \cdot 10^{-23} JK^{-1}$ is the Boltzmann's constant.

The Equation 2.68 can be written in the non-dimensional form by using normalized variables

$$\left[\frac{\partial^2 \tilde{p}}{\partial \tilde{x}^2} + \frac{\partial^2 \tilde{p}}{\partial \tilde{y}^2} \right] = \sigma \left[\frac{\partial \tilde{p}}{\partial \tau} + \frac{\partial \tilde{h}}{\partial \tau} \right] \quad (2.73)$$

where $\tilde{p} = \frac{p}{P_a}$, $\tilde{h} = \frac{h}{h_a}$, $\tilde{x} = \frac{x}{L}$, $\tilde{y} = \frac{y}{L}$ and $\tau = \omega t$, with L the characteristic length of the plate, ω the operating frequency and σ the squeeze number. In particular, the squeeze number σ is a measure of the compressibility of the fluid and it can be expressed as

$$\sigma = \frac{12\mu_{eff} L^2 \omega}{P_a h_a^2} \quad (2.74)$$

In literature, different closed form solutions for Equation 2.68 are proposed. For rigidly oscillating rectangular plate, Blech [13] solved the linearized Reynolds equation with ambient pressure at the

boundaries and presented closed form solution for the coefficients of the viscous damping force and elastic damping force of squeeze film air damping. They are summarized as follow [31]

$$c_d(\sigma) = \frac{64\sigma P_a L w}{\pi^6 h_a} \sum_{m,n \text{ odd}} \frac{m^2 + (nc)^2}{(mn)^2 \left[(m^2 + (nc)^2)^2 + \sigma^2 / \pi^4 \right]} \quad (2.75)$$

$$k_a(\sigma) = \frac{64\sigma^2 P_a L w}{\pi^8 h_a} \sum_{m,n \text{ odd}} \frac{1}{(mn)^2 \left[(m^2 + (nc)^2)^2 + \sigma^2 / \pi^4 \right]}$$

where $c = L/w$ is the length to width ratio of the rectangular plate, P_a is the ambient pressure, h_a is the air gap height, ω is the frequency of oscillations of the plate and m and n are odd integers. The central parameter in these expressions is the squeeze number σ , as it determines if the air damping force can be considered viscous or elastic. At low frequencies and, thus, low values of the squeeze number, the viscous component of the damping force dominates, then reaches a maximum and finally decreases at high frequencies. In contrast, the elastic component of the force always grows with ω . The crossover of the force components takes place at the the cut-off squeeze number σ_c : at this point either the viscous and elastic effects significantly influence the dynamic of the oscillating plate.

Finally, inertial effects of damping force should be taken into account considering the Reynolds number R_e , which can be expressed as follows [31]

$$R_e = \frac{\rho \omega h_a^2}{\mu_{eff}} \quad (2.76)$$

where h_a is thickness of the air gap, ρ is the density of air and ω is the operating frequency. For MEMS devices with small air gap dimension, or at low frequency values, $R_e \ll 1$ and the inertial effect can be neglected. However, for larger air-gap height, or at higher frequencies of oscillations $R_e \gg 1$ and the inertial effects may not be negligible.

Slide film damping

Slide-film damping occurs when two plates of an area A , separated by a constant distance d , slide parallel to each other (Figure 2.20a). The slide film damping coefficient can be expressed as [3]

$$c_{slide} = \frac{\mu_{eff} A}{d} \quad (2.77)$$

where A is the overlap area of the plates, d is the gap between plates and μ_{eff} is the effective viscosity of air. In the case of slide film damping, the effective viscosity of air μ_{eff} is expressed as [3]

$$\mu_{eff} = \frac{\mu}{1 + 2K_n + 0.2K_n^{0.788} e^{-K_n/10}} \quad (2.78)$$

where K_n is the Knudsen number, computed through Equation 2.70.

In MEMS gyroscopes, slide-film damping mainly affects in-plane modes where the sensor structure moves parallel to the substrate. Same for electrode structures with large overlap such as comb fingers that have similar geometric properties as the two parallel plates [28].

It is important to point out that, both squeezed and slide film air damping are dependent on the air viscosity which is strongly influenced by the changes in the operating temperature. In order to avoid to weighting down the discussion, the effect of temperature variations on air viscous damping will be provided in Chapter 6, where thermal effects on the MEMS gyroscope structure dynamics will be analyzed.

2.5.2 Thermoelastic damping

As previously introduced above, the viscous-air damping is the principle dissipation mechanism for vibratory MEMS gyroscope sensors that operate at ambient pressure. Indeed, under vacuum conditions, thermoelastic damping (TED) is one of the primary damping mechanisms. It is a source of internal loss present in all material, caused by the interaction of temperature fluctuations and oscillations within a vibratory structure. Structures that are vibrating exhibit stress/strain gradients, which in turn create localized temperature gradients within the structure. These temperature gradients inevitably result in heat transfer within the structure and an irreversible conversion of vibratory energy into heat. The degree of coupling between the temperature gradients and stress/strain gradients is controlled by the material's coefficient of thermal expansion CTE, which is an intrinsic property of the material [32].

Pioneer studies in thermoelastic damping were conducted by Zener. They indicate that a temperature gradient is generated when finite thermal expansion occurs, and this temperature gradient leads to energy dissipation due to the heat currents that it produces. Considering a beam resonator structure, Zener developed a model based on the classical Fourier thermal conduction theory, according to which there is no temperature gradient across the beam, and he defined the internal friction as the inverse of the quality factor [25]

$$Q_{TED}^{-1} = \frac{E\alpha^2 T}{C_V} \frac{\omega\tau}{1 + (\omega\tau)^2} \quad (2.79)$$

with

$$\tau = \frac{C_V b^2}{\kappa\pi^2} \quad (2.80)$$

where ω is the mechanical resonant frequency of the beam, b represents the width of the resonator in the plane of the resonance motion, E is the Young's Modulus, T is the temperature, α is the thermal coefficient expansion (CTE), κ is the thermal conductivity coefficient and C_V is the heat capacity at constant volume coefficient. As shown in Equation 2.80 the quality factor due to thermoelastic damping depends on the operating temperature but it is independent of other environment variables. Even if this analytical expression is not rigorous, it allows to connect thermoelastic effects with standard inelastic damping theory and offers intuition for the loss mechanism. In addition it is possible to extend this expression also to generic oscillating structures as MEMS gyroscope ones.

As shown from Equation 2.80, TED within a vibratory structure depends on a wide variety of factors, such as device geometry, vibration frequency, and operating temperature. In order to reduce TED:

- resonant frequency of the gyroscope can be chosen such that the frequency difference between the thermal and mechanical modes is maximized
- low CTE materials, such as fused silica, can be used for fabrication of the mechanical element. Low CTE materials can provide orders of magnitude reduction in TED due to a reduction in coupling between thermal and mechanical domains.

2.5.3 Anchor losses

Anchor losses are caused by elastic energy leakage through anchoring structure to the substrate. The elastic wave propagation highly depends on the stress distribution at the anchor. This distribution can be affected by many different variables such as thermal stress of the substrate and linear acceleration induced stress. The change of stress distribution differs from mode to mode and is not necessarily monotonic. Therefore, anchor loss can cause erratic changes in both damping

mismatch and principle damping axis misalignment. To achieve high bias stability, anchor loss of the gyroscopic modes must be minimized. At the same time, the anchoring structure should be robust to provide enough resistance against shock and vibration for consistent performance delivery [35].

As already stated in the introduction of the Chapter, these sections presented fundamental aspects of the mechanical design of vibratory MEMS gyroscopes. Basic gyroscope dynamical system structures and their corresponding flexure systems were covered. In addition, an overview of electrostatic actuation and capacitive sensing in vibratory MEMS gyroscope is presented. Finally, various dissipation mechanisms contributing to the total damping factors are discussed. Clearly, these sections have not the purpose to provide a complete and detailed catalogue of all the aspects correlated to vibratory MEMS gyroscopes design available in the open literature, but to introduce elements and topics useful for understanding the MEMS gyroscope structure developed for this thesis project.

Chapter 3

Simulation methodology

MEMS devices are complex micro-systems combining various domains, such as the electrostatic and mechanical ones. In the design phase of the new MEMS gyroscope structures proposed in this thesis project, finite element simulations are therefore necessary for an adequate understanding of static and dynamical behaviour.

In this chapter the simulation methodology used to analyze the MEMS gyroscope devices proposed in this thesis project is described. First, the general procedure of FEM simulation in Ansys is presented, including specialized simulation approaches using static, modal and harmonic FEM analysis. A special focus on the elements used for the structural mesh and electromechanical coupling modelling is given. For its generality, this initial treatment is not limited to the modelling of only MEMS gyroscope structures but it is adaptable to the modelling of several other microelectromechanical structures.

Finally, the last section has the aim of presenting a more specialized discussion on some of the most important aspects for the simulation of the MEMS gyroscope structures proposed in this thesis, such as the Coriolis effect and damping and modelling.

3.1 FEM simulation

There are several commercial tools for finite element method (FEM) calculations on the market, such as Ansys, Abaqus, Comsol Multiphysics and others. Although, they differ slightly in the numerical methods implementation, main features and handling are very similar such that the presented methods can be utilized with any FEM software available [28].

In this work, Ansys Mechanical APDL in the version 19 is used for the presented simulation methods and results. Ansys Mechanical APDL can be used via the graphical user interface (GUI) or via scripting in the Ansys Parametric Design Language (APDL). The Ansys Parametric Design Language (APDL) is one of the most powerful features of Ansys. It allows to define some or all parts of the model, such as geometry, material properties, loads, as parameters. In this way, creating and solving a new variation of a parameterized model is as simple as changing a few parameter values and rerunning the model. This makes Ansys a powerful tool for engineering analysis, optimization, root cause analysis, and for the design of new systems and technologies like those of MEMS devices. The FEM simulations can be run in both batch and interactive mode. In the batch mode, the input to the program is supplied in the form of a batch file and the program writes the results to the results file. In interactive mode, the input to the program is supplied through the GUI menus, the GUI command prompt, or input file [34].

Both input and batch files are collections of commands written in a plain text file with a .inp or a .txt extension. As summarized in Figure 3.1, each simulation script is build up in three

parts. In the pre-processor (/prep7), the model geometry is created, element types and material properties are defined and the geometry is then meshed. Next, loads and constraints are applied, solution options are defined and the underlying element equations are solved in the solution process (/solu). Finally, the simulation results are reviewed and extracted in the post-processor (/post1 and /post26). In /post1, the regular post-processing for stationary solutions is done. For time dependent results, /post26 is called to appropriately extract and review simulation results over time.

The reader can refer to the Ansys Theory Reference Guide [9] for more detailed information about the numerical methods implementation. Moreover, simulation procedures and scripting in APDL are documented in the Ansys Structural Analysis Guide [8] and in the Ansys Parametric Design Language Guide [10].

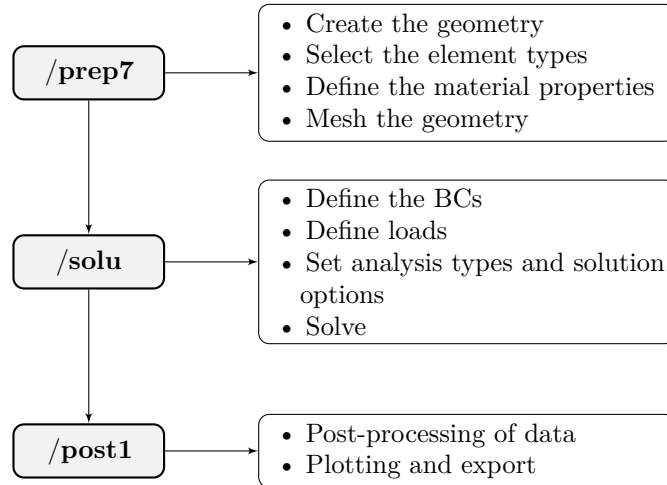


Figure 3.1: Structure of an APDL script for FE simulations in Ansys.

ANSYS can perform five type of structural analysis.

- *Static analysis:* it determines the displacements, stresses, strains, and forces in structures or components caused by loads that do not induce significant inertia and damping effects, such as those caused by time-varying loads. However, it is possible to include steady inertia loads (such as gravity and rotational velocity), and time-varying loads that can be approximated as static equivalent loads.
- *Modal analysis:* it determines the vibration characteristics, i.e. natural frequencies and mode shapes, of a structure. It can also serve as a starting point for another, more detailed, dynamic analysis, such as a transient dynamic analysis, a harmonic analysis, or a spectrum analysis.
- *Harmonic analysis:* identifies the steady-state solution for systems with harmonically varying applied loads. If damping is included in a harmonic analysis, both the real and the complex solutions are calculated.
- *Transient dynamic analysis:* it determines the dynamic response of a structure under the action of any general time-dependent loads. It is possible to determine the time-varying displacements, strains, stresses, and forces in a structure as it responds to any combination of static, transient, and harmonic loads. The time scale of the loading is such that the inertia or damping effects are considered to be important.

- *Buckling analysis*: it is a technique used to determine critical loads at which a structure becomes unstable, i.e. buckling loads, and the characteristic shape associated with a structure's buckled response, i.e. buckled mode shapes.

Since static, modal and harmonic analyses are carried out for the simulations which belong to this thesis project, a brief overview about them is presented in the following sections.

3.1.1 Static analysis

The static analysis is performed to obtain the response of a structure until applied static loads. The overall equilibrium equations for a linear structural static analysis are

$$[K]\{u\} = \{F\} \quad (3.1)$$

or, in another form

$$[K]\{u\} = \{F^r\} + \{F^a\} \quad (3.2)$$

where $[K]$ is the total stiffness matrix, $\{F^r\}$ is the reaction load vector and $\{F^a\}$ is the total applied load vector defined by the following expression

$$\{F^a\} = \{F^{nd}\} + \{F^{ac}\} + \sum_{m=1}^N (\{F_e^{th}\} + \{F_e^{pr}\}) \quad (3.3)$$

where:

- $\{F^{nd}\}$ is the applied nodal load vector

- $\{F^{ac}\} = -[M]\{a_c\}$ is the acceleration load vector

- $\{a_c\}$ is the total acceleration vector

- $[M] = \sum_{m=1}^N [M_e]$ is the total mass matrix

- $[M_e]$ is the element mass matrix

- $\{F_e^{th}\}$ is the element thermal load vector

- $\{F_e^{pr}\}$ is the element pressure load vector.

In presence of geometrical nonlinearities, the stiffness $[K]$ is a function of the displacement $\{u\}$. In this case, the system of equations is implicit and the software uses a Newton method to solve the static problem iteratively, as follows

$$[\bar{K}_i]\Delta u_i = F^a - F_i^{nr} \quad (3.4)$$

where $[\bar{K}_i]$ is the tangent stiffness matrix for the current displacement u_i , $\Delta u_i = u_{i+1} - u_i$ is the displacement increment, F^a are the applied loads and F_i^{nr} are the restoring forces calculated from the element stresses. The tangent stiffness can be expressed as

$$[\bar{K}] = [K] + [S] + [K]^{LD} + [K]^C + [K]^{SP} \quad (3.5)$$

where

- $[K]$ is the usual stiffness matrix

- $[S]$ is the stress-stiffness matrix
- $[K]^{LD}$ is the pressure loads
- $[K]^C$ is the contact stiffness
- $[K]^{SP}$ is the spin-softening due to rotational velocities.

Each matrix in Equation 3.5 is assembled from the corresponding element matrices that depend on the current displacement u_i . In case of displacement constraints, the underlying equation is evaluated directly to retrieve reaction forces of the structure. A code script that lists the commands to perform a generic static analysis in APDL is shown below.

```

1 /solu          ! Enter the solution processor
2
3 antype,static ! Set the analyse type
4 nlgeom,on     ! In case of nonlinear static analysis
5
6 D,...          ! Apply constrains
7 F,...          ! Apply loads
8
9 allsel,all     ! Select everything
10
11 solve         ! Obtain the solution
12
13 /post1        ! Enter the general post-processor
14 ...

```

3.1.2 Modal analysis

The modal analysis delivers the vibration characteristics of a structure, i.e natural frequencies and mode shapes. In Ansys, modal analysis is a linear analysis: any nonlinearities, such as plasticity and contact elements, are ignored even if they are defined. The other underlying assumptions are:

- The structure has constant stiffness and mass effects
- Free vibration, that is the structure has no time varying forces, displacements, pressures, or temperatures applied.

Assuming an undamped system and considering the above assumptions, the equation of motion expressed in matrix notation is

$$[M]\{\ddot{u}\} + [K]\{u\} = 0 \quad (3.6)$$

where $[M]$ is the structural mass matrix and $[K]$ is the structural stiffness matrix. For a linear system, free vibrations will be harmonic of the form

$$\{u\} = \{\phi_i\} \cos(\omega_{n(i)} t) = \{0\} \quad (3.7)$$

where $\{\phi_i\}$ is the eigenvector representing the mode shape of the i -th natural frequency $\omega_{n(i)}$. Substituting 3.7 in 3.6, the eigenvalue problem expression can be obtained

$$\left(-\omega_{n(i)}^2 [M] + [K] \right) \{\phi_i\} = \{0\} \quad (3.8)$$

This equality is satisfied if either $\{\phi_i\} = 0$ or if the determinant of $(-\omega_{n(i)}^2[M] + [K])$ is zero. The first option is the trivial one and, therefore, is not of interest. Thus, the eigenvalue problem reduces to solving the equation of the form

$$\det(-\omega_{n(i)}^2[M] + [K]) = 0 \quad (3.9)$$

which gives N values of $\omega_{n(i)}$, where N is the number of degrees of freedom of the system. Substituting each $\omega_{n(i)}$ back into Equation 3.8, also each $\{\phi_i\}$ eigenvectors can be obtained.

In ANSYS, the eigenvalue and eigenvector extraction procedures available include the Block Lanczos, PCG Lanczos, Supernode, Subspace, unsymmetric, damped, and QR damped methods. As the mode-extraction method is specified, the program automatically chooses the appropriate equation solver. For this thesis work only Block Lanczos and unsymmetric extraction methods are employed. The Block Lanczos methods are recommended to find many modes of large models consisting of shells or a combination of shells and solids, while the unsymmetric method is meant for problems where the stiffness and mass matrices are unsymmetric, such as electro-mechanical coupling problems. For more detailed information about the eigenvalue and eigenvector extraction techniques, the reader can refer to [9]. A code script that lists the commands to perform a generic modal analysis in APDL is shown below.

```

1 /solu          ! Enter the solution processor
2
3 antype,modal   ! Set the analyse type
4 modopt,lanb,n   ! Define the Block Lanczos extraction method
5                   ! and the number of modes (n) to extract
6 mxpand,nmode    ! Define the number of modes (nmode) to expand
7
8 allsel,all      ! Select everything
9
10 solve          ! Obtain the solution
11
12 /post1         ! Enter the general post-processor
13 ...

```

In addition, the structural stiffness matrix in Equation 3.6 may include prestress effects. A prestressed modal analysis uses results from a static analysis to calculate the natural frequencies and mode shapes of a prestressed structure. The procedure for performing a prestressed modal analysis from a linear base analysis is essentially the same as the one of a standard modal analysis, except that it is first necessary to prestress the structure by performing a static analysis. If the prestressed modal analysis follows a large-deflection static analysis or a static analysis including other nonlinearities, the linear perturbation analysis procedure should be adopted. A more detailed description with code examples is provided in Section 3.3.3, in which prestressed modal analyses are carried out to deal with the electromechanical coupling of MEMS structures.

3.1.3 Harmonic analysis

The harmonic analysis is performed to determine the steady-state response of a linear structure to loads that vary harmonically with time. Similarly to the modal analysis, in Ansys the harmonic analysis is a linear analysis and all nonlinearities are ignored, even if they are defined. The other underlying assumptions are:

- The structure has constant or frequency-dependent stiffness, damping, and mass effects

- All loads and displacements vary harmonically at the same known frequency, although not necessarily in phase
- Element loads are assumed to be in-phase only.

Consider the general equation of motion for a structural system expressed in matrix notation

$$[M]\{\ddot{u}\} + [C]\{\dot{u}\} + [K]\{u\} = F^a \quad (3.10)$$

where $[M]$ is the structural mass matrix, $[C]$ is the structural damping matrix, $[K]$ is the structural stiffness matrix, $\{\ddot{u}\}$ is the nodal acceleration vector, $\{\dot{u}\}$ is the nodal velocity vector, $\{u\}$ is the nodal displacement vector and F^a is the applied load vector. The applied load vector is harmonic of the form

$$\{F^a\} = \{F_{max} e^{j\psi}\} e^{j\omega t} \quad (3.11)$$

which can be rewritten with the following expression

$$\{F^a\} = F_{max} \{\cos \psi + j \sin \psi\} e^{j\omega t} \quad (3.12)$$

or as follows

$$\{F^a\} = (\{F_1\} + j\{F_2\}) e^{j\omega t} \quad (3.13)$$

where:

- F_{max} is the force amplitude
- ψ is the force phase shift
- ω is the imposed frequency
- $\{F_1\} = \{F_{max} \cos \psi\}$ is the real force vector
- $\{F_2\} = \{F_{max} \sin \psi\}$ is the imaginary force vector.

As stated above, all points in the structure are moving at the same known frequency, however, not necessarily in phase. Also, it is known that the presence of damping causes phase shifts. Therefore, using again the complex exponential form, the displacements may be defined as

$$\{u\} = \{u_{max} e^{j\phi}\} e^{j\omega t} \quad (3.14)$$

or with the following expression

$$\{u\} = u_{max} \{\cos \phi + j \sin \phi\} e^{j\omega t} \quad (3.15)$$

which can be rewritten as

$$\{u\} = (\{u_1\} + j\{u_2\}) e^{j\omega t} \quad (3.16)$$

where:

- u_{max} is the maximum displacement
- ϕ is the displacement phase shift
- ω is the imposed frequency
- $\{u_1\} = \{u_{max} \cos \phi\}$ is the real displacement vector
- $\{u_2\} = \{u_{max} \sin \phi\}$ is the imaginary displacement vector.

It is important to highlight that the use of the complex exponential function instead of sine and cosine functions simplifies considerably the discussion. Once the solution $\{u\}$ is found, the real part of $\{u\}$ gives the response to $\{F_1\}$ and the imaginary part is the response to $\{F_2\}$. Substituting Equation 3.13 and 3.16 into Equation 3.10 gives

$$(-\omega^2[M] + j\omega[C] + [K])(\{u_1\} + \{u_2\})e^{j\omega t} = (\{F_1\} + \{F_2\})e^{j\omega t} \quad (3.17)$$

The dependence on time is the same on both sides of the equation and may therefore be removed, obtaining

$$([K] - \omega^2[M] + j\omega[C])(\{u_1\} + \{u_2\}) = (\{F_1\} + \{F_2\}) \quad (3.18)$$

In Ansys, the complex displacement output at each degree-of-freedom can be given in one of these two forms:

- The same form as $\{u_1\}$ and $\{u_2\}$ as defined in Equation 3.16
- The form amplitude u_{max} and phase ϕ , as defined in Equation 3.15.

The relations between the two forms are

$$\begin{aligned} u_{max} &= \sqrt{u_1^2 + u_2^2} \\ \phi &= \arctan\left(\frac{u_2}{u_1}\right) \end{aligned} \quad (3.19)$$

The Equation 3.18 can be solved using three different methods: full, mode-superposition and frequency-sweep. The full method is the easiest one for performing a harmonic analysis, as it uses the full system matrices, which can be symmetric or unsymmetric, to calculate the harmonic response. This means that Equation 3.18 is solved directly. The mode-superposition method uses the natural frequencies and mode shapes to compute the harmonic response. Finally, the frequency-sweep method uses the underlying Variational Technology method, providing a high-performance solution for forced-frequency simulations in structural analyses. The frequency-sweep method is similar to the full method considering that it uses the full system matrices to compute the harmonic response. Instead of using the full system matrices to calculate the results at the last requested frequency, however, the Variational Technology method calculates the harmonic solution at the middle of the requested frequency range, then interpolates the system matrices and loading on the entire frequency range to approximate the results across the range [8]. All the dynamical simulations provided in this thesis work are carried out using only full harmonic analysis.

A code script that lists the commands to perform a generic full harmonic analysis in APDL is shown below. More details about how to consider damping properties in full harmonic analyses are instead provided in Section 3.3.2.

```

1 /solu           ! Enter the solution processor
2
3 antype,harmonic ! Set the analyse type
4 hropt,full      ! Perform a full harmonic response
5 hrout,off       ! Print results as amplitudes and phase angles
6 outpr,basic,1   ! Output control option
7 nsubst,nsol     ! Specify the number of harmonic solutions
8                 ! (nsol) within freq. range
9 harfrq,fmin,fmax ! Frequency range from fmin to fmax Hz
10 kbc,1          ! Step boundary condition
11
12 d,...          ! Apply constrains

```

```

13 f,...           ! Apply harmonic loads
14
15 allsel,all      ! Select everything
16
17 solve          ! Obtain the solution
18
19 /post1         ! Enter the general post-processor
20 ...

```

3.2 Element types

The basic idea of FEM is to make calculations at only limit number of points and then interpolate the results for the entire domain. Any continuous object has infinite degree of freedom and it is just not possible to solve the problem in this format. Finite Element Method reduce the degrees of freedom from infinite to finite with the help of discretization and meshing. In this context, choosing correctly the element types is essential to represent the structural behaviour with adequate precision and to minimize the computational efforts.

Elements in ANSYS are organized in families. Each element family has a family name and a shared set of properties. The reader can refer to the *Mechanical APDL Modeling and Meshing Guide* [6] for a more detailed documentation.

3.2.1 Mechanical domain

MEMS gyroscope structures simulated in this thesis project are composed by one or more masses suspended above the substrate using a beams suspension system. In addition, comb-drive and sensing parallel plates structures are employed for the electrostatic actuation and detection, respectively. With the purpose of optimizing as much as possible the required computational resources, the main idea for the elements choice is using lower dimension elements. For this reason, beam and shell elements are adopted to model the entire mechanical structure.

Beam188 element

Beam188 element is suitable for analyzing slender to moderately stubby/thick beam structures. The element is based on Timoshenko beam theory which includes the deformation contribution due to the shear stress. This model overcomes many limitations found in the Euler-Bernoulli beam and, for this reason, the Timoshenko beam is the most accurate model for the study of beam mechanics.

The Timoshenko beam theory is a first-order shear-deformation theory: transverse-shear strain is constant through the cross-section that is, cross-sections remain plane and undistorted after deformation. For this reason, only moderately thick beams may be analyzed. Slenderness ratio of a beam structure may be used in judging the applicability of the element. It is important to note that this ratio should be calculated using some global distance measures, and not based on individual element dimensions. A slenderness ratio greater than 30 is recommended.

Beam188 is a linear, quadratic, or cubic 3-D beam element and it is defined by two nodes, each of which provides six degree of freedom (Figure 3.2). These include translations in the x , y , and z directions and rotations about the x , y , and z directions. As a beam element, Beam188 is a one-dimensional line element in space and the cross-section details are provided separately. The material of the beam is defined either as an element attribute, or as part of section buildup (for multi-material cross-sections).

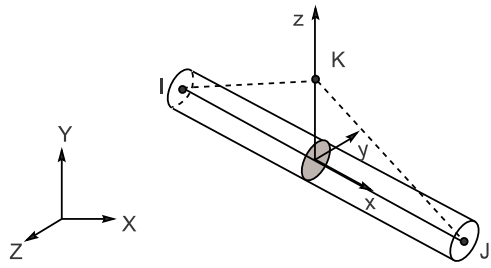


Figure 3.2: Beam188 element geometry: I and J are the element nodes, while the cross-section is represented in grey [6].

Shell181 element

Shell181 is suitable for analyzing thin to moderately-thick shell structures. It is a four-node element with six degrees of freedom at each node (Figure 3.3): translations in the x , y , and z directions, namely ux , uy and uz , and rotations about the x , y , and z directions, namely $rotx$, $roty$ and $rotz$. The thickness information is provided by defining the shell section.

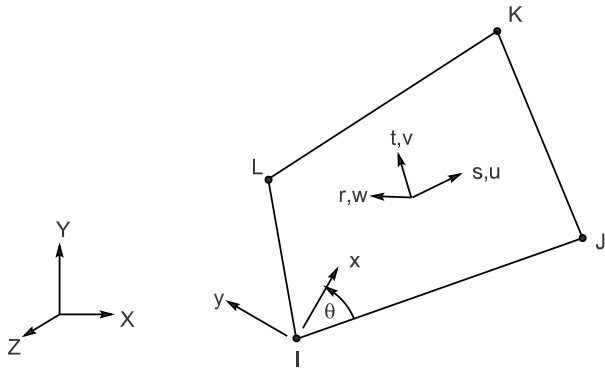


Figure 3.3: Shell181 element geometry: I, J, K, and L are the element nodes [6].

Joining shell and beam elements

As previously introduced, shell and beam elements are used together to model the entire MEMS gyroscope mechanical structures presented in this thesis project. A special care should be taken when different elements are directly joined, because there would be inconsistencies at the interface. When elements are not consistent with each other, the solution may not transfer appropriate forces or moments between different elements. To be consistent, two elements must have the same degrees of freedom. Furthermore, the degrees of freedom must overlay (be tied to) each other. This means that they must be continuous across the element boundaries at the interface. Even if both Beam188 and Shell181 elements have six degrees of freedom per node, they may be joined in a manner that is inconsistent. The $rotz$ degree of freedom of the shell element, namely drilling mode, is associated with the in-plane rotational stiffness. This is normally a fictitious stiffness thus, the rotational about the z direction $rotz$ is an artificial degree of freedom. For this reason, it

is inconsistent to connect only one node of a Beam188 element to a Shell181 element such that a rotational degree of freedom of the beam element corresponds to the *rotz* of the shell element [7]. CERIG command can be used to couple the *rotz* degree of freedom of the node shared by the Beam188 and Shell181 elements, namely master node, with the in-plane translational degrees of freedom of adjacent shell element nodes, namely slave nodes. A code script is provided as example for the use of the CERIG command.

```

1 nsel,s,,,master_node      ! Select master node
2 nsel,a,,,slave_node1     ! Select 1-st slave node
3 nsel,a,,,slave_node2     ! Select 2-nd slave node
4 ...
5 nsel,a,,,slave_nodei     ! Select i-th slave node
6
7 CERIG, master_node,all,rotz,ux,uy

```

3.2.2 Electromechanical coupling

As described in Section 2.4, vibratory MEMS gyroscopes are usually actuated electrostatically, instead capacitive sensing is used to detect the displacement due to the Coriolis effect. For this reason, a mutual interaction between the electrostatic field and the mechanical deflection is established. In more general terms, the electrostatic field produces a structure deflection which leads, on its own, to a variation in the electrical charge distribution and in the electrical field itself. Consequently, decoupling the two problems is not possible. In MEMS device models, capturing correctly the mutual dependence between the mechanical and electrostatic domain is essential. Analytical solutions of the coupled electromechanical problem are available only in the case of very simple geometries in small deflection conditions. A more effective approach is the numerical one based, for example, on the finite element method.

Ansys offers various methods for electromechanical modelling, which are presented in Table 3.1. They can be divided into two categories:

- Sequential (or Weak) coupling
- Direct (or Strong) coupling.

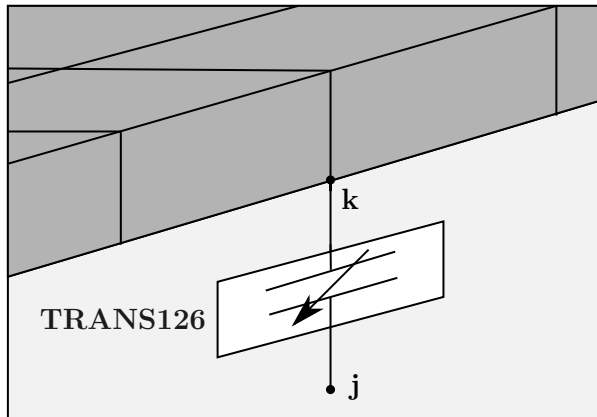
The multi-field solver makes use of sequential coupling for modelling coupling between energy domains. The mechanical and electrical parts of the model have to be modeled and separately meshed. A special flag is used to identify interface areas on which force and displacement transfer between the two domains takes place. The two domains are then solved iteratively. Since interactions that characterize electromechanical coupling take place only at the interface, hence at each step of the iteration only the portion of the model actually involved in the current analysis is considered. An update of the electrostatic mesh follows each mechanical iteration. The electrostatic problem is recomputed with the new mesh and the electrostatic forces updated and transferred to the mechanical domain. This loop is repeated till convergence is reached.

The direct (or strong) coupling method allows to solve the entire electromechanical coupling problem simultaneously. It relies on the modelling of the electrical domain of the problem with special elements, which have both mechanical and electrical degree of freedom. By using these elements, a single finite element system is assembled and electrical and mechanical degrees of freedom are solved simultaneously. When highly nonlinear problems have to be solved, strong coupling improves convergence. In this thesis project, Trans126 elements are used. A Trans126 element represents a mono-dimensional transducer, intended as an energy converter from an electrostatic domain into a structural domain. It is a reduced-order element as it captures the electrostatic characteristics of an electromechanical device in terms of the device's capacitance

Characteristic	Multi-field solver	TRANS126	TRANS109
Geometry	2-D, 3-D	1-D	2-D
Coupling	Sequential	Direct	Direct
Supported analysis	Static, Transient Harmonic, Modal	Static, Transient Harmonic, Modal	Static, Transient
Convergence	Slow, Not robust	Fast, Robust	Moderate

Table 3.1: Elecromechanical coupling methods in Ansys [11].

over a range of displacements. Each TRANS126 element has two nodes and two degrees of freedom at each node: translation in the nodal x , y , or z direction and electric potential. The elements are placed in such a way that they connect the nodes of the mechanical finite element model between which electrostatic forces act, thus replacing the 3-D mesh of air gaps. Fixed electrodes are not usually included in the model, because they can be described by the boundary conditions at TRANS126 mechanical nodes [11, 19]. Figure 3.4 shows an example of placement of this element between a 3-D mechanical mesh and a fixed electrode.

Figure 3.4: TRANS126 element connects a node of the mechanical mesh k to a fixed node j , representing the behaviour of a fixed electrode.

The capacitance between the nodes is a function of the distance between them, which is computed as the difference of the respective nodal displacement along a chosen coordinate direction, also referred to as stroke. Such a direction should coincide with the preferential direction of movement of the node when the mechanical structure deforms. The relation capacitance-stroke is in general a polynomial function and it is assigned to the element as input

$$C = \frac{C_0}{u} + C_1 + C_2 u + C_3 u^2 + C_4 u^3 \quad (3.20)$$

where u is the stroke and C_0, C_1, C_2, C_3, C_4 are the polynomial coefficients. Different possibilities are available, depending on the device to model. The first one is to assign directly polynomial law coefficients as real constants. Instead, if discrete pairs of capacitance stroke data are indicated, a

curve is fit to the discrete data sets represented by Equation 3.20. A representation of a generic stroke-capacitance law is shown in Figure 3.5.

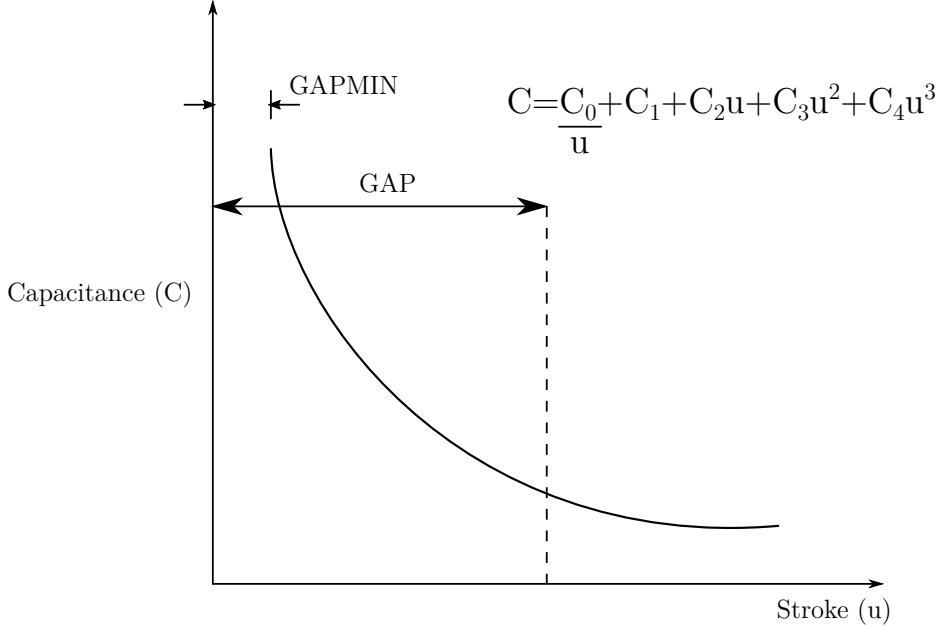


Figure 3.5: Generic capacitance-stroke law: C_0, C_1, C_2, C_3, C_4 are the polynomial coefficients, which can be directly assigned or fit from data sets. GAP represents the initial gap between conductors surfaces, while GAPMIN is the minimum gap.

The electrostatic force acting between the nodes of a Trans126 element is computed according to energy principles. Let $C_{kj} = C(u_i^k - u_i^j)$ be the capacitance between nodes k and j for a certain value of the distance $d = u_i^k - u_i^j$ along the coordinate direction u_i . The force is directed along u_i and its module is given by [19]

$$f_i^k = -f_i^j = -\frac{1}{2} \frac{\partial C_{kj}}{\partial u_i^k} (v_k - v_j)^2 \quad (3.21)$$

where v_k and v_j are the voltages at the nodes k and j , respectively. The current flowing in the element is computed as the charge time derivative

$$i_k = \frac{d}{dt} Q_{kj} = \frac{d}{dt} [C_{kj}(v_k - v_j)] \quad (3.22)$$

where Q_{kj} is the charge between conductors surfaces. According to the assumption that conductors are equipotential, all the nodes of the TRANS126 elements connected to a certain conductor are subjected to the same voltage boundary conditions. The total current flowing in the conductor is simply given by the sum of the currents at those nodes [19].

The Trans126 element supports static, transient, prestressed harmonic, and prestressed modal analysis. However, the use of Trans126 elements is geometrically limited to problems where the capacitance can be accurately described as a function of a single degree of freedom, usually the stroke. The element is nonlinear for static and transient analyses and requires an iterative solution to converge, producing an unsymmetric matrix. However, further details about the use of Trans126 elements in Ansys simulations are provided in the following sections.

3.2.3 Damping modelling

As it will be discussed in the following section, there are several methods to include damping in Ansys simulations. The one adopted for structures proposed in this thesis project is using a special element type having viscous damping characteristics, i.e. Combin14 element (Figure 3.6). Combin14 element is a spring-damper element, defined by two nodes, a spring constant k and damping coefficients c_v . It has longitudinal or torsional capability in 1-D, 2-D, or 3-D applications. The longitudinal spring-damper option is a uniaxial tension-compression element with up to three degrees of freedom at each node: translations in the nodal x , y , and z directions. No bending or torsion is considered. The torsional spring-damper option is a purely rotational element with three degrees of freedom at each node: rotations about the nodal x , y , and z axes. No bending or axial loads are considered. In addition, the spring-damper element has no mass but and the spring or the damping capability may be removed from the element, simply. Damping (or stiffness) characteristics are specified directly input the corresponding values as real constants of the element.

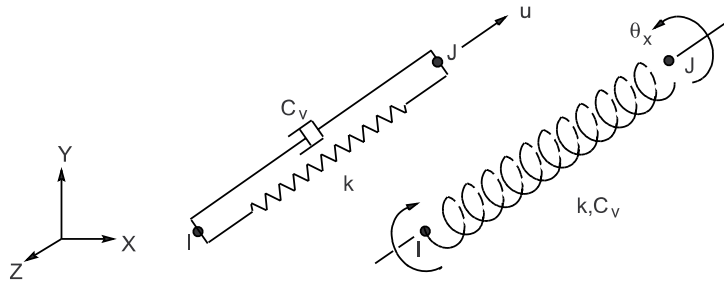


Figure 3.6: Combin14 elements geometry: I and J are the elements nodes [6].

3.3 MEMS gyroscope simulation methodology

The first part of this chapter was a general discussion of FEM modeling methods in Ansys related to MEMS devices. Instead, the following Section provides more particular details to the modelling of MEMS gyroscope structures developed in this thesis project.

3.3.1 Coriolis effect

Vibratory MEMS gyroscopes rely on the Coriolis force, a fictitious force which appears to act on objects that are in motion within a reference frame that rotates with respect to an inertial one. Consequently, properly modelling the Coriolis force is essential to capture the dynamical behaviour of MEMS gyroscope devices.

When a structure rotates, two different possibilities exist to specify the angular velocity in Ansys. By using OMEGA command, the angular velocity about the global Cartesian x , y and z axes is applied to the entire structure. Instead, CMOMEGA command allows to specify the angular velocity components of an element component about a user-defined rotational axis. Code scripts as examples for the use of these two commands are provided below.

¹ OMEGA, omegx, omegy, omegz ! Specify the angular velocity components

```

1 cmsel,s,cm_name           ! Select the element component cm_name
2                         ! to which apply the angular velocity
3
4 CMOMEGA, cm_name, omegx, omegy, omegz, x1, y1, z1, x2, y2, z2 ! Specify the angular
5                         ! velocity components

```

As introduced in Section 2.1, when a point P is moving in a reference frame that rotates at the angular velocity Ω with respect to a stationary inertial frame, the acceleration of the point as measured in the stationary reference frame is expressed by Equation 2.4. For clarification purposes Equation 2.4 is rewritten below, assuming that the linear acceleration of the rotating frame is negligible

$$\{a_s\} = \{a_r\} + \{\dot{\Omega}\} \times \{r\} + \{\Omega\} \times (\{\Omega\} \times \{r\}) + 2\{\Omega\} \times \{v_r\} \quad (3.23)$$

where

- $\{a_s\}$ is the acceleration vector of the point P as measured in the stationary reference frame
- $\{a_r\}$ is the acceleration vector of the point P as measured in the rotating reference frame
- $\{v_r\}$ is the velocity vector of the point P as measured in the rotating reference frame
- $\{r\}$ is the position vector of the point P as measured in the rotating reference frame
- $\{\Omega\}$ is the angular velocity vector
- $\{\dot{\Omega}\}$ is the angular acceleration vector.

In addition, the second term $\{\dot{\Omega}\} \times \{r\}$ in Equation 3.23 is the rotational acceleration and leads to a load sometimes called the Euler force. The third term $\{\Omega\} \times (\{\Omega\} \times \{r\})$ is the centrifugal acceleration which leads to the centrifugal load and the spin softening effect. The last term $2\{\Omega\} \times \{v_r\}$ leads to the Coriolis force.

By applying virtual work from the D'Alembert force, the contribution of the first term $\{a_r\}$ in Equation 3.23 to the virtual work introduces the mass matrix of the element [9]

$$[M_e] = \int_V [N]^T [N] \rho dv \quad (3.24)$$

where $[M_e]$ is the element mass matrix, $[N]$ is the shape function matrix and ρ is the element density. The Coriolis matrix is deduced from the last term of Equation 3.23 as [9]

$$[G_e] = 2 \int_V [N]^T [\Omega] [N] \rho dv \quad (3.25)$$

where $[G_e]$ is the element Coriolis damping matrix and $[\Omega]$ the rotational matrix associated with $\{\Omega\}$ expressed as

$$[\Omega] = \begin{bmatrix} 0 & -\Omega_z & \Omega_y \\ \Omega_z & 0 & -\Omega_x \\ -\Omega_y & \Omega_z & 0 \end{bmatrix} \quad (3.26)$$

where Ω_x , Ω_y , Ω_z are the x , y , and z components of the angular velocity. The governing dynamics equation of motion in a rotating reference frame can be written as [9]

$$[M]\{\ddot{u}\} + ([G] + [C])\{\dot{u}\} + ([K] + [K_{SP}])\{u\} = \{F\} \quad (3.27)$$

where

- $[M] = \sum_{i=1}^n [M_e]$ is the global mass matrix
- $[G] = \sum_{i=1}^n [G_e]$ is the global Coriolis matrix
- $[C] = \sum_{i=1}^n [C_e]$ is the global damping matrix
- n is the number of elements
- $[K]$ is global stiffness matrix
- $[K_{SP}]$ is the global stiffness matrix due to spin softening
- $\{F\}$ is the load vector, that is the sum of external and centrifugal loads.

The spin softening matrix is caused by the rotation of the structure and changes the apparent stiffness of the structure in a rotating reference frame. It can be expressed as

$$[K_{SP}] = [\Omega]^2 [M] \quad (3.28)$$

with

$$[\Omega]^2 = \begin{bmatrix} -(\Omega_y^2 + \Omega_z^2) & \Omega_x \Omega_y & \Omega_z \Omega_z \\ \Omega_z \Omega_y & -(\Omega_x^2 + \Omega_z^2) & \Omega_y \Omega_z \\ \Omega_x \Omega_z & \Omega_y \Omega_z & -(\Omega_x^2 + \Omega_y^2) \end{bmatrix} \quad (3.29)$$

In Ansys, the Coriolis effect on a rotating structure can be taken into account using the CORIOLIS command. Without the inertia effect applied via the CORIOLIS command, Ansys does not generate the $[G]$ matrix, and the usual effect of the angular rotation velocity specified by the OMEGA or CMOMEGA command applies. A command input to activate the Coriolis effect in a rotating reference frame is provided below. However the readear can refer to [5] for further details and examples.

1 coriolis, on,,,off	! Activate the Coriolis effect in rotating ! reference frame
----------------------	---

3.3.2 Modelling Damping

The drive and sense resonant mode response in a vibratory MEMS gyroscope strongly depends on their respective damping factors. As introduced in Section 2.5, several dissipation sources can influence the MEMS gyroscope dynamical behaviour. However, the viscous air damping is typically the dominant dissipation mechanics for devices operating at atmospheric pressure. There are several methods to include the damping in Ansys simulations. The damping matrix $[C]$ may be used in harmonic, damped modal and transient analysis as well as substructure generation. In its most general form, it is [9]

$$[C] = \alpha[M] + (\beta + \beta_c)[K] + \sum_{j=1}^{N_{mat}} \beta_j[K_j] + \sum_{k=1}^{N_{el}} [C_k] + [C_\zeta] \quad (3.30)$$

where:

- α is the constant mass matrix multiplier
- β is the constant stiffness matrix multiplier
- β_c is the variable stiffness matrix multiplier
- β_j is the constant stiffness matrix multiplier for material j
- $[C_k]$ is the element damping matrix
- $[C_\zeta]$ is the frequency-dependent damping matrix

Rayleigh Damping α and β

The most common form of damping is the so-called Rayleigh type damping. The damping matrix $[C]$ is calculated by using these constants to multiply the mass matrix $[M]$ and stiffness matrix $[K]$:

$$[C] = \alpha[M] + \beta[K] \quad (3.31)$$

The values of α and β are not generally known directly, but are calculated from modal damping ratios, ζ_i . It is the ratio of actual damping to critical damping for a particular mode of vibration, i . If $\omega_{n(i)}$ is the natural frequency of mode i , α and β satisfy the following relation

$$\zeta_i = \frac{\alpha}{2\omega_{n(i)}} + \frac{\beta}{2}\omega_{n(i)} \quad (3.32)$$

Rayleigh damping is suitable for single degree of freedom dynamical system because it depends on the dominant natural frequency and damping ratio. For multiple degree of freedom systems and continuum dynamical system, as structures analyzed in this thesis work, it is difficult to identify the dominant natural frequency and modal damping ratio. However, in many practical structural problems, the α damping (or mass damping) may be ignored ($\alpha = 0$). In such case, the β , which represents material structural damping, can be evaluated from known values of ζ_i and $\omega_{n(i)}$ as

$$\beta = 2\frac{\zeta_i}{\omega_i} \quad (3.33)$$

In case where the damping properties vary considerably in different parts of the structure, the above techniques cannot be used directly. The α and β damping coefficients can be specified in Ansys as follows

1 alphad,value	! Defines the mass matrix multiplier for damping
2 betad,value	! Defines the stiffness matrix multiplier for damping

Material dependent β_j

Material dependent β_j allows to specify β_j damping as a material property. The input in Ansys is provided below.

1 mp,betd,value	! Defines the stiffness matrix multiplier for damping
-----------------	---

Damping ratio ζ

The damping ratio ζ is the simplest way of specifying damping in the structure. Representing the ratio of actual damping to critical damping, it is used to compute β_c coefficient

$$\beta_c = \frac{2\zeta}{\omega} \quad (3.34)$$

In Ansys the damping ratio can be used only in mode-superposition transient or harmonic analysis and it is specified as a decimal number with the command provided below.

1 <code>dmprat,value</code>	<code>! Set the damping ratio</code>
-----------------------------	--------------------------------------

Mode-dependent damping ratio ζ_i

Mode dependent damping ratio ζ_i gives the ability to specify different damping ratios for different modes of vibration. It is specified with the MDAMP and is available only for the mode-superposition transient or harmonic analysis. The frequency dependent-damping matrix $[C_\zeta]$ can be computed from the specified ζ_i ad follows

$$2\omega_{n(i)}\zeta_i = \{u_i\}^T [C_\zeta] \{u_r\} \quad (3.35)$$

where $\{u_i\}$ is the i -th mode shape and $\omega_{n(i)}$ is the frequency associated with mode shape i .

Element damping

Element damping involves using some special element types having viscous damping characteristics, such as Combin14 element described in the previous section. Element damping is applied via element real constant.

For MEMS gyroscope structures simulated in this thesis work, damping coefficients related to the drive and sense mode are first estimated using the analytical approach described in Section 2.5. Then, damping coefficient can be specified using Combin14 elements, directly input the corresponding values as real constants of the elements. However, a further detailed discussion about damping modelling for MEMS gyroscope structures proposed in this thesis will be provided in Chapters 4 and 5.

3.3.3 Modelling electromechanical coupling

Electromechanical coupling strongly influences the dynamical behaviour of MEMS gyroscope devices. As introduced in Section 3.2.2, Trans126 elements can be used to model the mutual interaction between the electrostatic field and the mechanical domain. In order to simulate electromechanical dynamical problems in Ansys, modal and harmonic analysis may be performed following the steps provided below.

Prestressed modal analysis

In order to analyze the effect of frequency shift phenomena on MEMS gyroscope frequency behaviour, modal analysis should be carried out. The routine is first to proceed with a static analysis of the device with the DC voltage applied to Trans126 elements, and then performing a prestressed modal analysis on the structure. There are usually two available methods which allows to add prestress effects to a modal analysis in Ansys:

- Prestressed modal analysis via PSTRES command
- Linear perturbation analysis procedure.

Linear perturbation is the preferred method for a prestressed modal analysis. Alternatively, prestress effects can be included using PSTRES command when using TRANS126 with other element types that do not support linear perturbation.

The main steps to carry out a modal analysis in Ansys which incorporates electrostatic effect are summarised in Table 3.2. The prestressed modal analysis via PSTRES command is applicable only if the base analysis is a purely linear, small deflection solution. In this case, the procedure is essentially the same as the one of a standard modal analysis, except for the fact that the structure must be first prestressed by performing a static analysis. Prior to the modal analysis, the nodal coordinate are updated with the deflections from the static analysis. The included prestress is responsible for the effects of the applied voltage on the system frequency characteristic. The program outputs are mechanical displacements and eigenfrequencies with electrostatic effects incorporated. If large deflection and/or stress stiffening effects play an important role in the final eigensolution or, if the prior static analysis includes other nonlinearities, the linear perturbation procedure should be adopted. However, this procedure is also valid for cases where the base analysis is linear. In order to avoid weighting down the discussion, the reader can refer to *Appendix C* for detailed information about the prestressed modal analysis via PSTRES command and the linear perturbation analysis procedure with typical command input to accomplish the steps summarized in Table 3.2.

Prestressed harmonic analysis

As described in Section 2.4.1, the electrostatic drive actuation is generally harmonic and is provided by comb-drive based actuators. Typically, a MEMS gyroscope device operates with a DC bias voltage superposed on an alternating AC voltage. If the AC voltage value is small compared to the *DC* one, nonlinear effects caused by the electromechanical coupling can be neglected and a prestressed harmonic analysis can be performed to analyze the device harmonic behaviour. The routine is first to proceed with a static analysis with the DC voltage applied to Trans126 elements, and then performing a prestressed harmonic analysis on the structure with the applied AC excitation. As in the case of modal analysis, there are usually two available methods which allows to add prestress effects to a full harmonic analysis in Ansys:

- Prestressed full harmonic analysis via PSTRES command
- Linear perturbation analysis procedure.

Linear perturbation is the preferred method for a prestressed harmonic analysis. Alternatively, prestress effect can be included using PSTRES command when using Trans126 with other element types that do not support linear perturbation.

The main steps to carry out a modal analysis in Ansys which incorporates electrostatic effect are summarised in Table 3.3. The procedure described to perform a prestressed full-harmonic analysis via PSTRES command is essentially the same as that for any other full-harmonic analysis except that the structure must be first prestressed by performing a static analysis.

In order to avoid weighting down the discussion, the reader can refer to *Appenadix C* for detailed information about the prestressed full harmonic analysis via PSTRES command and the linear perturbation analysis procedure with typical command input to accomplish the steps summarized in Table 3.3.

Prestressed modal analysis via PSTRES command	<ul style="list-style-type: none"> • Build the model and obtain a static solution with prestress effects turned on ('PSTRES,ON'). • Enter the solution processor once again and update the nodal coordinate with the deflections from the static analysis. Then, obtain the modal solution, also with prestress effects activated (reissue 'PSTRES,ON'). • Expand the modes and review them in the post-processor.
Modal analysis based on linear perturbation procedure	<ul style="list-style-type: none"> • Build the model and include large-deflection effect, if necessary. Specify at which time points the necessary data is to be saved for the multiframe restart ('RESCONTROL') and obtain the static solution. • Restart the previous static solution from the desired load step and substep via ANTYPE command. • Specify the type of linear perturbation analysis as modal ('PERTURB,MODAL'). • Issue SOLVE,ELFORM to regenerate the element stiffness matrices, which are generally unsymmetric. • Issue MODOPT and MXPAND to specify the modal analysis option. • Perform the linear perturbation modal analysis.

Table 3.2: Main steps to carry out a prestressed modal analysis in Ansys [8].

Prestressed full harmonic analysis via PSTRES command	<ul style="list-style-type: none">• Build the model and obtain a static solution with prestress effects turned on ('PSTRES,ON').• Enter the solution processor once again and obtain the full-harmonic solution, also with prestress effects activated (reissue 'PSTRES,ON').
Full harmonic analysis based on linear perturbation procedure	<ul style="list-style-type: none">• Build the model and include large-deflection effect, if necessary. Specify at which time points the necessary data is to be saved for the multiframe restart ('RESCONTROL') and obtain the static solution.• Restart the previous static solution from the desired load step and substep via ANTYPE command.• Specify the type of linear perturbation analysis as modal ('PERTURB,MODAL').• Issue SOLVE,ELFORM to regenerate the element stiffness matrices, which are generally unsymmetric.• Issue MODOPT and MXPAND to specify the modal analysis option.• Perform the linear perturbation modal analysis.

Table 3.3: Main steps to carry out a prestressed full harmonic analysis in Ansys [8].

Chapter 4

Preliminary design and analysis

In this chapter the preliminary design of a single mass z-axis resonant MEMS gyroscope is developed. The number of proof masses in resonant MEMS gyroscopes can affect the common mode errors and hence the performance of the device. The designs utilizing multiple proof masses result in a larger overall size but better performance as they can operate in the anti-phase mode: this motion assures minimization of the net reaction forces and moments on the anchors, which mitigates the energy loss through the substrate. In addition, the presence of multiple masses could allow to decouple the drive and sense mode motion, minimizing the cross-axis sensitivity and common mode error. Another approach is to use a single proof mass which results in a smaller footprint of the device but the performance is worst, since the drive and sense mode cannot be decoupled. Consequently, trade-offs have to be made between optimal performance and keeping the size of the device to a minimum.

The simple model proposed in this Chapter has been designed with the precise objective of getting familiar with the basic MEMS design techniques both from an analytical perspective and from a FEM model implementation. Consequently, the analyses which have been carried out are only the basic ones, while a complete and detailed description of the design methodology is provided in the following chapters, in conjunction with the presentation and analysis of the complex structure which represents the core of this thesis project.

4.1 Mechanical design and working principle

The schematic of the preliminary MEMS gyroscope design is shown in Figure 4.1. This is a resonant mode-matched electrostatic z-axis device, which means that it is operated at resonance and both the drive and sense mode frequency values are matched. It consists in a single proof mass, referred as m in the Figure, suspended by four crab-leg beams, which make the mass free to oscillate in two orthogonal direction, namely the drive (x-axis) and sense (y-axis) direction. The proof mass is set into oscillations along the drive direction using comb-drive based electrostatic actuators attached to the proof mass m . When the gyroscope is subjected to an external angular velocity, a Coriolis force and a consequent vibration is induced in the sense direction, which is orthogonal both to the drive direction and to the angular rotation axis. The resulting oscillation amplitude in the sense direction is proportional to the Coriolis force and thus to the angular velocity to be measured. Sensing parallel plates which are arranged in a gap–antigap-based differential configuration, are used to pick up the resulting sense displacement.

It is important to highlight that, even if a simpler design results in a smaller footprint, its performance may be worse with respect to the one of a multiple-mass device, as the single mass design does not allow the decoupling of drive and sense mode oscillations. Indeed, the crab-leg

suspension beams are compliant in two orthogonal directions and the same beams experience deflections in both modes, resulting in undesired coupling between the drive and sense modes. It often causes undesired energy transfer into the sense-mode. Since the drive-mode amplitude is orders of magnitude larger than the sense-mode, it is often required to isolate the drive motion from the sense motion, limiting the deflection direction of the drive and sense electrodes, so that drive electrodes deflect only in drive direction, and sense electrodes deflect only in sense direction. This enhances the precision and stability of the drive actuation and sense detection electrodes. The MEMS gyroscope is designed following the constraints of the commercially available and low-cost multiuser SOIMUMPs micromachining process, offered by MEMSCAP Inc. USA [17]. Since the design proposed in this chapter is only preliminary, a detailed discussion about the SOIMUMPs microfabrication rules to be followed for an accurate release of microstructures and structural integrity will not be provided here. However, the reader could refer to the following Chapter for a more detailed treatment of the main structure developed in this thesis project.

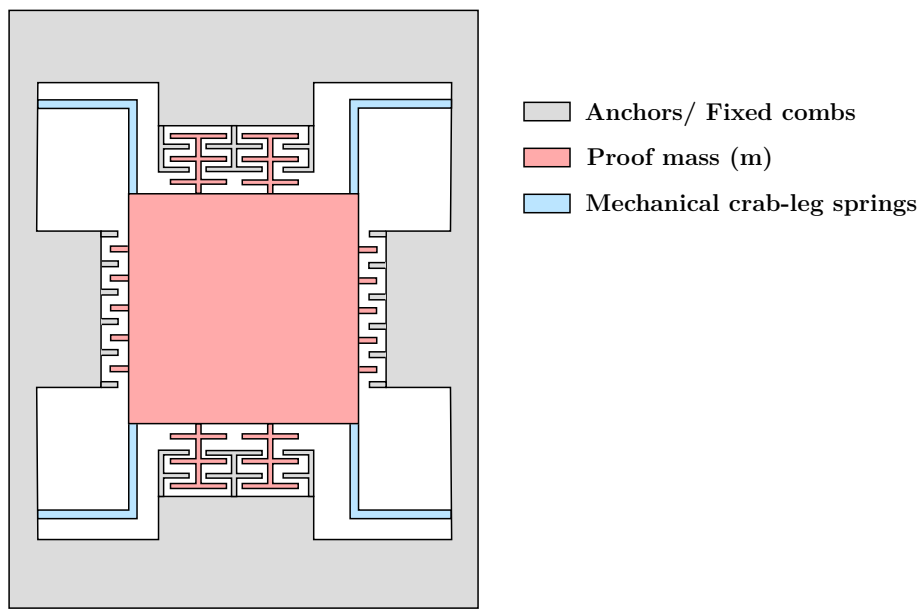


Figure 4.1: Single mass resonant MEMS gyroscope design: it consists of a single proof mass free to oscillate in two orthogonal directions. It is set into oscillations in the x-axis by using comb-drive based electrostatic actuator, while parallel sensing plates arranged in the gap-antigap configuration are used to detect the displacement due to the Coriolis force.

The silicon structural material data are summarized in Table 4.1, while referring to Figure 4.2 which shows the single mass MEMS gyroscope structure components in detail, Table 4.2 provides the main design parameters. For the sake of clarity, a complete characterization of the electrical design elements and flexure system will be provided in the following sections.

Parameter	Symbol	Value	Unit
Young's Modulus	E	169	GPa
Densitiy	ρ	$2.5e - 15$	$\text{kg}/\mu\text{m}^3$
Poisson's ratio	ν	0.29	-

Table 4.1: Silicon structural material data.

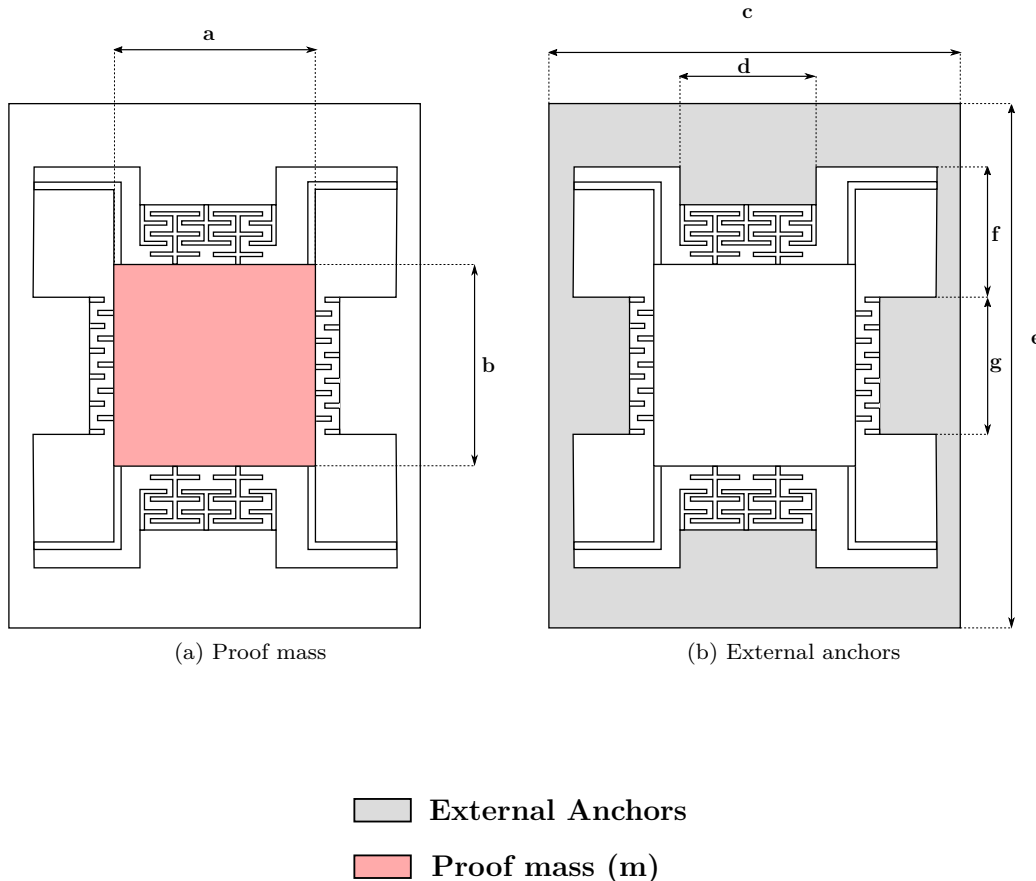


Figure 4.2: Details of drive mass, sense frame and external anchors for the single mass MEMS gyroscope design.

Parameter	Symbol	Value	Unit
Overall device size	-	0.904	mm ²
Structural layer thickness	<i>t</i>	25	μm
Proof mass horizontal length	<i>a</i>	530	μm
Proof mass vertical length	<i>b</i>	530	μm
External anchors horizontal length	<i>c</i>	923	μm
External anchors horizontal length	<i>d</i>	320	μm
External anchors vertical length	<i>e</i>	980	μm
External anchors vertical length	<i>f</i>	218	μm
External anchors vertical length	<i>g</i>	504	μm

Table 4.2: Design parameters of the single mass resonant MEMS gyroscope.

4.2 Analytical model

Before performing a FEM-based analysis, a detailed analytical model is implemented with the purpose of determining the dynamical behavior of the proposed MEMS gyroscope device. Figure 4.3 shows the lumped mass-spring-damper model of the proposed MEMS gyroscope design. The proof mass m is suspended through four crab-leg spring beams, which are compliant both in the drive and sense direction, making the mass free to oscillate in two orthogonal directions. The equivalent stiffness coefficients of the suspension system in the drive and sense direction are represented by k_x and k_y , respectively. The air damping between the comb-drive based actuators and sensing parallel plates, both attached to the proof mass m , are represented by c_x and c_y coefficients, respectively. As previously discussed in Chapter 2, when an angular velocity Ω_z is applied in the z-axis, the dynamical behaviour is that of a two degree-of-freedom system.

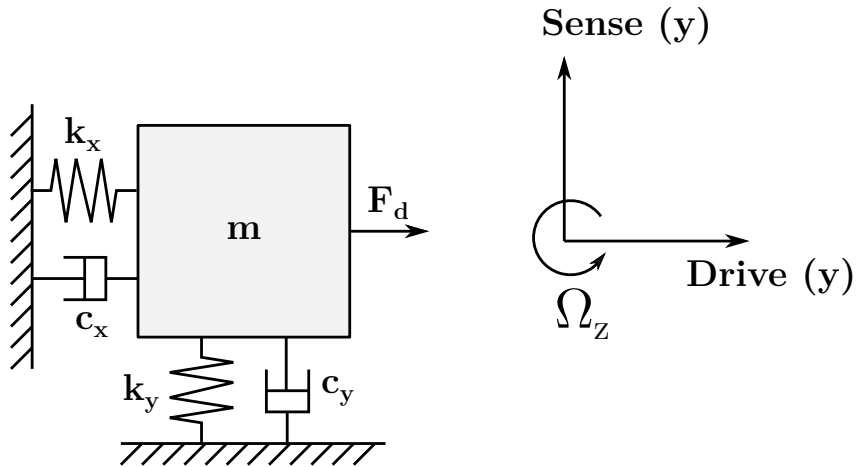


Figure 4.3: Two degrees-of-freedom mass–spring–damper model for the proposed single mass MEMS gyroscope. The arrow in x-direction indicates the drive direction, whereas the arrow orthogonal to the first shows the sense direction of motion.

Following the procedure illustrated in Section 2.2, the second-order differential equations of motion for the proposed single mass MEMS gyroscope can be obtained as

$$\begin{aligned} m\ddot{x} + c_x\dot{x} + k_x x &= F_d \\ m\ddot{y} + c_y\dot{y} + k_y y &= -2m\Omega_z\dot{x} \end{aligned} \quad (4.1)$$

where

- m is the proof mass
- c_x is the damping coefficient in the drive direction
- c_y is the damping coefficient in the sense direction
- k_x is the global stiffness coefficient in the drive direction
- k_y is the global stiffness coefficient in the sense direction.

The electrostatic actuation force F_d is applied by comb-drive based actuators, while $-2m\Omega_z\dot{x}$ is the Coriolis force acting on the one degree-of-freedom oscillator in the sense direction. The major assumption made to obtain the equations in 4.1 is that the coupling effects arising from nonidealities, which are anisoelasticity and anisodamping terms coupling drive and sense mode, are negligible. In this ideal case, the driving and sensing axes are coupled only through the Coriolis force.

The aim of the following sections is to compute the lumped coefficients of Equations 4.1, considering the basics of the mechanical and electrical gyroscope design previously provided in Chapter 2.

4.2.1 Calculation of mechanical stiffness

Figure 4.4 shows in detail the configuration of the crab-leg flexures which suspend the proof-mass. The crab-leg suspension beams are compliant both in the drive and sense direction. The overall stiffness coefficient values are computed considering that the suspension system is composed by four crab-leg spring beams, which can be modelled as springs connected in parallel. Consequently, as previously expressed in Table 2.1, the overall stiffness coefficients in the drive and sense direction k_x and k_y are [21]

$$k_x = \frac{Etw_y^3(L_x + 4\gamma L_y)}{L_y^3(L_x + 4\gamma L_y)} \quad (4.2)$$

$$k_y = \frac{Etw_x^3(4L_x + \gamma L_y)}{L_x^3(L_x + 4\gamma L_y)} \quad (4.3)$$

where E is the Young's modulus, t is the thickness of the beams, L_x and L_y are respectively horizontal and vertical length of the beams, w_x and w_y are respectively the horizontal and vertical width of the beams and $\gamma = w_x/w_y$. The design parameters of the mechanical springs previously described are summarized in Table 4.3. It is important to highlight that they have been chosen in order to match the drive and sense mode frequency values, matching stiffness coefficients k_x and k_y , and to respect the SOIMUMPs microfabrication process constraints.

Parameter	Value	Unit
L_x	200	μm
L_y	200	μm
w_x	4	μm
w_y	4	μm
t	25	μm

Table 4.3: Mechanical crab-leg springs design parameters.

4.2.2 Electrical design

Based on the discussion of Chapter 2, the following paragraphs provide the design parameters of comb-drive based actuators and sensing parallel-plates structures implemented in the proposed single mass MEMS gyroscope design, respectively for the actuation and sensing mechanism.

Comb-drive actuators

As previously stated, the proof mass is set into oscillations by using two comb-drive based electrostatic actuators attached on both sides of the drive mass. Referring to Figure 4.5 for further

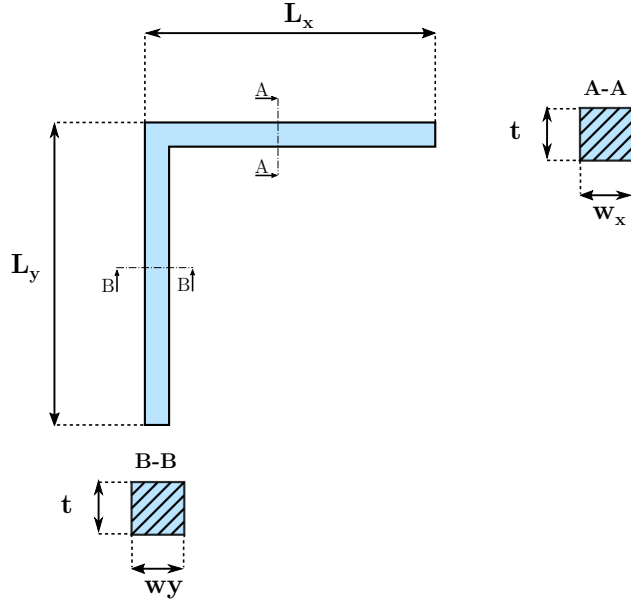


Figure 4.4: Detail of crab-leg mechanical spring for the proposed single mass MEMS gyroscope design.

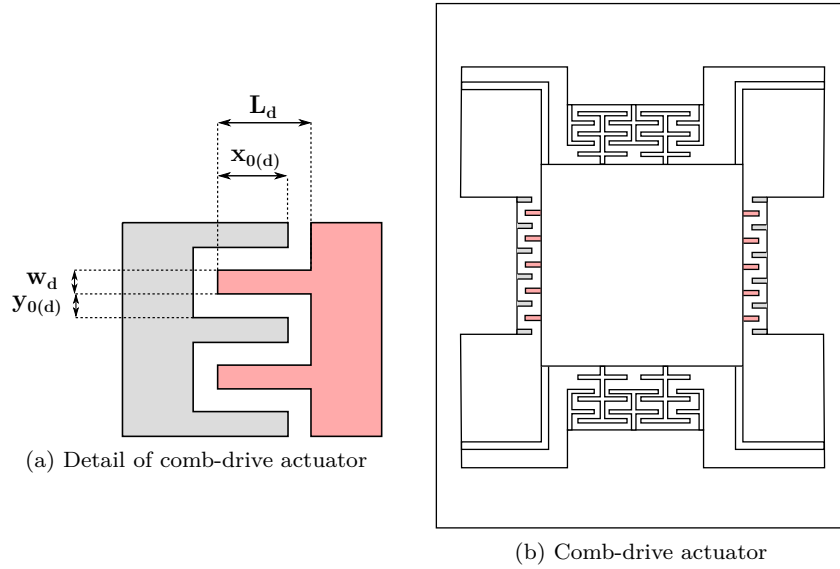


Figure 4.5: Comb-drive based electrostatic actuator implemented in the MEMS gyroscope design.

details, Table 4.4 provides the parameter design of the comb-drive structures implemented in the proposed MEMS gyroscope device.

Each fingers of the two comb-drive structures attached on the both side of the drive mass forms two parallel-plate pairs. Accordingly to Equation 2.34, when a constant bias voltage V_{DC} is applied to one of the two stationary electrodes, the electrostatic actuation force can be expressed

as

$$F_d = N_d \frac{\epsilon_0 t}{y_{0(d)}} V_{DC}^2 \quad (4.4)$$

where ϵ_0 is the free space permittivity, N_d is the total number of moving comb attached to one side of the drive mass, $x_{0(d)}$ is the overlap length, t is the structure thickness and $y_{0(d)}$ is the gap between comb drive fingers. On the contrary, when a constant bias voltage V_{DC} is superimposed to a sinusoidal time-varying voltage V_{AC} applied to the stationary electrodes, a harmonic actuation force occurs. Adopting the balanced actuation scheme and according to Equation 2.40, the resulting electrostatic harmonic force is expressed as follows

$$F_d = 4N_d \frac{\epsilon_0 t}{y_{0(d)}} V_{DC} V_{AC} \sin(\omega t) \quad (4.5)$$

where ω is the excitation frequency.

Parameter	Symbol	Value	Unit
Number of drive comb fingers (each side)	N_d	37	-
Length of drive combs	l_d	50	μm
Width of drive combs	w_d	4	μm
Overlap length between the moving and fixed fingers	$x_{0(d)}$	40	μm
Gap between drive combs	$y_{0(d)}$	3	μm

Table 4.4: Comb-drive based electrostatic actuator design parameters.

Sensing parallel plates

For the proposed MEMS gyroscope design, an input angular rotation in the z-axis will result in the Coriolis force in the y-axis which will lead to entire structure displacement in the y-axis. To detect this displacement, sensing parallel plates, arranged in differential gap–antigap configuration, are attached to the proof mass. Referring to Figure 4.6 for further details, Table 4.5 provides the design parameters of the sensing parallel-plate structures implemented in the proposed MEMS gyroscope device.

According to Equation 2.50 the overall capacitance change, corresponding to the sense mass displacement in the y-axis, can be calculated as

$$\Delta C = \frac{2\epsilon_0 N_s x_{0(s)} t y (d_2^2 - d_1^2)}{(d_1^2 - y^2) \cdot (d_2^2 - y^2)} \quad (4.6)$$

where ϵ_0 is free space permittivity, N_s is the number of parallel plates on each side, $y_{0(s)}$ is the overlap length of the fixed and moving parallel plates, y is the sense mass displacement and d_1 and d_2 are the small and large air gaps respectively.

4.2.3 Air damping analysis

As widely discussed in Section 2.5, viscous air damping is typically the dominant dissipation mechanism for the vibratory MEMS gyroscopes operated at atmospheric pressure. In resonant MEMS gyroscopes, the accurate estimation of the viscous air damping is very critical since it affects the overall quality factor and hence sensitivity. For the proposed single mass MEMS gyroscope design, both the slide and squeeze film air damping contribute towards the energy dissipation. The following section has only the aim of explaining how to compute the equivalent damping coefficients

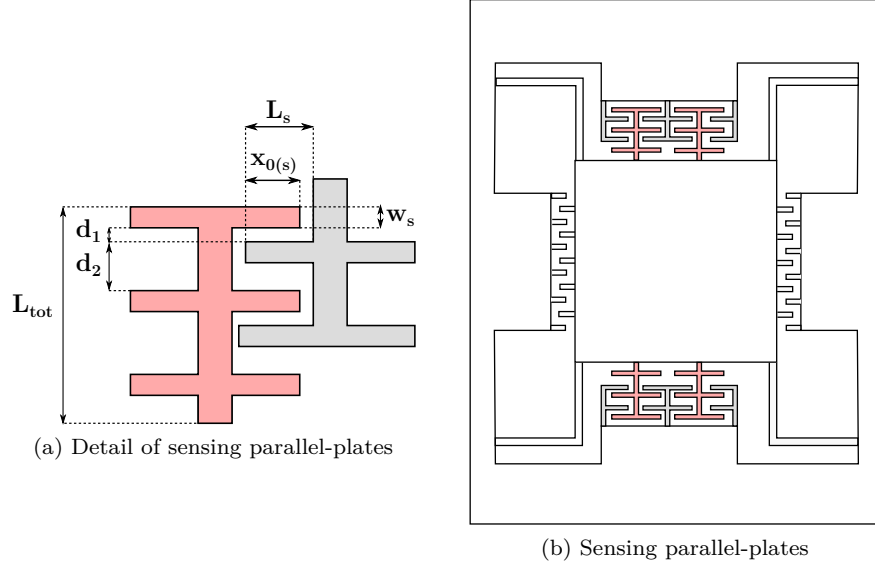


Figure 4.6: Sensing parallel-plates arranged in differential gap–antigap configuration implemented in the MEMS gyroscope design.

Parameter	Symbol	Value	Unit
Number of parallel plates (each side)	N_s	40	-
Length of parallel plates	l_s	65	μm
Width of parallel plates	w_d	4	μm
Overlap length between the moving and fixed fingers	$x_{0(s)}$	55	μm
Smaller sense gap size	d_1	3	μm
Larger sense gap size	d_2	9	μm
Total vertical parallel-plates length	L_{tot}	189	μm

Table 4.5: Sensing parallel-plates design parameters.

in drive and sense directions. However, a detailed discussion about air damping analysis applied to the dual mass MEMS gyroscope design will be provided in Chapter 5 and it is also suitable for the simple single mass design.

The slide film air damping is the only energy dissipation mechanism in the drive direction. The moving drive combs and moving sense parallel plates both move laterally in the drive direction and slide over the fixed parallel plates, hence contributing to the slide film air damping. The movement of the proof mass in the sense direction results in the squeezed film air damping phenomenon. Due to this movement, the moving drive combs and moving parallel plates displace towards the fixed parallel plates and the thin air film between moving and fixed parallel plates is squeezed in. Accordingly, the damping coefficient in drive and sense direction c_x can be obtained applying the following expression

$$c_x = \mu_{eff} 2N_d x_{0(d)} t \left(\frac{1}{y_{0(d)}} + \frac{1}{y_{0(d)}} \right) + \mu_{eff} 2N_s x_{0(s)} t \left(\frac{1}{d_1} + \frac{1}{d_2} \right) \quad (4.7)$$

where

- N_d is the total number of the drive combs attached on each side of the drive mass
- N_s is the total number of sensing parallel plates attached on each side of the sense frame
- $x_{0(d)}$, and $x_{0(s)}$ are the overlap length of drive combs and sensing parallel plates, respectively
- y_{0d} is the gap between comb drive fingers
- d_1 and d_2 are the comb smaller and larger gap sizes of the sensing parallel plates, respectively.

The effective air viscosity μ_{eff} was previously expressed by Equation 2.78 in Section 2.5.1 but it is reported here below for clarification purposes

$$\mu_{eff} = \frac{\mu}{1 + 2K_n + 0.2K_n^{0.788} e^{-K_n/10}} \quad (4.8)$$

where K_n is the Knudsen number μ is the viscosity of air at ambient temperature T . The Knudsen number is a measure of the gas rarefaction effect and it can be defined as the ratio of the mean free path of air λ to the thickness of the air gap $y_{0(d)}$ as in the following expression

$$K_n = \frac{\lambda}{d} \quad (4.9)$$

where d is the air gap thickness in drive combs and sensing parallel plates, respectively equal to $y_{0(d)}$ and d_1 . Indeed, the mean free path of air λ at a given operating temperature and pressure is expressed by the previously cited Equations 2.71 or 2.72. Table 4.6 shows data related to slide-film damping in the drive direction for the proposed single mass MEMS gyroscope design.

Property	Symbol	Value	Unit
Temperature	T	298	K
Pressure	P_a	1	atm
Air viscosity	μ	$1.86e - 11$	MPa.s
Mean free path of air	λ	0.0672	μm
Knudsen number	K_n	0.0224	-
Effective viscosity of air	μ_{eff}	1.7632e-11	MPa.s
Damping coefficient in the drive mode	c_x	$1.7318e - 6$	N.s/m

Table 4.6: Data related to slide-film damping in the drive direction for the proposed MEMS gyroscope design.

On the contrary, the damping coefficient in the sense direction can be obtained as follows

$$c_y = \mu_{eff} 2N_d x_{0(d)} t^3 \left(\frac{1}{y_{0(d)}^3} + \frac{1}{y_{0(d)}^3} \right) + \mu_{eff} 2N_s x_{0(s)} t^3 \left(\frac{1}{d_1^3} + \frac{1}{d_2^3} \right) \quad (4.10)$$

In this case, the effective viscosity of air μ_{eff} at a given temperature and pressure can be expressed using Equation 2.69, which is reported here below for clarification purposes

$$\mu_{eff} = \frac{\mu}{1 + 9.638 K_n^{1.1}} \quad (4.11)$$

where K_n is the Knudsen number. Table 4.7 shows data related to squeeze-film damping in the sense direction for the proposed single mass MEMS gyroscope design.

Property	Symbol	Value	Unit
Temperature	T	298	K
Pressure	P_a	1	atm
Air viscosity	μ	$1.86e - 11$	MPa.s
Mean free path of air	λ	0.0672	μm
Knudsen number	K_n	0.0224	-
Effective viscosity of air	μ_{eff}	1.6206e-11	MPa.s
Damping coefficient in the sense mode	c_y	$5.7231e - 5$	N.s/m

Table 4.7: Data related to squeeze-film damping in the sense direction.

4.3 Analytical model results

The development of the analytical model can help in the first stages of the design process. Indeed, as it will be discussed in detail in Chapter 5 of this thesis, it allows to choose initial geometrical parameters to achieve the desired dynamical behaviour. The following sections provide analytical model static and dynamical results, while a comparison with FEM simulations results will be provided in Section 4.5.

4.3.1 Static analysis

The static deflection of the single mass MEMS gyroscope structure can be determined by setting to zero all time derivatives in Equation 4.1. Therefore, the static response of the system in the drive direction can be expressed as

$$x = \frac{F_d}{k_x} \quad (4.12)$$

The electrostatic actuation force F_d can be computed using the expression of Equation 5.4. Figure 4.7 shows the displacement in the drive direction x obtained with an increasing bias tension V_{DC} value applied to one of the two fixed combs attached to the external anchors.

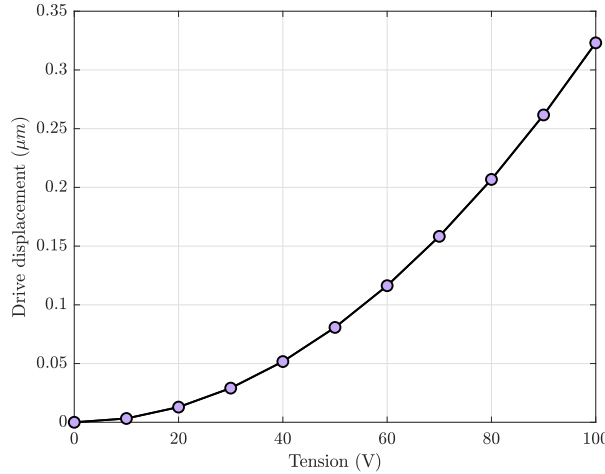


Figure 4.7: Analytical static displacement in the drive direction for the proposed single mass MEMS gyroscope design.

4.3.2 Modal analysis

As explained at the beginning of this Chapter, mechanical design parameters are determined in order to match the drive and sense mode frequency values and obtain highest performance, matching stiffness coefficients k_x and k_y . For this reason, the modal analysis plays a key role in the design phase. Rewriting the second-order differential equations of motion 4.1 for the proposed MEMS gyroscope in a matrix form, the free motion in the undamped condition is described by

$$\begin{bmatrix} m & 0 \\ 0 & m \end{bmatrix} \begin{Bmatrix} \ddot{x} \\ \ddot{y} \end{Bmatrix} + \begin{bmatrix} k_x & 0 \\ 0 & k_y \end{bmatrix} \begin{Bmatrix} x \\ y \end{Bmatrix} = \begin{Bmatrix} 0 \\ 0 \end{Bmatrix} \quad (4.13)$$

As previously discussed in Section 3.1.2, for the calculation of the resonant frequency values corresponding to the drive and sense modes, namely respectively ω_d and ω_s , the eigenvalue problem expressed in Equation 3.8 should be solved. Since the device is modelled by a two degrees-of-freedom system and all the matrices are in a diagonal form, the calculation of the eigenvalue problem easily leads to the following expressions

$$\begin{aligned} \omega_d &= \sqrt{\frac{k_x}{m}} \\ \omega_s &= \sqrt{\frac{k_y}{m}} \end{aligned} \quad (4.14)$$

Table 4.8 lists the obtained resonant frequency value for the proposed single mass MEMS gyroscope design. As expected, since $k_x = k_y$, the drive and sense mode frequencies are perfectly matched.

Mode	Symbol	Value	Unit
Drive	ω_d	10257	Hz
Sense	ω_s	10257	Hz

Table 4.8: Analytical resonant frequency values of the proposed single mass MEMS gyroscope design.

4.3.3 Harmonic analysis

The analysis of the dynamical behaviour of the proposed MEMS gyroscope should include a frequency response analysis with the aim of determining the frequency behaviour of the device and, at last, its mechanical sensitivity. Since the MEMS gyroscope design proposed in this chapter consists simply in a single proof mass suspended by four flexible beams, the drive and mode dynamic is the one of a single degree-of-freedom oscillator previously described in Section 2.2.1 and 2.2.2. Consequently, in order to weight down the discussion, the reader can refer to Chapter 2 for the complete equations related to drive and sense mode dynamical response.

A harmonic force is applied to the proof mass, simulating the actuation along x-direction. In Figure 4.8, the response of the proof mass is plotted in terms of magnitude and phase. The displacement of the drive mass is normalized with respect to the driving force amplitude F_0 . As expected, the system amplifies the response at the driving frequency. In addition, at the resonant frequency, the phase is -90° shifted from the excitation force phase. At a frequency lower than the resonant frequency, the phase approaches 0° meaning that the solution follows the excitation force closely. At a frequency higher than the resonant frequency, the phase approaches to -180° . When an angular velocity Ω_z is applied in the z-axis, a Coriolis force occurs and the proof mass

oscillates along the y-axis. Figure 4.9 shows the response of the proof mass in the sense direction normalized with respect to the driving force amplitude F_0 , considering that $\Omega_z = 300^\circ/\text{s}$. The sense displacement has one single peak, as the drive and sense mode resonant frequency are matched. This also means that the phase decreases with a uniform trend from -90° to -450° .

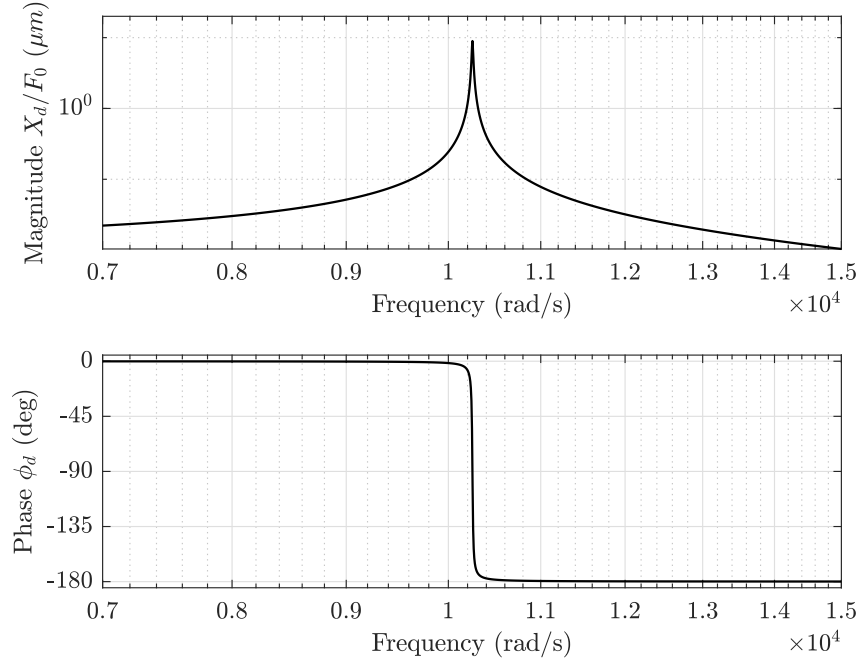


Figure 4.8: The analytical frequency response in the drive direction for the proposed single mass MEMS gyroscope design (*logarithmic scale*), normalized with respect to the driving force amplitude F_0 .

4.4 FEM Model

The analytical results of the proposed single mass MEMS gyroscope design are verified through FEM based simulations in Ansys. The FEM model is built following the procedure discussed in Chapter 3. Since the single mass structure is only preliminary, the modelling methodology adopted is not described in detail in this section, while the reader can refer to the following chapters of this thesis for more details about the dual mass MEMS gyroscope modelling in Ansys, which is still valid for a simplest structure.

4.4.1 Structural mesh

Figure 4.10 shows the meshed model of the MEMS gyroscope design. The adopted mesh has been designed to optimize as much as possible the required computational resources. The structure is meshed using Shell181 elements for the drive mass and sense mass, while Beam188 elements are adopted to model the suspension systems, the comb-drive fingers and the sense parallel plates. In addition, as explained in chapter 3, constraints equations are necessary to couple the rot_z degree-of-freedom of the single nodes shared by the Beam188 and Shell181 elements with the

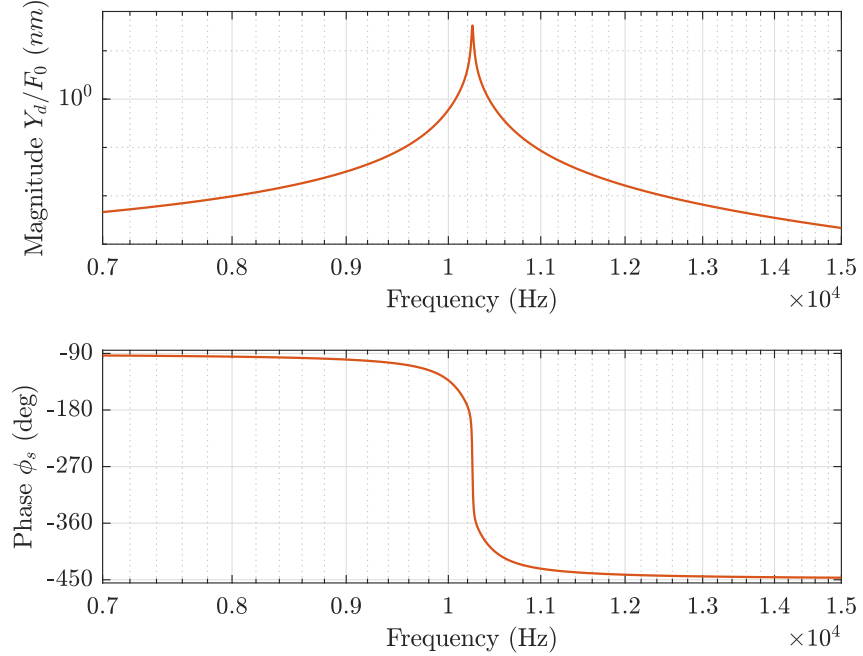


Figure 4.9: The analytical frequency response in the sense direction for the proposed single mass MEMS gyroscope design (*logarithmic scale*), normalized with respect to the driving force amplitude F_0 , with $\Omega_z = 300^\circ/s$.

in-plane translations degrees-of-freedom, namely ux and uy , of adjacent shell element nodes. Finally, fixed supports are added at the end of crab-leg spring beams connected to the external anchors. In the Figure, constraints equations used to couple Beam188 and Shell181 elements are represented in violet, while fixed supports are the ones at the end each crab-leg beams represented in yellow and light blue.

4.4.2 Damping modelling

In resonant MEMS gyroscopes, as the ones proposed in this thesis project, the accurate modelling of the viscous air damping is crucial since it affects the overall quality factor and hence the mechanical sensitivity. Through the analytical model, damping coefficient values in drive and sense directions c_x and c_y are computed. Air viscous damping effect is therefore directly included in Ansys model based on the analytical estimation. As previously discussed in Section 3.3.2 there are several methods to include damping in Ansys. The one adopted here is using a special element type having viscous damping characteristics, i.e. Combin14 element. The damping coefficients related to the drive and sense mode are specified directly input the corresponding values as real constants of the element. Real constants relating to stiffness values are instead set to zero, as the suspension systems are modelled. Relying on the lumped mass-spring damper model representation shown in Figure 4.3, at least two Combin14 elements should be used, oriented along the x and y-axis and connected to the external anchors. It is crucial to obtain a reliable modeling of damping effects that Combin14 and Shell181 elements are bounded together by connecting the two contact nodes. To coupling the degrees of freedom along x and y directions, CP command is used. Figure 4.11 shows a detail of Combin14 elements inserted in the FEM model in Ansys.

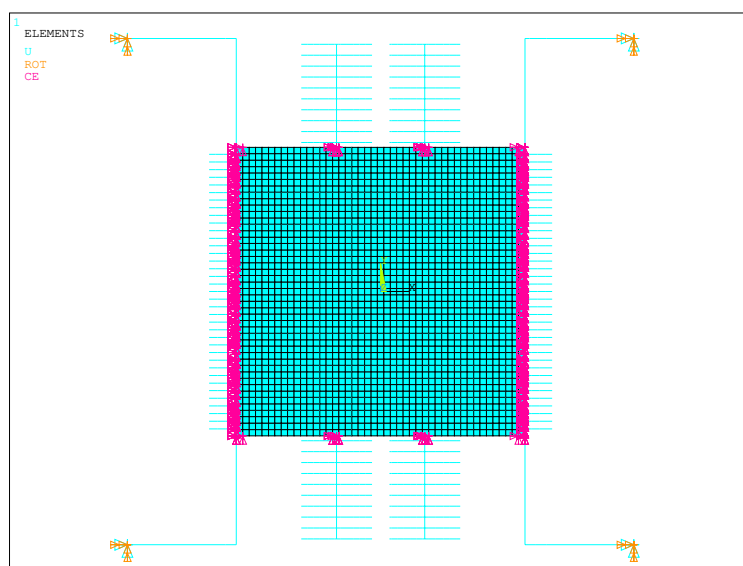


Figure 4.10: Meshed FEM model of the MEMS gyroscope mechanical structure.

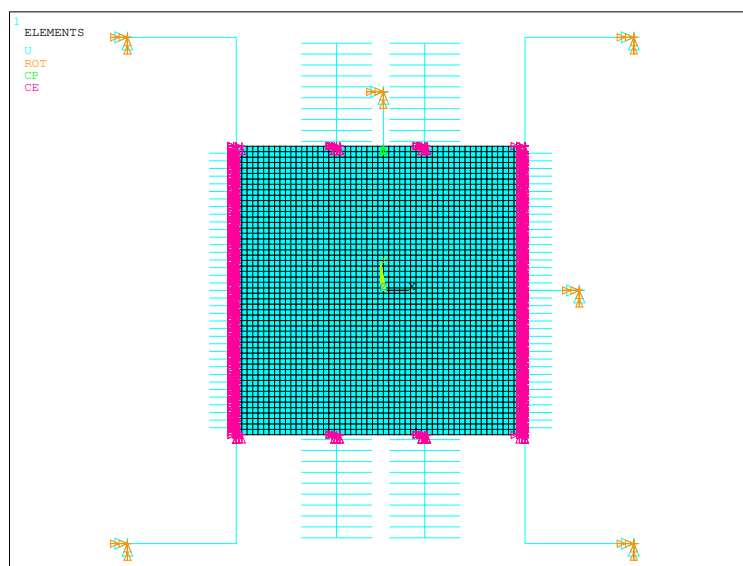


Figure 4.11: Combin14 elements in FEM model for the MEMS gyroscope mechanical structure.

4.4.3 Electromechanical coupling modelling

As previously stated, since the structure presented in this chapter is only preliminary, a detailed discussion about the electromechanical coupling will not be provided, while the reader can refer to

the following chapter for further details. It is only important to point out that, comb-drive based electrostatic actuator are modelled as series of capacitors, since each couple of moving fingers forms a pair of parallel plates. Only moving fingers are modelled using Beam188 elements, while the fixed ones are represented adding fixed constraints in the FEM model. The one-dimensional transducer Tran126 elements are used to model the capacitance of comb drive-based actuators. Two elements are connected at the end of each moving finger, while all degrees of freedom of nodes connected to the fixed fingers are fixed. An electromechanical coupling is thus realized between a distributed mechanical domain and a lumped electrical one. The setup of Trans126 elements in the FEM model for the proposed single mass MEMS gyroscope is shown in Figure 4.12.

4.5 FEM model results

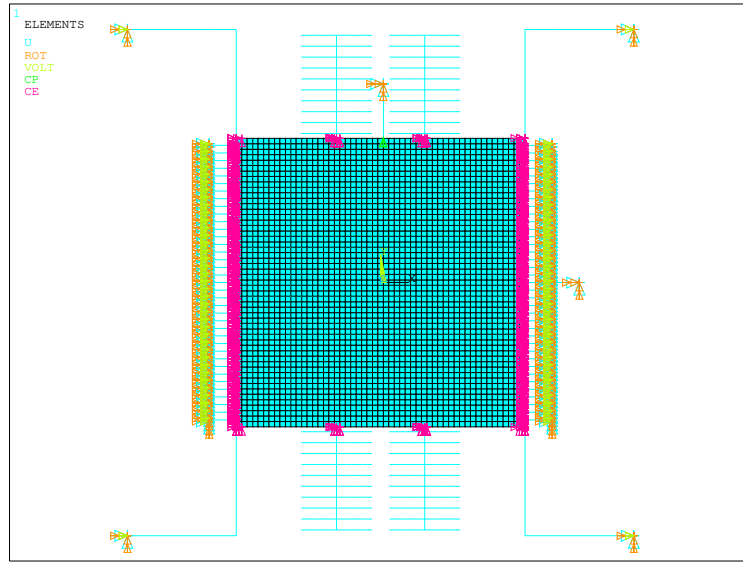
During the design process of a generic MEMS gyroscope device, an accurate prediction of the sensor behaviour is ensured by FEM model based analyses. Accordingly, the single mass MEMS gyroscope design proposed in this chapter is simulated in Ansys. The static analysis is carried out to determine the effective stiffness of the system, while the dynamical behaviour is analyzed through modal and harmonic analysis. A comparison with analytical model results is finally necessary to verify that the devices performance is the one expected.

4.5.1 Static Analysis

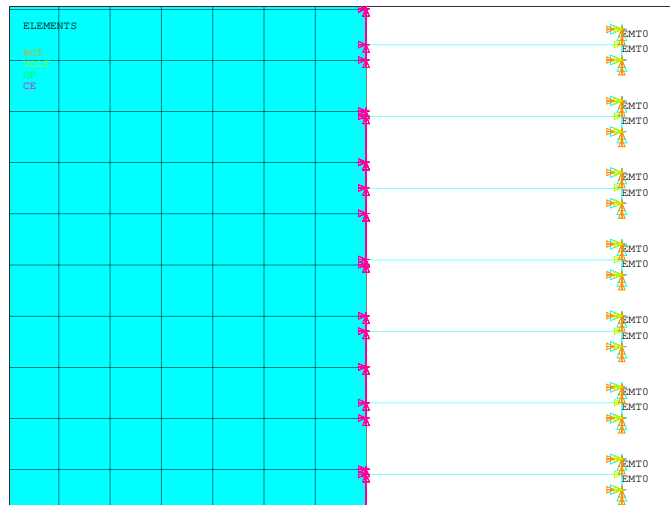
As it was previously introduced, the static analysis gives the response of the structure to a static load, meaning that it allows to estimate the response the stiffness of the overall MEMS gyroscope structure. A DC tension is applied on Trans126 nodes attached to comb-drive moving fingers of one of the two proof mass sides. A comparison with the analytical results is therefore performed. The structure deflection in x-direction for an increasing value of DC tension applied is shown in Figure 4.13. Since the considered structure is quite simple from a structural complexity point of view, it follows that the analytical model and fem model results are very close to each other which confirms a correct capturing of the system dynamics.

4.5.2 Modal Analysis

The analytical modal analysis has shown that drive and sense resonance frequency values are matched and, even for the FEM-based model, matching between resonant frequencies should be guaranteed. The convergence with respect to mesh size is first checked. Figure 4.14 shows the drive and sense resonant frequency variation with increase of the number of elements in the mesh. Clearly, a higher number of elements leads to an increase in the accuracy of frequency estimation, meaning that a finer mesh is able to better capture the system dynamics. Indeed, an increase in the number of elements allows to decrease the mismatch between drive and sense mode frequency, as desired. It is important to highlight that, even if a very finer mesh is adopted, a slight mismatch between the drive and sense mode resonant frequencies still remains. This means that the mechanical design parameters, which have been chosen based on the analytical results, should be slightly modified. However, since this single mass MEMS gyroscope design is only preliminary, an iterative steps design to determine the design parameters which allow to guarantee the mode-matching condition is avoided. In addition, choosing the mesh size is always a trade-off between accuracy, i.e. matching resonant frequency values, and efficiency, i.e. lower CPU time. In order to limit the CPU time, which is shown in Figure 4.15, and achieve adequate accuracy, a mesh with a number of elements in the range of 8000 to 12000 elements can be considered acceptable. Choosing the mesh size already shown in Figure 4.10, a FEM-based modal analysis is performed. In Figure 4.16, the first four mode shapes of the single mass MEMS gyroscope are shown. The



(a) Trans126 elements detail



(b) Trans126 elements in the FEM model with detail of boundary conditions

Figure 4.12: Setup of Trans 126 elements for FEM based electrostatic analysis.

first mode of the structure (Figure 4.16a) is related to drive-mode, in which only the proof mass is moving along the x-direction and the crab-leg spring beams are bending in the same direction. This mode implies a purely in-plane deformation of the structure. Similarly, the second mode is described by an in-plane motion and is related to the sense-mode (Figure 4.16b). Indeed, when

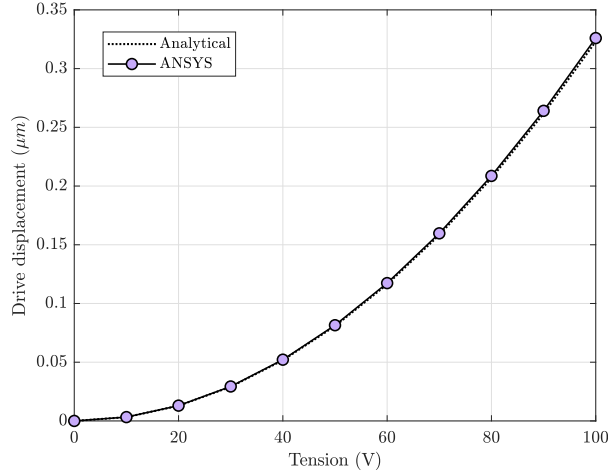


Figure 4.13: Comparison between analytical and Ansys static displacement in the drive direction for the proposed single mass MEMS gyroscope design.

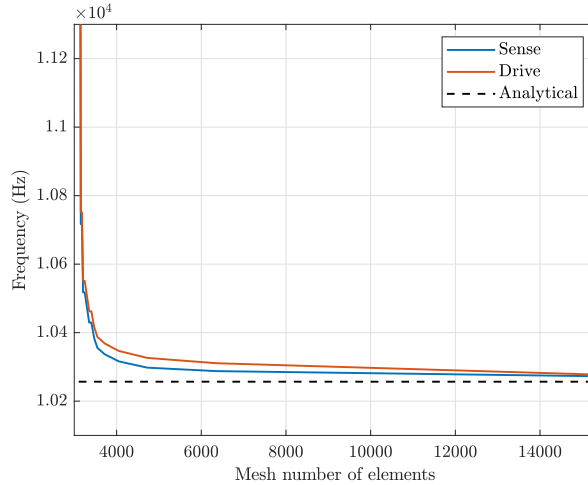


Figure 4.14: Drive and sense resonant frequencies variation with increase of mesh number of elements.

the device is subjected to an external angular velocity in the z-direction, the proof mass moves in the y-direction due to the Coriolis force. The third (Figure 4.16c) and fourth (Figure 4.16d) modes are associated to the tilting of the mass and do not affect the operation of the gyroscope. These modes are called spurious modes.

Table 4.9 compares the FEM-based modal analysis results related to the drive and sense mode with the analytical model ones, which shows a very small difference. This is mainly due to the fact that the analytical model does not exactly estimate the stiffness of suspension beam systems.

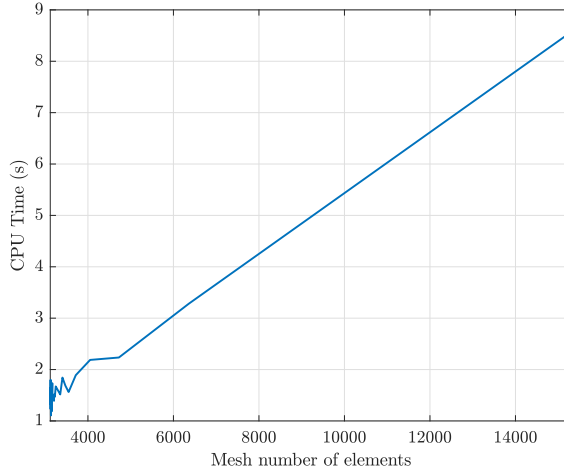


Figure 4.15: CPU time variation to perform FEM-based modal analysis with increase of mesh number of elements.

Mode shape	Analytical Hz	Ansys Hz	Error (%)
Drive	10257	10273	0.156
Sense	10257	10278	0.205

Table 4.9: Comparison of the analytical and FEM-based modal analysis results related to the drive and sense mode.

4.5.3 Harmonic analysis

With the aim of determining the frequency behaviour of the device and, at last, its mechanical sensitivity, a frequency response analysis is carried out in Ansys. A harmonic force is applied to the proof mass along the x-axis by applying an actuation voltage of 50 V DC and 5 VAC to comb drive-based actuators. The analysis is performed considering the air damping effect previously estimated through the analytical model. As described in section 3.3.3, since the AC voltage value is small with respect to the DC one, nonlinear effects caused by the electromechanical coupling can be neglected and a prestressed harmonic analysis can be performed to analyze the device harmonic behaviour. Accordingly, a static analysis with the applied DC voltage is first performed, followed by a prestressed full harmonic analysis with the applied AC excitation.

Figure 4.17 shows the obtained frequency response of the structure in the drive direction in terms of magnitude and phase. As already stated, in the drive direction, the dynamical of the structure is the one of a single-degree of freedom system. Accordingly, frequency response is amplified at the driving frequency and the phase is -90° . A comparison between FEM-based harmonic analysis and analytical results is provided in Figure 4.18, which shows a close correspondence.

The frequency response in the sense direction is obtained by applying to the device an angular velocity of $\Omega_z = 300^\circ/\text{s}$ and the electrostatic actuation force. In this case, the drive and sense mode are coupled by the Coriolis force and the sense mass dynamics in y-direction is the one of a single degree-of-freedom system. Figure 4.19 shows the obtained frequency response of the structure in the sense direction in terms of magnitude and phase. Since the difference between drive and sense mode frequency values is only of 5 Hz, in the frequency response only one peak

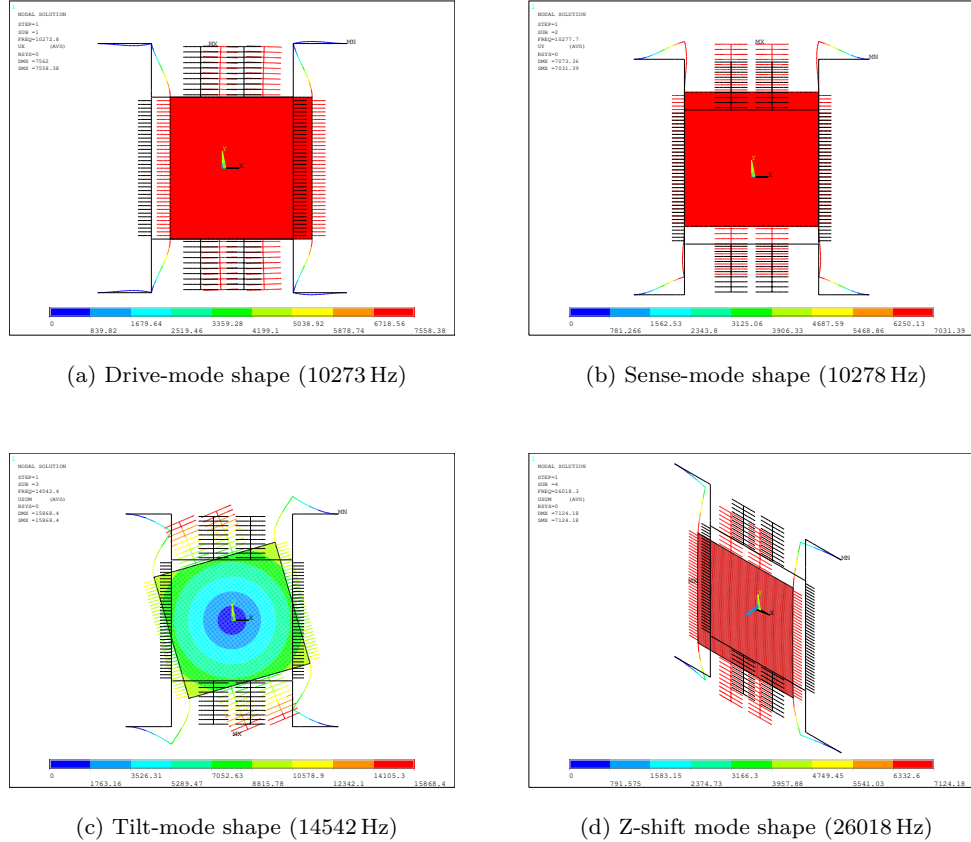


Figure 4.16: Modal analysis results and the corresponding mode shapes for the proposed MEMS gyroscope (a) 1st mode (10273 Hz) (b) 2nd mode (10278 Hz) and (c) 3rd mode (14542 Hz) and (d) 4th mode (26018 Hz).

is recognizable. In this condition, the phase decreases continuously from -90° to -450° . A comparison between FEM-based harmonic analysis and analytical results in the sense direction is instead provided in Figure 4.20, which shows again a close correspondence.

Finally, Table 4.10 compares the frequency response amplitudes at resonance of the drive and sense mode obtained through the FEM-based harmonic and analytical analysis. Since the structure is very simple, the analytical model represents very well the dynamic of the device.

It is important to highlight that in this simple case, when the drive and sense mode frequencies are matched, the mechanical sensitivity is 0.0174 unit $\mu\text{m}/\text{rad}/\text{s}$. However, as it will be discussed in the following chapters, any variation in ambient conditions and fabrications imperfections can cause a shift in resonance frequency which in turn causes a mismatch between the drive and sense mode frequencies. Clearly, this frequency mismatch causes the performance of the gyroscope to reduce dramatically as the even a slight mismatch can reduce the amplitude response of a mode matched gyroscope significantly. Therefore, the fluctuation in the performance parameter should be compensated and corrected by designing a new more complex structure, which is the main aim of this thesis project.

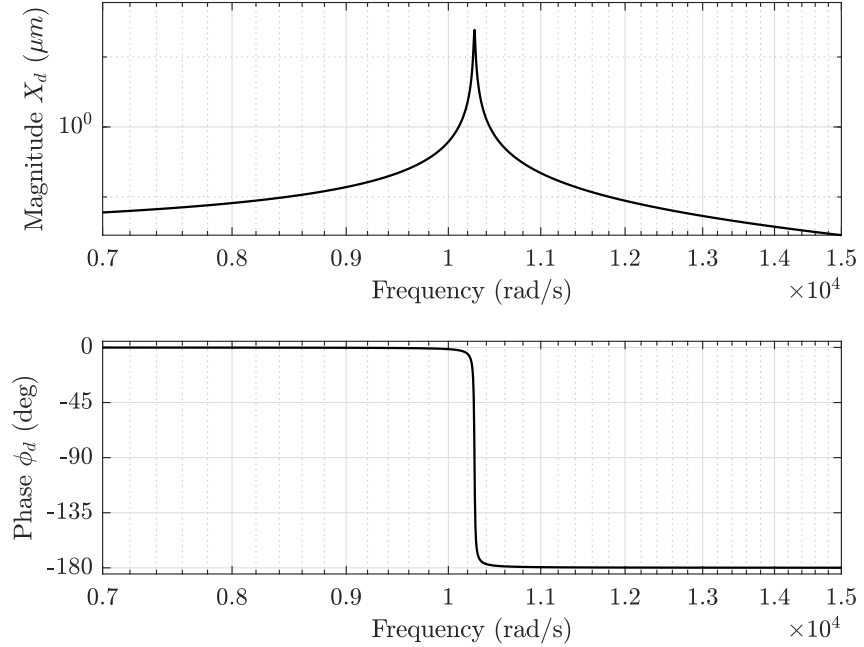
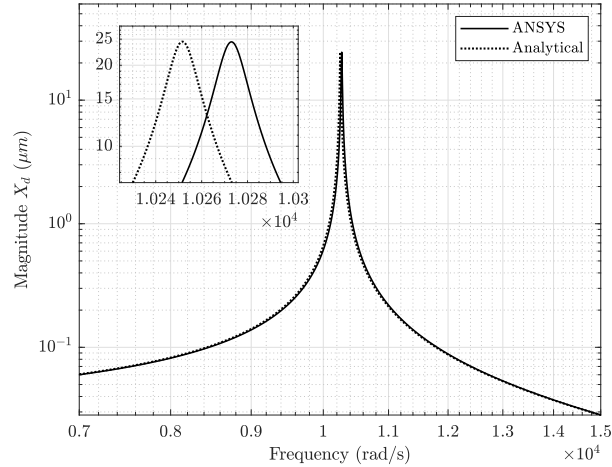


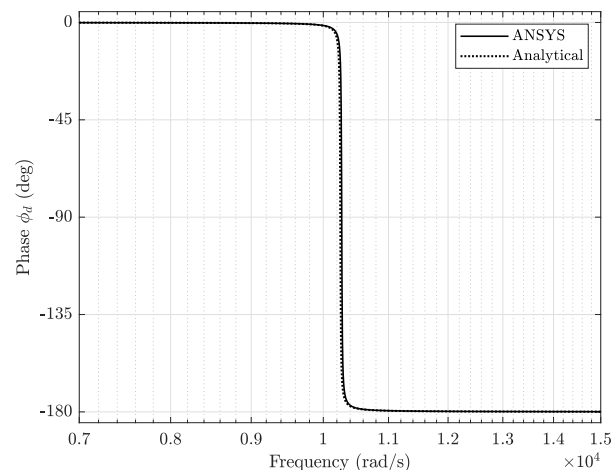
Figure 4.17: The FEM-based frequency response in the drive direction for the proposed MEMS gyroscope design (*logarithmic scale*), with $V_{DC} = 50$ V and $V_{AC} = 5$ V.

Mode	Model	Magnitude	Unit
Drive	Analytical	24.4716	μm
	Ansys	24.4217	μm
	Error	-0.21	%
Sense	Analytical	91.19	μm
	Ansys	90.99	nm
	Error	-0.22	%

Table 4.10: Comparison of the analytical and FEM-based harmonic analysis results related to the drive and sense resonant frequency.



(a) Magnitude comparison



(b) Phase comparison

Figure 4.18: Comparison of the analytical and FEM-based harmonic analysis results in the drive direction (*logarithmic scale*), with $V_{DC} = 50$ V and $V_{AC} = 5$ V (a) Magnitude and (b) Phase.

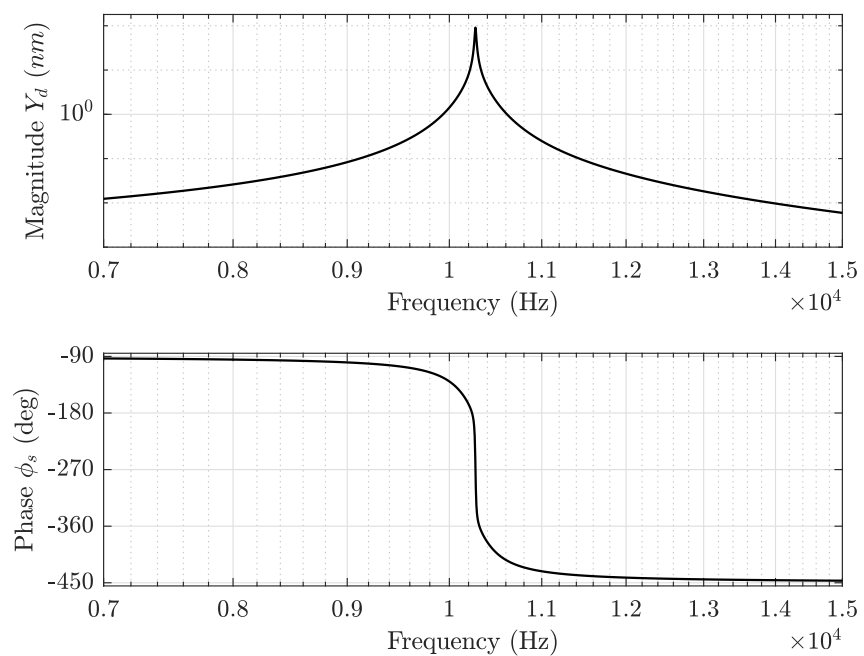
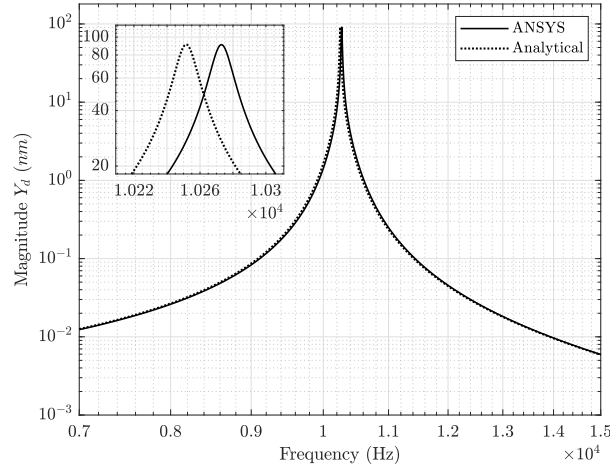
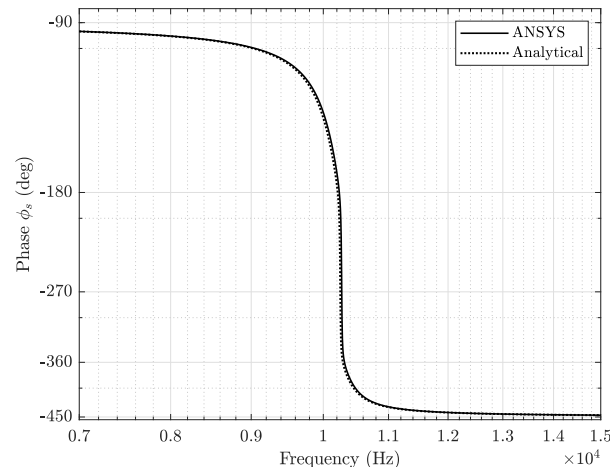


Figure 4.19: The FEM-based frequency response in the sense direction for the proposed MEMS gyroscope design (*logarithmic scale*), with $\Omega_z = 300^\circ /s$.



(a) Magnitude comparison



(b) Phase comparison

Figure 4.20: Comparison of the analytical and FEM-based harmonic analysis results in the sense direction (*logarithmic scale*), with $\Omega_z = 300^\circ/\text{s}$ (a) Magnitude and (b) Phase.

Chapter 5

Dual mass resonant MEMS gyroscope model

The main goal of this thesis project is to develop and present a new design of MEMS resonant gyroscope. As introduced in the previous chapters, a resonant MEMS gyroscope is operated at resonance and both the drive and sense mode resonant frequency values are generally matched. This leads to high mechanical sensitivity. However, the major challenge faced by the MEMS designer is the fluctuation in the performance parameters of resonant MEMS gyroscopes, as they are easily affected by any variation in ambient conditions and fabrication imperfections. These imperfections can cause a shift in resonance frequency, which in turn causes a mismatch between the drive and sense mode frequencies.

In this chapter the new design of resonant MEMS gyroscope consisting of two separate masses for the drive and sense mode is presented which allows to minimize the cross-axis sensitivity and common mode error. The design considers the foundry constraints of relatively low cost and commercially available Silicon-on-Insulator (SOI) based SOIMUMPs process. For the compensation of the frequency mismatch between the drive and sense mode frequency due to microfabrication process tolerances and device operating temperature variations, comb-drive based electrostatic tuning is implemented in the design.

First, the MEMS gyroscope structure is described in detail, with a focus on the design process steps followed to determine the geometrical parameters. Then, the analytical model is developed and static and dynamical behaviour analyses are presented. A FEM-based model is successively implemented in Ansys and a comparison between analytical and FEM-based model results is finally provided.

5.1 Mechanical design and working principle

The schematic of the new MEMS gyroscope design proposed in this thesis project is shown in Figure 5.1. This is a resonant mode-matched electrostatic z-axis device, which means that it is operated at resonance and both the drive and sense mode resonant frequency values are matched. The design consists of two separate masses for the drive and sense mode while minimizing the cross-axis sensitivity by decoupling the drive and sense mode displacements using a unique configuration of mechanical springs. The drive mass, referred to m_d in the figure, is nested inside the sense frame m_s through four folded beams namely k_x and placed such that they permit motion of the mass m_d in the drive direction, but restrict any motion in the sense direction. Another set of eight folded spring beams namely k_y connects the sense frame to the anchors and allows its displacement in the sense direction only. An oscillatory motion along the drive direction (x-axis) is obtained through a

comb-drive based electrostatic actuator which is attached to the drive mass m_d . When the gyroscope is subjected to an external angular velocity in the z-axis, a Coriolis force and a consequent vibration is induced in the sense direction (y-axis), which is orthogonal to both the drive direction and angular rotation axis. The mechanical suspensions attached to the drive mass does not allow its oscillation in the y-axis. However, since the drive mass is nested inside the sense mass, both the drive and sense mass move in the y-axis corresponding to a rotation induced Coriolis force. Since sensing parallel plates are attached to the sense frame, their relative motion along the drive direction is prevented. This approach minimizes the undesired capacitance change in the sense electrodes due to the drive motion. The parallel sensing plates are arranged in gap-antigap based differential configuration and, acting as capacitive transducers, allow to detect the resulting displacement due to the Coriolis force.

Finally, for the compensation of the frequency mismatch between the drive and sense mode resonant frequencies for the proposed MEMS gyroscope due to microfabrication process tolerances or thermal variations, electrostatic tuning combs, attached to the sense frame and based on the electrical spring softening concept, are implemented in the design.

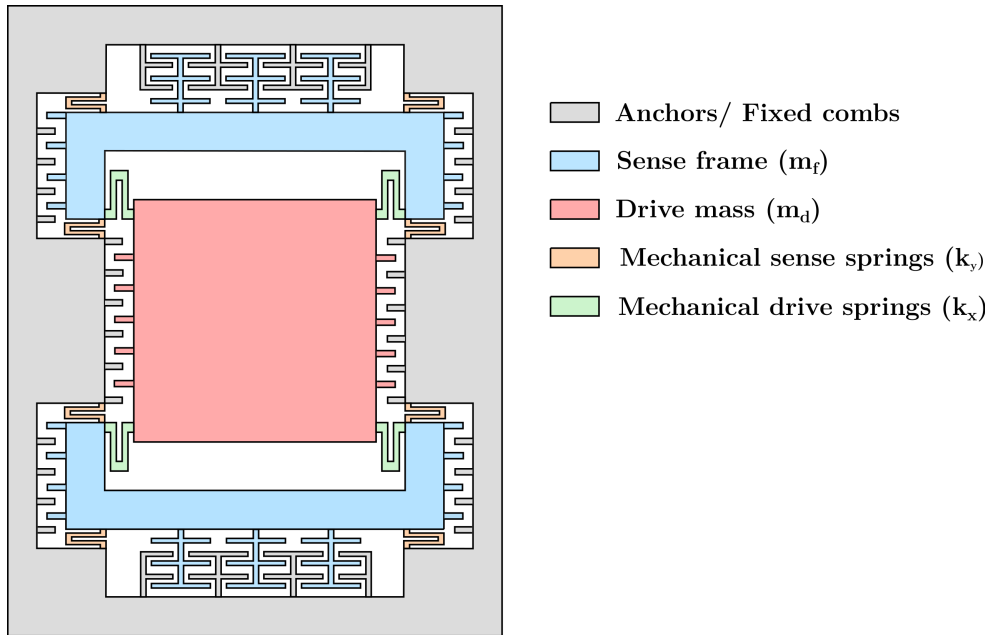


Figure 5.1: Dual mass resonant MEMS gyroscope design: it consists of two separate masses for the drive and sense axis which are fully decoupled. The drive mass is set into oscillations in the x-axis by using comb-drive based electrostatic actuator, while parallel sensing plates arranged in the gap-antigap configuration are used to detect the displacement due to the Coriolis force.

The MEMS gyroscope is designed following the constraints of the commercially available and low-cost multiuser SOIMUMPs micromachining process, offered by MEMSCAP Inc. USA [17]. In addition to being a mature fabrication process, SOIMUMPs offers to fabricate high aspect ratio micro structures with minimum air damping, due to absence of substrate below the moving microstructure. Both of these attributes are generally desired in the design of high-performance MEMS inertial sensors [15]. The SOIMUMPs microfabrication process is a single-wafer silicon-on-insulator (SOI) micromachining process and allows patterning and etching on the SOI wafer using four mask layers with different thickness. The topmost layer, called Padmetal, is followed by a device layer of 25 μm thickness. An oxide layer of 2 μm thickness is sandwiched between the device

layer and the 400 μm thick substrate layer. In order to weight down the discussion, general details of the SOIMUMPs microfabrification process steps are provided in *Appendix B*.

For the accurate release of microstructures and structural integrity, the SOIMUMPs microfabrification process has certain design rules to be followed. For the complex MEMS devices, like MEMS gyroscopes, this limits the design options for the MEMS designer. The main limitation that are considered for the proposed MEMS gyroscope design are provided below [15]:

- Limitation 1: This process does not allow anchor region in the center since it does not survive during the etching step of the microfabrification process. For the proposed resonant MEMS gyroscope, this implies that, in comparison to traditional resonant MEMS gyroscope designs reported in the literature, the drive mass cannot be completely enclosed within a sense frame due to the requirement of anchor part for the fixed comb-drive fingers. Consequently, for the proposed MEMS gyroscope design, all the fixed parts are moved on the periphery.
- Limitation 2: As the silicon substrate is completely etched in the SOIMUMPs process, bottom electrodes for the out-of-plane actuation and sensing cannot be fabricated in this process. This leaves the MEMS designer to use only comb-drive actuators and in-plane sensing parallel plates mechanisms.
- Limitation 3: The uniformity of the etching processes are strongly dependent upon feature size and the amount of silicon area that is etched. To make sure that the structural integrity of the device remains intact after fabrication and to minimize non-uniformities, the etched part of the silicon layer must be less than 33% of the total chip area. This is achieved by minimizing the air gaps between the masses and by reducing the unused empty spaces in the design.

In addition to the previous limitations, another important design consideration is that the minimum feature size for the device layer is 2 μm , but to avoid buckling due to the residual stresses it is suggested, by the foundry, that the beams must have a thickness of 4 μm or more for a length of more than 100 μm . In addition, the minimum air gap allowed by the microfabrification process is 2 μm . However, to meet the microfabrification process constraints and to minimize the Brownian noise and air damping effect, slightly larger gap dimensions are considered.

The silicon structural material data are summarized in Table 5.1, while referring to Figure 5.2 which shows the dual mass resonant MEMS gyroscope structure components in detail, Table 5.2 provides the main design parameters. For the sake of clarity, a complete characterization of the electrical design elements and flexure system will be provided in the following sections.

Parameter	Symbol	Value	Unit
Young's Modulus	E	169	GPa
Density	ρ	$2.5e - 15$	$\text{kg}/\mu\text{m}^3$
Poisson's ratio	ν	0.29	-

Table 5.1: Silicon structural material data.

The design process for the MEMS gyroscope proposed in this thesis project has required, in addition to respecting the limits imposed by the microfabrification process, to ensure the matching of the drive and sense mode resonant frequency values. Moreover, it is necessary to consider that electrostatic tuning will be implemented to compensate for the frequency mismatch between the drive and sense mode frequency due to microfabrification process tolerances and device operating temperature variations. This means that the sense frequency value must be slightly greater than the drive one. Accordingly, the design routine has been somewhat iterative and Figure 5.3 shows

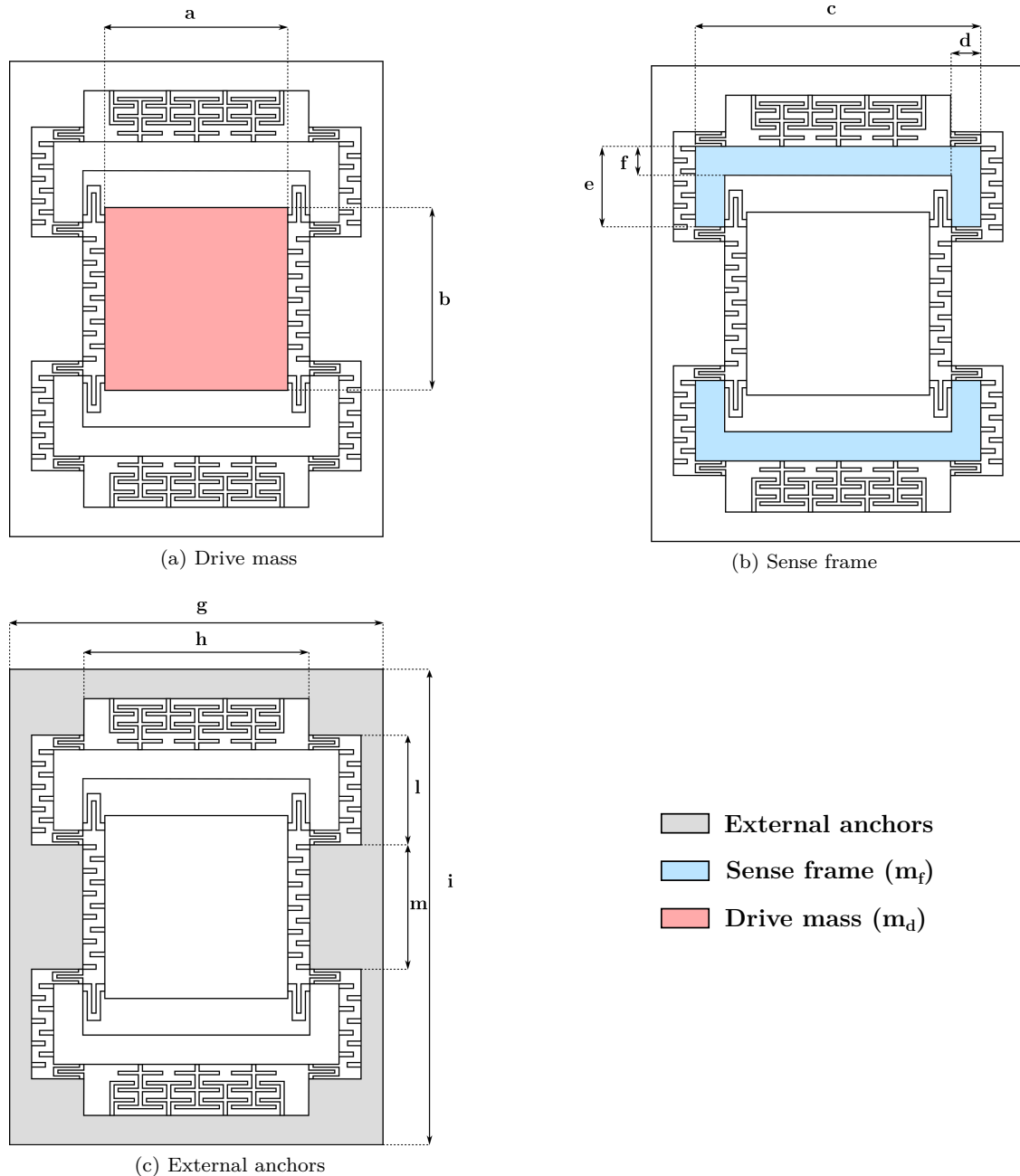


Figure 5.2: Details of drive mass, sense frame and external anchors for the dual mass MEMS gyroscope design.

Parameter	Symbol	Value	Unit
Overall device size	-	2.827	mm ²
Structural layer thickness	<i>t</i>	25	μm
Drive mass horizontal length	<i>a</i>	700	μm
Drive mass vertical length	<i>b</i>	700	μm
Sense frame horizontal length	<i>c</i>	1117	μm
Sense frame horizontal length	<i>d</i>	123.5	μm
Sense frame vertical length	<i>e</i>	348	μm
Sense frame vertical length	<i>f</i>	125	μm
External anchors horizontal length	<i>g</i>	1557	μm
External anchors horizontal length	<i>h</i>	1030	μm
External anchors vertical length	<i>i</i>	1816	μm
External anchors vertical length	<i>l</i>	438	μm
External anchors vertical length	<i>m</i>	522	μm

Table 5.2: Design parameters of the dual mass resonant MEMS gyroscope.

the adopted iteration scheme. Starting having to guarantee the dynamical performance, first design parameters are chosen based on the analytical model results. Then, check that these parameters meet the constraints attributed to the SOIMUMPs microfabrication process and, if not, back to the previous point. A finite element simulation is finally necessary to validate the analytical model results and eventually repeat the iterations.

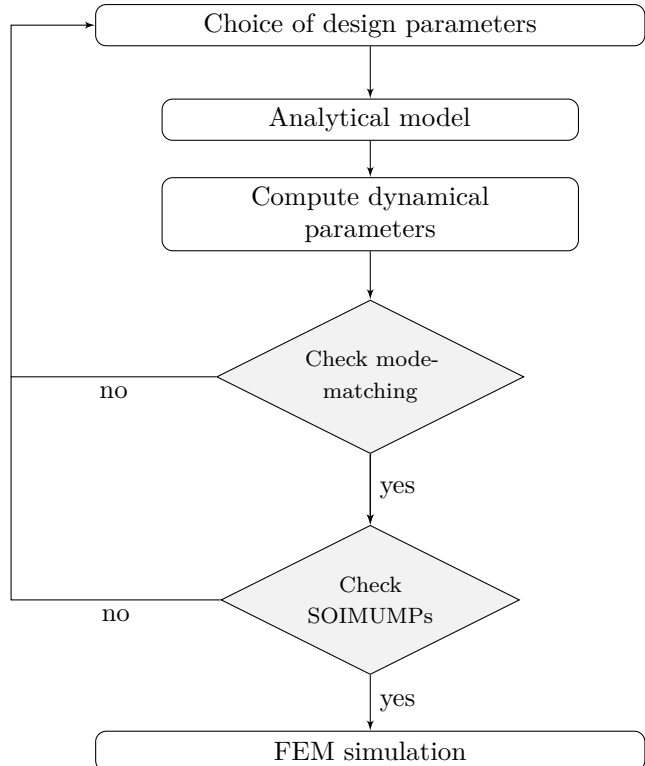


Figure 5.3: Iteration scheme for design process of the proposed dual mass MEMS gyroscope.

5.2 Analytical model

As previously introduced, a detailed analytical model is implemented with the purpose of determining the dynamical behavior of the proposed MEMS gyroscope device. Figure 5.4 shows the lumped mass-spring-damper model of the proposed MEMS gyroscope design. The drive mass m_d is nested inside the sense frame m_f through the mechanical spring k_x and is free to oscillate along the drive direction (x-axis), while the sense frame is anchored to the substrate by means of the mechanical spring k_y and is constrained to move only in the sense direction (y-axis). The air damping between the comb-drive based actuators attached to the drive mass, m_d , tuning-combs and sensing parallel plates attached to sense frame m_f are represented by c_x and c_y coefficients, respectively. When an angular velocity Ω_z is applied in the z-axis, the dynamical behaviour is that of a two degree-of-freedom system.

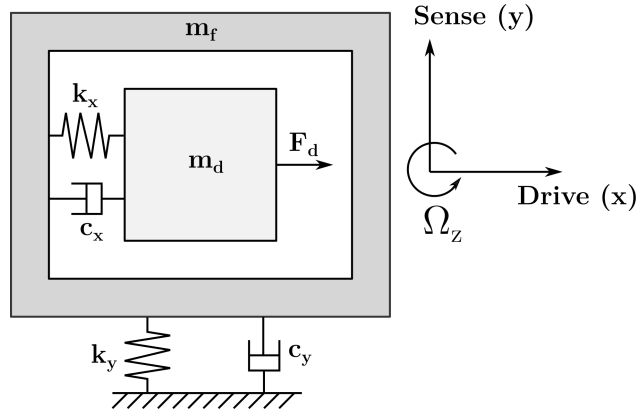


Figure 5.4: Two degrees-of-freedom mass–spring–damper model for the proposed dual mass MEMS gyroscope. The arrow in x-direction indicates the drive direction, whereas the arrow orthogonal to the first shows the sense direction of motion.

Following the procedure illustrated in Section 2.2, the second-order differential equations of motion for the proposed MEMS gyroscope can be obtained as

$$\begin{aligned} m_d \ddot{x} + c_x \dot{x} + k_x x &= F_d \\ m_s \ddot{y} + c_y \dot{y} + k_y y &= -2m_d \Omega_z \dot{x} \end{aligned} \quad (5.1)$$

where

- m_d is the drive mass
- m_f is the sense frame mass
- $m_s = m_d + m_f$ is the sense mass
- c_x is the damping coefficient in the drive direction
- c_y is the damping coefficient in the sense direction
- k_x is the global stiffness coefficient in the drive direction
- k_y is the global stiffness coefficient in the sense direction.

The electrostatic actuation force F_d is applied by comb-drive based actuators, while $-2m_d\Omega_z\dot{x}$ is the Coriolis force acting on the one degree-of-freedom oscillator in the sense direction. The major assumption made to obtain equations in 5.1 is that the coupling effects arising from nonidealities, which are anisoelasticity and anisodamping terms coupling drive and sense mode, are negligible. In this ideal case, the driving and sensing axes are coupled only through the Coriolis force. Actually, the quadrature error may affect the gyroscope changing its dynamical behaviour. Fabrication process unavoidably leads to imperfections and non-ideal geometries in the gyroscope layout. This causes a cross-coupling and a loss in orthogonality of the modes. However, this error can be compensated based on the same principle of electrostatic tuning implemented in the proposed design [3]. For this reason, the assumption of neglecting such defects is plausible.

The aim of the following sections is to compute the lumped coefficients of Equations 5.1, considering the basics of the mechanical and electrical gyroscope design previously provided in Chapter 2.

5.2.1 Calculation of mechanical stiffness

Figure 5.5 shows the configuration of mechanical springs attached to the drive mass and sense frame, whose details are also represented in Figure 5.6. There are two sets of mechanical springs in the x and y-axis. One set of mechanical springs, namely k_x is placed such that it permits motion of the drive mass m_d in the drive direction, but restricts any motion in the sense direction. Another set of mechanical springs namely k_y is placed such that it allows movement of the sense frame m_f in the sense direction only. Accordingly, this configuration of mechanical suspension systems allows to decouple the drive and sense motions and minimize the cross-axis displacement.

A unique configuration of folded beams is used for the mechanical springs both in the drive and sense direction. In particular, four folded-beams which are compliant in the x-axis are used to connect the drive mass to the sense frame, while in the sense direction eight folded-beams connect the sense frame to the external anchors.

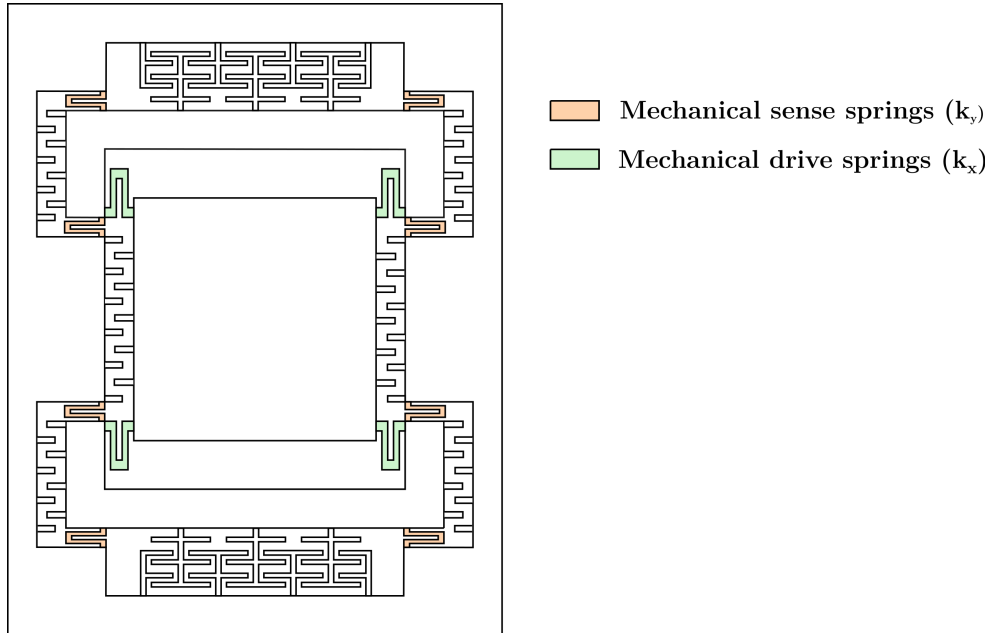


Figure 5.5: Mechanical suspension systems for the proposed dual mass MEMS gyroscope design.

The mechanical springs, both in drive and sense direction, can be modeled as fixed-guided beams

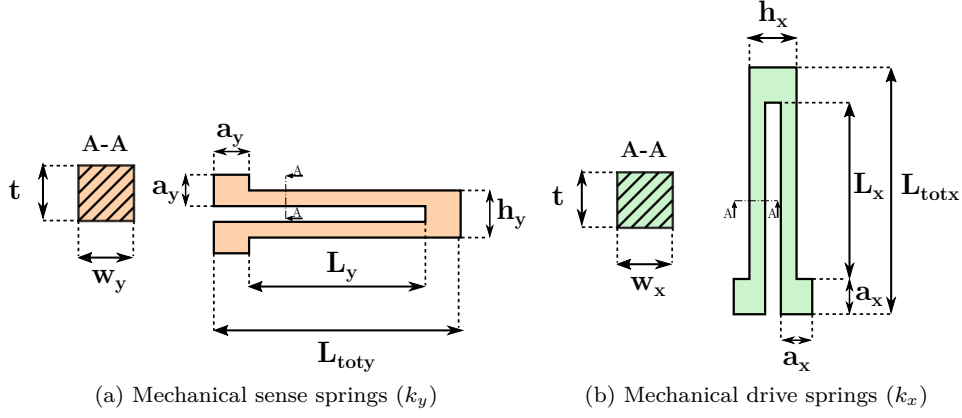


Figure 5.6: Details of drive and sense mechanical springs for the proposed dual mass MEMS gyroscope design.

connected in parallel. The overall stiffness in the drive axis k_x due to the four folded beams can be computed as follows

$$k_x = 4 \frac{Etw_x^3}{2L_x^3} \quad (5.2)$$

where E is the Young's modulus, t is the thickness of the beams, w_x and L_x are their width and length, respectively. Instead, the sense axis mechanical stiffness can be calculated with the following expression

$$k_y = 8 \frac{Etw_y^3}{2L_y^3} \quad (5.3)$$

where w_y and L_y are the width and length of the folded beams respectively in the sense axis. Referring to Figure 5.6, design parameters of the mechanical springs previously described are summarized in Table 5.3.

Parameter	Value	Unit	Parameter	Value	Unit
L_{totx}	210	μm	L_{toty}	190	μm
L_x	150	μm	L_y	150	μm
a_x	40	μm	a_y	20	μm
h_x	13	μm	h_y	13	μm
w_x	4	μm	w_y	4	μm
t	25	μm	t	25	μm

(a) Mechanical drive springs
(b) Mechanical sense springs

Table 5.3: Mechanical springs design parameters.

It is important to point out that, the analytical stiffness expression in drive and sense directions is only an approximation. This approximation assumes that the compliance of the proof-mass, frame structures, and flexures in other directions are negligible. In reality, these factors dramatically reduce the overall stiffness. Thus, FEM-based modal analyses in Ansys will be absolutely necessary for accurate estimation and design of resonant frequencies.

5.2.2 Electrical Design

The following paragraphs provide the design parameters of comb-drive based actuators, electrostatic tuning-combs and sensing parallel-plates structures implemented in the MEMS gyroscope design, respectively for the actuation, electrostatic tuning and sensing mechanism. For the sake of clarity, the complete analytical characterization of electrostatic tuning-comb structures will be provided in Chapter 6 with the analysis of the electrostatic tuning concept.

Comb-drive actuators

As previously stated, the drive mass is set into oscillations by using two comb-drive based electrostatic actuators attached on both sides of the drive mass. Referring to Figure 5.7 for further details, Table 5.4 provides the design parameters of the comb-drive structures implemented in the proposed MEMS gyroscope device.

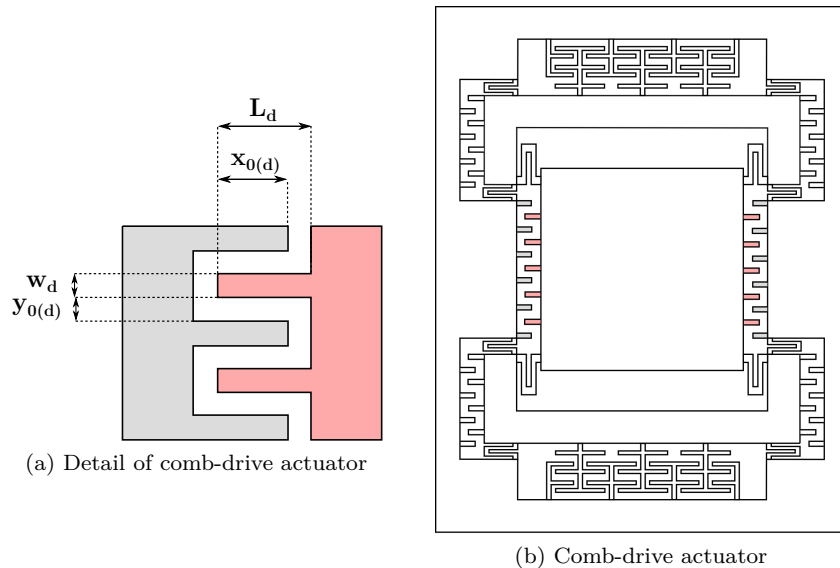


Figure 5.7: Comb-drive based electrostatic actuator implemented in the dual mass MEMS gyroscope design.

Each fingers of the two comb-drive structures attached on the both side of the drive mass forms two parallel-plate pairs. Accordingly to Equation 2.34, when a constant bias voltage V_{DC} is applied to one of the two stationary electrodes, the electrostatic actuation force can be expressed as

$$F_d = N_d \frac{\epsilon_0 t}{y_0(d)} V_{DC}^2 \quad (5.4)$$

where ϵ_0 the free space permittivity, N_d is the total number of moving comb attached to one side of the drive mass, $x_0(d)$ is the overlap length, t is the structure thickness and $y_0(d)$ is the gap between comb drive fingers. On the contrary, when a constant bias voltage V_{DC} is superimposed to a sinusoidal time-varying voltage V_{AC} applied to the stationary electrodes, a harmonic actuation force occurs. Adopting the balanced actuation scheme and according to Equation 2.40, the resulting electrostatic harmonic force is expressed as follows

$$F_d = 4N_d \frac{\epsilon_0 t}{y_0(d)} V_{DC} V_{AC} \sin(\omega t) \quad (5.5)$$

where ω is the excitation frequency.

Parameter	Symbol	Value	Unit
Number of drive comb fingers (each side)	N_d	37	-
Length of drive combs	l_d	50	μm
Width of drive combs	w_d	4	μm
Overlap length between the moving and fixed fingers	$x_{0(d)}$	40	μm
Gap between drive combs	$y_{0(d)}$	3	μm

Table 5.4: Comb-drive based electrostatic actuator design parameters.

Sensing parallel plates

For the proposed MEMS gyroscope design, an input angular rotation in the z-axis will result in the Coriolis force in the y-axis which will lead to sense frame and drive mass displacement in the y-axis. To detect this displacement, the sensing parallel plates, arranged in differential gap–antigap configuration, are attached to the sense frame. Referring to Figure 5.8 for further details, Table 5.5 provides the parameter design of the sensing parallel-plate structures implemented in the proposed MEMS gyroscope device.

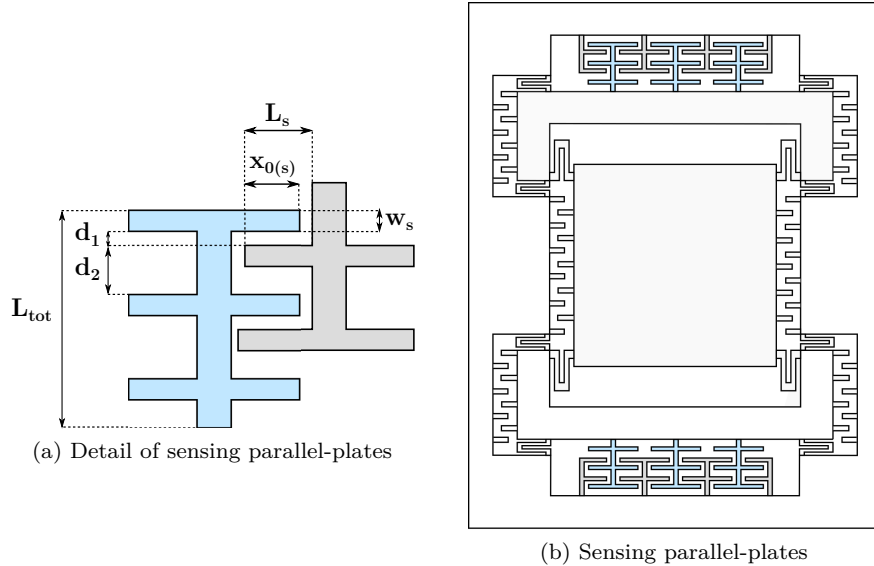


Figure 5.8: Sensing parallel-plates arranged in differential gap–antigap configuration implemented in the dual mass MEMS gyroscope design.

According to Equation 2.50 the overall capacitance change, corresponding to the sense mass displacement in the y-axis, can be calculated as

$$\Delta C = \frac{2\epsilon_0 N_s x_{0(s)} t y (d_2^2 - d_1^2)}{(d_1^2 - y^2) \cdot (d_2^2 - y^2)} \quad (5.6)$$

where ϵ_0 is free space permittivity, N_s is the number of parallel plates on each side, $y_{0(s)}$ is the overlap length of the fixed and moving parallel plates, y is the sense mass displacement and d_1 and d_2 are the small and large air gaps respectively.

Parameter	Symbol	Value	Unit
Number of parallel plates (each side)	N_s	50	-
Length of parallel plates	l_s	65	μm
Width of parallel plates	w_d	4	μm
Overlap length between the moving and fixed fingers	$x_{0(s)}$	55	μm
Smaller sense gap size	d_1	3	μm
Larger sense gap size	d_2	9	μm
Total vertical parallel-plates length	L_{tot}	89	μm

Table 5.5: Sensing parallel-plates design parameters.

Electrostatic tuning combs

As previously introduced, electrostatic tuning combs are implemented in the proposed MEMS gyroscope design in order to compensate of the frequency mismatch between the drive and sense mode frequency due to microfabrication process tolerances and device operating temperature variations. Referring to Figure 5.9, for further details, Table 5.6 provides the parameters design of tuning comb structures.

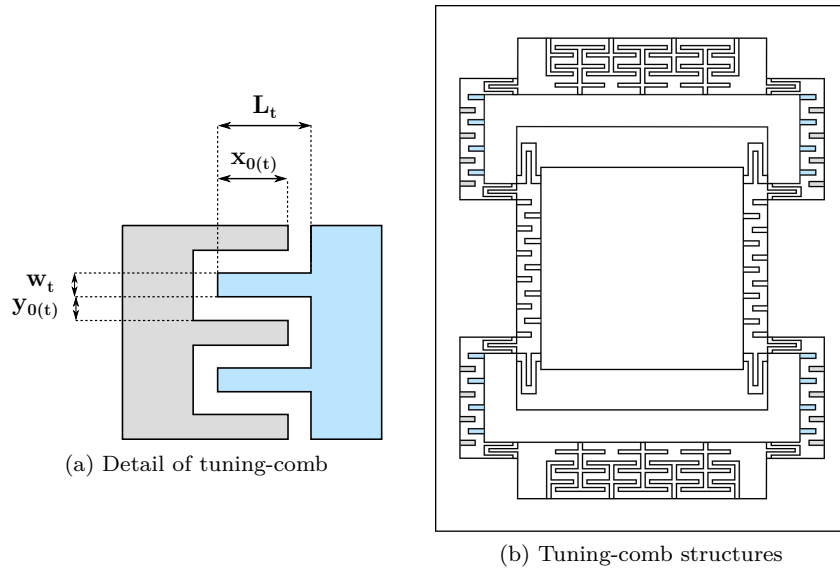


Figure 5.9: Electrostatic tuning combs implemented in the dual mass MEMS gyroscope design.

5.2.3 Air Damping Analysis

As widely discussed in Section 2.5, viscous air damping is typically the dominant dissipation mechanism for the vibratory MEMS gyroscopes operated at atmospheric pressure. In resonant MEMS gyroscopes, the accurate estimation of the viscous air damping is very critical since it affects the overall quality factor and hence sensitivity. For the proposed MEMS gyroscope design, both the slide and squeeze film air damping contribute towards the energy dissipation.

The slide film air damping is the only energy dissipation mechanism in the drive direction. Since

Parameter	Symbol	Value	Unit
Number of tuning comb fingers (each side)	N_d	21	-
Length of drive combs	l_t	50	μm
Width of drive combs	w_t	4	μm
Overlap length between the moving and fixed fingers	$x_{0(d)}$	40	μm
Gap between drive combs	$y_{0(d)}$	3	μm

Table 5.6: Electrostatic tuning combs design parameters.

only comb-drive structures can move laterally in the drive direction, the slide film damping occurs between fixed and moving fingers, which slide parallel to each other. Accordingly, applying the previously introduced Equation 2.77, the damping coefficient in the drive direction c_x can be obtained as

$$c_x = \mu_{eff} A_d \left(\frac{1}{y_{0(d)}} + \frac{1}{y_{0(d)}} \right) \quad (5.7)$$

where $A_d = 2N_d x_{0(d)} t$ is the total overlap area between comb-drive fingers, N_d is the total number of moving comb attached on each side of the drive mass, $x_{0(d)}$ is the overlap length, t is the structure thickness and $y_{0(d)}$ is the gap between comb-drive fingers. The effective air viscosity μ_{eff} was previously expressed by Equation 2.78 in Section 2.5.1 but it is reported here below for clarification purposes

$$\mu_{eff} = \frac{\mu}{1 + 2K_n + 0.2K_n^{0.788} e^{-K_n/10}} \quad (5.8)$$

where K_n is the Knudsen number μ is the viscosity of air at ambient temperature T . The Knudsen number is a measure of the gas rarefaction effect and it can be defined as the ratio of the mean free path of air λ to the thickness of the air gap $y_{0(d)}$ as in the following expression

$$K_n = \frac{\lambda}{y_{0(d)}} \quad (5.9)$$

where the mean free path of air λ at a given operating temperature and pressure is expressed by the previously cited Equations 2.71 or 2.72. Table 5.7 shows data related to slide-film damping in the drive direction for the proposed MEMS gyroscope design.

Property	Symbol	Value	Unit
Temperature	T	298	K
Pressure	P_a	1	atm
Air viscosity	μ	$1.86e - 11$	MPa.s
Mean free path of air	λ	0.0672	μm
Knudsen number	K_n	0.0224	-
Effective viscosity of air	μ_{eff}	1.7632e-11	MPa.s
Damping coefficient in the drive mode	c_x	$8.6983e - 7$	N.s/m

Table 5.7: Data related to slide-film damping in the drive direction for the proposed dual mass MEMS gyroscope design.

The movement of the sense frame together with the drive mass in the sense direction results in the squeezed film air damping phenomenon. Indeed, due to the movement of sense mass, the moving parallel plates displace towards the fixed parallel plates and the thin air film between moving

and fixed parallel plates is squeezed in. The same happens with the interdigitated drive comb and tuning comb fingers. Accordingly, the damping coefficient in the sense direction c_y can be obtained as the combination of three contributions:

$$c_y = c_{y(d)} + c_{y(t)} + c_{y(s)} \quad (5.10)$$

where

- $c_{y(d)}$ is the squeeze film damping coefficient between the interdigitated drive comb fingers
- $c_{y(t)}$ is the squeeze film damping coefficient between the interdigitated electrostatic tuning comb fingers
- $c_{y(s)}$ is the squeeze film damping coefficient between moving and fixed sensing parallel plates.

These contributions can be expressed as follows

$$\begin{aligned} c_{y(d)} &= \mu_{eff} 2N_d x_{0(d)} t^3 \left(\frac{1}{y_{0(d)}^3} + \frac{1}{y_{0(d)}^3} \right) \\ c_{y(t)} &= \mu_{eff} 2N_t x_{0(t)} t^3 \left(\frac{1}{y_{0(t)}^3} + \frac{1}{y_{0(t)}^3} \right) \\ c_{y(s)} &= \mu_{eff} 2N_s x_{0(s)} t^3 \left(\frac{1}{d_1^3} + \frac{1}{d_2^3} \right) \end{aligned} \quad (5.11)$$

where

- N_d is the total number of the drive combs attached on each side of the drive mass
- N_t is the total number of the tuning combs attached on each side of the sense frame
- N_s is the total number of sensing parallel plates attached on each side of the sense frame
- $x_{0(d)}$, $x_{0(t)}$ and $x_{0(s)}$ are the overlap length of drive and tuning combs and sensing parallel plates, respectively
- y_{0d} and y_{0t} are the gap between comb drive fingers and tuning comb fingers
- d_1 and d_2 are the comb smaller and larger gap sizes of the sensing parallel plates, respectively.

In case of squeeze film damping, the effective viscosity of air μ_{eff} at a given temperature and pressure can be expressed using Equation 2.69, which is reported here below for clarification purposes

$$\mu_{eff} = \frac{\mu}{1 + 9.638K_n^{1.1}} \quad (5.12)$$

The Knudsen number K_n can be defined as follows

$$K_n = \frac{\lambda}{d} \quad (5.13)$$

where d is the air gap thickness in drive combs, tuning combs and sensing parallel plates, respectively equal to $y_{0(d)}$, $y_{0(t)}$ and d_1 . Table 5.8 shows data related to squeeze-film damping in the sense direction for the proposed dual mass MEMS gyroscope design.

Property	Symbol	Value	Unit
Temperature	T	298	K
Pressure	P_a	1	atm
Air viscosity	μ	$1.86e - 11$	MPa.s
Mean free path of air	λ	0.0672	μm
Knudsen number	K_n	0.0224	-
Effective viscosity of air	μ_{eff}	1.6206e-11	MPa.s
Damping coefficient in the sense mode	c_y	$1.2068e - 4$	N.s/m

Table 5.8: Data related to squeeze-film damping in the sense direction.

As widely explained in Section 2.5.1 the Knudsen number is a measure of the gas rarefaction effect of air since it defines the operating flow regime. For the proposed MEMS gyroscope, the air gap between the sensing parallel plates and drive and electrostatic tuning combs fingers is $3\ \mu\text{m}$ which results in a Kn value 0.0224 at atmospheric pressure and room temperature. This shows that, since this value is within $0.01 < Kn < 0.1$, the flow regime for the proposed MEMS gyroscope can be considered as slip flow regime.

The air damping force acting on the MEMS gyroscope can be either viscous or elastic and is dependent on the oscillation frequency of the masses. As previously discussed in Section 2.5.1, the relative effect of the air damping force is generally classified based on the dimensionless squeeze number σ , which is given as

$$\sigma = \frac{12\mu_{eff}t^2\omega}{P_a d^2} \quad (5.14)$$

where t is the structure thickness, μ_{eff} is the effective viscosity, ω is the operating frequency, P_a is the ambient pressure and d is the air gap thickness in drive combs, tuning combs and sensing parallel plates, respectively equal to $y_{0(d)}$, $y_{0(t)}$ and d_1 . At low values of the squeeze number, the viscous damping force dominates over the elastic force. In contrast, at high values of the squeeze number the elastic force component, which always grows with ω , is dominant. Figure 5.10 shows the effect of oscillation frequency on the squeeze film air damping at operating temperature and pressure of $T = 298\ \text{K}$ and 1 atm and the relative contribution of both the viscous and elastic damping forces. It is important to highlight that viscous and elastic damping forces are analytically computed following the Equation 2.75.

The results in Figure 5.10a shows that, for the oscillation frequency in the range of 12 kHz, the viscous damping force is the main energy dissipation mechanism and effect of the elastic force of air damping is negligible. These results were also verified by the Equation 5.14, since the squeeze number value for the MEMS gyroscope, at 12 kHz and temperature and pressure of 298 K and 1 atm is only 0.01. Figure 5.10b shows that with higher values of oscillation frequency, the elastic air forces becomes dominant and increases with the oscillation frequency, while the viscous damping forces decreases. Since the proposed MEMS gyroscope operates at frequencies lower than 12 kHz, as it will be demonstrated by the modal analysis results provided in the next section, only the viscous damping effect can be considered.

Finally, as previously explained in Section 2.5.1, the inertial effect of damping force should be taken into account depending on the the Reynolds number R_e , which is given as

$$R_e = \frac{\rho\omega d^2}{\mu_{eff}} \quad (5.15)$$

where ρ is the air density at the operating temperature and pressure of 298 K and 1 atm and equal to $1.16e - 18\ \text{kg}/\mu\text{m}^3$, d is the air gap thickness in drive combs, tuning combs and sensing parallel

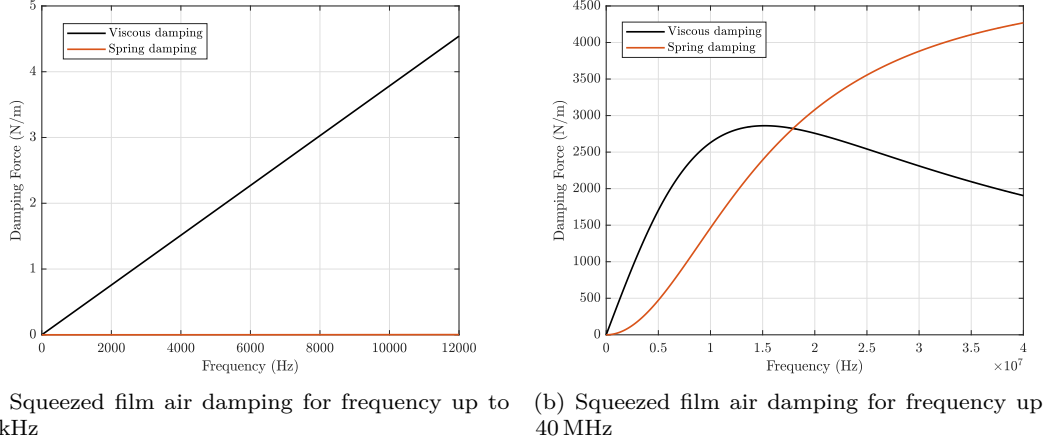


Figure 5.10: Effect of oscillation frequency on squeeze film air damping.

plates, respectively equal to $y_{0(d)}$, $y_{0(t)}$ and d_1 , and ω is the operating frequency. For low values of Reynolds number i.e., $R_e \ll 1$, the inertial effects are very small and hence can be neglected. For the proposed MEMS gyroscope R_e value is equal to 0.0459 and this shows that the inertial effect of the damping force is in practice negligible.

5.3 Analytical model results

The major aim of the analytical model previously presented is determining the design parameters which allow to respect SOIMUMPs fabrication process constrains and guarantee the resonant frequency values matching condition. Considering that the device is modeled as a two degrees-of-freedom system, a static and dynamical analyses are carried out. The results of the analytical model are provided and discussed in the following paragraphs of this section, while a comparison with FEM simulations results will be provided in Section 5.6.

5.3.1 Static analysis

If the electrostatic actuation force is constant in time, all the time derivatives in Equations 5.1 are set equal to zero

$$\begin{aligned}\ddot{x} &= \dot{x} = 0 \\ \ddot{y} &= \dot{y} = 0\end{aligned}\tag{5.16}$$

Thus, according to Equation 5.1, it is possible to evaluate the static response of the system in the drive direction as

$$x = \frac{F_d}{k_x}\tag{5.17}$$

The electrostatic actuation force F_d can be computed using the expression of Equation 5.4. Figure 5.11 shows the displacement in the drive direction x obtained with an increasing bias tension V_{DC} value applied to one of the two fixed combs attached to the external anchors.

As expected, a higher voltage value leads to a higher static deflection. It is important to highlight that static analysis is useful to estimate the stiffness of the overall MEMS gyroscope structure and then, compare it with the one resulting from the FEM model simulation.

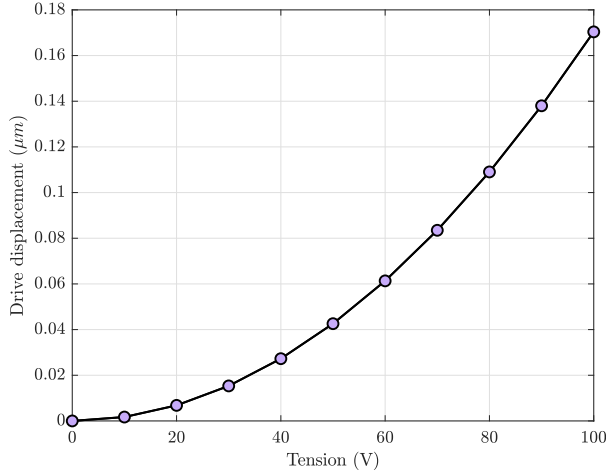


Figure 5.11: Analytical static displacement in the drive direction for the proposed dual mass MEMS gyroscope design.

5.3.2 Modal analysis

As explained at the beginning of this chapter, since the mismatch between drive and sense resonant frequency values determines the performance of the MEMS gyroscope device, the modal analysis plays a key role in the design phase. Rewriting the second-order differential equations of motion 5.1 for the proposed MEMS gyroscope in a matrix form, the free motion in the undamped condition is described by

$$\begin{bmatrix} m_d & 0 \\ 0 & m_s \end{bmatrix} \begin{Bmatrix} \ddot{x} \\ \ddot{y} \end{Bmatrix} + \begin{bmatrix} k_x & 0 \\ 0 & k_y \end{bmatrix} \begin{Bmatrix} x \\ y \end{Bmatrix} = \begin{Bmatrix} 0 \\ 0 \end{Bmatrix} \quad (5.18)$$

As previously discussed in Section 3.1.2, for the calculation of the resonant frequency values corresponding to the drive and sense modes, namely respectively ω_d and ω_s , the eigenvalue problem expressed in Equation 3.8 should be solved. Since the device is modelled by a two degrees-of-freedom system and all the matrices are in a diagonal form, the calculation of the eigenvalue problem easily leads to the following expressions

$$\begin{aligned} \omega_d &= \sqrt{\frac{k_x}{m_d}} \\ \omega_s &= \sqrt{\frac{k_y}{m_s}} \end{aligned} \quad (5.19)$$

If the electrostatic tuning effect, which will be discussed in detail in Chapter 6, is not considered, the stiffness value k_y corresponds to the mechanical stiffness expressed by Equation 5.3. Table 5.9 lists the obtained resonant frequency values for the proposed MEMS gyroscope design.

It is important to highlight that, the resonant frequency value of the sense mode is designed slightly greater than the drive one as the electrostatic tuning will be implemented to compensate for the frequency mismatch between the drive and sense mode frequencies due to microfabrication process tolerances and device operating temperature variations.

Mode	Symbol	Value	Unit
Drive	ω_d	11348.1	Hz
Sense	ω_s	11757.1	Hz

Table 5.9: Analytical resonant frequency values of the proposed dual mass MEMS gyroscope design.

5.3.3 Harmonic analysis

The analysis of the dynamical behaviour of the proposed MEMS gyroscope should include a frequency response analysis with the aim of determining the frequency behaviour of the device and, at last, its mechanical sensitivity. When the electrostatic actuation force F_d in Equation 5.1 is harmonic, the dynamic of the MEMS gyroscope system is the one of a single degree-of-freedom oscillator both in the drive and sense direction. Therefore, the dynamic of the drive mass in the x-direction is governed the following equation

$$m_d \ddot{x} + c_x \dot{x} + k_x x = F_d \quad (5.20)$$

Considering a balanced actuation scheme, the electrostatic actuation force F_d varies harmonically and is expressed as

$$F_d = 4N_d \frac{\epsilon_0 t}{y_{0(d)}} V_{DC} V_{AC} \sin(\omega t) = F_0 \sin(\omega t) \quad (5.21)$$

where ω is the excitation frequency. According to the discussion stated in Section 2.2.1, the drive-mode steady-state response becomes

$$x = X_d \sin(\omega t + \phi_d) \quad (5.22)$$

where X_d and ϕ_d are the amplitude and the phase of the drive-mode response, respectively expressed by the two following expressions

$$X_d = \frac{F_0/k_x}{\sqrt{\left[1 - \left(\frac{\omega}{\omega_d}\right)^2\right]^2 + \left[\frac{1}{Q_d} \frac{\omega}{\omega_d}\right]^2}} \quad (5.23)$$

$$\phi_d = -\arctan \left[\frac{\frac{1}{Q_d} \frac{\omega}{\omega_d}}{1 - \left(\frac{\omega}{\omega_d}\right)^2} \right] \quad (5.24)$$

where Q_d is the drive-mode quality-factor, which is a function of the damping coefficient in the drive direction c_x

$$Q_d = \frac{m_d \omega_d}{c_x} \quad (5.25)$$

In Figure 5.12, the response of the drive mass is plotted in terms of magnitude and phase. The displacement of the drive mass X_d along the x-direction is normalized with respect to the driving force amplitude F_0 . As expected, the system amplifies the response at the driving frequency with a factor of 16.13. In addition, at the resonant frequency, the phase is -90° shifted from the excitation force phase. At frequency lower than the resonant frequency, the phase approaches 0° meaning that the solution follows the excitation force closely. At frequency higher than the resonant frequency, the phase approaches to -180° .

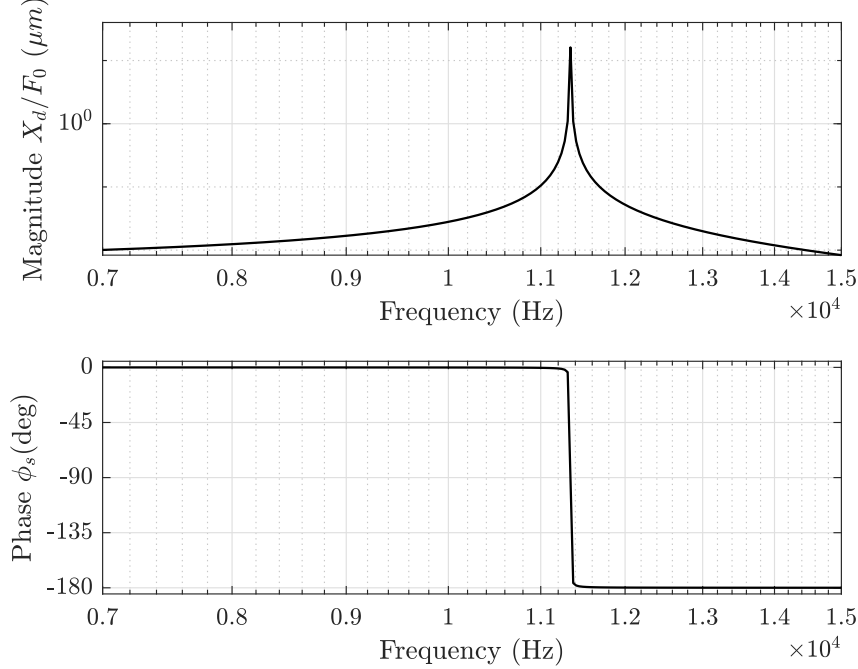


Figure 5.12: The analytical frequency response in the drive direction for the proposed dual mass MEMS gyroscope design (*logarithmic scale*), normalized with respect to the driving force amplitude F_0 .

When an angular velocity Ω_z is applied in the z-direction, the drive and sense mode are coupled by the Coriolis force. In this case, also the sense mass dynamics in the y-direction is governed by the equation of motion of a single degree-of-freedom oscillator as follows

$$m_s \ddot{y} + c_y \dot{y} + k_y y = -2m_d \Omega_z \dot{x} \quad (5.26)$$

According to the discussion previously exposed in Section 2.2.2, the sense-mode steady-state response becomes

$$y = Y_d \sin(\omega t + \phi_s) \quad (5.27)$$

where Y_d and ϕ_s are the amplitude and the phase of the sense-mode response, respectively expressed by the two following expressions

$$Y_d = \Omega_z \frac{m_d \omega}{m_s \omega_s^2} \frac{2X_d}{\sqrt{\left[1 - \left(\frac{\omega}{\omega_s}\right)^2\right]^2 + \left[\frac{1}{Q_s} \frac{\omega}{\omega_s}\right]^2}} \quad (5.28)$$

$$\phi_s = -\arctan \left[\frac{\frac{1}{Q_s} \frac{\omega}{\omega_s}}{1 - \left(\frac{\omega}{\omega_s}\right)^2} \right] + \phi_d - 90^\circ \quad (5.29)$$

where Q_s is the sense-mode quality factor, which is a function of the damping coefficient in the sense direction c_y

$$Q_s = \frac{m_s \omega_s}{c_y} \quad (5.30)$$

Figure 5.13 shows the response of the sense mass in terms of magnitude and phase. The displacement of the sense mass Y_d along the y-direction is normalized with respect to the driving force amplitude F_0 . If no external angular velocity is applied to the system, no displacement in the sense direction occurs. On the contrary, when a constant angular velocity is applied in the z-axis, the displacement Y_d presents two distinct resonant peaks, as the resonant frequency values in the drive and sense direction are slightly different. Each resonant peaks gives -180° of phase shift. The decreasing of the phase is more abrupt for the drive mode as the corresponding damping coefficient is higher than the one of sense mode.

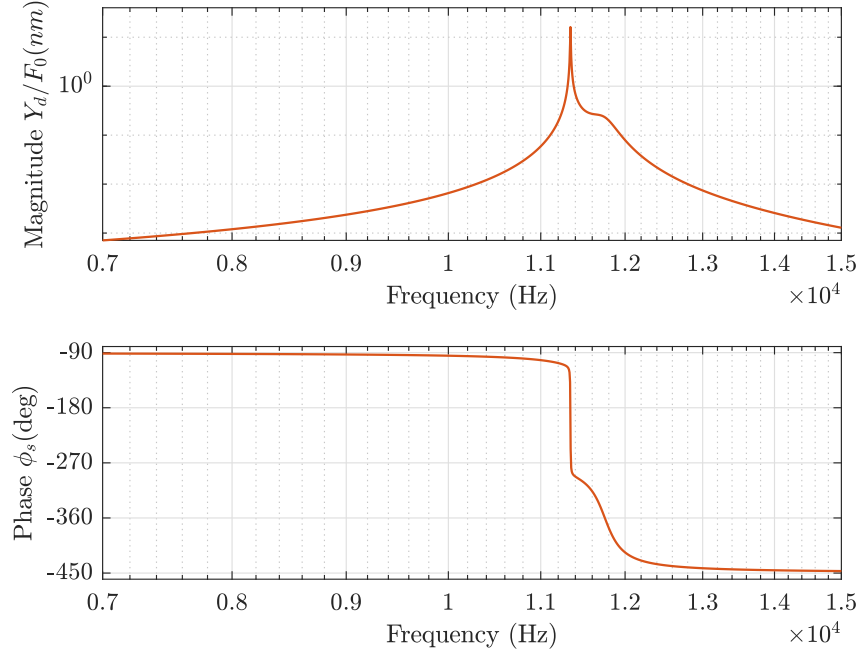


Figure 5.13: The analytical frequency response in the sense direction for the proposed MEMS gyroscope design (*logarithmic scale*), normalized with respect to the driving force amplitude F_0 , with $\Omega_z = 300^\circ/\text{s}$.

5.4 FEM Model

During the design steps, the analytical model results are used to verify that the chosen design parameters respect SOIMUMPs microfabrication process constrains and give the required dynamical characteristic, i.e. sense resonant frequency slightly larger than drive one. The analytical results of the proposed MEMS gyroscope design should be verified through FEM based simulations in Ansys. The FEM model is built following the procedure discussed in Chapter 3.

5.4.1 Structural mesh

The MEMS gyroscope mechanical structure proposed in this thesis project is composed by two masses, the drive mass end the sense frame, four and eight mechanical suspension beams in the drive and sense direction, respectively. With the purpose of optimizing as much as possible the required computational resources, the main idea for the element choice is using lower dimension elements, modeling only the moving parts of the structure. Therefore, the drive mass and sense frame are meshed using Shell181 elements, while Beam188 elements are adopted to model the suspension systems, the moving comb-drive fingers, the tuning-comb fingers and the sense parallel plates. A detailed description about elements used for the structural mesh of the proposed MEMS gyroscope was provided in Section 3.2.1. Figure 5.14 shows the meshed FEM model of the MEMS gyroscope mechanical structure.

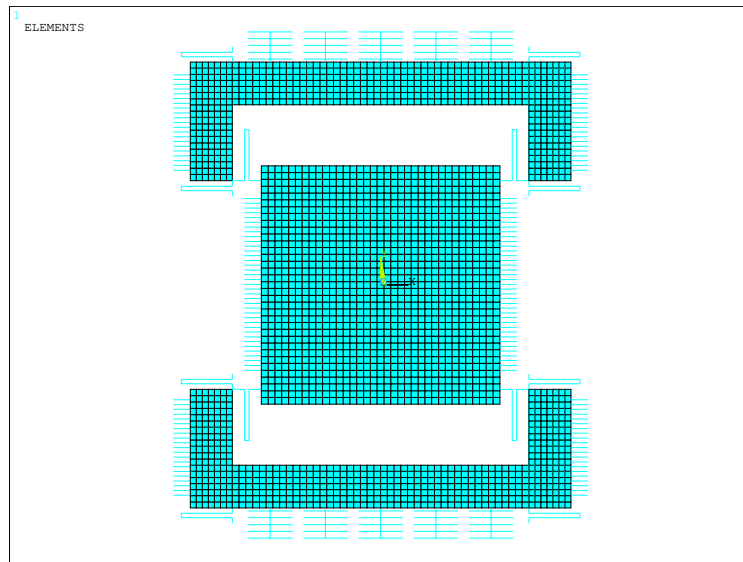


Figure 5.14: Meshed FEM model of the MEMS gyroscope mechanical structure.

It is important to point out that, the *rotz* stiffness of Shell181 elements is an artificial value. Shell181 elements actually rely on in-plane shear stiffness to resist in-plane twisting moments. Accordingly, when beam and shell elements are bounded together, relying on the default *rotz* stiffness of Shell181 elements introduces its own approximation to the stiffness, which is not a good approximation. Accordingly, it is inconsistent to connect only one node of a Beam188 element to a Shell181 element such that a rotational degree of freedom of the beam element corresponds to the *rotz* of the shell element. Constraint equations are used to couple the *rotz* degree of freedom of the single nodes shared by the Beam188 and Shell181 elements with the in-plane translations degrees of freedom, namely *ux* and *uy*, of adjacent shell element nodes. Finally, fixed supports are added at the end of sense spring beams connected to the external anchors. Figure 5.15 shows the overall boundary conditions and constraint equations applied to the mechanical structure of the MEMS gyroscope, while details of constraint equations applied to mechanical spring beams, comb-drive moving fingers, moving sensing parallel-plates and electrostatic tuning-comb fingers are provided in Figure 5.16a,b,c and d, respectively.

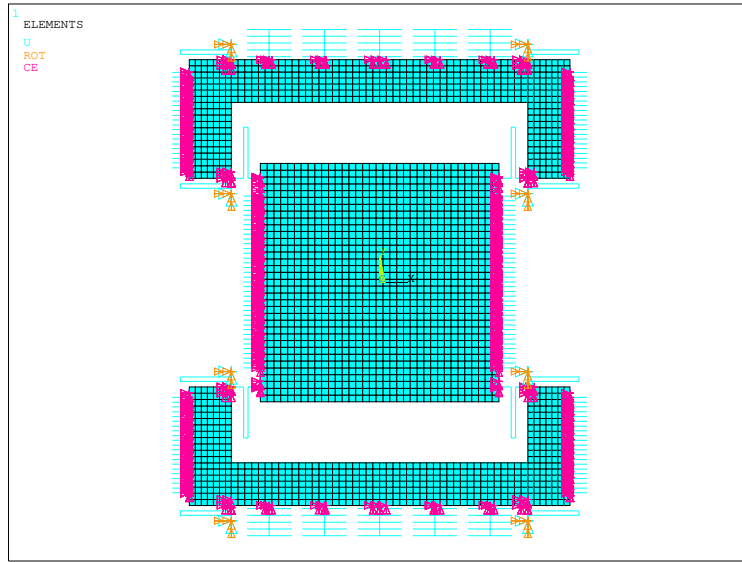


Figure 5.15: Boundary conditions and constraint equations applied to the mechanical structure of the dual mass MEMS gyroscope.

5.4.2 Damping modelling

In resonant MEMS gyroscopes, as the one proposed in this thesis project, the accurate modelling of the viscous air damping is very critical since it affects the overall quality factor and hence the mechanical sensitivity. Through the analytical model, damping coefficient values in drive and sense directions c_x and c_y are computed. Air viscous damping effect is therefore directly included in Ansys model based on the analytical estimation.

As previously discussed in Section 3.3.2 there are several methods to include damping in Ansys. The one adopted here is using a special element type having viscous damping characteristics, i.e. Combin14 element. The damping coefficients related to the drive and sense mode are specified directly input the corresponding values as real constants of the element. Real constants relating to stiffness values are instead set to zero, as the suspension systems are modelled. Relying on the lumped mass-spring damper model representation shown in Figure 5.4, at least two Combin14 elements should be used: an element oriented according to the x-axis and connecting the drive mass and sense frame is used to model damping in the drive direction, while sense damping is represented by an element oriented according to the y-axis and connecting the sense frame with the external anchors. It is crucial to obtain a reliable modeling of damping effects that Combin14 and Shell181 elements are bounded together by connecting the two contact nodes. To coupling the degrees of freedom along x and y directions, CP command is used. An alternative is instead using the same constrains equations that are adopted to couple Beam188 and Shell181 elements.

Figure 5.17 shows a detail of Combin14 elements inserted in the FEM model in Ansys, while boundary conditions applied to these elements are represented in Figure 5.18a and Figure 5.18b.

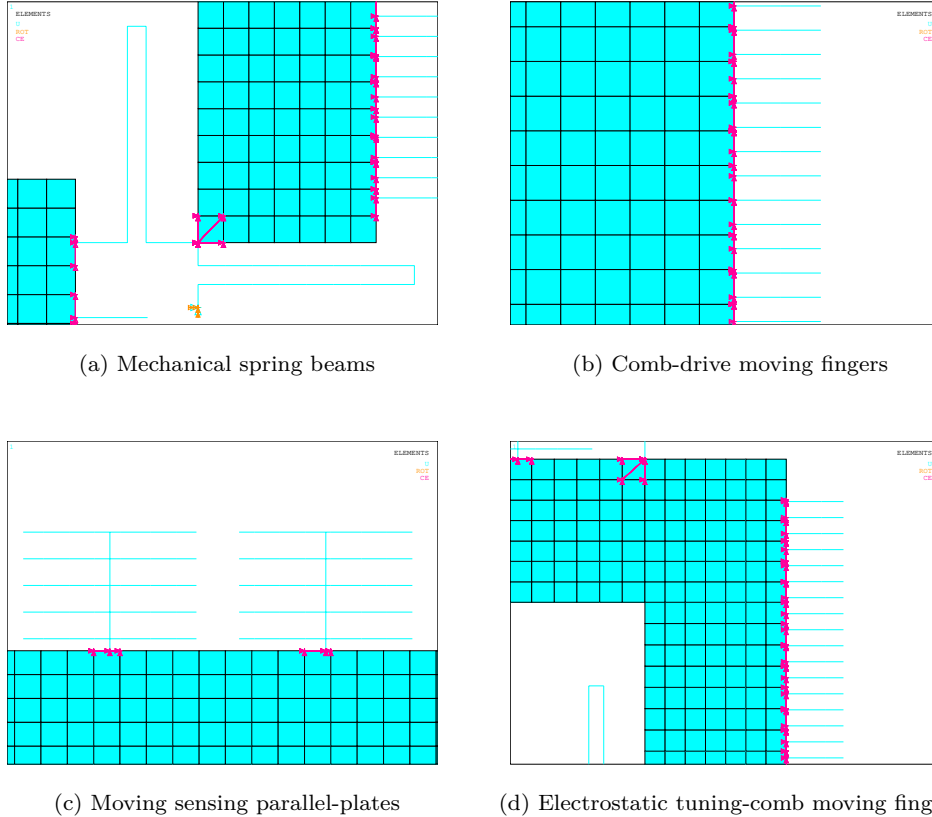


Figure 5.16: Details of constraint equations to couple Beam188 and Shell181 elements of the FEM model for the MEMS gyroscope mechanical structure.

5.4.3 Electromechanical coupling modelling

As previously described, the MEMS gyroscope device proposed in this thesis project is electrostatically actuated by comb drive-based actuators attached to the both sides of the drive mass. Since each couple of moving fingers forms a pair of parallel plates, comb drive-based actuators are modelled as series of capacitors. Only moving fingers are modelled using Beam188 elements, while the fixed ones are represented adding fixed constraints in the FEM model. The one-dimensional transducer Tran126 elements are used to model the capacitance of comb drive-based actuators. Two elements are connected at the end of each moving finger, while all degrees of freedom of nodes connected to the fixed fingers are fixed. An electromechanical coupling is thus realized between a distributed mechanical domain and a lumped electrical one. A clarifying scheme and the setup of Trans126 elements in the FEM model for the proposed MEMS gyroscope are respectively shown in Figure 5.19a and 5.19b.

The Trans126 element has up to two degrees-of-freedom at each node, namely: the translation in the nodal x , y or z -direction and the electric potential. This makes it possible to represent the capacitive response of a structure to a movement in one direction. In addition, a null electrostatic potential is specified for nodes attached to moving fingers, while the electrostatic potential of fixed nodes is equal to the actuation voltage. In this chapter, only the electromechanical coupling between comb-drive fingers is analyzed, while the one between electrostatic tuning-combs finger

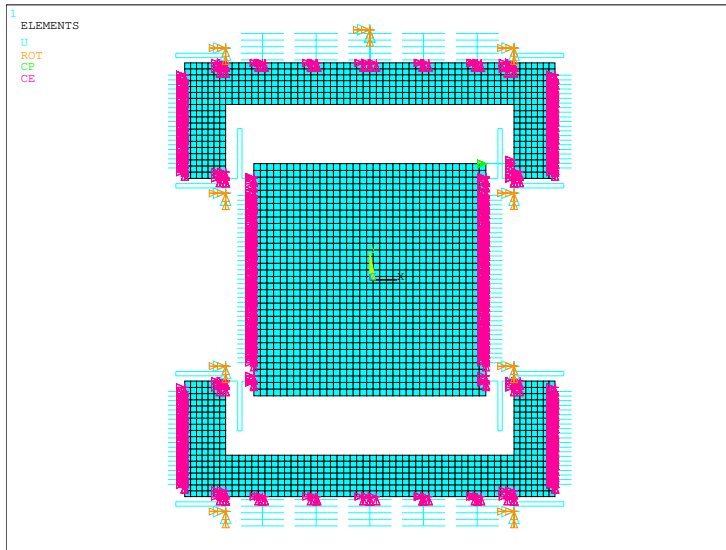


Figure 5.17: Combin14 elements in FEM model for the MEMS gyroscope mechanical structure.

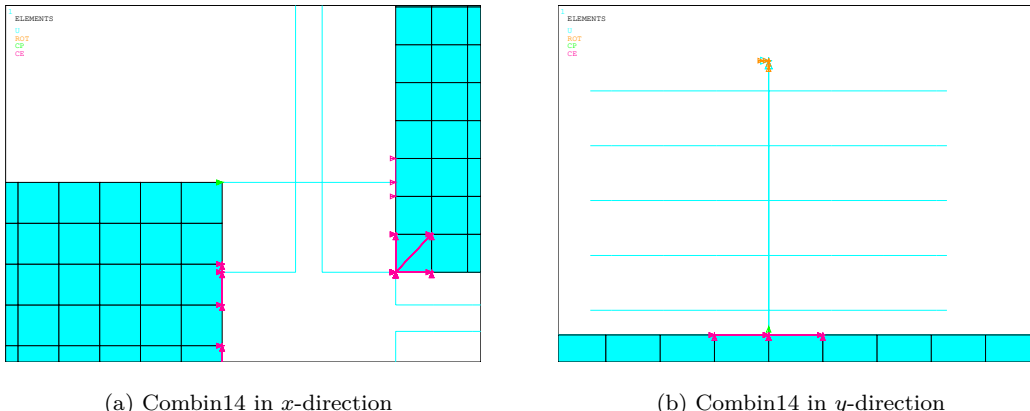


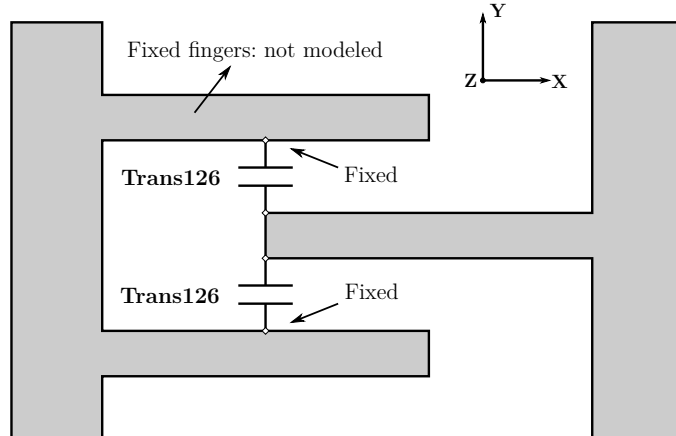
Figure 5.18: Details of boundary conditions applied to Combin14 elements.

will be discussed in Chapter 6.

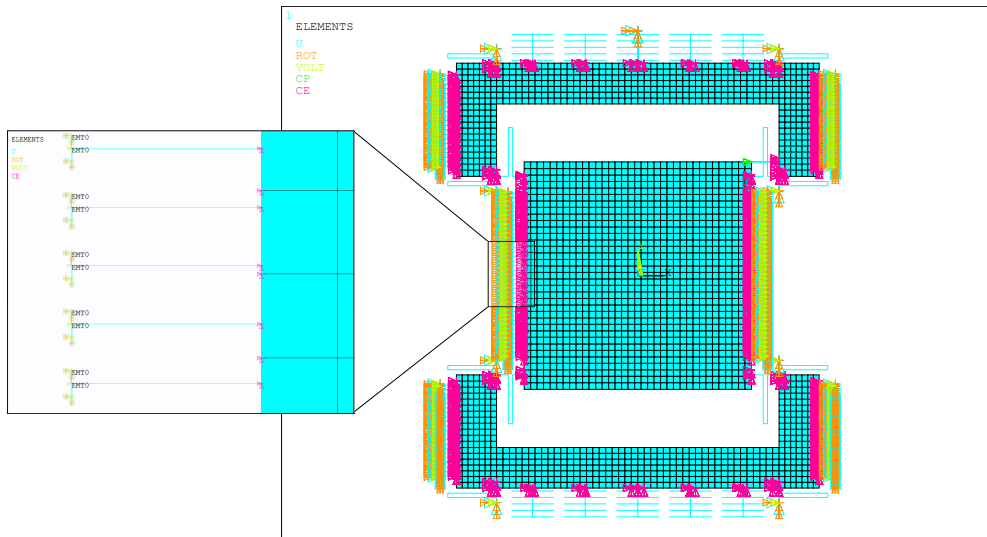
If the indefinite capacitor theory can be reasonably considered valid, i.e. if the fringing field effect can be neglected as the gap between fingers is small enough, the capacitance between comb-drive fingers is a function of he drive-displacement x . Accordingly, the capacity characteristics of the elements connected to the comb-drive fingers is a polynomial function of the x-displacement

$$C(x) = \frac{x_{0(d)}}{y_{0(d)}} \epsilon_0 t(\pm) \frac{x}{y_{0(d)}} \epsilon_0 t \quad (5.31)$$

where the sign + or - respectively depends on whether the capacity increases or decreases with according to the displacement in the x -direction. Polynomial coefficients of Equitation 5.31 are



(a) Trans126 pictorial scheme



(b) Trans126 elements in the FEM model with detail of boundary conditions

Figure 5.19: Setup of Trans 126 elements for FEM based electrostatic analysis.

assigned directly to Trans126 elements as real constants.

5.5 FEM model results

During the design process of a generic MEMS gyroscope device, an accurate prediction of the sensor behaviour is ensured by FEM model based analyses. Accordingly, the MEMS gyroscope design proposed in this thesis project is simulated in Ansys. The static analysis is carried out to determine the effective stiffness of the system, while the dynamical behaviour is analyzed through modal and harmonic analysis. A comparison with analytical model results is finally necessary to verify that the devices performance is the one expected.

5.5.1 Static analysis

The static analysis gives the response of the structure to a static load and is important to estimate the stiffness of the overall MEMS gyroscope structure. A DC tension is therefore applied to one of the two comb-drive structure attached to the drive mass and a comparison with analytical results is made. The structure deflection in x-direction for an increasing value of DC tension applied is shown in Figure 5.20. FEM model matches very well the analytical one at lower voltage values, which correspond to smaller displacements. As the x deflection gets larger compared to the beam dimensions, the analytical model results are slightly different from the Ansys ones. In the analytical model, the total stiffness in the x direction was approximated by the sum of all flexures stiffness values in that direction, assuming that the compliance of the drive mass, sense frame and spring beams in that direction is negligible. In reality, as shown in Figure 5.20, these factors slightly reduce the overall stiffness values. For this reason, modal analyses in Ansys is absolutely necessary for accurate estimation and design of resonant frequencies.

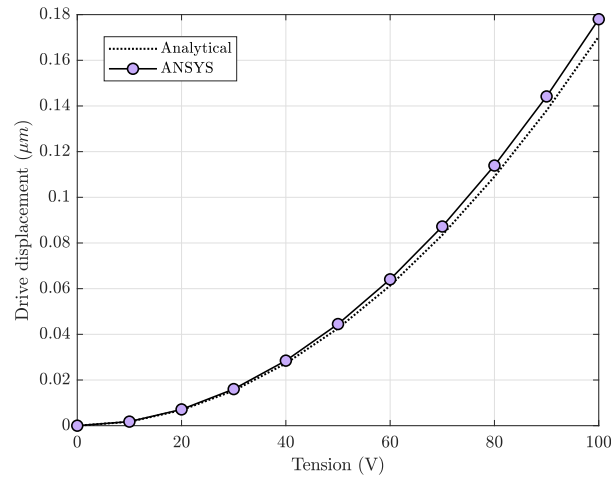


Figure 5.20: Comparison between analytical and Ansys static displacement in the drive direction for the proposed dual mass MEMS gyroscope design.

5.5.2 Modal analysis

To determine the resonant frequency values and corresponding mode shapes for the MEMS gyroscope, a FEM-based modal analysis is carried out in Ansys. Since the electrostatic tuning effect is not analyzed in this chapter, a prestressed modal analysis is not necessary. In figure 5.21, the first four mode shapes of the MEMS gyroscope are shown. The first mode of the structure (Figure 5.21a) is related to drive-mode, in which only the drive mass is moving along the x-direction and the spring beams which connect it to the sense frame are bending in the same direction. This mode implies a purely in-plane deformation of the structure. Similarly, the second mode is described by an in-plane motion and is related to the sense-mode (Figure 5.21b). Indeed, when the device is subjected to an external angular velocity in the z-direction, the sense frame moves together with the drive mass in the y-direction due to the Coriolis force. The third (Figure 5.21c) and fourth (Figure 5.21d) modes are associated to the tilting of the mass and do not affect the operation of the gyroscope. These modes are called spurious modes.

Table 5.10 compares the FEM-based modal analysis results related to the drive and sense mode

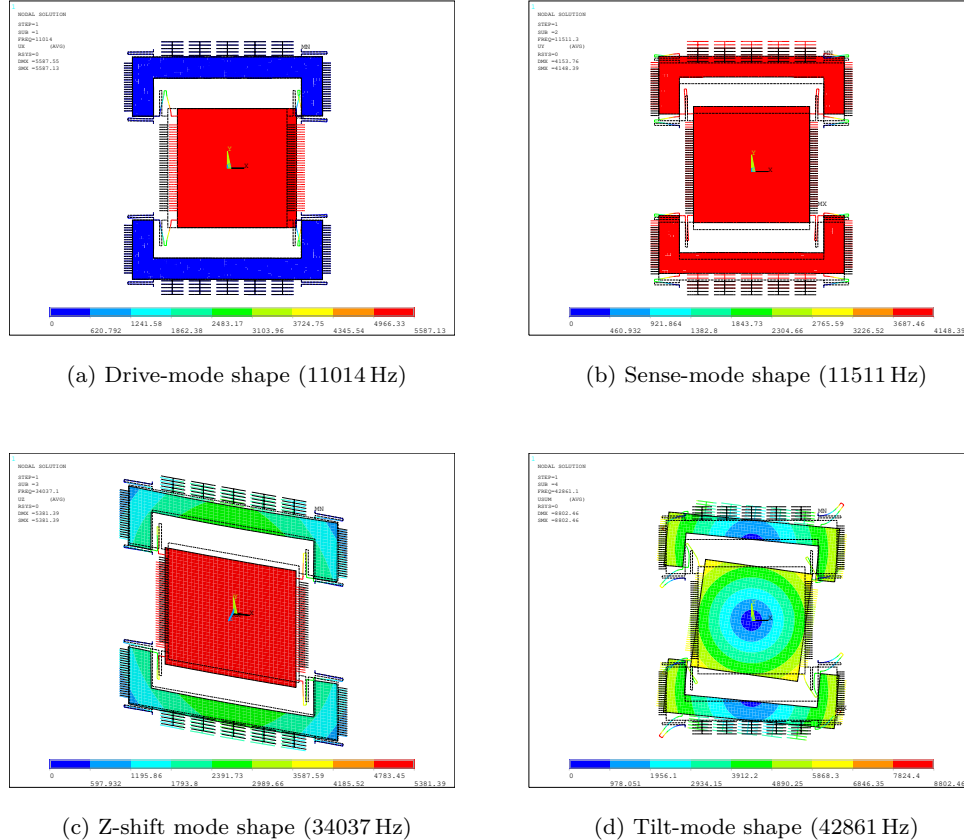


Figure 5.21: Modal analysis results and the corresponding mode shapes for the proposed dual mass MEMS gyroscope (a) 1st mode (11014 Hz) (b) 2nd mode (11511 Hz) and (c) 3rd mode (34037 Hz) and (d) 4th mode (42861 Hz).

with the analytical model ones, which shows a small difference. This is mainly due to the fact that the analytical model does not exactly estimates the stiffness of suspension beam systems.

Mode shape	Analytical Hz	Ansys Hz	Error (%)
Drive	11348	11014	-2.94
Sense	11757	11511	-2.09

Table 5.10: Comparison of the analytical and FEM-based modal analysis results related to the drive and sense mode.

It is important to highlight that a slight difference between resonant frequency values related to the drive and sense mode is necessary as the electrostatic tuning will be applied for the compensation of the frequency mismatch between the drive and sense mode frequency due to microfabrication process tolerances and device operating temperature variation.

5.5.3 Harmonic analysis

The analysis of the dynamical behaviour of the proposed MEMS gyroscope should include a frequency response analysis with the aim of determining the frequency behaviour of the device and, at last, its mechanical sensitivity. A harmonic force is applied to the drive mass along the x -axis by applying an actuation voltage of 50 V DC and 5 V AC to comb drive-based actuators. The analysis is performed considering the air damping effect previously estimated through the analytical model. As described in section 3.3.3, since the AC voltage values is small compared to the DC one, nonlinear effects caused by the electromechanical coupling can be neglected and a prestressed harmonic analysis can be performed to analyze the device harmonic behaviour. Accordingly, a static analysis with the applied DC voltage is first performed, followed by a prestressed full harmonic analysis with the applied AC excitation.

Figure 5.22 shows the obtained frequency response of the structure in the drive direction in terms of magnitude and phase. In the drive direction the system behaviour is the one of single degree-of-freedom. As already shown for the analytical model, the drive mass displacement is amplified at the driving frequency. In addition, at the resonant frequency, the phase is -90° shifted from the excitation force phase. At frequency lower than the resonant frequency, the phase approaches 0° meaning that the solution follows the excitation force closely. At frequency higher than the driving frequency, the phase approaches to -180° . A comparison between FEM-based harmonic analysis and analytical results in the drive direction is instead provided in Figure 5.24. As it was shown in Table 5.10, analytical and FEM-based modal analysis provided slightly different resonant frequency values. Consequently, the frequency response in the drive direction obtained through Ansys simulation is shifted in frequency compared with the one obtained analytically.

The frequency response in the sense direction is obtained by applying to the device an angular velocity Ω_z of $300^\circ/s$ and the electrostatic actuation force. In this case, the drive and sense mode are coupled by the Coriolis force and the sense mass dynamics in y -direction is the one of a single degree-of-freedom system. Figure 5.23 shows the obtained frequency response of the structure in the sense direction in terms of magnitude and phase. Since drive and sense resonant frequency values are slightly different, two resonant peaks are present, respectively equals to 41.09 nm and 0.62018 nm. As it will be discussed in Chapter 6, the resonant frequency mismatch causes the performance of the gyroscope to reduce dramatically as the even a slight mismatch can reduce the amplitude response of the mode matched gyroscope significantly. In addition, each resonant peak gives -180° of phase shift. The decreasing of the phase is more abrupt at frequency lower than the first resonant frequency, i.e the drive resonant frequency, as the damping coefficient in drive direction is higher than the one in sense direction. A comparison between FEM-based harmonic analysis and analytical results in the sense direction is instead provided in Figure 5.25. As it was already shown for the drive response, the slight difference between analytical and FEM-based modal analysis resonant frequency values leads to a shift in the sense frequency response obtained through Ansys simulation compared with the one obtained analytically. Finally, Table 5.11 and 5.12 compare the frequency response amplitudes at resonance of the drive and sense mode obtained through the FEM-based harmonic and analytical analysis, which shows a close correspondence.

Model	Magnitude	Unit
Analytical	44.03	μm
Ansys	46.93	μm
Error	6.6349	(%)

Table 5.11: Comparison of the analytical and FEM-based harmonic analysis results related to the drive resonant frequency.

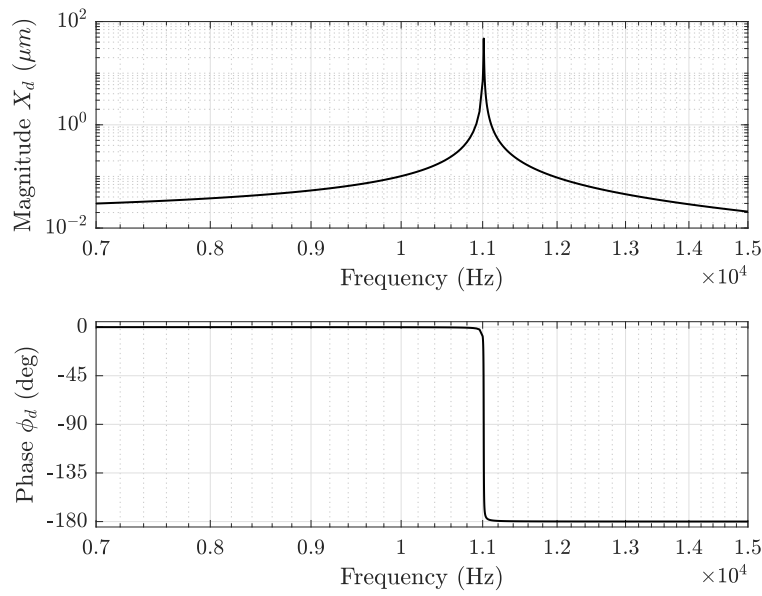


Figure 5.22: The FEM-based frequency response in the drive direction for the proposed dual mass MEMS gyroscope design (*logarithmic scale*), with $V_{DC} = 50$ V and $V_{AC} = 5$ V.

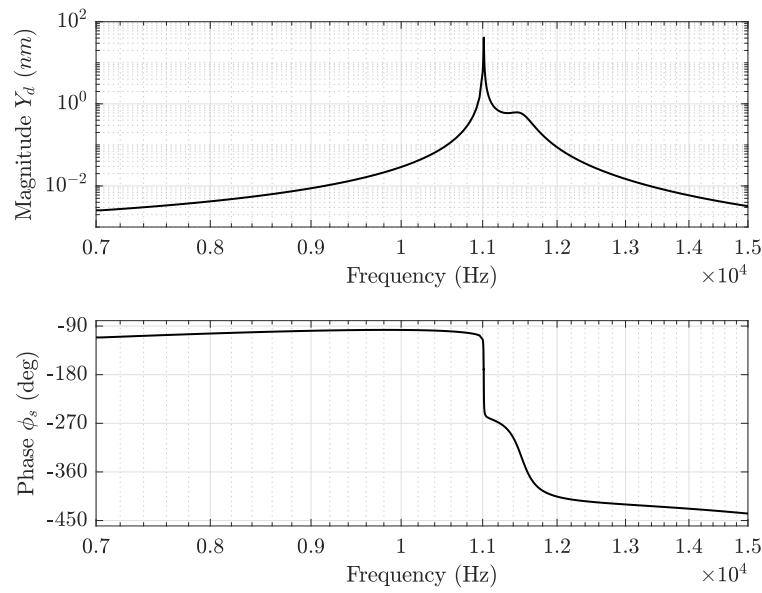


Figure 5.23: The FEM-based frequency response in the sense direction for the proposed dual mass MEMS gyroscope design (*logarithmic scale*), with $\Omega_z = 300^\circ/s$.

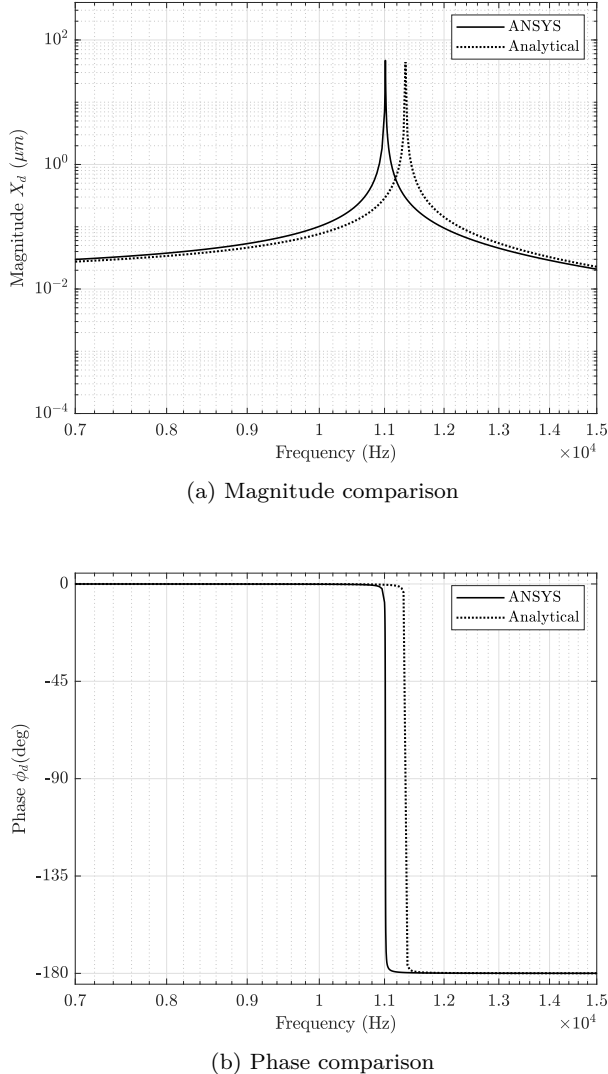
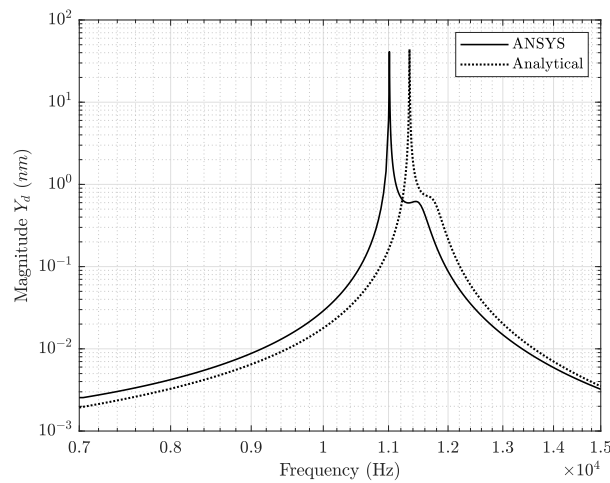


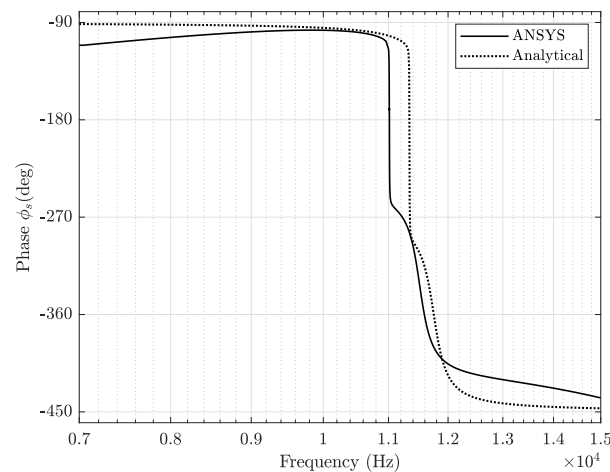
Figure 5.24: Comparison of the analytical and FEM-based harmonic analysis results in the drive direction (*logarithmic scale*), with $V_{DC} = 50\text{ V}$ and $V_{AC} = 5\text{ V}$ (a) Magnitude and (b) Phase.

Peak	Model	Magnitude	Unit
1	Analytical	44.04	nm
	Ansys	41.09	nm
	Error	-6.6985	(%)
2	Analytical	0.6268	nm
	Ansys	0.62	nm
	Error (%)	-1.0849	(%)

Table 5.12: Comparison of the analytical and FEM-based harmonic analysis results related to the sense resonant frequency.



(a) Magnitude comparison



(b) Phase comparison

Figure 5.25: Comparison of the analytical and FEM-based harmonic analysis results in the sense direction (*logarithmic scale*), with $\Omega_z = 300^\circ/s$ (a) Magnitude and (b) Phase.

Chapter 6

Electrostatic tuning

In the previous chapter the dual mass resonant MEMS gyroscope design developed in this thesis project has been introduced. For the compensation of the frequency mismatch between the drive and sense mode frequency due to microfabrication process tolerances and device operating temperature variations, comb-drive based electrostatic tuning is implemented in the design. The electrostatic tuning technology is based on the spring softening effect to change the stiffness of the structure electronically and, hence, to change the frequency. This method allows the designer to reduce the mismatch and to get the optimal performance of the gyroscope.

First the electrostatic tuning is modelled analytically, based on the models available in literature, then a FEM-based analysis is carried out to check the actual device behaviour subjected to a tuning electrostatic voltage. A preliminary automatic mode-matching closed-loop system control is then implemented in SIMULINK environment to tune automatically the sense mode frequency. The automatic control is realized based on the frequency response characteristic of the mass-spring oscillator related to the drive and sense mode. When the gyroscope structure is excited in the drive direction at the natural frequency and the drive and sense mode frequencies are perfectly matched, the vibration amplitude in the sense direction achieves its maximum value and the phase delay caused by the sense dynamic is 90° degree. Finally, the performance improvement is checked against operating temperature variations.

6.1 Analytical model

The main purpose of the MEMS gyroscope design proposed in this thesis project is to guarantee that drive and sense resonant frequency values are perfectly matched as this condition leads to high mechanical sensitivity and optimal performance. However, the major challenge faced during the MEMS resonant gyroscopes design phase is the fluctuation in the performance parameters of devices as they are easily affected by any variation in environment conditions and fabrication imperfections. Indeed, these imperfections can cause a shift in resonance frequency which in turn causes a mismatch between the drive and sense mode frequencies.

As shown in the previous chapter, for the compensation of the frequency mismatch between the drive and sense mode frequency due to microfabrication process tolerances and device operating temperature variations, comb-drive based electrostatic tuning is implemented in the design. This variable-gap capacitor structure allows to tune the resonant mode frequencies of the gyroscope by an adjustable DC potential, which relies on the effect of electrostatic spring softening previously discussed in Section 2.4.3. In particular, the sense mode resonant frequency is tuned to be almost identical to the drive mode resonant frequency by using the electrostatic tuning capability of the comb-drive based tuning structure. As it will be discussed in the following sections, the main

motivation behind this method is to achieve the mode-matching condition using a closed-loop automatic frequency control, which allows to automatically tune the sense mode resonant frequency based on the FEM simulation results.

The automatic mode-matching system control developed in this thesis project relies on an analytical modelling of the electrostatic tuning effect. In addition, a FEM-based modal analysis is used to validate the dynamical behaviour of the MEMS gyroscope design subjected to the tuning DC potential and, thus, to guarantee the actual achievement of the mode-matching condition. Figure 6.1 provides a pictorial scheme of this main idea behind the automatic mode-matching system control development.

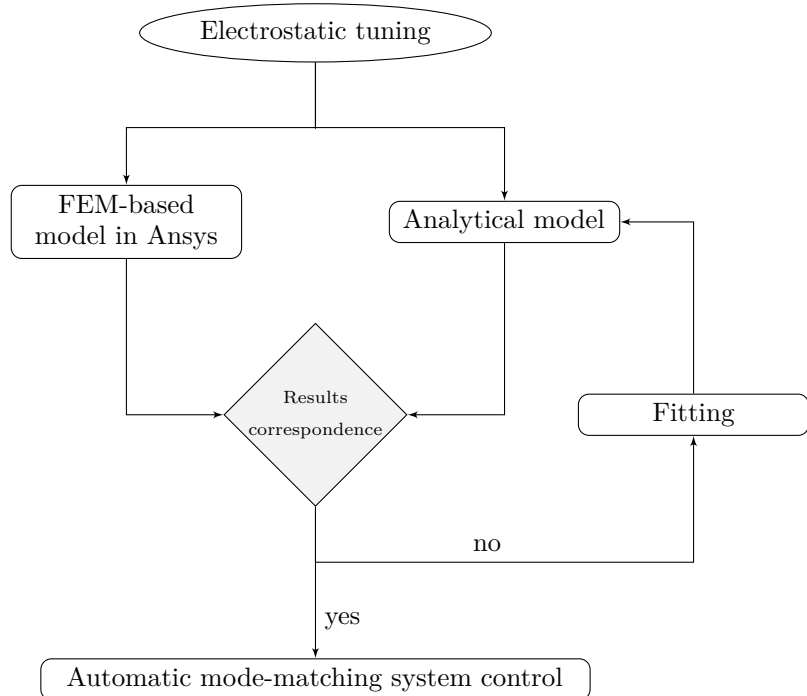


Figure 6.1: Scheme of the main idea behind the automatic mode-matching system control development.

The configuration scheme of comb-drives electrostatic tuning structure implemented in the MEMS gyroscope device to achieve the frequency matching between modes has been already provided in Figure 5.9. The tuning-comb varying-gap structures are attached to both sides of the sense frame and, considering that the sense-frame can move only in the sense direction, the comb-drive based tuning structures only affect the sense mode dynamics. Since design parameters of tuning-combs structures has been already shown in Table 5.6, the only aim of this section is modelling the electrostatic tuning effect.

Figure 6.2 shows a single tuning comb scheme as an example. For each moving finger, the sense frame displacement in the positive y-direction leads to an increase in the upper capacitance $C_{1(t)}$ and a decrease in the bottom capacitance $C_{2(t)}$ between the fixed and moving comb fingers,

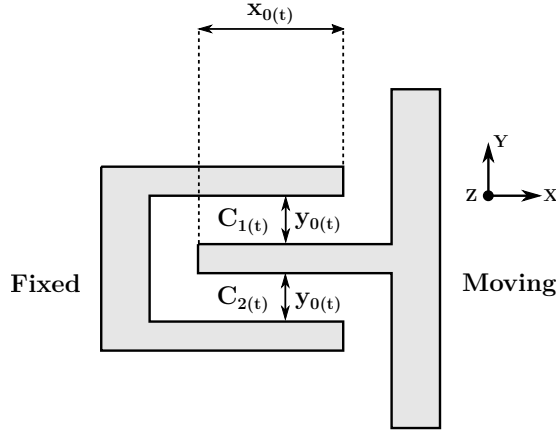


Figure 6.2: Configuration scheme of comb-drive based electrostatic tuning.

according to the following expressions

$$\begin{aligned} C_{1(t)} &= \frac{\epsilon_0 x_{0(t)} t}{(y_{0(t)} - y)} \\ C_{2(t)} &= \frac{\epsilon_0 x_{0(t)} t}{(y_{0(t)} + y)} \end{aligned} \quad (6.1)$$

where ϵ_0 is the free space permittivity, $x_{0(t)}$ is the overlap length, t is the structural thickness and $y_{0(t)}$ is the nominal gap. Consequently, each finger is subjected to two electrostatic forces, namely F_{el1} and F_{el2} , which can be expressed as follows

$$\begin{aligned} F_{el1} &= \frac{1}{2} \frac{\partial C_{1(t)}}{\partial y} V^2 = \frac{1}{2} \frac{\epsilon_0 x_{0(t)} t}{(y_{0(t)} - y)^2} V_t^2 \\ F_{el2} &= \frac{1}{2} \frac{\partial C_{2(t)}}{\partial y} V^2 = -\frac{1}{2} \frac{\epsilon_0 x_{0(t)} t}{(y_{0(t)} + y)^2} V_t^2 \end{aligned} \quad (6.2)$$

where V_t is the DC tuning tension applied to the fixed combs. Considering N_t moving fingers, the comb-drive based electrostatic tuning structures can be modeled as a series of capacitors. Accordingly, the total electrostatic force F_{el} can be obtained as

$$F_{el} = N_t (F_{el1} + F_{el2}) = \frac{N_t}{2} \left(\frac{\epsilon_0 x_{0(t)} t}{(y_{0(t)} - y)^2} - \frac{\epsilon_0 x_{0(t)} t}{(y_{0(t)} + y)^2} \right) V_t^2 \quad (6.3)$$

which is a nonlinear function of the y displacement. According to the passages described in Section 2.4.3, the electrostatic spring constant due to the force nonlinearity can be found by taking the derivative of the total electrostatic force F_{el} with respect to the y -displacement

$$k_{el} = \frac{\partial F_{el}}{\partial y} = -N_t V_t^2 \left(\frac{\epsilon_0 x_{0(t)} t}{(y_{0(t)} - y)^3} + \frac{\epsilon_0 x_{0(t)} t}{(y_{0(t)} + y)^3} \right) \quad (6.4)$$

Considering $y \ll y_{0(t)}$, Equation 6.4 becomes

$$k_{el} = -2N_t V_t^2 \frac{\epsilon_0 x_{0(t)} t}{y_{0(t)}^3} \quad (6.5)$$

Since the electrostatic spring constant is a negative quantity, it always reduces the resonant frequency value with increasing DC tension across the tuning electrodes. In addition, the electrostatic tuning force acts only in the y-direction and does not cause a change in the drive resonant frequency ω_d .

Equation 5.19, previously introduced in Chapter 5 and expressing the drive and sense mode resonant frequency values, can be then modified as follows

$$\begin{aligned} \omega_d &= \sqrt{\frac{k_x}{m_d}} \\ \omega_s &= \sqrt{\frac{k_y - k_{el}}{m_s}} = \sqrt{\frac{k_y - k_{el}}{m_s}} = \sqrt{\frac{k_y - 2N_t V_t^2 \frac{\epsilon_0 x_{0(t)} t}{y_{0(t)}^3}}{m_s}} \end{aligned} \quad (6.6)$$

According to Equation 6.6, the sense resonant frequency can be tuned by adjusting the tuning tension V_t applied to stationary electrodes, so that $\omega_s = \omega_d$ at certain voltage value. Therefore, the tuning voltage value guarantying the mode-matching condition is equal to

$$V_t = \sqrt{\frac{\frac{k_y}{m_s} - \omega_d^2}{\eta}} \quad (6.7)$$

where η coefficient is

$$\eta = \frac{2N_t \epsilon_0 x_{0(t)} t}{m_s y_{0(t)}^3} \quad (6.8)$$

Since the electrostatic tuning effect only influences the dynamical behaviour of the proposed MEMS gyroscope design, analytical modal and harmonic analyses are carried out. The results are provided in the following sections with a special focus on the electrostatic tuning application effect on the mechanical sensitivity of the device.

6.2 Analytical model results

In the previous chapter, the comparison between FEM-based modal and analytical analysis results has provided a slightly difference between resonant frequency values. In addition, as it was stated by Equation 6.7, the tuning tension V_t value only depends on the frequency mismatch between the drive and sense mode. This means that, considering resonant frequency values obtained through Ansys simulations rather than analytical ones leads to a different estimation of the tuning tension V_t value guarantying the mode-matching condition. Since the main focus of this chapter is the analysis of the electrostatic tuning effect, it is reasonable to adopt the resonant frequency values obtained from the FEM-based modal analysis to compute, by using Equation 6.7, the tuning tension V_t necessary to compensate the frequency mismatch.

According to Equation 6.6, Figure 6.3 shows the analytical frequency tuning characteristic of the drive and sense mode of the proposed MEMS gyroscope structure as a function of the tuning voltage V_t applied on the tuning electrodes. As expected, the drive mode resonant frequency value remains constant at 11014 Hz, while the sense resonant frequency value decreases by varying the tuning tension. The resonance mode frequencies are perfectly matched at the tuning tension V_t of 21.73 V, which will guarantee the highest theoretical mechanical sensitivity.

In order to analyze how the electrostatic tuning influences the dynamical behaviour of the proposed MEMS gyroscope device, a frequency response analysis should be performed. The drive and sense frequency response can be computed following the same procedure already discussed in Section 5.3.2.

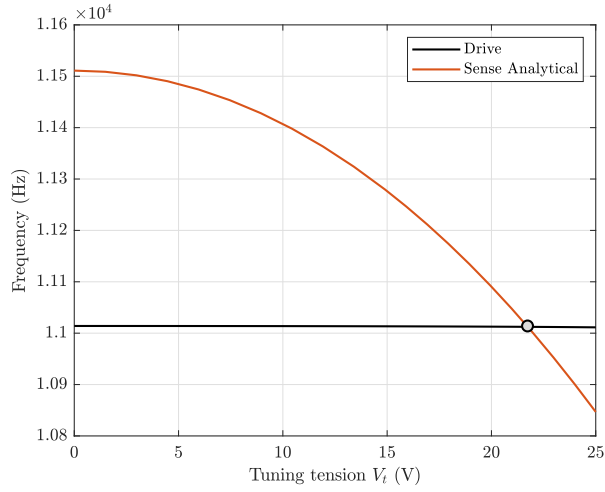


Figure 6.3: Analytical frequency tuning characteristics of drive and sense resonant modes as a function of the applied tuning tension V_t . The mode-matching condition (represented in grey) is achieved with $V_t = 21.73$ V.

The only differences are that, the sense resonant frequency could vary with the tuning tension V_t applied on the tuning electrodes and the equation of motion of single degree-of-freedom oscillators representing the drive and sense mode dynamics should be corrected considering frequency results of the FEM-based modal analysis presented in Chapter 5. In Figure 6.4, the response of the drive mass is plotted in terms of magnitude and phase. The displacement of the drive mass X_d along the x-direction is normalized with respect to the driving force amplitude F_0 . As expected, electrostatic tuning does not influence the drive response, which is amplified at the driving frequency with the same factor of 16.13, as in the case without tuning. Similarly, the phase decreases from 0° to -180° , assuming the value of -90° at the drive resonant frequency.

On the contrary, the frequency response in the sense direction is influenced by the electrostatic tuning effect. When the device is subjected to an angular velocity $\Omega_z = 300^\circ/\text{s}$ in the z-direction, the sense frame together the drive mass moves along the y-direction due to the Coriolis effect. Referring to Figure 6.5a, if no tension is applied to tuning-combs, the sense response has two distinct resonant peaks (represented in red in the plot). Instead, when the tuning tension $V_t = 21.73$ V, which guarantees the mode-matching condition, is applied on the stationary tuning electrodes, only one peak (represented in black on the plot) is present and the maximum possible gain is achieved. In addition, when resonant frequency values are matched, the phase, which is shown in Figure 6.5b, decreases continuously from -90° to -450° without changing the shape of the curve.

6.3 FEM model

In the previous Section it has been shown that, the analytical model, representing the dynamics of the MEMS gyroscope in the drive and sense direction, can be modified to take into account the spring softening effect. This effect is used to modify the stiffness of the structure electronically hence changing the resonant sense frequency and reduce the frequency mismatch. Since the automatic mode-matching control system developed in this thesis project to automatically tune the sense mode resonant frequency relies on this analytical model, it is necessary to check that the analytical model represents correctly the MEMS gyroscope behaviour. For this purpose, a FEM-based analysis should be carried out.

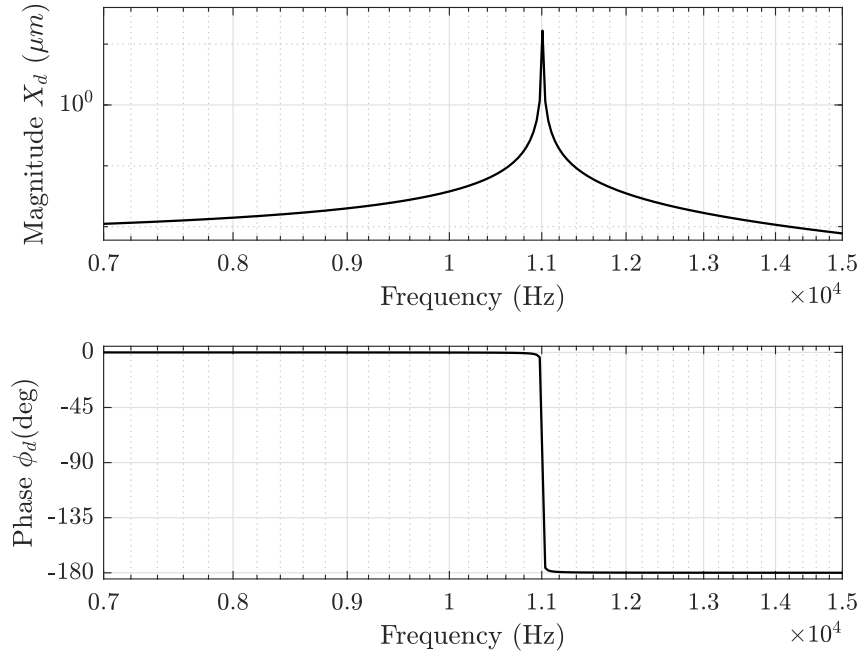
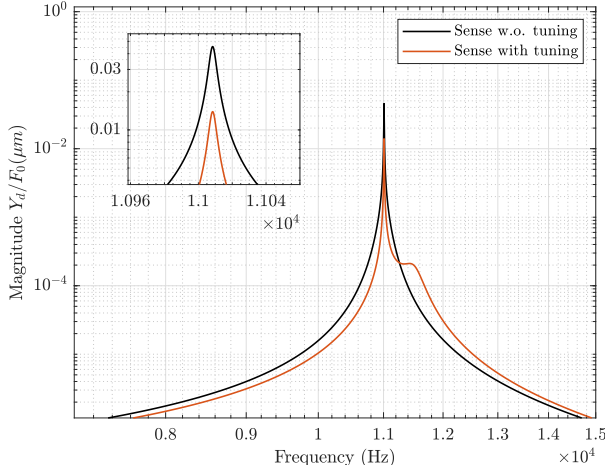


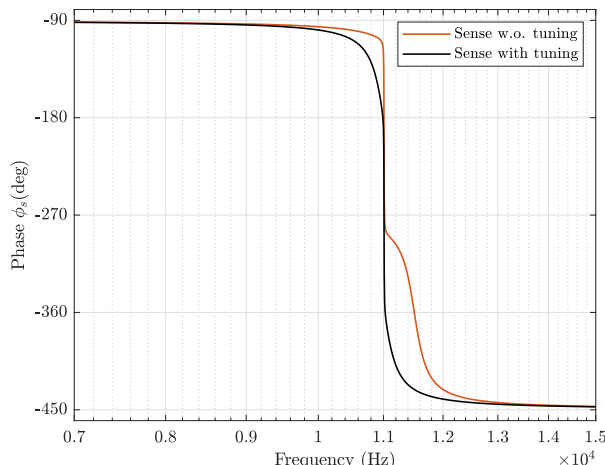
Figure 6.4: The analytical frequency response in the drive direction for the proposed dual mass MEMS gyroscope design with tuning application (*logarithmic scale*), normalized with respect to the driving force amplitude F_0 .

As it was shown in Chapter 5, the analytical model does not perfectly represent the dynamical behaviour of the proposed MEMS gyroscope device. This is principally caused by a slight error in the mechanical spring beams stiffness estimation, which results in a slight difference between resonant frequency values computed analytically and obtained through FEM-based modal analysis. However, this mismatch could be easily corrected simply taking into account in the analytical model the resonant frequency values deriving from the Ansys simulations. In addition, the electrostatic tuning used to change the sense stiffness of the structure and achieve the mode-matching condition relies on a nonlinear electrostatic force, which should be adequately computed. Accordingly, the coupling between the electrostatic field and the mechanical domain is simulated through a FEM-based analysis in order to investigate the validity of analytical model representation.

In Ansys, electrostatic tuning-combs can be modelled in the same way as for the comb drive-based electrostatic actuators previously described in Chapter 5. Since each finger of the moving tuning combs forms two parallel plates pairs, tuning combs can be modeled as a series of capacitors. Only moving fingers are modelled using Beam188 elements, while the fixed ones are represented adding fixed constraints in the FEM model. Capacitance between tuning comb fingers is modelled using one-dimension transducer Trans126 elements. Two elements are added at the end of each tuning comb finger, while all degrees of freedom of nodes connected to the fixed fingers are fixed. A generic Trans126 element has up to two degrees of freedom at each node: translation in the nodal x , y , or z -direction and electric potential. The structural displacement degree-of-freedom associated to Trans126 elements is the y -displacement: this makes it possible to fully characterize the coupled electromechanical response of the sense frame moving in the y -direction. In addition, a null electrostatic potential is specified for nodes attached to moving fingers, while the electrostatic



(a) Magnitude

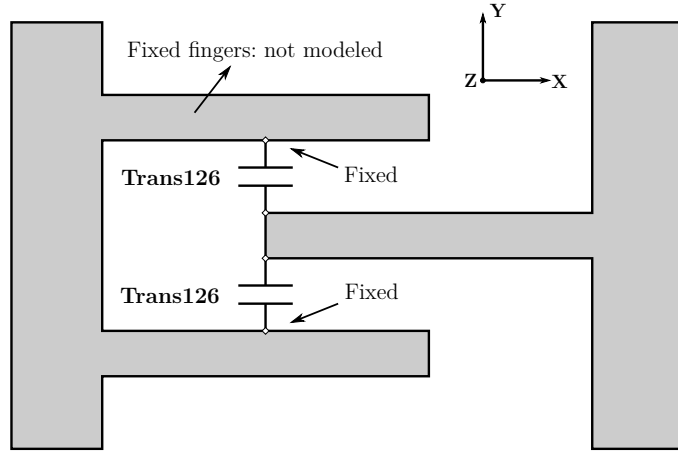


(b) Phase

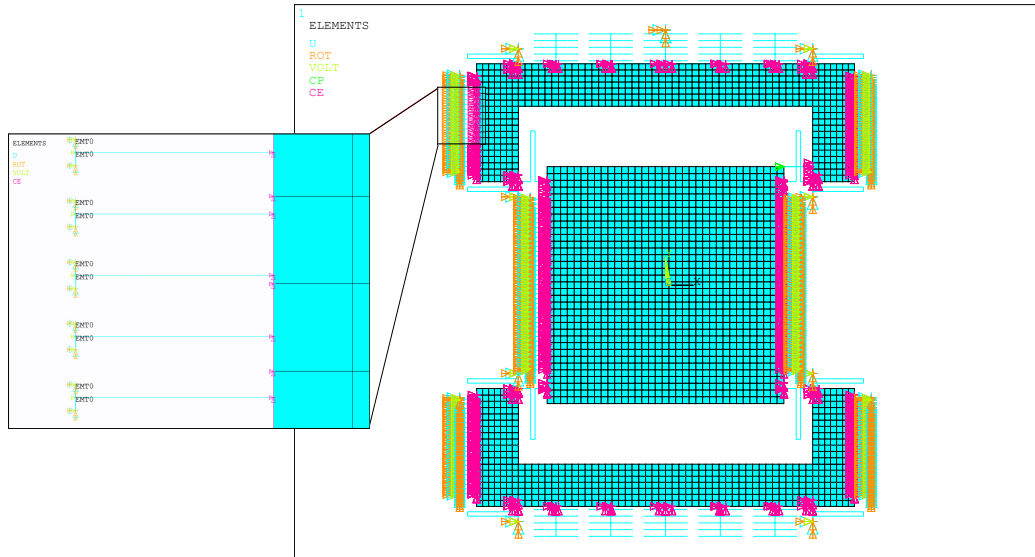
Figure 6.5: The analytical frequency response in the sense direction for the proposed dual mass MEMS gyroscope design (*logarithmic scale*), normalized with respect to the driving force amplitude F_0 , with $\Omega_z = 300^\circ/\text{s}$. In black and red are represented the responses with and without the tuning application, respectively.

potential of fixed nodes is equal to the tuning tension. A clarifying scheme and the setup of Trans126 elements used to model the electromechanical coupling for the tuning-comb structures implemented in the FEM model are respectively shown in Figure 6.6a and 6.6b.

Similarly to the comb drive-based electrostatic actuators, the fringing field along the lateral edges of tuning-comb fingers can be neglected, as the gap between fingers is small enough: indefinite capacitor theory is thus adopted. As a consequence, the capacity characteristics of each of the two Trans126 elements attached to the moving finger is a nonlinear function of the gap distance between their corresponding nodes, which also depends on the y-displacement. According to Equation 6.1, in order to represent this capacity characteristics, it is possible to set as real constant



(a) Trans126 pictorial scheme



(b) Trans126 elements in the FEM model with detail of boundary conditions

Figure 6.6: Setup of Trans 126 elements for FEM based electrostatic analysis.

of Trans126 elements the proportionality coefficient obtained with the following equation

$$C_{0(t)} = \epsilon_0 x_{0(t)} t \quad (6.9)$$

In addition, also the initial gap $y_{0(t)}$ is assigned as real constant.

6.4 FEM model results

The electrostatic tuning effect on the MEMS gyroscope device behaviour proposed in this thesis project is analyzed performing a FEM-based modal and harmonic analysis in Ansys. A comparison

with analytical model results is finally necessary to verify that the spring softening effect analytically modelled represents adequately the change of the structure stiffness due to the tuning tension applied on tuning electrodes. As previously anticipated, this represents a crucial point since the automatic mode-matching system control, which will be further developed, strongly depends on this modelling.

The effect of electrostatic tuning is firstly investigated performing a FEM-based modal analysis in Ansys applying an increasing tuning DC tension on tuning comb structures. In this case, the routine is first to proceed with a static analysis of the device with the DC voltage applied to Trans126 elements attached to moving tuning comb fingers, and then performing a prestressed modal analysis on the structure. The included prestress is responsible for the effects of the applied voltage on the system frequency characteristic. The program outputs are mechanical displacements and eigenfrequencies with incorporated electrostatic effects. However, the reader can refer to Section 3.3.3 and *Appendix C* for a detailed description of the procedure to carry out a generic prestressed modal analysis in Ansys.

Figure 6.7 shows the frequency tuning characteristic of the drive and sense resonant modes of the proposed gyroscope structure as a function of the tuning voltage applied on the tuning electrodes. As expected, by increasing the DC tuning voltage applied to the fixed electrodes the drive mode resonant frequency remains constant at 11014 Hz, while the sense mode resonance frequency is adjusted by tuning the electrostatic spring constant. The resonant mode frequencies are perfectly matched at the DC tension of 14.903 V.

For the sake of completeness, Figure 6.8 shows the first four mode shapes of the MEMS gyroscope subjected to the tuning tension which guarantees the mode-matching condition. The first two modes (Figure 6.8a and b), corresponding to the drive and sense-mode, have the same resonant frequency value. In particular, the electrostatic tuning effect does not influence the first mode of the structure, which maintains constant its own resonant frequency value, while the second mode frequency value is tuned to be exactly equal to the drive one. The third (Figure 6.8c) and fourth (Figure 6.8d) modes are also influenced by tuning tension applied on fixed electrodes. Since these modes do not affect the operation of the gyroscope, the small decreasing in the corresponding frequency values can be neglected.

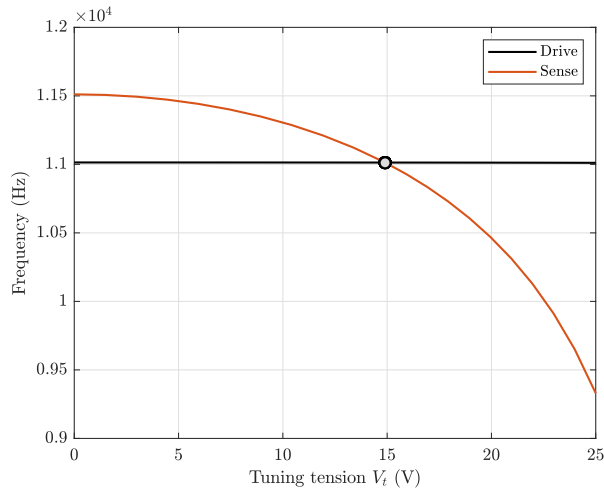


Figure 6.7: FEM-based frequency tuning characteristics of drive and sense resonant modes as a function of the applied tuning tension V_t . The mode-matching condition (represented in grey) is achieved with $V_t = 14.903$ V.

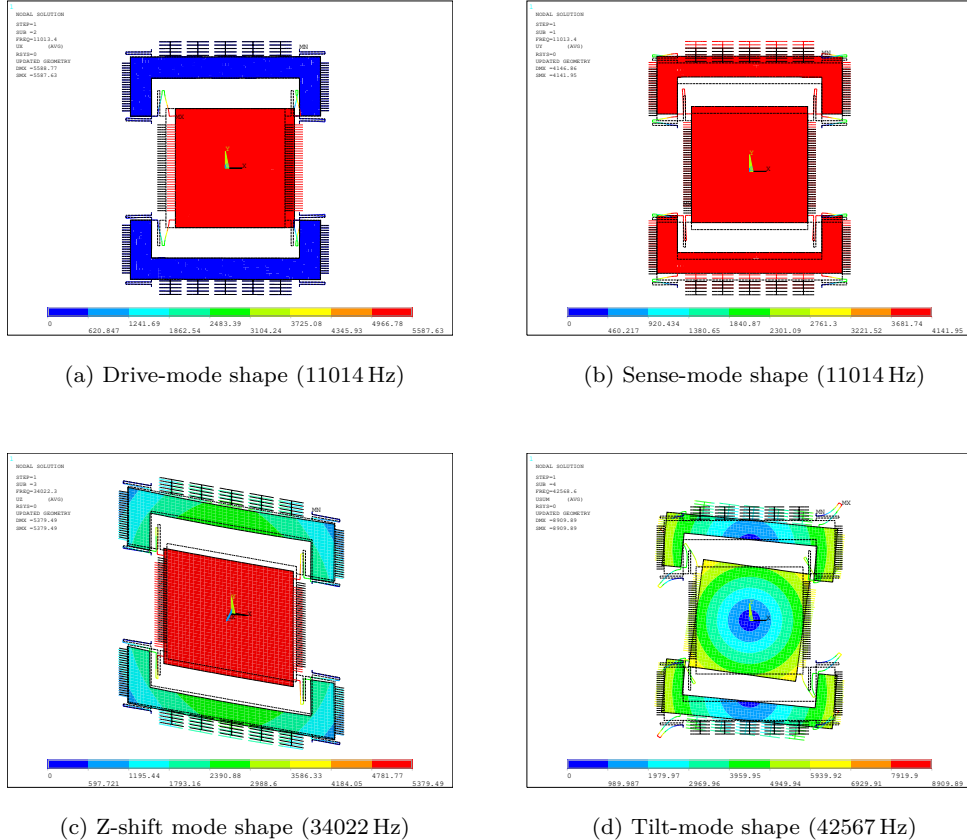


Figure 6.8: Modal analysis results and the corresponding mode shapes for the proposed dual mass MEMS gyroscope (a) 1st mode (11014 Hz) (b) 2nd mode (11014 Hz) and (c) 3rd mode (34022 Hz) and (d) 4th mode (42567 Hz).

A comparison between frequency characteristics obtained through the analytical and FEM-based modal analysis is performed. Referring to Figure 6.9a, when a low DC tension is applied on the tuning fixed electrodes, the resulting sense resonant frequency value obtained with the analytical formulation and through the FEM simulation in Ansys are matched. This means that, if the frequency difference between the drive and sense mode would be such that as a tuning voltage lower than about 5 V it would be necessary to guarantee the mode-matching condition, the analytical model represents correctly the electromechanical coupling simulated in the FEM-based modal analysis. As a consequence, the analytical model formulation proposed in Equation 6.6 to estimate the sense frequency variation with the DC tuning tension can be adopted in the automatic mode-matching system control. However, as in the proposed MEMS gyroscope design, a tuning tension higher than 5 V may be necessary to have resonant mode frequencies perfectly matched. Since an higher tuning tension implies an increase of the difference between the analytical and FEM-based sense frequency characteristics, the mode-matching condition is achieved at different tuning tension values. For the proposed MEMS gyroscope design, the drive and sense mode initial frequency mismatch of 497 Hz leads to an error between analytical and Ansys resulting tuning voltage of 45%. This error can be reduced modifying the sense frequency expression ω_s provided by Equation 6.6, by using a proper coefficient β_{FIT} to fit the FEM-based sense frequency tuning

characteristics, as follows

$$\omega_s = \sqrt{\frac{k_y - \beta_{FIT} \frac{2N_t \epsilon_0 x_{0(t)} t}{y_{0(t)}^3} V_t^2}{m_s}} \quad (6.10)$$

The fitting results are provided in Figure 6.9b. The FEM-based and analytical sense frequency characteristics, respectively represented in blue and red in the plot, are roughly coincident for a DC tuning tension with value between 0 and 15.5 V. Such a tuning range is sufficient for the proposed system to compensate for an initial frequency split of up to 787 Hz between the drive and sense modes. This means that, as the automatic mode-matching system control is based on the analytical model formulation, it will provide reasonable results, similar to the one obtained through the Ansys simulation, only for a frequency difference between the drive and sense modes below 787 Hz.

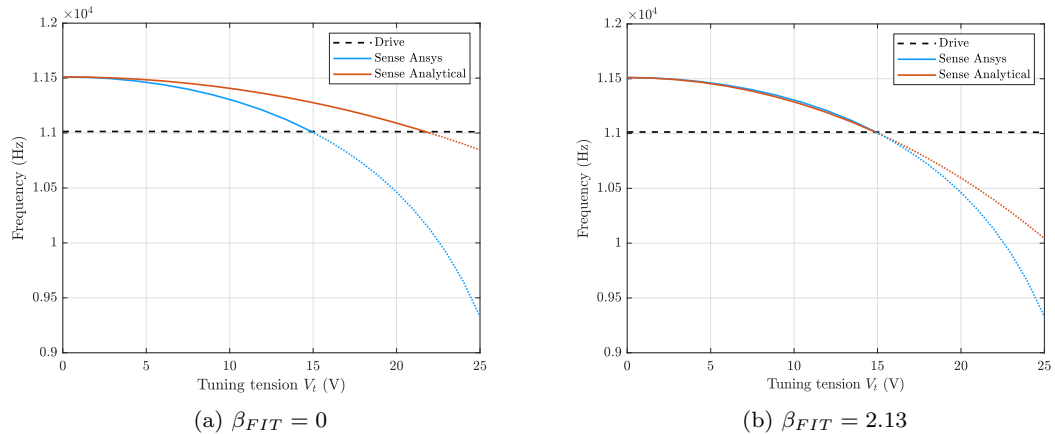


Figure 6.9: Comparison FEM-based and analytical frequency tuning characteristics of drive and sense resonant modes as a function of the applied tuning tension V_t (a) without fitting (b) with fitting.

For the sake of completeness, the effect of electrostatic tuning on the frequency response of the proposed MEMS gyroscope device is analyzed. As shown in the FEM-based modal analysis, the drive mode is not influenced by the electrostatic tuning effect. Accordingly, when an harmonic force is applied to the drive mass along the x-axis by applying an actuation voltage of 50 V DC and 5 V AC to comb drive-based actuators and considering that the damping coefficient in the drive direction does not change, the harmonic response of the drive mass in the x-direction can be obtained exactly as described in Section 5.5.3. Since in the drive direction the excitation voltage consists in a DC voltage superimposed on a small-signal AC voltage, a static analysis with the applied DC voltage is first performed, followed by a prestressed full harmonic analysis with the applied AC excitation voltage. In order to avoid repetitions, the reader can refer to Figure 5.22 for the frequency response representation of the structure in the drive direction in terms of magnitude and phase.

As already shown in Section 6.2, the sense mode dynamics is strongly influenced by the electrostatic tuning effect, therefore a prestressed full harmonic analysis is now necessary to include the effects of the applied voltage on the fixed tuning combs structure. The harmonic analysis is performed using the same procedure described in Section 5.5.3. The only difference is that the static analysis should be performed with also the DC tension applied to the Trans126 nodes attached to tuning

comb fingers. Figure 6.10 shows the obtained frequency response of the structure in the sense direction in terms of magnitude and phase with an angular velocity $\Omega_z = 300^\circ/\text{s}$ in the z-direction, applying the tuning tension $V_t = 14.903 \text{ V}$ which guarantees the mode-matching condition. As expected, when the resonant mode frequencies are perfectly matched, only one peak is present and the phase decreases continuously from -90° to -450° .

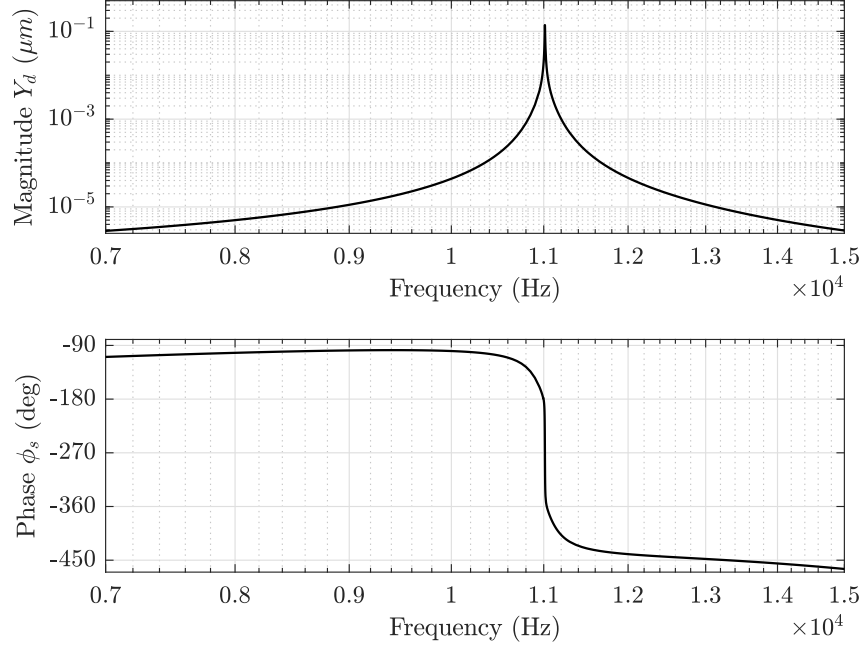


Figure 6.10: The FEM-based frequency response in the sense direction for the proposed dual mass MEMS gyroscope (*logarithmic scale*), with $\Omega_z = 300^\circ/\text{s}$ and tuning tension $V_t = 14.903 \text{ V}$.

As it has been repeated several times, the main goal of tuning the sense resonant frequency is the compensation of the frequency mismatch between the drive and sense mode frequency due to microfabrication process tolerances and device operating temperature variations, in order to achieve the maximum possible mechanical sensitivity. In order to verify that the electrostatic tuning results in an increase in the sense response amplitude and, thus, in the mechanical sensitivity, a comparison between the FEM-based frequency response amplitude obtained with and without the tuning tension application, considering $\Omega_z = 300^\circ/\text{s}$ and an actuation voltage of 50 V DC and 5 V AC, is provided in Figure 6.11. The curve in red represents the frequency response amplitude in the sense direction when no tuning DC tension V_t is applied on the tuning electrodes. In this case, since the frequency mismatch leads to two resonant peaks, the maximum gain for the proposed MEMS gyroscope design is not achieved. Referring to the black curve, when the tuning tension guaranteeing a perfect match between resonant mode frequencies is applied to the system, only one peak is present and this leads to the highest mechanical sensitivity.

Figure 6.12 is useful to clarify the importance of the electrostatic tuning. The drive and sense mode amplitudes, obtained applying an actuation voltage of 50 V DC and 5 V AC, a DC tuning tension $V_t = 14.903 \text{ V}$ and an angular velocity $\Omega_z = 300^\circ$ in the z-direction, are respectively represented with the red and black curve in the plot. Since resonant frequency values are matched, resonant peaks are perfectly matched too. In addition, even if the drive amplitude at resonance is

equal to $46.93 \mu\text{m}$, the sense one is much smaller and equal to $0.1393 \mu\text{m}$. This means that, even a slight mismatch between resonant mode frequencies involves a decrease of an already very small amplitude, which can cause the performance of the gyroscope to reduce dramatically.

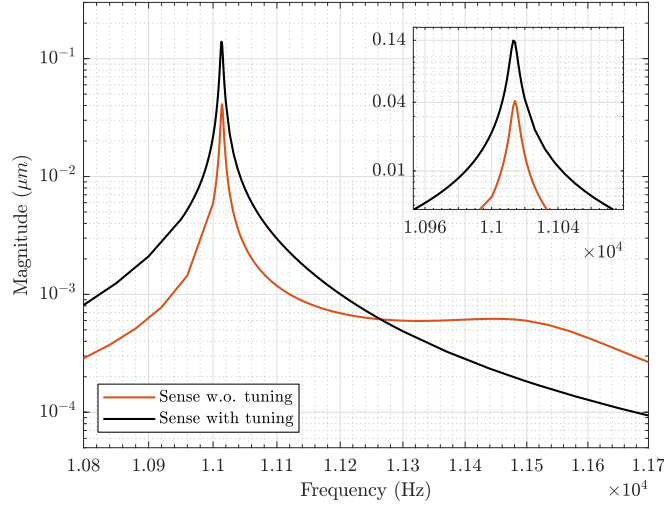


Figure 6.11: Comparison between the FEM-based frequency response amplitudes in the sense direction (*logarithmic scale*) obtained applying a tuning tension $V_t = 0$ and $V_t = 14.903 \text{ V}$, with $\Omega_z = 300^\circ/\text{s}$.

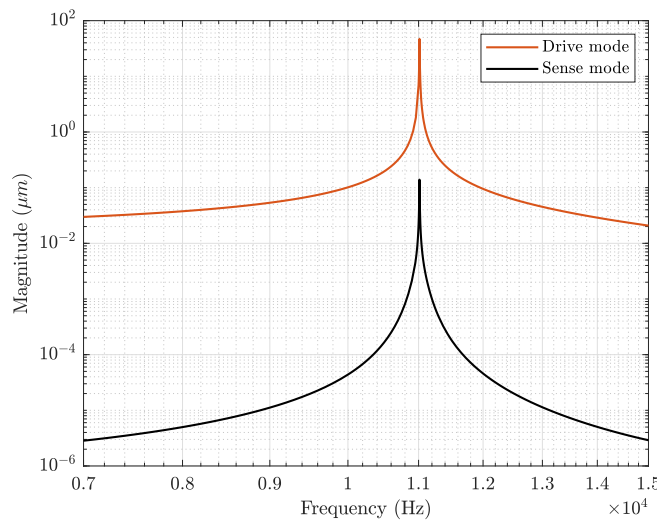


Figure 6.12: Comparison between drive and sense FEM-based frequency response amplitudes (*logarithmic scale*), obtained applying an actuation voltage of 50 V DC and 5 V AC , a DC tuning tension $V_t = 14.903 \text{ V}$ and an angular velocity $\Omega_z = 300^\circ/\text{s}$ in the z-direction.

In order to understand the potentiality of the electrostatic tuning application, Table 6.1 provides a comparison between sense response amplitudes, with an actuation voltage of 50 V DC and 5 V

AC and an angular velocity in the z-axis $\Omega_z = 300^\circ/s$ applied to the structure, considering two different conditions: the first with a frequency mismatch of 497 Hz and the second with drive and sense resonant frequency perfectly matched due to the tuning voltage application. Clearly, the tuning application allows an increase in the mechanical sensitivity of 241%.

Frequency Mismatch (Hz)	Amplitude (μm)	Sensitivity (μm/rad/s)
497	0.0411	0.0078
0	0.13930	0.0266

Table 6.1: Mechanical sensitivity comparison in the case of different frequency mismatch values.

6.5 Automatic mode-matching control system

In the previous sections it was shown how the electrostatic stiffness effect can be used to compensate the mismatch between drive and sense resonant frequency values. This method relies on the electrostatic spring softening phenomenon to change the equivalent stiffness of the sense mode by applying an adjustable DC voltage to the frequency tuning electrodes of the MEMS gyroscope, thereby altering the sense resonant frequency to achieve the purpose of mode-matching and get the optimal performance of the gyroscope. The main goal behind the MEMS gyroscope design proposed in this thesis project is to compensate automatically any kind of frequency mismatch, such as due to microfabrication process tolerances and device operating temperature variations. A closed-loop mode-matching control is therefore necessary to tune automatically the sense mode frequency to approximate the drive mode frequency and guarantee high and stable performance over a wide range of environmental conditions.

6.5.1 Control-loop system design

For the compensation of the frequency mismatch between the drive and sense mode frequency due to microfabrication process tolerances and device operating temperature variations, a closed-loop control system is developed to automatically achieve the mode-matching condition by tuning the sense mode frequency value. Since the main objective of this thesis project is the implementation of the electrostatic tuning technology in the proposed MEMS gyroscope design, at this point of the analysis two assumptions have been made:

- The quadrature error is considered negligible. In reality, fabrication imperfections result in non-ideal geometries in the gyroscope structure, which in turn causes the drive oscillation to partially couple into the sense-mode. This mechanical coupling will lead to an undesired quadrature error in sense mode. However, literature offers several approaches that could be adopted also in the proposed MEMS gyroscope design to compensate for mechanical quadrature. A possible future implementation will be provided in the last chapter of this thesis.
- The proposed MEMS gyroscope operates exactly at the drive-mode resonant frequency. This is guaranteed by the use of an amplitude regulated positive feedback loop ensuring that the system responds with a well-controlled displacement amplitude at the drive resonance.

The proposed automatic mode-matching system operation mainly relies on the frequency characteristics of the gyroscope vibration modes, and in particular, on the phase relationship between

the sense and drive signals in the gyroscope. Both the drive and sense oscillator can be assumed as a second-order mass-damper-spring system, as previously described in Chapter 2. Assume the electrostatic driving force in the drive mode is $F_d = F_0 \sin(\omega t)$, where F_0 is the amplitude of electrostatic driving force and ω is the frequency of electrostatic driving force. According to Equations 5.22, the drive-mode steady state response is $x = X_d \sin(\omega t + \phi_d)$, where the amplitude X_d and phase ϕ_d expressions can be obtained applying Equations 5.23 and 5.24. Since the gyroscope system uses a closed control-loop technology to track the resonant frequency of the driving mode ω_d , the excitation frequency corresponds to the drive resonant frequency, i.e. $\omega = \omega_d$, and the amplitude and phase of the drive-mode response become

$$X_d = \frac{F_0}{c_x \omega_d} \quad (6.11)$$

$$\phi_d = -90^\circ \quad (6.12)$$

In this condition, when the device is subjected to an angular velocity Ω_z in the z-direction, a Coriolis force of $F_c = -2m_d \Omega_z \omega_d X_d \cos(\omega_d t - 90^\circ)$ excites the sense mode dynamics. Consequently, the sense-mode steady-state response can be expressed as $y = -Y_d \cos(\omega_d t + \phi_s)$. According to Equations 5.28 and 5.29, the amplitude Y_d and phase ϕ_s of the sense-mode response are

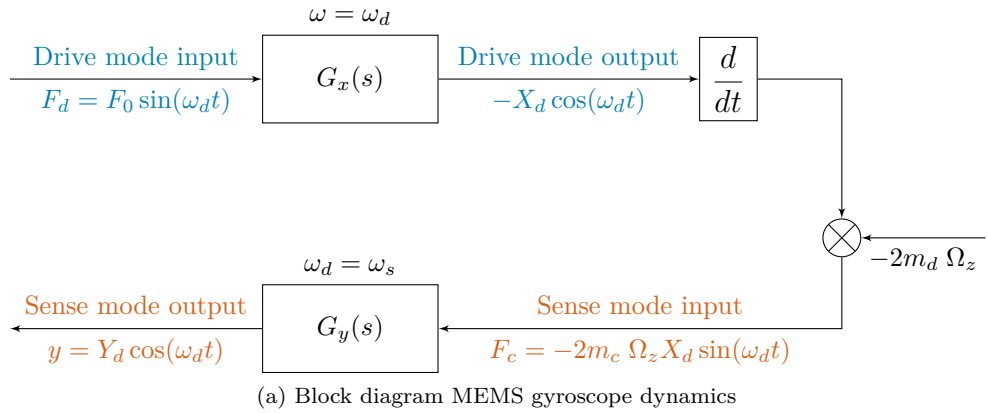
$$Y_d = 2m_d \Omega_z \omega_d X_d \cdot \frac{1/m_s}{\sqrt{(\omega_s^2 - \omega_d^2)^2 + \frac{c_y}{m_s} \omega_d}} \quad (6.13)$$

$$\phi_s = \phi_y - 90^\circ = -\arctan \left[\frac{\frac{c_y}{m_s} \omega_d}{(\omega_s^2 - \omega_d^2)} \right] - 90^\circ \quad (6.14)$$

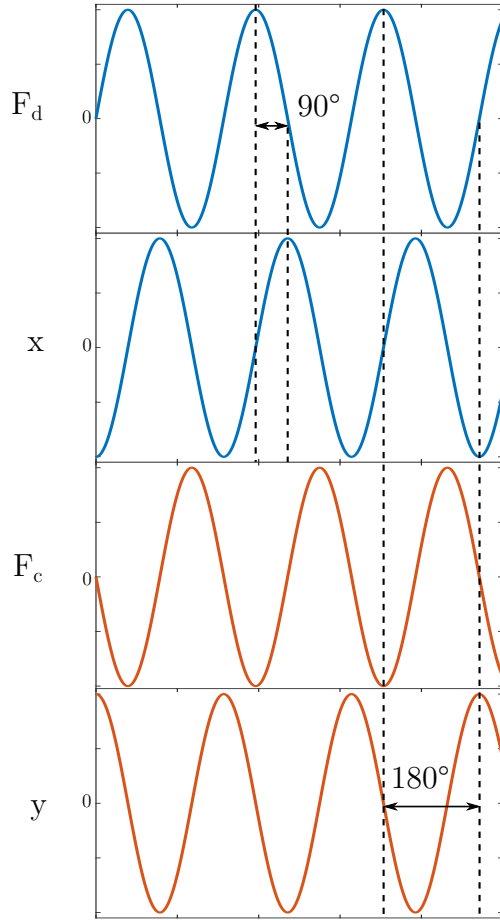
where ϕ_y is the phase delay caused by the sense mode dynamics. When the resonant frequencies of the two modes are equal, that is $\omega_d = \omega_s$, the phase delay caused by the sense mode becomes $\phi_y = -90^\circ$ and $\phi_s = 180^\circ$. This means that the phase delay information of the sense mode can be used to determine whether the two modes are matched. For the sake of clarity, Figure 6.13 shows the phase relationship between the drive mode and sense mode signals in the case of mode-matching condition, considering a constant angular velocity Ω_z to simplify the representation.

The block diagram of the automatic mode-matching closed-loop control is shown in Figure 6.14. The dynamics of drive and sense mode oscillators are represented by the corresponding transfer functions. The detection of the sense displacement y due to the Coriolis force through the sensing parallel plates attached to the sense frame and arranged in differential gap-antigap configuration, and the conversion of the resulting overall capacitance change to an equivalent output voltage is modelled with the $y - V_s$ transform block. Therefore, the output voltage V_s contains the amplitude response information of the sense-mode. This signal is demodulated by $-\sin(\omega_d t)$, and then the output of the demodulator is low-pass filtered to obtain the phase difference information of the sense-mode response. The demodulator together with the low-pass filter equivalently operates as a phase detector. The phase difference information, which can reflect whether the modes are matched, is fed to a PI controller that adjusts the tuning voltage V_t to change the sense-mode frequency to a value which is close to the ideally desired value of $\phi_y = -90^\circ$. Next, the DC tuning voltage V_t is applied to the tuning electrodes to change the sense-mode frequency value ω_s by the electrostatic negative stiffness effect and realize the automatic mode-matching.

A detailed analysis of the implementation of proposed mode-matching closed-loop control system and the system simulations carried out in SIMULINK environment are provided in the following sections.



(a) Block diagram MEMS gyroscope dynamics



(b) Qualitative signal shape representation

Figure 6.13: The phase relationship between the drive mode and sense mode signals.

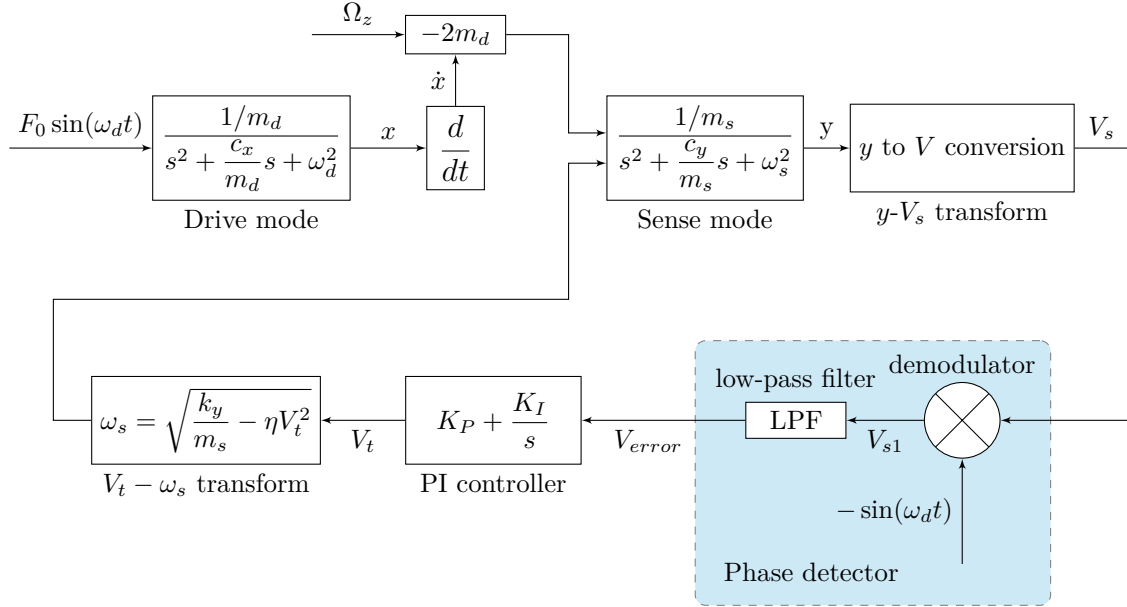


Figure 6.14: Schematic control-loop for the automatic frequency tuning system.

6.5.2 Control-loop system analysis

The development of the closed-loop control systems, which will be successively implemented in SIMULINK environment, requires to derive the equations of each of the blocks shown in Figure 6.14. This process is shown in detail in the following paragraphs.

Drive mode block

As discussed upon several times, the drive-mode dynamics is the one of a single degree-of-freedom system. In the time domain it is regulated by Equation 5.1, which is reported below for the sake of clarity

$$\ddot{x} + \frac{c_x}{m_d} \dot{x} + \omega_d^2 x = \frac{F_d}{m_d} \quad (6.15)$$

Transforming Equation 6.15 into the Laplace domain, the transfer function $G_x(s)$ of the drive-mode is given as

$$G_x(s) = \frac{X(s)}{F_d(s)} = \frac{1/m_d}{s^2 + \frac{c_x}{m_d}s + \omega_d^2} \quad (6.16)$$

where s is the Laplace complex variable. As expected, $G_x(s)$ has the form of a second-order system transfer function.

Sense mode block

When the gyroscope system is subjected to an angular velocity Ω_z in the z-direction, a Coriolis force F_c occurs in the y-direction

$$F_c = -2m_d\Omega_z\dot{x} \quad (6.17)$$

This force excites the sense-mode dynamics, which is in turn the one of a single degree-of-freedom system. In the time domain it is described by Equation 5.1, reported below

$$\ddot{y} + \frac{c_y}{m_s} + \omega_s^2 = F_c \quad (6.18)$$

Accordingly, the transfer function of the sense-mode can be expressed as

$$G_y(s) = \frac{Y(s)}{F_c(s)} = \frac{1/m_s}{s^2 + \frac{c_y}{m_s}s + \omega_s^2} \quad (6.19)$$

where the value of the sense-mode frequency ω_s can be adjusted by applying the tuning voltage V_t . Similarly to the drive-mode, also $G_y(s)$ has the form of a second-order system transfer function.

$y - V_s$ transform block

Sensing parallel-plates arranged in the gap-antigap-based differential configuration are used to detect the sense displacement due to the Coriolis force. As described by Equation 5.6 the overall capacitance change, corresponding to the sense mass displacement, can be computed as

$$\Delta C = \frac{2y \epsilon_0 t N_s (d_2^2 - d_1^2)}{(d_2^2 - y^2)(d_1^2 - y^2)} \quad (6.20)$$

Under small deflection approximation, i.e $y \ll d_1$ and $y \ll d_2$ the capacitance change value becomes

$$\Delta C = 2\epsilon_0 t N_s y \left(\frac{1}{d_1^2} - \frac{1}{d_2^2} \right) \quad (6.21)$$

The capacitance change, corresponding to an input rotation, is converted to an equivalent output voltage through a charge amplifier. The amplified output voltage of the charge amplifier is obtained by

$$V_s = \frac{2\Delta C}{C_F} V_{sense} \quad (6.22)$$

where the nominal value of the feedback capacitor C_F can be changed according to the sense capacitance range to make the output voltage reside within the desired range. Substituting Equation 6.21 in 6.22, the output voltage expression becomes

$$V_s = \frac{4\epsilon_0 t N_s y \left(\frac{1}{d_1^2} - \frac{1}{d_2^2} \right)}{C_F} V_{sense} \quad (6.23)$$

and considering that $y = -Y_d \cos(\omega_d t + \phi_s)$, V_s can be expressed in a more compact form

$$V_s = -Y_d G_{y-V} \sin(\omega_d t + \phi_y) \quad (6.24)$$

where $G_{y-V} = \frac{4\epsilon_0 t N_s \left(\frac{1}{d_1^2} - \frac{1}{d_2^2} \right)}{C_F} V_{sense}$ is the gain which converts the sense displacement to the output voltage.

Phase detector block

A demodulator followed by a low-pass filter equivalently operates as a phase detector. The sense voltage V_s is demodulated by reference signal $-\sin(\omega_d t)$ and V_{s1} signal is obtained

$$V_{s1} = [-\sin(\omega_d t)] \cdot [-Y_d G_{y-V} \sin(\omega_d t + \phi_y)] \quad (6.25)$$

which can be rewritten as

$$V_{s1} = \frac{Y_d G_{y-V}}{2} [\cos(\phi_y) - \cos(2\omega_d t + \phi_y)] \quad (6.26)$$

The demodulated signal V_{s1} is then filtered by the low-pass filter to get rid of the high frequency components in the output of the phase detector. The obtained V_{error} signal contains the phase information of the sense-mode response and its expression is

$$V_{error} = \frac{Y_d G_{y-V}}{2} \cos(\phi_y) \quad (6.27)$$

Figure 6.15 shows V_{error} and phase ϕ_y curves as functions of the sense frequency ω_s , considering the value of ω_d as fixed.

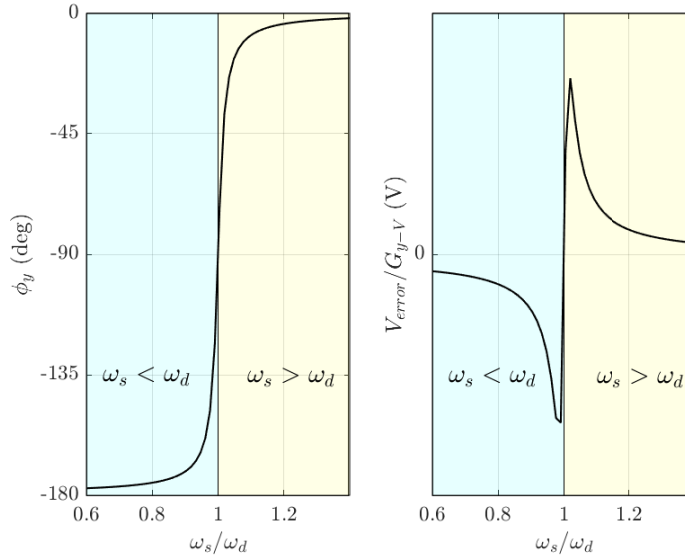


Figure 6.15: Relationship between resonant mode frequency mismatch and ϕ_y and V_{error} .

When the drive and sense-mode frequencies are matched, i.e. $\omega_d = \omega_s$, $\phi_y = -90^\circ$ and $V_{error} = 0$. Instead, when $\omega_s < \omega_d$, V_{error} is negative, while when $\omega_s > \omega_d$, V_{error} is positive. Therefore, V_{error} can be used as an input variable to control the tuning voltage by the PI controller, and whether V_{error} is equal to 0 is used as a judgment basis for the mode-matched condition.

PI controller

This signal V_{error} is then fed into a proportional-integral PI controller to be compensated. The tuning tension expression in the Laplace domain can be obtained from the PI controller transfer function as follows

$$V_t(s) = K_p V_{error}(s) + \frac{K_I}{s} V_{error}(s) \quad (6.28)$$

where K_P is the proportional gain and K_I is the integral gain. It is important to highlight that K_P and K_I should be chosen in order to meet the desired controller response characteristics, that is reducing the rise time and avoiding overshoots.

$V_t - \omega_s$ transform block

The tuning tension V_t is finally used to adjust the sense-mode frequency by changing the stiffness value of the structure based on the electrostatic negative stiffness effect. As previously discussed, when DC tuning tension V_t is applied on the tuning electrodes of the MEMS gyroscope, the sense-mode resonant frequency can be simplified as

$$\omega_s = \sqrt{\frac{k_y}{m_s} - \eta V_t^2} \quad (6.29)$$

According to Equation 6.10, the constant coefficient η can be expressed as

$$\eta = \beta_{FIT} \frac{2N_t \epsilon_0 x_{0(t)} t}{m_s y_{0(t)}^3} \quad (6.30)$$

where β_{FIT} is imposed equal to 2.13 to obtain consistent results with FEM-based simulations, as discussed in Section 6.4.

6.5.3 Simulation analysis for automatic mode-matching

In order to verify the feasibility of the proposed closed-loop mode-matching control system and the effectiveness of the theoretical analysis, according to the block diagram shown in Figure 6.14, the simulation analysis is performed in MATLAB SIMULINK environment. For legibility reasons, the complete block diagram of the implemented system control can be observed in *Appendix D*. The simulation parameters of the proposed MEMS gyroscope dynamics are set according to the FEM-based analysis results proposed in the previous Sections and they are provided in Table 6.2, while Table 6.3 and 6.4 show the main electrical parameters used in the simulation system and the parameter of the displacement-to-voltage conversion block, respectively.

In the SIMULINK model, the effect of the electrostatic spring constant on the sense mode resonance frequency is modeled considering the tuning voltage V_t applied to the electrostatic tuning electrodes. In addition, the SIMULINK model includes the complete analytical model of the MEMS gyroscope, the sense displacement-to-voltage conversion block, the second-order low-pass filter with 100 Hz cutoff frequency and gain 1 in the phase detector and the PI controller. Since the order of magnitude of V_{error} signal is of mV, the signal is amplified with a gain $G = 1000$ before being fed to the PI controller. The PI controller gains K_P and K_I are assigned to 9 and 50, in order to satisfy the constraints of limiting overshoots and obtaining low rise time response. Simulations are carried out with a driving harmonic force obtained applying an actuation voltage of 50 V DC and 5 V AC to the comb drive-based electrostatic actuators and of input angular velocity Ω_z of 300°/s.

Figure 6.16 shows the simulated tuning voltage V_t , the phase detector output V_{error} and the resonant frequency of the sense mode ω_s obtained during the mode-matching operation for the proposed MEMS gyroscope design. The tuning voltage, applied to the electrostatic tuning electrodes, tends to be stable during mode-matching operation: as represented in 6.16a, it continuously rises until the mode-matching condition is achieved, and then it stabilizes at 14.89 V, with an error of -0.067% compared to the tuning tension value obtained with the FEM-based analysis. The curve indicates also that the system is in a stable state after 0.72 s and the output fluctuation of V_t is less than 0.3 mV. Referring to Figure 6.16b, the phase detector output represents the error to be compensated by the PI controller. After starting the mode-matching

Parameter	Symbol	Value	Unit
Drive mass	m_d	$3.16e - 8$	kg
Sense mass	m_s	$5.88e - 8$	kg
Drive mode resonant frequency	ω_x	11014	Hz
Sense mode resonant frequency	ω_x	11511	Hz
Drive mode damping coefficient	c_x	$8.6983e - 7$	N/m/s
Sense mode damping coefficient	c_x	$1.2068e - 4$	N/m/s

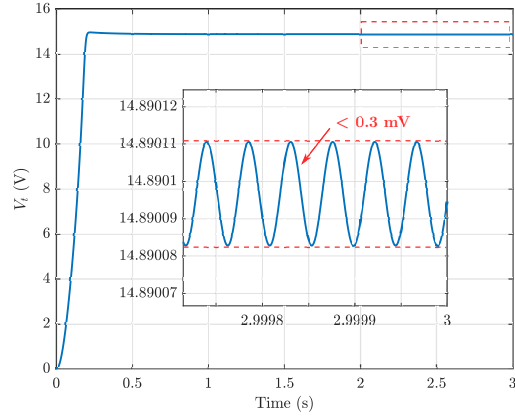
Table 6.2: Simulation dynamical parameters of the proposed dual mass MEMS gyroscope dynamics.

Parameter	Symbol	Value	Unit
Number of parallel plates (each side)	N_s	50	-
Overlap length between the moving and fixed parallel sensing plates	$x_{0(s)}$	55	μm
Smaller sense gap size	d_1	3	μm
Larger sense gap size	d_2	9	μm
Number of tuning comb fingers	N_t	84	-
Overlap length between the moving and fixed tuning comb fingers	$x_{0(t)}$	40	μm
Gap between tuning combs	$y_{0(t)}$	3	μm
Number of drive comb fingers (each side)	N_d	37	-
Overlap length between the moving and fixed drive comb fingers	$x_{0(d)}$	40	μm
Gap between drive combs	$y_{0(d)}$	3	μm
Structural thickness	t	25	μm

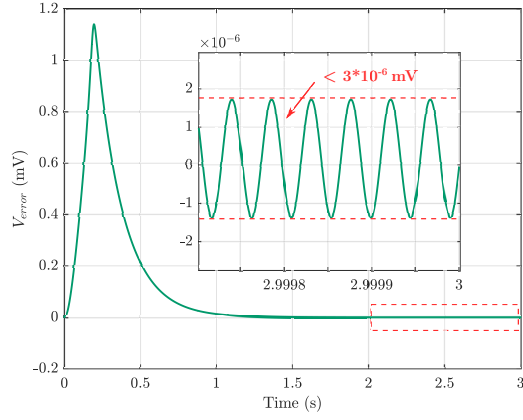
Table 6.3: Simulation electrical parameters of the proposed dual mass MEMS gyroscope.

operation, as the sense frequency value is higher than the drive one, the phase detector output is positive and when the resonance mode frequencies becomes closer during the mode-matching operation, the phase detector output sharply increases. However, when the controller reaches the steady-state condition and mode-matching is accomplished, the phase delay caused by the sense mode dynamics becomes $\phi_y \simeq 90^\circ$, and the phase detector outputs converges to zero as expected. Figure 6.16c represents the changes in the sense-mode frequency during the mode-matching operation. The electrostatic negative stiffness effect produced by the tuning voltage V_t softens the resonant frequency of the sense mode, which decreases from 11511 Hz to 11013.52 Hz when the mode-matching condition is achieved. In addition the curve shows that the fluctuation of the corresponding ω_s during mode-matching is approximately less than 0.002 Hz.

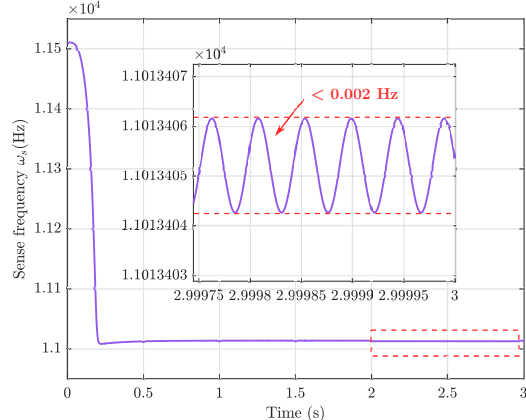
Figure 6.17 shows the simulated response amplitude of the drive and sense mode during the mode-matching operation of the proposed MEMS gyroscope, in a presence of angular velocity $\Omega_z = 300^\circ/s$ and a driving actuation force obtained applying to the drive combs 50 V DC and 5 V AC. Since the amplitude of the sense mode is much smaller than the drive one, for legibility reason it is multiplied by a gain $G = 100$. When $\omega_d \neq \omega_s$, the phase difference between the sense and drive mode signal is not -90° and the sense response amplitude is small (Figure 6.17a). During the mode-matching operation, the amplitude of the sense mode output significantly increases due to the sensitivity improvement until reaching the maximum when $\omega_d = \omega_s$. In this condition, the phase difference between the sense and drive mode signal becomes exactly -90° , which ensures



(a) Tuning voltage V_t



(b) Phase detector output V_{error}



(c) Resonant frequency of sense mode ω_s

Figure 6.16: Simulation outputs obtained during the automatic mode-matching operation for the proposed MEMS gyroscope device: (a) Tuning voltage V_t (b) Phase detector output V_{error} and (c) Resonant frequency of sense mode ω_s .

Parameter	Symbol	Value	Unit
Sense plates bias tension	V_{sense}	2.25	V
Feedback capacitance	C_F	2.8	pF

Table 6.4: Simulation parameters of the displacement-to-voltage conversion block.

that mode-matching is accomplished (Figure 6.17b).

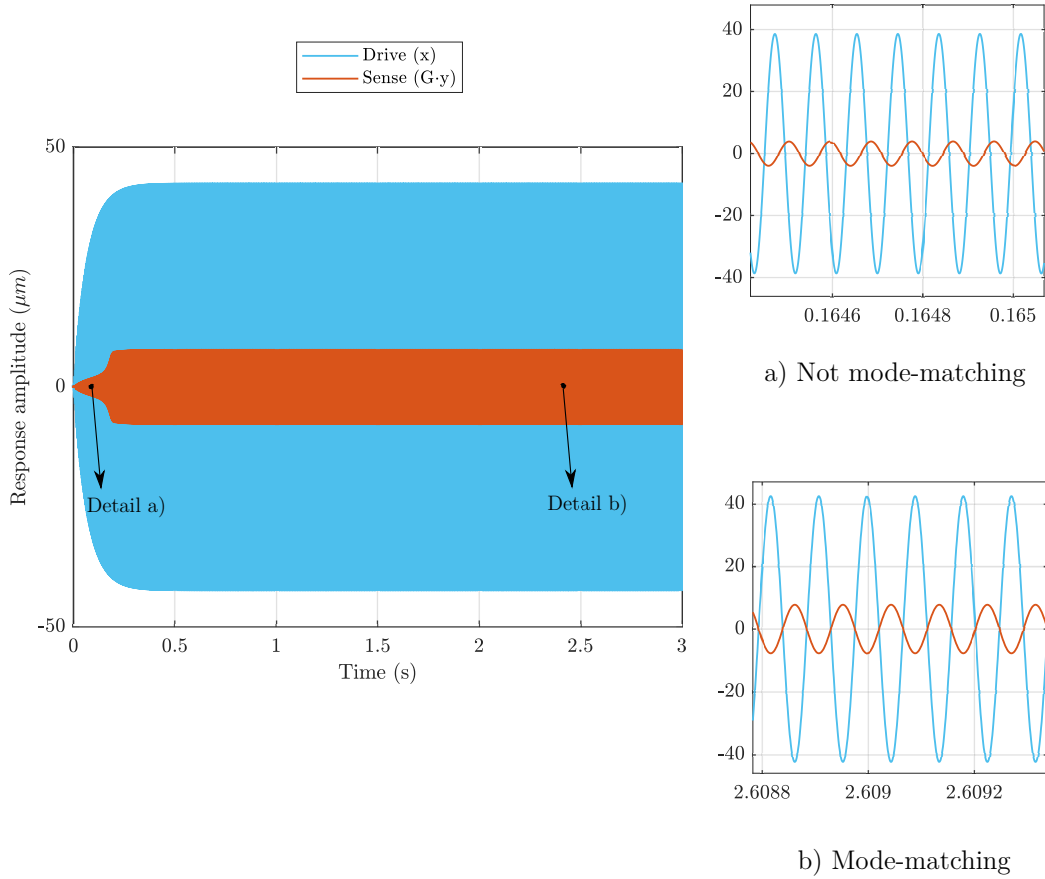


Figure 6.17: Simulated response amplitude of drive and sense mode outputs of the gyroscope in the presence of a Coriolis force during the mode-matching operation (a) Not mode-matching ($\omega_d \neq \omega_s$) and (b) Mode-matching ($\omega_d = \omega_s$).

The effect of different input angular velocities Ω on the tuning voltage and sense resonance frequency is shown in Figure 6.18. The interference fluctuation of the different Ω to the resonance frequency ω_s is less than 0.002 Hz. The interference fluctuation of the different Ω to the tuning voltage V_t is less than 0.03 mV. This shows that when Ω exists, the closed-loop mode-matching system can still work normally and finally stabilize at the desired frequency.

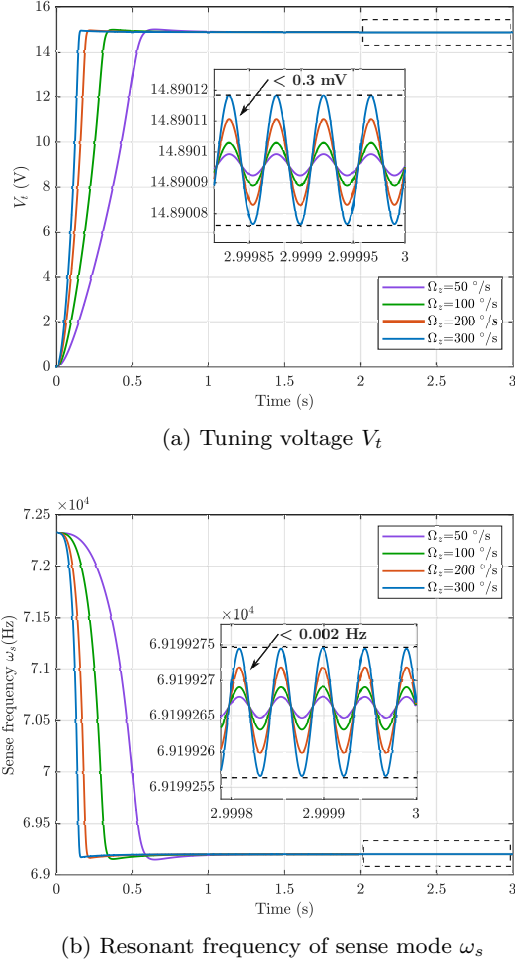


Figure 6.18: Influence of different input angular velocity on tuning voltage and sense-mode resonant frequency: (a) influence of different input angular velocities on tuning voltage V_t and (b) influence of different input angular velocities on sense mode resonant frequency ω_s .

6.6 Temperature variations

As repeatedly discussed, the main challenge in the resonant MEMS gyroscopes design is the fluctuation of the performance parameters of the device as they are affected by any variation in ambient conditions and fabrication imperfections, as these imperfections can cause a shift in resonance frequency which in turn causes a mismatch between the drive and sense mode frequencies. However, it was previously demonstrated that the electrostatic tuning effect can be used to compensate the frequency mismatch between the drive and sense mode frequency due to microfabrication process tolerances and device operating temperature variations. In addition, a mode-matching closed-loop control system can be implemented to automatically tune the sense frequency and achieve the maximum possible gain. This section provides an example of the electrostatic tuning application to compensate the device operating temperature variations, with a special focus on the performances improvement due to the sense-mode frequency tuning.

6.6.1 Thermal effects

In MEMS gyroscopes, it is necessary to maintain the performance stability. As it was demonstrated in previous sections, even small deviations between drive and sense modes result in high errors in the output signal gain. Temperature variations could cause resonant frequency shift of drive and sense mode, which directly affects the performance of MEMS gyroscopes. Accordingly, the effects of thermal fluctuations on the MEMS gyroscope should be considered when estimate the actual performance of the device. Temperature variations could cause changes in Young's modulus, thermal expansion or contraction and thermally induced stresses which would induce change of the stiffness matrix and therefore of the resonant frequencies values and degradation of the device performances. In addition, as discussed in Chapter 2, both the squeezed and slide film air damping air dependent on the effective air viscosity, which is strongly influenced by the changes in the operating temperature conditions. Accordingly, the modelling and simulation of these thermal induced effects on the proposed MEMS gyroscope behaviour is provided in the following paragraphs.

Changes in Young's modulus

The proposed MEMS gyroscope was designed considering the SOIMUMPs microfabrication process with silicon as a structural material. The material properties of silicon thin-film, including elasticity, are affected by the temperature. The change in Young's modulus of silicon with temperature can result in variation in the resonant frequency of the MEMS gyroscope. The semi-empirical expression for the effect of temperature on Young's modulus of the silicon is given as [15]

$$E(T) = E_0 - BT \exp\left(-\frac{T_0}{T}\right) \quad (6.31)$$

where E_0 is the Young's modulus at 0 K, T is the temperature, B and T_0 are constants which are dependent on the Grueneisen parameter, Debye temperature, Anderson–Grueneisen parameter and material volume at 0 K. For silicon, the values of B and T_0 are estimated as 15.8 MPa and 317 K respectively [15]. The silicon Young's modulus value for the operating temperature range of -40°C to 100°C for the proposed MEMS gyroscope is shown in Figure 6.19. The results show that, for the MEMS gyroscope and over the desired operating temperature range, the effect of temperature variation on Young's modulus and, thus, on stiffness variation is negligible.

Thermal deformation and thermally induced stresses

In addition to material properties changing, the device operating temperature may result in thermal deformation, that are expansion and contraction in the microstructure. For the proposed MEMS gyroscopes thermal deformation may lead to change in the gap and planarity between the electrostatic comb drive-based actuators, electrostatic tuning combs and parallel plate-based capacitive sensor. In addition, temperature variations could result in thermal stresses. A FEM-based thermal analysis is carried out to capture resonant frequency changes due to thermal deformation and thermally induced stresses for the proposed MEMS gyroscope operating between temperatures of -40°C and 100°C . First a uniform temperature T , varying in the range -40°C and 100°C is assigned to all structural nodes. A static analysis is run with prestress effects turned on, considering the ambient temperature $T_F = 25^\circ\text{C}$ as reference temperature.

Figure 6.20a and 6.20b show the thermally induced localized stresses resulting from the FEM-based static analysis, respectively at -40°C and 100°C . In the region where the sensing spring beams are connected to the structure there is a large concentration of thermal stress, while nearly no thermal stress is induced in the regions of driving spring beams and in the rest of the structure. Clearly, this would have different effects on resonant frequency shift of drive and sense mode

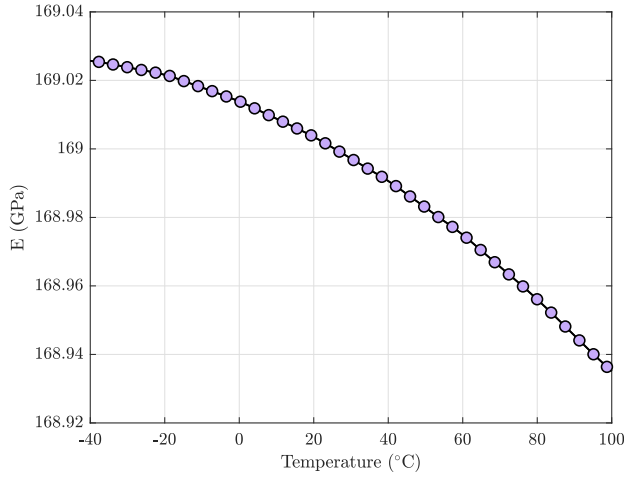


Figure 6.19: Young's modulus of silicon in the temperature range of 40° C to 100° C.

when environment temperature changes. The maximum value of Von Mises stress caused by temperature change in the range from -40°C to 100°C is determined and it is provided in Figure 6.21. This value comes to be larger when the temperature difference is larger with respect to room temperature.

Thermal deformations from -40°C to 100°C with respect to the reference temperature are computed. Figure 6.23 and 6.24 show the thermal deformation results at -40°C and 100°C , respectively. The thermal deformation at -40°C results in a structural contraction with a maximum value of $0.47\mu\text{m}$ in the mechanical sensing suspension beams, while at 100°C the mechanical structure expands and maximum deformation in the sensing mechanical springs is $0.545\mu\text{m}$. Although the deformation in the sensing spring beams is high, the maximum expansion and contraction in the drive and sense mass and in the driving spring beams is very low, with a maximum value of $0.104\mu\text{m}$ at -40°C and $0.121\mu\text{m}$ at 100°C . The maximum value of the thermal deformation caused by temperature changes in the range -40°C to 100°C is determined and is provided in Figure 6.22. This value comes to be larger when the temperature difference is larger with respect to room temperature.

Temperature variations induce thermal deformations and stresses in the MEMS gyroscope spring beams, which change the drive and sense-mode stiffness values and, thus, the corresponding resonant frequencies. As the thermal deformations and stresses are higher in the sensing spring beams, it is reasonable to expect that the sense-mode resonant frequency value will be more affected by temperature operating variations. Indeed, thermal analysis has shown that sensing spring beams are subjected by a stress gradient while the stress is roughly uniformly null in the drive spring beams and in the rest of the structure. In addition, sensing spring beams are subjected to the highest thermal deformation. In order to analyze the difference of thermal effects on drive and sense-mode resonant frequency, a FEM-based modal analysis is carried out in Ansys. Prior to the modal analysis, the nodal coordinate are updated with the deflections from the previous static analysis and then, including the prestress effects, the stresses stored from the static analysis are applied to the modal analysis. FEM-based modal analysis results are provided in Figure 6.25, which shows that in the temperature range of -40°C to 100°C , the drive and sense-mode resonant frequencies do not change in the same way. The drive-mode resonant frequency (Figure 6.25a) always descends while the temperature increases, instead the sense-mode resonant frequency (Figure 6.25b) changes with a parabolic trend due to thermal operating variations.

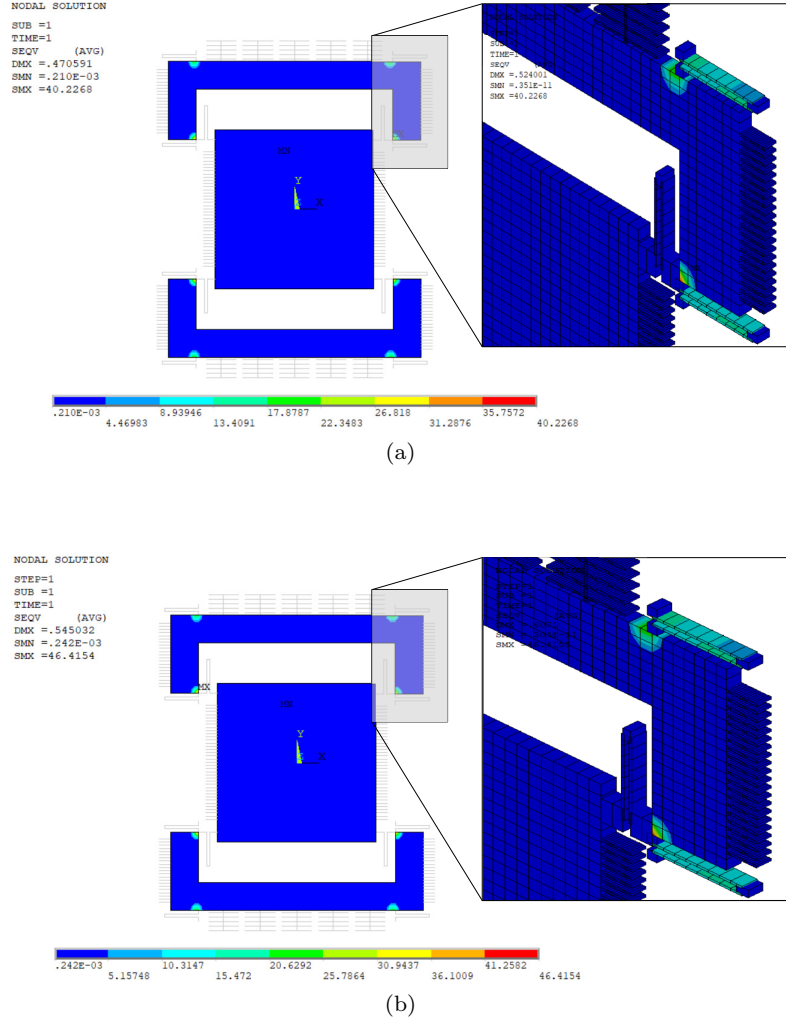


Figure 6.20: Thermally induced Von Mises stress in MEMS gyroscope (a) at -40° C , (b) at 100° C , with reference temperature T_F of 25° C .

Figure 6.26 shows the mismatch between the drive and sense-mode frequencies in the temperature range of -40° C to 100° C . When temperature is lower than the room temperature, frequency mismatch is also lower than the one at 25° C , i.e. 497 Hz, while the temperature increase with respect to the room temperature leads to an increase in the frequency mismatch. As already stated, an electrostatic compensation of the frequency mismatch between the drive and sense mode frequency is then necessary to avoid a decadence in the gyroscope performances.

In addition, thermal deformation may result in the change in the gap and planarity between the electrostatic comb drive-based actuators, comb-drive based electrostatic tuning and parallel plate-based capacitive sensor. To get more detailed information on the thermal deformation and its effect on the comb-drive actuators, on electrostatic tuning combs and on the capacitive sensing plates, deformation paths are added in the FEM analysis along the drive mass and sense frame, as shown in Figure 6.27.

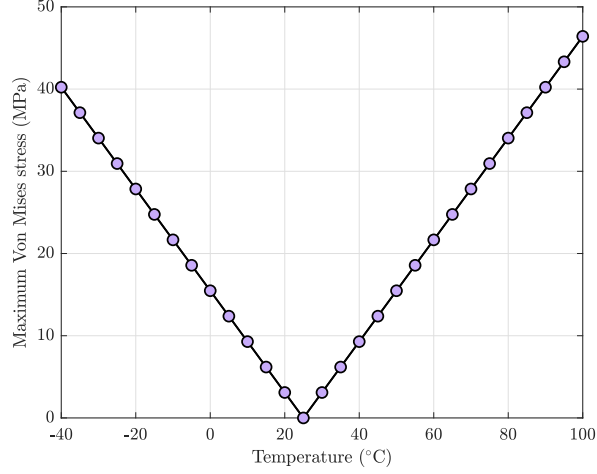


Figure 6.21: Maximum Von Mises stress with temperature change in the range of -40°C to 100°C .

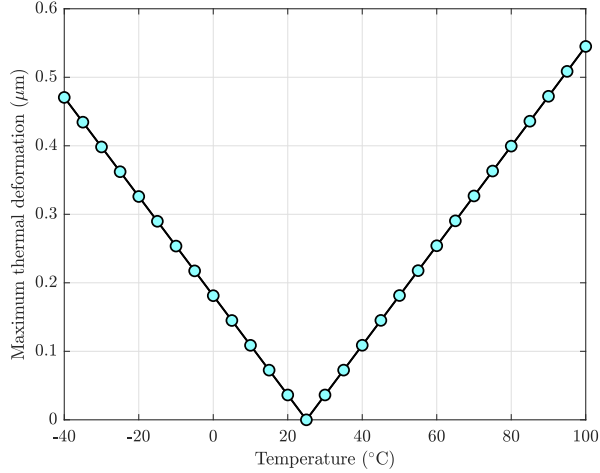


Figure 6.22: Maximum thermal deformation with temperature change in the range of -40°C to 100°C .

The results of the expansion and contraction along the drive mass to which comb-drive actuator fingers attach (referred as path *a* in Figure 6.27), at -40°C and 100°C are shown in Figure 6.28a and 6.28b, respectively. The results show that the total deformation (represented in black in the plot) due to temperature does not remain constant throughout the length of the drive-mass attached to the drive-comb actuators and it is minimized at the center and increased on either sides. Thermal deformation in the x-direction (represented in blue in the plot) may lead to changes in the initial overlap length value between comb-fingers. However, the deformation in the x-axis is only $0.059\text{ }\mu\text{m}$ at -40°C and $0.091\text{ }\mu\text{m}$ at 100°C , which is much less than the initial overlap length of $40\text{ }\mu\text{m}$ between comb-fingers. In addition the driving actuation force does not depend on the overlap length and, thus, the deformation in the x-direction can be neglected. In the z-axis,

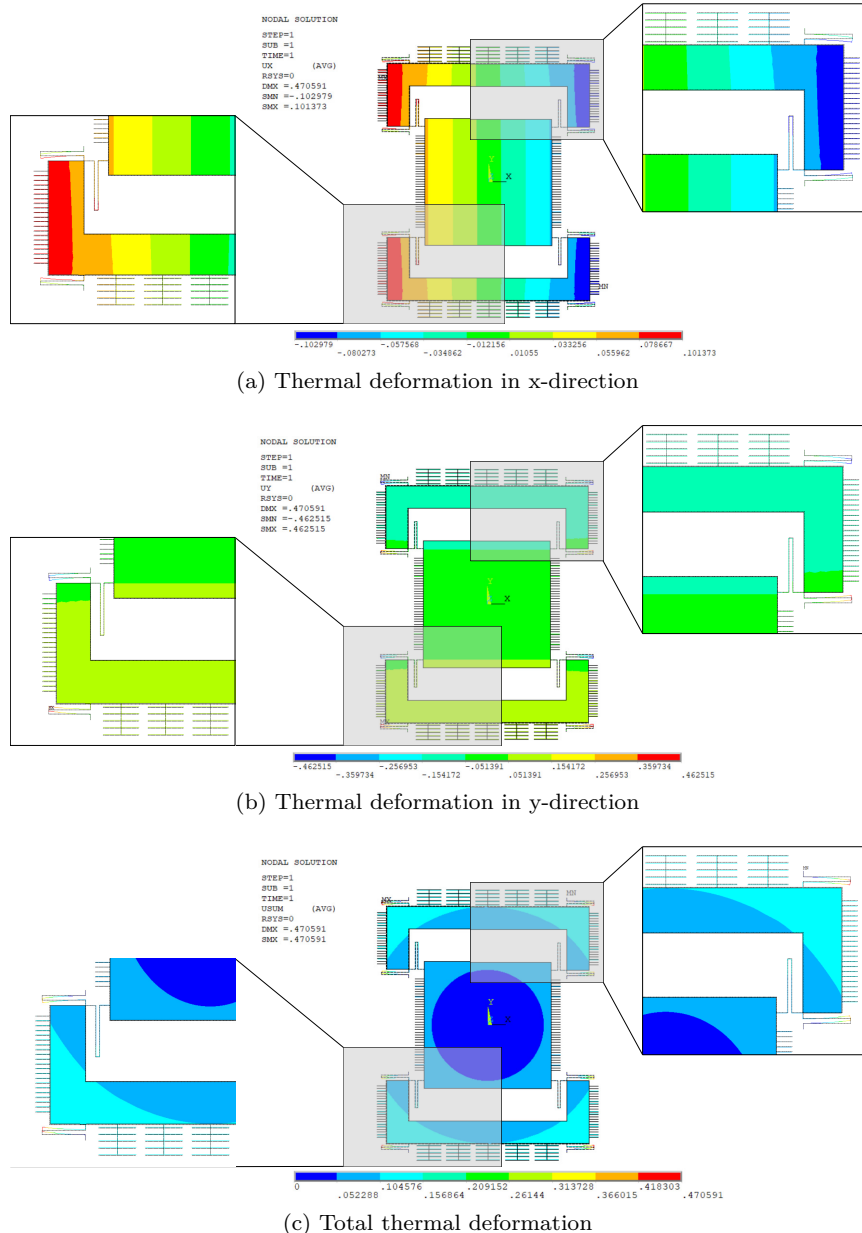


Figure 6.23: Structural thermal deformation in MEMS gyroscope at -40°C , with reference temperature T_F of 25°C (scale 20).

thermal deformation (represented in green in the plot) may lead to changes in the overlap thickness value but it is null and does not have effects. However, in the y-direction, thermal deformation (represented in red in the plot) may lead to changes in the initial gap-size between comb-fingers. The deformation is $0.04292\text{ }\mu\text{m}$ and $0.06585\text{ }\mu\text{m}$ at -40°C and 100°C , respectively. This results in an effective air gap of nearly $2.957\text{ }\mu\text{m}$ and $2.934\text{ }\mu\text{m}$ between the comb fingers. This decrease in the initial gap results in a slight increase in the driving actuation force when an equal voltage is applied to the fixed electrodes.

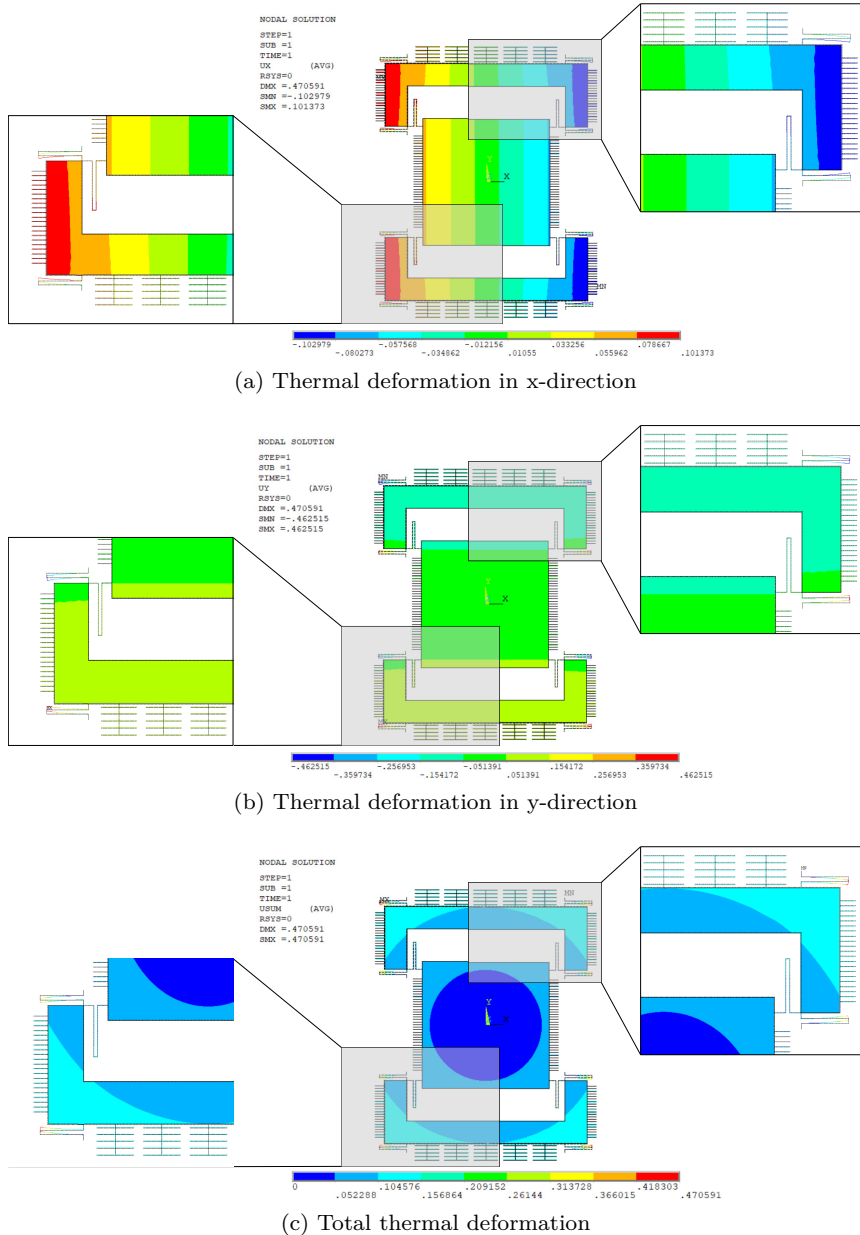


Figure 6.24: Structural thermal deformation in MEMS gyroscope at 100°C , with reference temperature T_F of 25°C (scale 20).

The results of the expansion and contraction along the sense frame to which electrostatic tuning-comb fingers attach (referred as path *b* in Figure 6.27), at -40°C and 100°C are shown in Figure 6.29a and 6.29b, respectively. The results shows that the total thermal deformation (represented in black in the plot) does not remain constant throughout the length of the external frame attached to the tuning combs, similarly to the comb-drive total deformation. Also in this case, thermal deformation in the x-direction (represented in blue) may lead to change in the initial overlap length between tuning-comb fingers, However, the maximum deformation in the x-axis is nearly

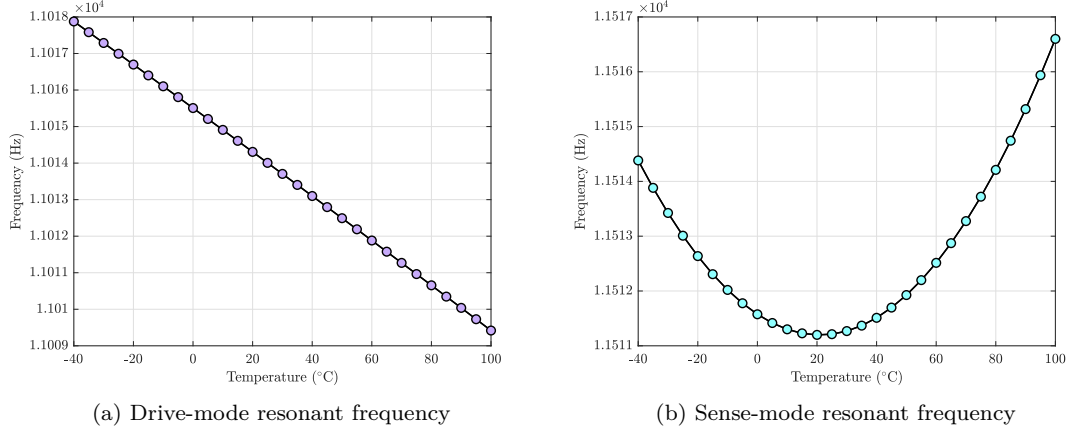


Figure 6.25: Drive and sense mode resonant frequency variation in the temperature range of -40°C to 100°C , with reference temperature of $T_F = 25^\circ\text{C}$.

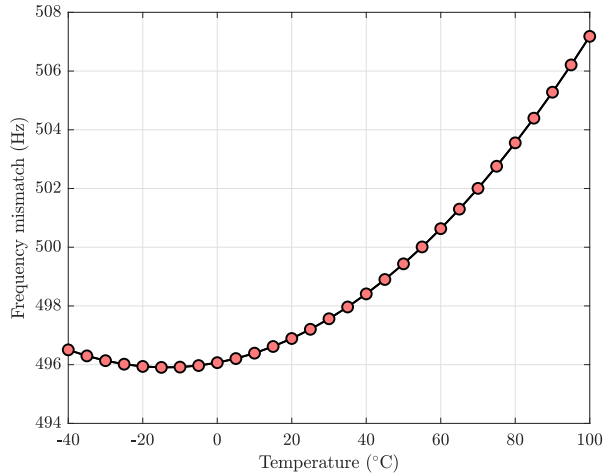


Figure 6.26: Frequency mismatch between drive and sense mode resonant frequency in the temperature range of -40°C to 100°C , with reference temperature of $T_F = 25^\circ\text{C}$.

0.0581 μm at -40°C and 0.0145 μm at 100°C , which is much less than the initial overlap length of 40 μm between tuning-comb fingers. In the z-axis, thermal deformation (represented in green in the plot) may lead to change in the overlap thickness value but it is null and does not have effects. However, in the y-direction, thermal deformation (represented in red in the plot) may lead to change in the initial gap-size between tuning-comb fingers. The maximum deformation is nearly 0.06157 μm and 0.154 μm at -40°C and 100°C , respectively. It is important to highlight that this deformation is not uniform along the sense frame attached to tuning combs but its value is lower in the region where the frame is connected to drive and sense spring beams. This non uniform deformation results in a different value of the effective air gap between tuning-comb fingers. Indeed, the maximum deformation results in an effective air gap of nearly 2.8384 μm and 2.846 μm at -40°C and 100°C , while the effective air gap is nearly 2.9749 μm and 2.9365 μm in the region where the thermal deformation is minimum. The non uniform decrease in the initial gap results in

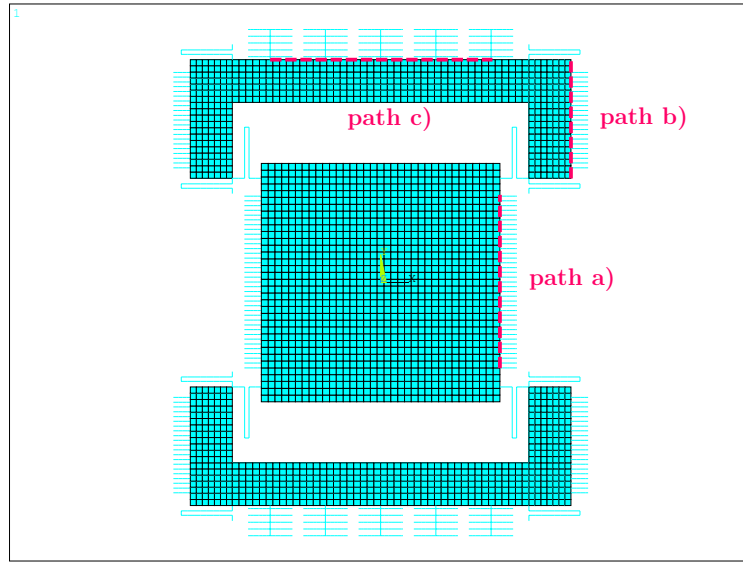


Figure 6.27: Thermal deformation paths along with the drive mass and sense frame.

a different increase in the electrostatic spring softening effect generated by each fingers pair. Finally, the results of the expansion and contraction along the sense frame to which electrostatic capacitive sensing plates are attached (referred as path *c* in Figure 6.27), at -40°C and 100°C are shown in Figure 6.30a and 6.30b, respectively. The results show that the total deformation (represented in black in the plot) does not remain constant throughout the length of the sense frame and it is minimized at the center and increased on either side. In addition, the thermal deformation in the *x*-direction (represented in blue in the plot) may lead also to change in the overlap length between sensing parallel plates. The maximum deformation in the *x*-axis is nearly $0.056\text{ }\mu\text{m}$ at -40°C and $0.0065\text{ }\mu\text{m}$ at 100°C , which is much less than the initial overlap length of $55\text{ }\mu\text{m}$ between parallel sensing plates. In the *z*-axis, thermal deformation (represented in green in the plot) may lead to change in the overlap thickness value but it is null and does not have effects. However, in the sense *y*-axis, the deformation (represented in red in the plot) may lead to change in the initial gap-size between sensing parallel plates. The maximum deformation is nearly $0.1048\text{ }\mu\text{m}$ and $0.1209\text{ }\mu\text{m}$ at -40°C and 100°C , respectively. This results in an effective initial air gap of nearly $2.8952\text{ }\mu\text{m}$ and $2.8791\text{ }\mu\text{m}$ between the parallel capacitive sensing plates. This decrease in the initial gap results in the decrease in the maximum pull-in voltage value and maximum input angular rate measurement.

Temperature dependence of viscous damping

As discussed in Section 5.2.3, both the squeezed and slide film air damping are dependent on the effective air viscosity which is strongly influenced by the changes in the operating temperature conditions. Therefore, the effect of temperature variations on the MEMS gyroscope should be analyzed.

The Knudsen number K_n , which in turn depends on the mean free path of air λ , contributes to the change of the effective air viscosity due to temperature variations. Considering that the mean free path of air λ at a given operating temperature can be expressed by the previously cited Equations

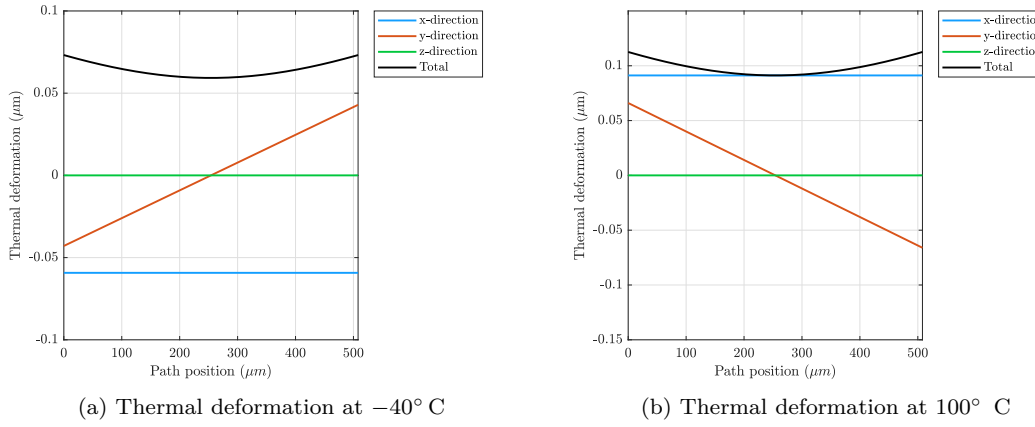


Figure 6.28: Thermal deformation analysis path *a* along with the drive mass (a) thermal deformation at -40° C (b) thermal deformation at 100° C .

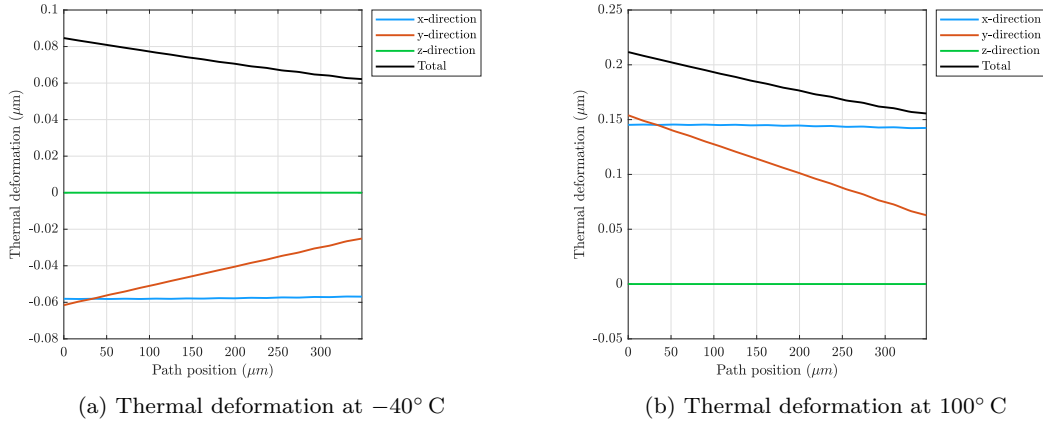


Figure 6.29: Thermal deformation analysis path *b* along with the sense frame (a) thermal deformation at -40° C (b) thermal deformation at 100° C .

2.71 or 2.72, in the proposed MEMS gyroscope operating temperature range of -40° C to 100° C and constant pressure of 1 atm, the Knudsen value varies from 0.0175 to 0.0275. Consequently, since this value is within $0.01 < K_n < 0.1$, the dominant flow regime remains slip flow. Since the drive and sense response amplifications at resonance directly depends on their respective quality factor values, a more effective information about the influence of the temperature variations on the MEMS gyroscope response could be obtained computing the quality factor values due to air damping, taking into account the effective viscosity of air. Figure 6.31 shows that, the effect of temperature change in the range of -40° C to 100° C on energy loss factor functions in the drive and sense direction ($1/Q_d$ and $1/Q_s$) are in practice negligible. With the aim of investigating only the temperature influence, the calculation of Q_d and Q_s is made using Equations 2.13 and 2.21, considering that the drive and sense frequencies are matched and correspond to the one obtained through the FEM-based thermal analysis, i.e $\omega_d = \omega_s$. Figure 6.31 shows that, as it will be demonstrated in the last section of this chapter, the variation of the mechanical sensitivity of

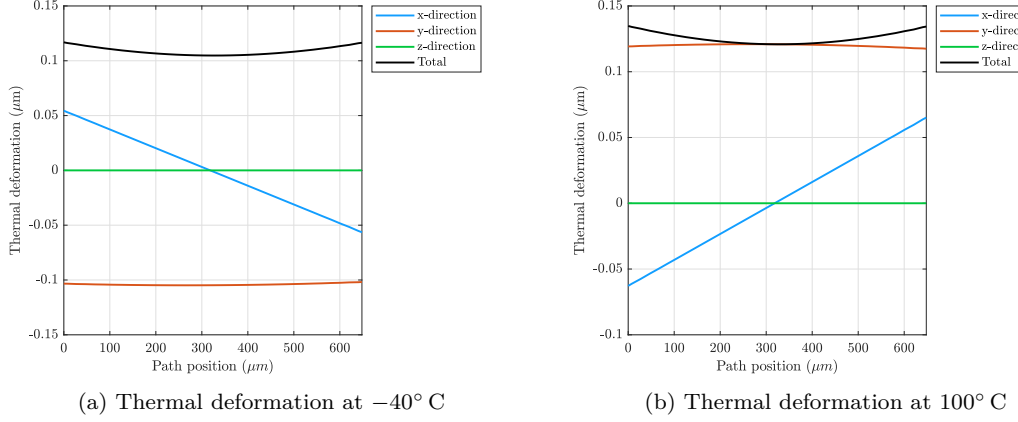


Figure 6.30: Thermal deformation analysis path c along with the sense frame (a) thermal deformation at -40°C (c) thermal deformation at 100°C .

the proposed MEMS gyroscope does not depend on the viscous damping variation but on the frequency mismatch due to thermal effects.

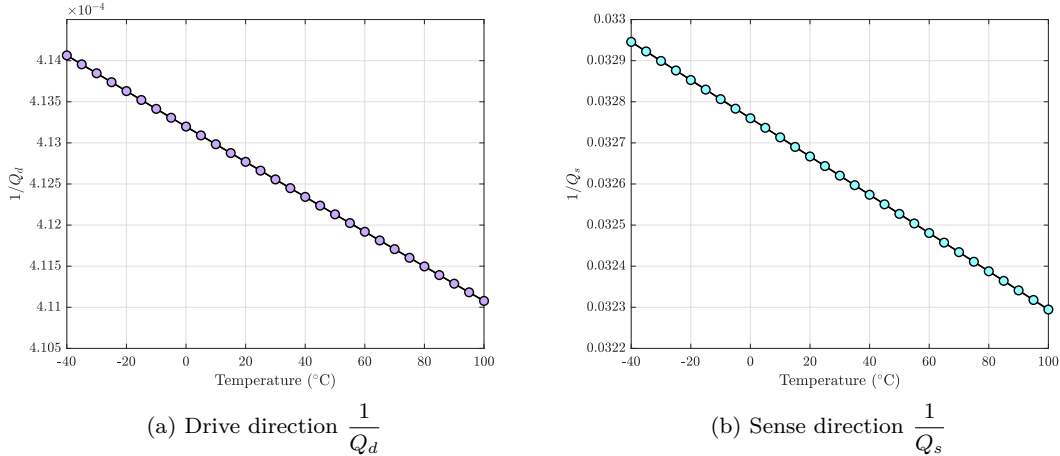


Figure 6.31: Energy loss factor for the proposed MEMS gyroscope with varying operating temperature in the range of -40°C to 100°C (a) Drive direction $\frac{1}{Q_d}$ (b) Sense direction $\frac{1}{Q_s}$.

6.6.2 Compensation of temperature variation effects

The mismatch between drive and sense mode frequency can cause the performance of the MEMS gyroscope to reduce dramatically since even a slight mismatch can reduce the amplitude response of the resonant gyroscope significantly. As previously demonstrated in this chapter, this error can be mitigated through the electrostatic frequency tuning, which allows to tune the sense mode frequency to approximate the drive mode one, guarantying the maximum possible mechanical sensitivity. In addition, since the sense frequency can be automatically tuned using the closed-loop

mode-matching control system, resonant frequency values can be maintained perfectly matched over the operating temperature range, achieving high and stable performance.

The tuning voltage V_t necessary to compensate the mismatch between drive and sense mode for a temperature variation in the range of -40°C to 100°C can be analytically computed from Equation 6.29, considering that at mode-matching $\omega_s = \omega_d$

$$V_t = \sqrt{\frac{\frac{k_y}{m_s} - \omega_d^2}{\eta}} \quad (6.32)$$

where the drive ω_d and mechanical sensing $\frac{k_y}{m_s}$ frequencies are those resulting from FEM-based modal analysis. In addition, according to Equation 6.30, η coefficient can be expressed as

$$\eta = \beta_{FIT} \frac{2N_t \epsilon_0 x_{0(t)} t}{m_s y_{0(t)}^3} \quad (6.33)$$

with $\beta_{FIT} = 2.13$. Since the tuning voltage V_t directly depends on the frequency mismatch, the curves in Figure 6.32a and 6.26, respectively representing the analytical tuning voltage and the mismatch between drive and sense mode in the temperature operating range, have a similar trend. As expected, an increase in the frequency mismatch results in an increase in the tuning voltage necessary to guarantee the mode-matching condition.

In the previous section it was shown that thermal deformations induce air-gap variation between tuning-comb fingers that clearly influences the electrostatic tuning force generated by each fingers pair. Accordingly, a FEM-based modal analysis should be carried out to determine the exact value of tuning tension V_t to compensate the mismatch between drive and sense mode for temperature variation in the rage of -40°C to 100°C . The exact tuning voltage value V_t is determined by applying the iterative approach of bisection method. At each iteration, the tuning voltage applied to the fixed electrodes is gradually increased and the drive and sense mode resonant frequencies are computed. If the driving frequency value is lower than the sensing one, it is concluded that the applied voltage is below the necessary voltage value to compensate the frequency mismatch. On the other hand, if the driving frequency is higher than the sensing one, it is conclude that the applied voltage is higher the necessary voltage value. The interval between these two limits is continuously decreased until the voltage interval is smaller than a predetermined accuracy. Figure 6.32b provides the tuning voltage V_t compensating the mismatch between the drive and sense mode resonant frequency in the temperature operating range of -40°C to 100°C . As expected, the temperature increase with respect to the room temperature leads to an increase in the frequency mismatch and, thus, in the tuning voltage value V_t .

As it was previously discussed, expansion or contraction due to temperature variation leads to change in the initial-gap between tuning comb-fingers and, thus, in the resulting electrostatic spring softening effect. However, this effect is not taking into account in the analytical model and this results in slight difference between the analytical and FEM-based tuning voltage values, as it is shown comparing the two curves in Figure 6.32, representing the analytical and FEM-based tuning voltage respectively.

Finally, a mechanical sensitivity analysis is carried out to investigate the effect of electrostatic tuning on the proposed MEMS gyroscope performances in the temperature operating range of -40°C to 100°C . Since the mechanical sensitivity of the gyroscope to an angular velocity input Ω_z depends on the frequency response amplitude in the sense direction, which in turn depends on the one in the drive direction, a FEM-based full harmonic analysis is performed considering temperature variations in the operating range. As it was shown in the previous section, the effect of temperature variation on the viscous damping coefficients can be neglected. This means that

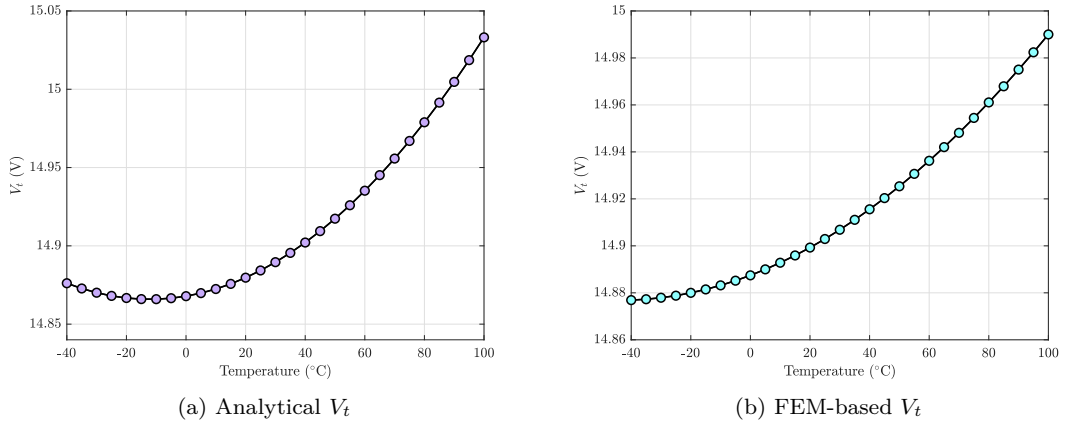


Figure 6.32: Tuning voltage V_t compensating the mismatch between drive and sense mode for a temperature variation in the range of -40°C to 100°C , with a reference temperature of $T_F = 25^\circ\text{C}$
 (a) Analytical (b) FEM-based analysis.

mechanical sensitivity is only influenced by the frequency mismatch between modes.

Two different harmonic analysis are performed: the first with no tuning voltage applied on the fixed tuning electrodes, i.e. $V_t = 0\text{ V}$, and the second with the tuning voltage V_t which allows to compensate the mismatch between drive and sense resonant frequency due to thermal change. The procedure is first to assign a uniform temperature varying in the range -40°C to 100°C to all structural nodes. In addition, the tuning voltage V_t , and the DC actuation voltage are respectively applied to Trans126 element nodes connected to tuning and drive combs moving fingers. A static analysis is then run with prestress effects turned on, considering the ambient temperature $T_F = 25^\circ\text{C}$. Finally a full harmonic analysis is carried out, applying an angular velocity $\Omega_z = 300\text{ rad/s}$ in the z-direction and an AC actuation voltage, including the prestress for the effects of the applied DC voltages and temperature change.

Figure 6.33 shows the mechanical sensitivity of the proposed MEMS gyroscope devices, when the actuation voltage is 50 V DC and 5 V AC and the angular velocity is $\Omega_z = 300^\circ/\text{s}$. Figure 6.33a shows the mechanical sensitivity variation in the temperature range of -40°C to 100°C , when no tuning voltage is applied on fixed tuning electrodes, i.e. $V_t = 0\text{ V}$, while Figure 6.33b shows the mechanical sensitivity when the tuning tension guarantying the mode-matching condition is applied to tuning electrodes. It is important to point out that there is a discontinuity in the plots, which corresponds to the reference temperature: in this condition, no thermal induced stresses and deformations are present. In addition, as previous discussed, the frequency mismatch leads to a decreasing in the sense output and MEMS gyroscope performance. Indeed, as it is evident by comparing mechanical sensitivity values obtained, the tuning application allows to maintain the MEMS gyroscope mechanical sensitivity at the highest possible value, even in the presence of temperature variations. Consequently, the drastically reduction of the device performance due to the frequency mismatch is prevented.

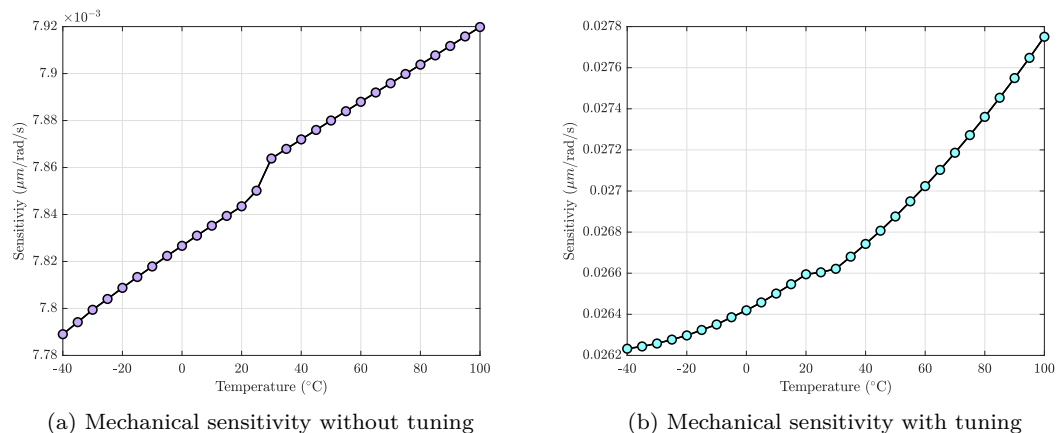


Figure 6.33: Mechanical sensitivity of the proposed dual mass MEMS gyroscope design in the temperature range of -40°C to 100°C , with reference temperature of $T_F = 25^{\circ}\text{C}$ (a) without tuning and (b) with tuning.

Chapter 7

Conclusion

7.1 Project findings

The research project described in this Thesis started with the aim of developing a new and innovative design of resonant mode-matched electrostatic z-axis MEMS gyroscope considering the foundry constraints of relatively low cost and commercially available Silicon-on-Insulator (SOI) based SOIMUMPs process.

The novelty of the proposed MEMS gyroscope design lies in the use of two separate masses for the drive and sense axis while minimizing the cross-axis sensitivity by decoupling the drive and sense mode displacements using a unique mechanical springs configuration.

Given that the prerogative of the resonant MEMS gyroscope is to operate with the drive and sense mode resonant frequency values perfectly matched in order to achieve the highest mechanical sensitivity, it is necessary to guarantee that the mode-matching condition is met during the device operations. However, manufacturing imperfections and variations in environment conditions may cause a shift in the resonant frequencies which in turn causes a mismatch between the drive and sense mode frequencies which leads to a drastic reduction in the device performances. For the compensation of the frequency mismatch between the drive and sense mode frequency due to microfabrication process tolerances and device operating temperature variations, comb-drive based electrostatic tuning has been implemented in the design. Tuning combs rely on the electrostatic spring softening phenomenon, which is used to tune electrostatically the sense frequency in order to be almost identical to the drive one.

Starting from scratch, the design process has been carried out iteratively in order to meet the constraints attributed to the SOIMUMPs microfabrication process and achieve the desired frequency characteristics, namely: the sense frequency has to be slightly higher than the drive one in order to apply the electrostatic tuning. Firstly the analytical model has been developed followed by the structural design. For the latter, the design process started from having to guarantee the dynamical performance: first design parameters are chosen based on the analytical model results. Then, it has been checked that these parameters meet the constraints attributed to the SOIMUMPs microfabrication process and, if not, a new iteration is required. A finite element simulation is finally necessary to validate the analytical model results, the structural design and eventually repeat the previous iterations.

At this stage, the comparison of the FEM-based modal results against the analytical ones has put in evidence a slight difference in the resonant frequency values which is mostly due to the fact that the analytical model does not exactly estimate the stiffness of suspension beam systems. A preliminary automatic mode-matching closed-loop system control is developed, based on the frequency response characteristic of the mass-spring oscillator related to the drive and sense mode.

Given the fact that the analytical model is the base for the developed automatic closed-loop mode-matching control, it has been calibrated by adopting the frequencies obtained with the FEM-based simulation in order to reach more accurate and reliable performances for the control system. The main objective of the developed automatic closed-loop mode-matching control is to tune automatically the sense mode resonant frequency in order to guarantee the already mentioned mode matching condition.

Finally, as proof of the reliability of the proposed MEMS gyroscope design and control system, and especially the effectiveness of the electrostatic tuning implementation, the device behaviour has been analyzed using a FEM-based simulations, considering operating temperature variations. It has been demonstrated that, even in the presence of temperature variations, the MEMS gyroscope mechanical sensitivity is maintained the highest possible, thanks to the electrostatic tuning implementation and, consequently, the drastically reduction of the device performance is prevented.

7.2 Future works

The results achieved during this thesis project and summarized in the previous paragraph underlines the value of the proposed MEMS gyroscope design. However, some future steps are required in order to validate and increase the design robustness.

In particular, the first step that should follow as future work is represented by the experimental validation of the proposed architecture in order to have a tangible feedback about the performance and the validity of the results obtained in simulations. Based on the outcome of such activity a new iteration in the design procedure may be required for minor fixes if the performance differs from the one observed through simulations. Moreover this activity could give the opportunity to better analyse the impact of the manufacturing process over the system and to incorporate those effects through the development of empirical correlations.

Once the design is validated, a particular focus could be in the improvement of the gyroscope model through the incorporation of the thermal effects inside the analytical model. Those improvements would then require a new validation phase about the compensation developed or incorporated in the system closed-loop control.

In addition, it would be also valuable to study more in detail the preliminary automatic mode matching control strategy, in particular from that point of view, a lot of effort should be directed into the development of real time control thorough control strategies different from the proposed PI, which may have better and more robust performance.

Another important open question is the modelling of the quadrature effect, as this is not included in the gyroscope model developed in this thesis. Several researches present in literature can be a good initial point. Finally, with the purpose of compensating the quadrature error, the design could be modified and the closed-loop system control implemented for the electrostatic tuning could be improved, including the quadrature error cancellation loop.

Appendix A

Single-degree-of-freedom oscillator

Consider the linear, single-degree-of-freedom oscillator of Figure A.1. It consists of a mass m , constrained by a linear spring of stiffness k and subject to a viscous damping force $c\dot{u}$ and to an additional external force F . The equation of motion is the following second order linear differential equation

$$m\ddot{u} + c\dot{u} + ku = f \quad (\text{A.1})$$

which can be rewritten as

$$\ddot{u} + 2\zeta\omega_n\dot{u} + \omega_n^2 u = \frac{f}{m} \quad (\text{A.2})$$

where $\omega_n = \sqrt{\frac{k}{m}}$ is the undamped natural frequency and $\zeta = \frac{c}{2m\omega_n}$ is the nondimensional damping factor.

If the oscillator is excited with a harmonic force $f = Fe^{j\omega t}$ at the frequency ω ¹, the governing equations A.2 becomes

$$\ddot{u} + 2\zeta\omega_n\dot{u} + \omega_n^2 u = \frac{F}{m}e^{j\omega t} \quad (\text{A.3})$$

The steady-state component u of the solution is still harmonic, of the form

$$u = Ue^{j\omega t} \quad (\text{A.4})$$

with U being a complex quantity. Substituting into the equation A.3, one finds

$$U = \frac{F/k}{1 - (\omega/\omega_n)^2 + 2j\zeta\omega/\omega_n} \quad (\text{A.5})$$

Since U is a complex quantity, it can be rewritten as a function of its amplitude $|U|$ and phase ϕ

$$U = |U|e^{j\phi} \quad (\text{A.6})$$

where both quantities $|U|$ and ϕ are functions of the excitation frequency ω

$$\begin{aligned} |U| &= \frac{F/k}{\sqrt{[1 - (\omega/\omega_n)^2]^2 + [2\zeta\omega/\omega_n]^2}} \\ \phi &= -\arctan\left(\frac{2\zeta\omega/\omega_n}{1 - (\omega/\omega_n)^2}\right) \end{aligned} \quad (\text{A.7})$$

¹The use of the complex exponential function $e^{j\omega t}$ instead of sine and cosine functions will simplify considerably the discussion. Once the solutions u is found, the real part of u gives the response to $f = F \cos \omega t$ and the imaginary part is the response to $f = F \sin \omega t$.

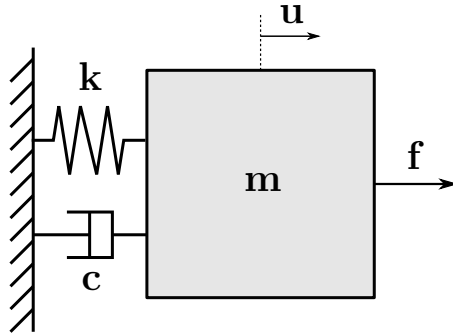


Figure A.1: Single-degree-of-freedom oscillator.

Consequently, substituting A.6 in Equation A.4, the solution u at the steady-state becomes

$$u = |U|e^{j(\omega t + \phi)} \quad (\text{A.8})$$

Therefore, if the excitation were of the form $f = F \cos \omega t$, at the steady-state the solution would be $u = |U| \cos(\omega t + \phi)$, while if the excitation were of the form $f = F \sin \omega t$, the solution would be $u = |U| \sin(\omega t + \phi)$.

As shown in Figure A.2, the damping strongly affects the amplitude and phase diagrams of U . In the undamped case, when the excitation frequency $\omega = \omega_n$, the dynamic response goes to infinity. When the damping is present, the amplitude expression is instead maximized at the frequency:

$$\omega_r = \omega_n \sqrt{1 - 2\zeta^2} \quad (\text{A.9})$$

For lightly damped systems, i.e. $\zeta \ll 1$, since the maximum of the amplitude occurs around at $\omega = \omega_n$, the following expression for the amplitude at resonance can be considered as a sufficient approximation

$$u_{res} = \frac{F}{2k\zeta} = \frac{F}{c\omega_n} \quad (\text{A.10})$$

The Quality factor or Q factor of the system is defined as maximum ratio of the amplitude to the static deflection, which is F/k . Taking the ratio of the amplitude at resonance to the static deflection, the Q factor of a lightly damped system reduces to

$$Q = \frac{1}{2\zeta} = \frac{m\omega_n}{c} \quad (\text{A.11})$$

It should be noticed that the Quality factor is one of the most important parameters of a single-degree-of-freedom oscillator, since it directly scales the amplitude at resonance

$$u_{res} = Q \frac{F}{k} \quad (\text{A.12})$$

At the resonant frequency, the phase is always -90° shifted from the excitation force phase. At frequency lower than the resonant frequency, the phase approaches 0° meaning that the solution u follows the excitation force closely. At frequency higher than the resonant frequency, the phase approaches to -180° . The transition from 0° to -180° is more abrupt for lower ζ value and the phase assumes an indeterminate form going from 0° to -180° for the undamped case.

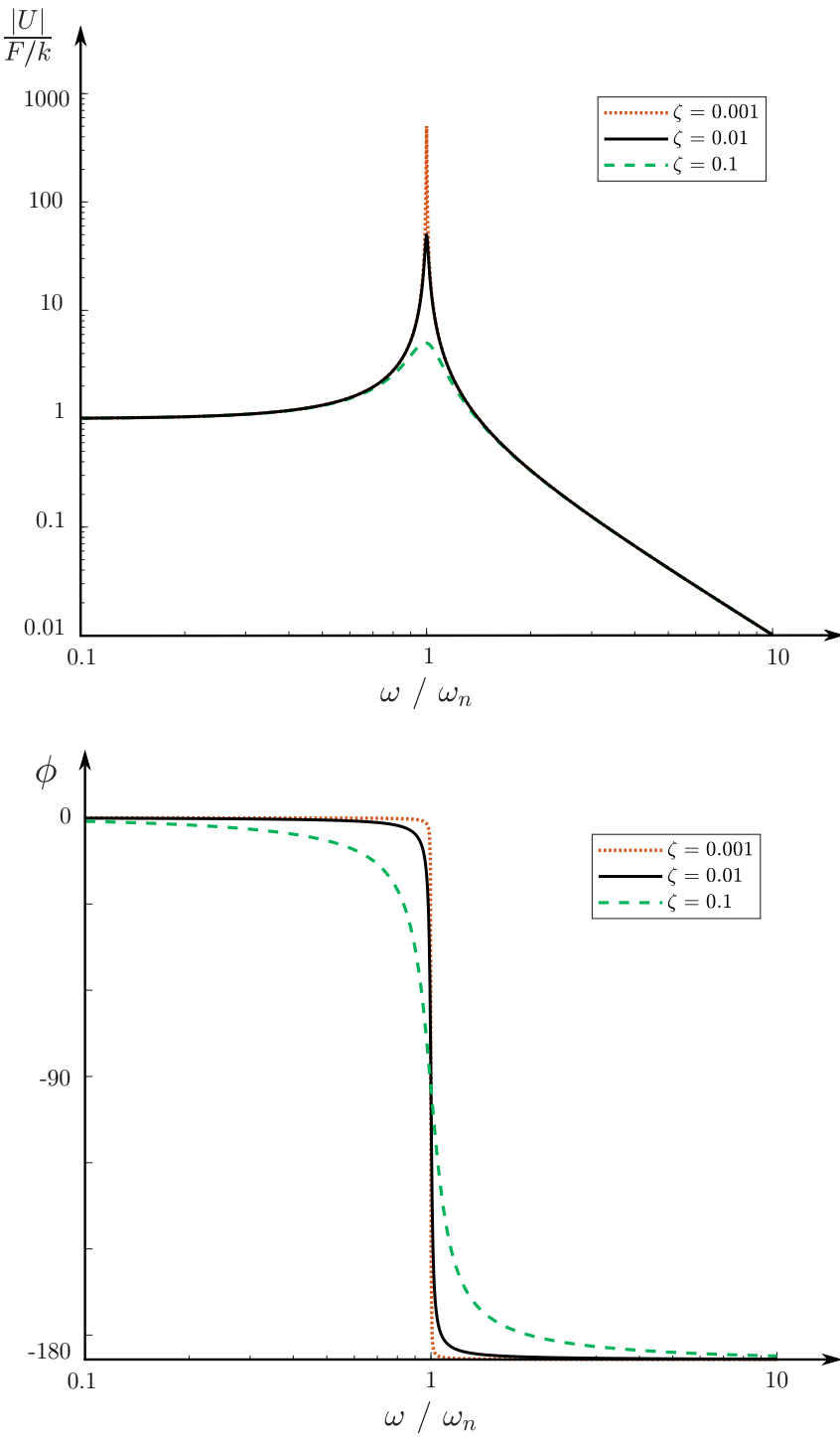


Figure A.2: Harmonic response of the damped linear oscillator $U(\omega) = |U(\omega)|e^{j\phi(\omega)}$. Amplitude $|U|$ normalized by using the factor F/k and phase ϕ diagrams.

Appendix B

SOIMUMPs Fabrication process

The objective of this appendix is to give a brief overview of relatively low cost and commercially available Silicon-on-Insulator (SOI) based SOIMUMPs process. SOIMUMPs process stands for Silicon on Insulator Multi-User MEMS Processes. It offers to fabricate high aspect ratio microstructures with minimum air damping, due to absence of substrate below the moving microstructure. Both of these attributes are generally desired in the design of high-performance MEMS inertial sensors.

The SOIMUMPs microfabrication process is a single-wafer silicon-on-insulator (SOI) micromachining process and allows patterning and etching on the SOI wafer using four mask layers with different thickness. The standard crystal silicon thicknesses offered are 10 μm and 25 μm , whereas the minimum feature size allowed is 2 μm . An overview of the microfabrication SOIMUMPs process steps is provided below.

1. The process starts with a SOI wafer as shown in Figure B.1a. This wafer consists of a 10 microm Silicon layer, a 1 μm Oxide layer, and a 400 μm Substrate layer. A Bottom Side Oxide layer is also initially present on the wafer.
2. The top surface of the silicon layer is doped by depositing a phosphosilicate glass (PSG) layer and then annealing is done at 1050° C in Argon (Figure B.2). It is followed by the removal of the PSG layer using wet chemical etching.
3. The first deposited layer in the process is the Pad Metal. First the wafer is coated with a negative photoresist and lithographically patterned by exposing the photoresist with light through the first level mask, also namely Padmetal mask, and then developing it. A metal stack consisting of 20 nm chrome and 500 nm gold is deposited over the photoresist pattern by e-beam evaporation (Figure B.3). The photoresist is then dissolved to leave behind metal in the opened areas(Figure B.4).
4. The wafers are coated with UV-sensitive photoresist and lithographically patterned by exposing the photoresist to UV light through the second level mask, namely SOI mask, and then developing it. The photoresist in exposed areas is removed, leaving behind a patterned photoresist mask for etching. Deep reactive ion etching (DRIE) is used to etch the Silicon down to the Oxide layer (Figure B.5). After etching, the photoresist is chemically stripped.
5. A frontside protection material is applied to the top surface of the Silicon layer. The wafer is then reversed, and the Substrate layer is lithographically patterned from the bottom side using the third mask level, namely TRENCH mask. This pattern is then etched into the Bottom Side Oxide layer using Reactive Ion Etching (RIE). A DRIE silicon etch is

subsequently used to etch completely through the Substrate layer, stopping on the Oxide layer. After the etch is completed, the photoresist is removed (Figure B.6).

6. A wet oxide etch process is used to remove the Oxide layer in the regions defined by the TRENCH mask. The frontside protection material is then stripped using a dry etch process. The remaining “exposed” Oxide layer is removed from the top surface using a vapor HF process. This allows for an electrical contact to the Substrate layer, and provides an undercut of the Oxide layer (Figure B.7).
7. A separate silicon wafer is used to fabricate a shadow mask for the Metal pattern. Standoffs are prefabricated into the shadow mask so that the shadow mask does not come into contact with patterned features in the Silicon layer of the SOI wafer. The shadow mask wafers are then coated with photoresist and the fourth level BLAKNMETAL is lithographically patterned. DRIE silicon etching is used to etch completely through the shadow mask wafer, producing through holes for the Metal to be evaporated. After the etch is completed, the photoresist is removed.
8. The shadow mask is then aligned and temporarily bonded to the SOI wafer, and the Metal is evaporated using an E-Beam tool. The Blanket Metal layer, consisting of 50 nm Cr and 600 nm Au, is deposited on the top surface of the Silicon layer only in the through hole regions of the shadow mask (Figure B.8).
9. After evaporation, the shadow mask is removed, leaving a patterned Metal layer on the SOI wafer (Figure B.9). The wafers are then diced using a laser, sorted and shipped to the SOIMUMPs user.

For the accurate release of microstructures and structural integrity, the SOIMUMPs microfabrication process has certain design rules to be followed. For the complex MEMS devices, like MEMS gyroscopes, this limits the design options for the MEMS designer. However, the author can refer to [17] for more detailed information about the SOIMUMPs process and rules to be followed during the design steps. The following Figures provide a graphical representation of the process steps.

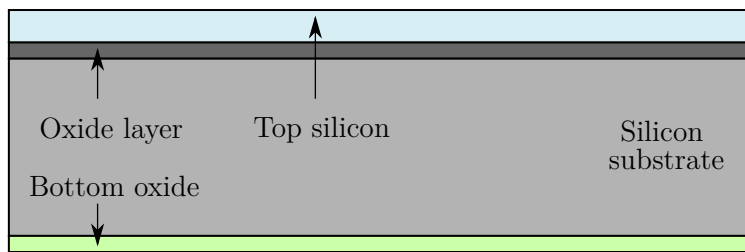


Figure B.1: The SOI wafer consists of a 10 μm Silicon layer, a 1 μm Oxide layer, and a 400 μm Substrate layer. A Bottom Side Oxide layer is also initially present on the wafer.

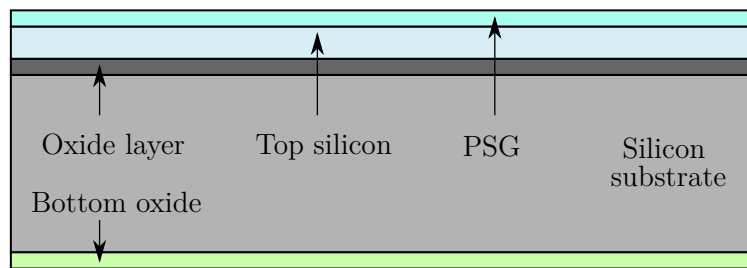


Figure B.2: The top surface of the silicon layer is doped by depositing a phosphosilicate glass (PSG) layer and then annealing is done at 1050°C in Argon. The PSG layer is subsequently removed using wet chemical etching.

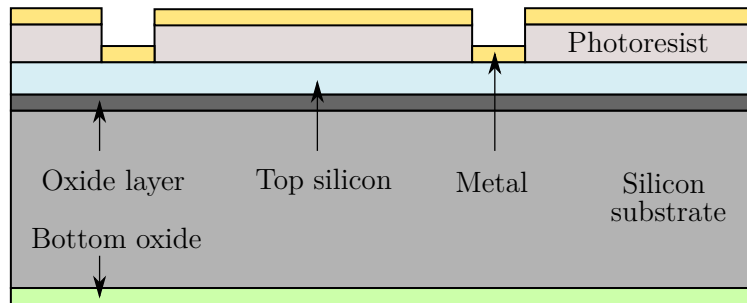


Figure B.3: The wafer is coated with a negative photoresist and lithographically patterned by exposing the photoresist with light through the first level mask, also namely Padmetal mask, and then developing it. A metal stack of 20 nm of chrome and 500 nm of gold is deposited using e-beam evaporation.

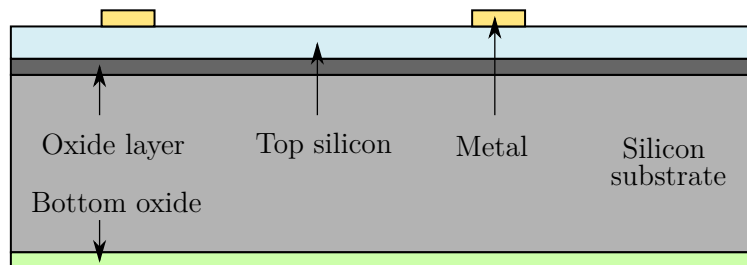


Figure B.4: The photoresist is lifted-off and the metal layer on top is also removed this way. The remaining metal parts define the first metallization layer.

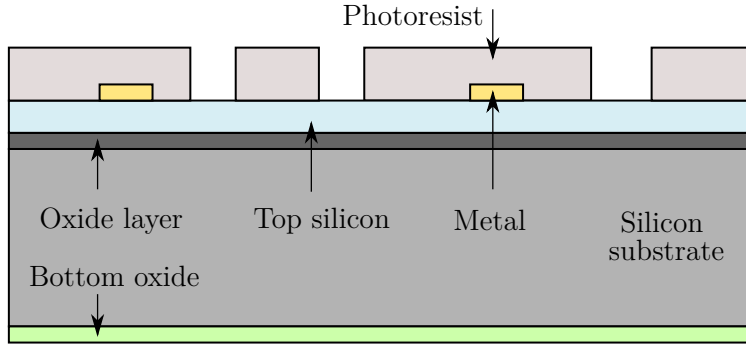


Figure B.5: Silicon is lithographically patterned with second mask level SOI. DRIE (Deep Reactive Ion Etching) is used for etching the silicon down to the Oxide layer. Photoresist is removed afterwards.

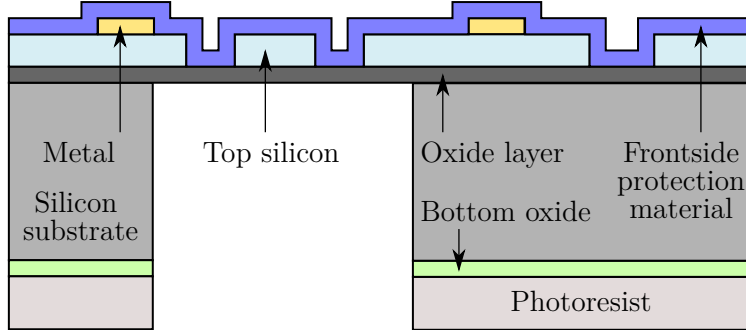


Figure B.6: A frontside protection material is applied to the top surface of the Silicon layer. The wafers are then reversed, and the Substrate layer is lithographically patterned from the bottom side using the third mask level, TRENCH. This pattern is then etched into the Bottom Side Oxide layer using Reactive Ion Etching (RIE). A DRIE silicon etch is subsequently used to etch these features completely through the Substrate layer.

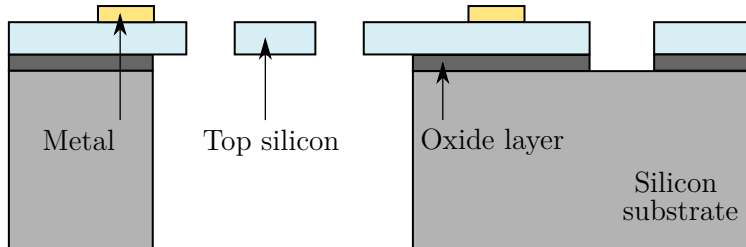


Figure B.7: A wet oxide etch process is then used to remove the Oxide layer in the regions defined by the TRENCH mask. The protective layer is then removed by dry etch process. After that, the remaining oxide layer is removed from the top surface using a vapor HF process and making the structures suspended.

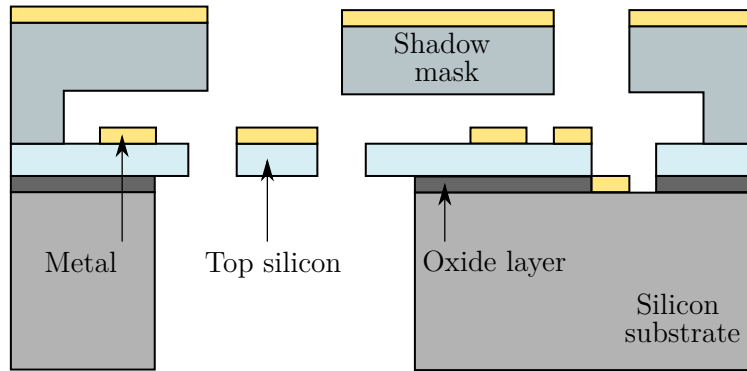


Figure B.8: The shadow mask is then aligned and temporarily bonded to the SOI wafer, and the Metal is evaporated using an E-Beam tool. The Blanket Metal layer, consisting of 50 nm Cr and 600 nm Au, is deposited on the top surface of the Silicon layer only in the through hole regions of the shadow mask.

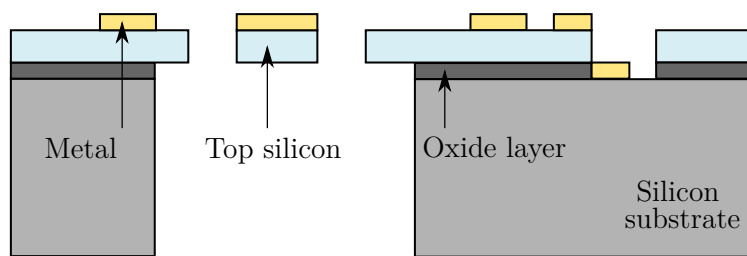


Figure B.9: The shadow mask is removed, leaving a patterned Metal layer on the SOI wafer. The wafers are diced using a laser, then the chips sorted and packaged for shipment.

Appendix C

Applying Prestress Effects in a Modal Analysis

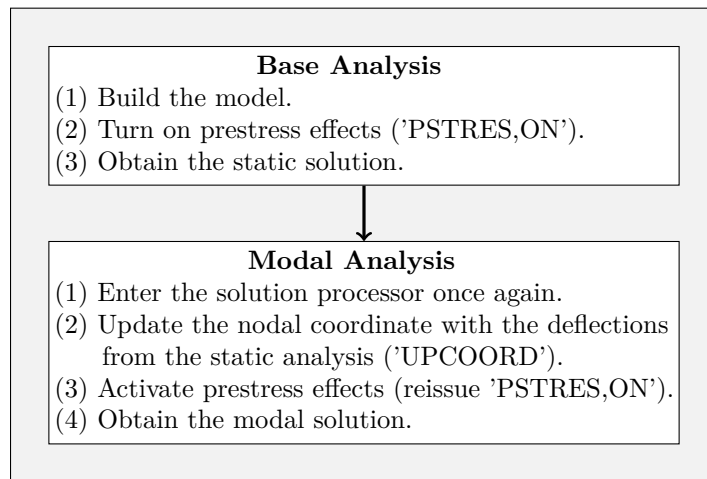


Figure C.1: Main steps to carry out a prestressed modal analysis in Ansys via PSTRES command.

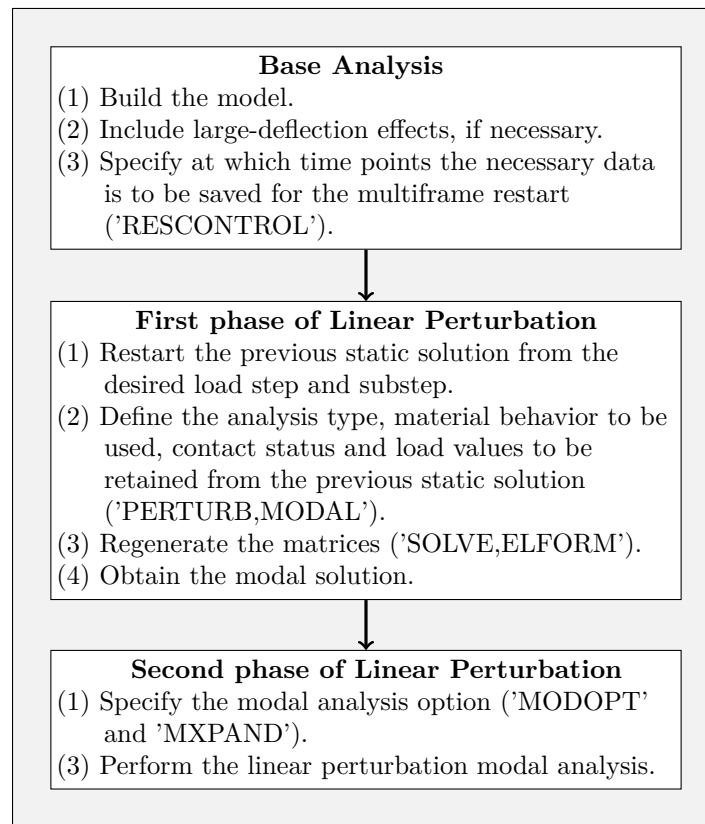


Figure C.2: Main steps to carry out a prestressed modal analysis in Ansys using Linear perturbation analysis procedure.

Appendix D

Automatic mode-matching system control implemented in SIMULINK

A closed-loop automatic mode-matching system control has been presented in this thesis for the compensation of the frequency mismatch between the drive and sense mode frequency due to microfabrication process tolerances and device operating temperature variations. The entire block diagram implemented in SIMULINK environment is provided in the following Figures.

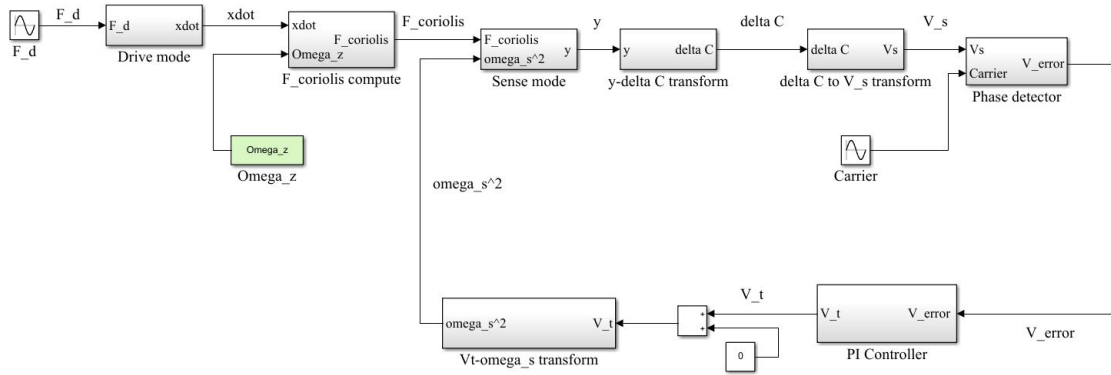


Figure D.1: Entire model of the automatic mode-matching system control implemented in SIMULINK.

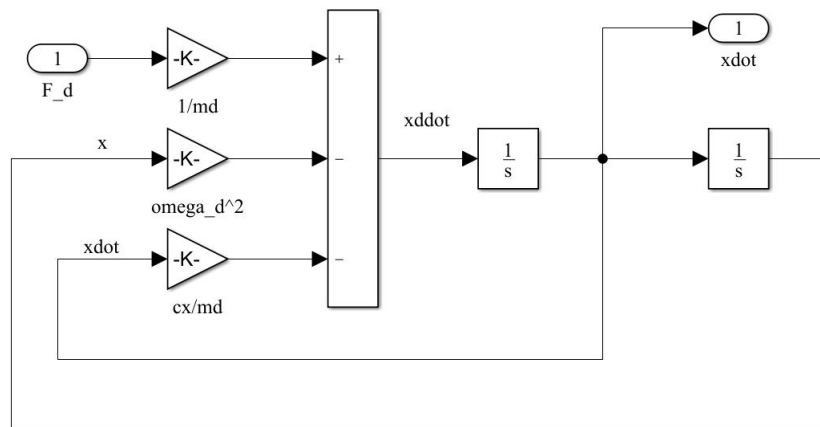


Figure D.2: Drive mode oscillator block.

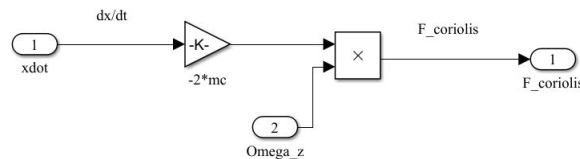


Figure D.3: $F_{Coriolis}$ computation block.

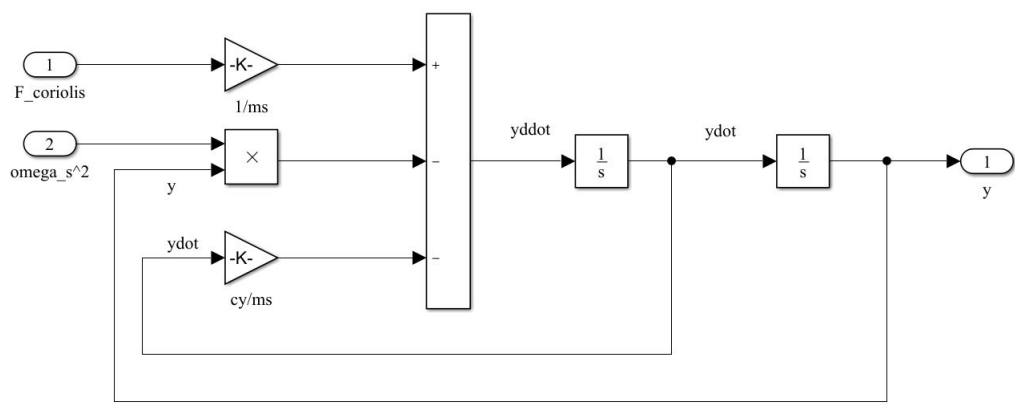


Figure D.4: Sense mode oscillator block.

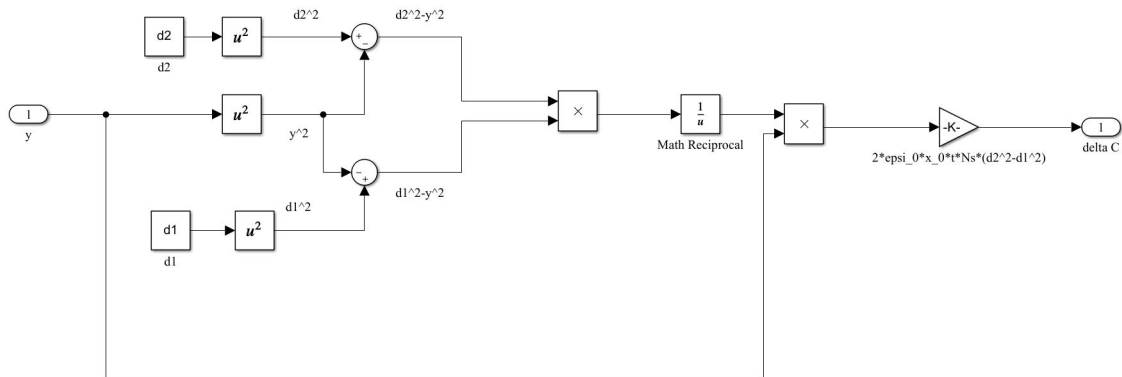


Figure D.5: Sense displacement to ΔC transform block.

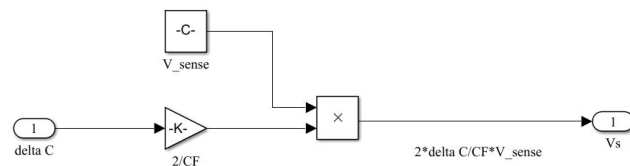


Figure D.6: ΔC to V_s transform block.

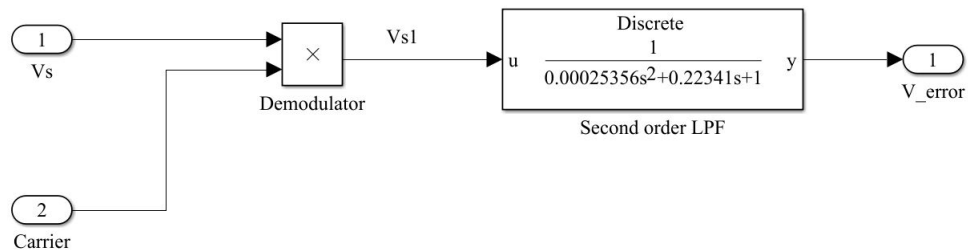


Figure D.7: Phase detector block.

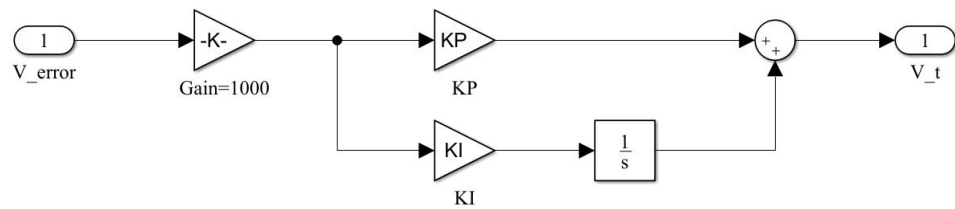


Figure D.8: PI controller block.

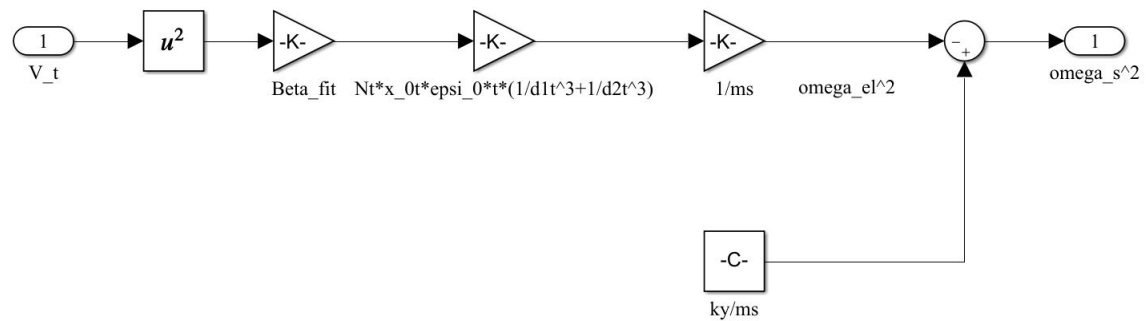


Figure D.9: V_t to ω_s transform block.

Bibliography

- [1] IEEE Standard Specification Format Guide and Test Procedure for Coriolis Vibratory Gyros. *IEEE Std 1431-2004*, pages 1–78, 2004.
- [2] IEEE Standard for Inertial Sensor Terminology. *IEEE Std 528-2019*, pages 1–35, 2019.
- [3] Cenk Acar and Andrei Shkel. *MEMS vibratory gyroscopes: structural approaches to improve robustness*. Springer Science & Business Media, 2008.
- [4] Giorgio Allegato, Carlo Valzasina, and Luca Zanotti. *Gyroscopes*, pages 899–914. 01 2020.
- [5] ANSYS, Inc. *Advanced Analysis Guide*, 2019.
- [6] ANSYS, Inc. *ANSYS Mechanical APDL Element reference*, 2019.
- [7] ANSYS, Inc. *ANSYS Mechanical APDL Modeling and Meshing Guide*, 2019.
- [8] ANSYS, Inc. *ANSYS Mechanical APDL Structural Analysis Guide*, 2019.
- [9] ANSYS, Inc. *ANSYS Mechanical APDL Theory Reference*, 2019.
- [10] ANSYS, Inc. *ANSYS Parametric Design Language Guide*, 2019.
- [11] ANSYS, Inc. *Mechanical APDL Coupled-Field Analysis Guide*, 2019.
- [12] Minhang Bao and Heng Yang. Squeeze film air damping in mems. *Sensors and Actuators A: Physical*, 136(1):3–27, 2007.
- [13] J. J. Blech. On Isothermal Squeeze Films. *Journal of Lubrication Technology*, 105(4):615–620, 10 1983.
- [14] Kenneth Brecher. On the Late Invention of the Gyroscope. In *APS April Meeting Abstracts*, volume 2012 of *APS Meeting Abstracts*, page J15.001, March 2012.
- [15] Syed Ali Raza Bukhari, Muhammad Mubasher Saleem, Umar Shahbaz Khan, Amir Hamza, Javaid Iqbal, and Rana Iqtidar Shakoor. Microfabrication process-driven design, fem analysis and system modeling of 3-dof drive mode and 2-dof sense mode thermally stable non-resonant mems gyroscope. *Micromachines*, 11(9):862, Sep 2020.
- [16] Alberto Corigliano, Raffaele Ardito, Claudia Comi, Attilio Frangi, Aldo Ghisi, and Stefano Mariani. *Mechanics of Microsystems*. John Wiley & Sons, 2017.
- [17] Allen Cowen, Greg Hames, D Monk, Steve Wilcenski, and Busbee Hardy. Soimumps design handbook (revision 8.0).
- [18] G De Pasquale and A Somà. Dynamic identification of electrostatically actuated mems in the frequency domain. *Mechanical Systems and signal processing*, 24(6):1621–1633, 2010.
- [19] Laura Del Tin. *Reduced-order modelling, circuit-level design and SOI fabrication of micro-electromechanical resonators*. PhD thesis, Alma Mater Studiorum - Università di Bologna, 2007.
- [20] JianCheng Fang and Jie Qin. Advances in atomic gyroscopes: A View from Inertial Navigation Applications. *Sensors (Basel, Switzerland)*, 12:6331–46, 12 2012.
- [21] G. K. Fedder. *Simulation of Microelectromechanical Systems*. PhD thesis, Department of Electrical Engineering and Computer Sciences University of California at Berkeley, 1994.
- [22] V. Kaajakari. *Practical MEMS*. Small Gear Pub., 2009.
- [23] C Kavitha and M Ganesh Madhan. Study of squeeze film damping characteristics under different gas mediums in a capacitive mems accelerometer. *Journal of the Brazilian Society*

- of Mechanical Sciences and Engineering*, 38(1):241–252, 2016.
- [24] Volker Kempe. *Inertial MEMS: principles and practice*. Cambridge University Press, 2011.
 - [25] Bongsang Kim, Matthew Hopcroft, Rob Candler, Chandra Jha, Manu Agarwal, Renata Melamud, Saurabh Chandorkar, Gary Yama, and Thomas Kenny. Temperature dependence of quality factor in mems resonators. *Microelectromechanical Systems, Journal of*, 17:755 – 766, 07 2008.
 - [26] M.J. Madou. *Fundamentals of Microfabrication: The Science of Miniaturization, Second Edition*. Taylor & Francis, 2002.
 - [27] N. Maluf and K. Williams. *An Introduction to Microelectromechanical Systems Engineering*. Artech House Microelectromechanical Systems. Artech House, 2004.
 - [28] Jan Mehner. *Simulation methods for the mechanical nonlinearity in MEMS gyroscopes*. PhD thesis, Technische Universität Chemnitz, 2019.
 - [29] Damiano Milani. *A new approach for mechanical design and quadrature compensation of MEMS gyroscopes*. PhD thesis, Department of Mechanical Engineering Politecnico di Milano, 2016.
 - [30] L Mol, LA Rocha, E Cretu, and RF Wolffentbuttel. Squeezed film damping measurements on a parallel-plate mems in the free molecule regime. *Journal of micromechanics and microengineering*, 19(7):074021, 2009.
 - [31] Rudra Pratap, Suhas Mohite, and Ashok Pandey. Squeeze film effects in mems devices. *Journal of the Indian Institute of Science*, 87, 01 2007.
 - [32] Doruk Senkal and A.M. Shkel. *Whole-Angle MEMS Gyroscopes: Challenges and Opportunities*. 05 2020.
 - [33] S.D. Senturia. *Microsystem Design*. Springer US, 2005.
 - [34] M.K. Thompson and J.M. Thompson. *ANSYS Mechanical APDL for Finite Element Analysis*. Elsevier Science, 2017.
 - [35] Haoran Wen. *Toward Inertial-Navigation-on-Chip: The Physics and Performance Scaling of Multi-Degree-of-Freedom Resonant MEMS Gyroscopes*. Springer Nature, 2019.
 - [36] Guo Zhanshe, Cheng Fucheng, Li Boyu, Cao Le, Lu Chao, and Song Ke. Research development of silicon MEMS gyroscopes: a review. *Microsystem Technologies*, 21(10):2053–2066, 2015.